


DIFFUSION DISTRIBUTION OF Cr AND Mn IMPURITY ATOMS IN SILICON

Giyosiddin H. Mavlonov^a, Khurshid Kh. Uralbaev^a,  Bobir O. Isakov^{a,b,*},
 Zabarjad N. Umarchodjaeva^a,  Shakhzod I. Hamrokulov^a

^aTashkent State Technical University, University St., 2, 100095, Tashkent, Uzbekistan

^bTashkent State Technical University Kokand Branch, Usman Nasir St., 66A, 150700, Fergana, Uzbekistan

Corresponding Author e-mail: bobir6422isakov@gmail.com

Received February 8, 2025; revised April 1, 2025; accepted April 14, 2025

This work presents theoretical calculations of the diffusion coefficient, solubility, and diffusion distribution of Mn and Cr impurity atoms in silicon. The results of theoretical studies showed that the distribution of Cr element atoms in silicon is slightly different from the distribution of Mn element atoms in silicon, while the remaining physical and chemical properties are almost identical. Also, if a Mn atom is placed at a node in a silicon single crystal, it will have three charge states: neutral – Mn^0 , one electron lost – Mn^{+1} , and two electrons lost – Mn^{+2} . Similarly, if a Cr atom is placed at the node of a silicon single crystal, it will have four different charge states: neutral – Cr^0 , one electron lost – Cr^{+1} , two electrons lost – Cr^{+2} , and three electrons lost – Cr^{+3} . Therefore, it is relevant to study the properties of doped silicon with Cr impurity atoms.

Keywords: Silicon; Impurity atoms; Diffusion; Manganese; Chromium; Distribution

PACS: 61.72.uf, 68.43.Jk

1. INTRODUCTION

It is known that in the Si semiconductor, B, Al, In, and Ga impurities form acceptor energy levels, and P, Sb, and As impurities form donor energy levels. These inclusions have high solubility ($N_{\text{III,V}} \sim 10^{19} \div 10^{21} \text{ cm}^{-3}$) in Si semiconductor, but their diffusion coefficients ($D_{\text{III,V}}(T) \sim 10^{-14} \div 10^{-11} \text{ cm}^2/\text{s}$) are very small [1-4]. Group III and V elements are doped into the Si semiconductor to form a p - n structure to develop various electronic devices such as solar cells, semiconductor diodes, and transistors [5-8]. It is very difficult to doped group III and V elements through the entire thickness of a Si sample by diffusion. Therefore, it is not possible to obtain strongly compensated Si using these impurities. Also, almost 100% of the atoms of elements of groups III and V are located at the crystal lattice node of the Si semiconductor and participate in sp^3 hybrid bonding. Therefore, magnetic properties are not observed in Si samples doped with group III and V elements.

It is known from the authors' work that the magnetic properties of the Si semiconductor are mainly formed as a result of doping with d and f group elements [9-11]. The use of electron spin in semiconductor devices opens up a new area of potential applications in high-speed, low-power spintronic devices [12-14]. One of the main research areas in this field is ferromagnetic semiconductors, which are created by magnetic and electrical doping of classical semiconductor materials [15,16]. Determining the ferromagnetic properties of Si, the most important material in the electronics industry, is important. To this end, many scientists are conducting theoretical and practical research. The electronic configuration of the element Mn is $1s^2 2s^2 2p^6 3s^2 3p^6 3d^5 4s^2$, the electronic configuration of the element Cr is $1s^2 2s^2 2p^6 3s^2 3p^6 3d^5 4s^1$, and these elements are d group elements, and their physical and chemical properties are very similar to each other. Therefore, this work is devoted to theoretical calculations of the distribution of charge carriers in silicon doped with Mn and Cr impurity atoms.

2. THEORETICAL PART

2.1. Charge carrier distribution

It is known that diffusion is divided into diffusion from a finite (1) [17] and an infinite (2) [17] source, depending on the ratio of the amount of impurity and the solubility in the semiconductor. The diffusion distribution of impurity atoms is calculated using the following function:

$$C(T) = C_0 \cdot \exp\left(\frac{-x^2}{4 \cdot D \cdot t}\right) \quad (1)$$

$$C_{\infty}(T) = C_0 \cdot \operatorname{erfc}\left(\frac{x}{2\sqrt{D \cdot t}}\right) \quad (2)$$

where, x – is the depth of penetration of the impurity atoms into the crystal, D – is the diffusion coefficient, t – is the diffusion time, C_0 – is the maximum solubility of the impurity atoms in the crystal at temperature T , $C(T)$ (from a finite source) and $C_{\infty}(T)$ (from an infinite source) are the concentrations of the impurity atoms, $\operatorname{erfc}(\eta)$ – is the Gaussian error function, and η – is the argument of the Gaussian error function.

Therefore, to calculate the diffusion distribution of impurity atoms in silicon, we need to determine the temperature dependence of the diffusion coefficient, the temperature dependence of the maximum solubility of impurity atoms, and the Gaussian error function.

2.2. Diffusion coefficient

The diffusion coefficient is determined using the following expression (3):

$$D(T) = D_0 \cdot \exp\left(-\frac{E_a}{kT}\right) \quad (3)$$

where E_a – is the activation energy, k – is the Boltzmann constant, D_0 – is the diffusion constant at infinite temperature, and T – is the absolute temperature.

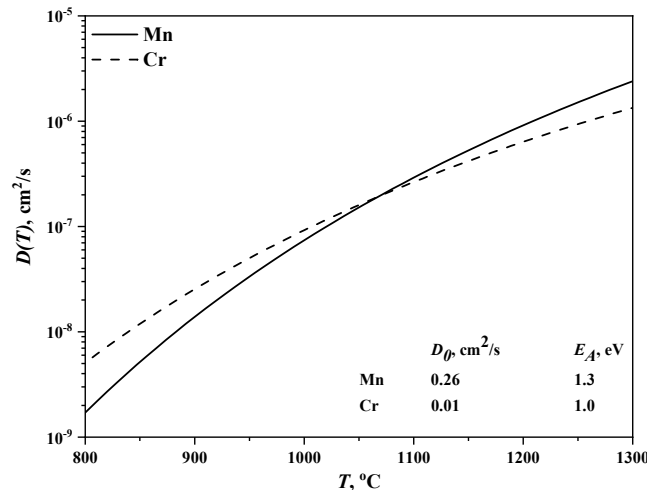


Figure 1. Diffusion coefficient of Mn and Cr impurity atoms in silicon.

From Figure 1, it can be seen that $D_{\text{Cr}} > D_{\text{Mn}}$ up to temperatures $T_1 < 1050$ °C, $D_{\text{Cr}} \approx D_{\text{Mn}}$ in the temperature range 1050 °C $\leq T_2 \leq 1100$ °C, and $D_{\text{Cr}} < D_{\text{Mn}}$ at temperatures above $T_3 > 1100$ °C.

2.3. Solubility of impurity atoms

The temperature dependence of the maximum solubility of impurity atoms in a crystal is determined by the following formula:

$$N(T) = N_0 \cdot \exp\left(-\frac{E_s}{k \cdot T}\right) \quad (4)$$

where N_0 – is a quantity equal to the maximum solubility of the impurity atoms at infinitely high temperature, and E_s – is the solubility energy.

From Figure 2, it can be seen that the solubility of Mn and Cr impurity atoms in silicon is almost equal to each other.

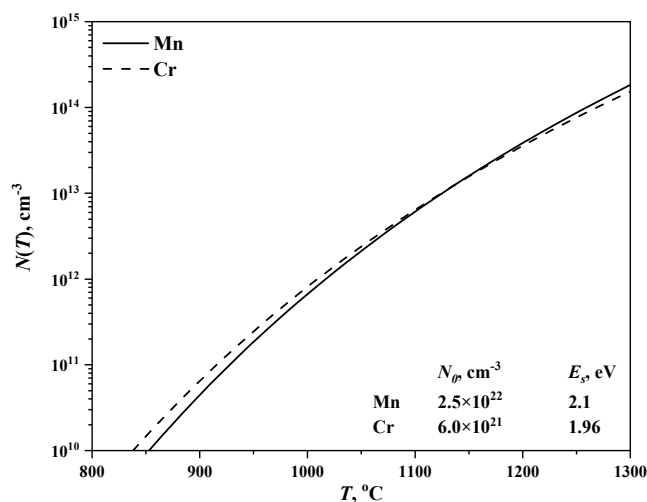


Figure 2. Solubility of Mn and Cr impurity atoms in silicon

2.4. Gaussian error function

The Gaussian error function is defined using the following expression:

$$\operatorname{erfc}(\eta) = 1 - \operatorname{erf}(\eta), \quad (5)$$

$$\operatorname{erf}(\eta) = \frac{2}{\sqrt{\pi}} \int_0^{\eta} \exp(-t^2) dt, \quad (6)$$

$$\operatorname{erfc}(\eta) = 1 - \frac{2}{\sqrt{\pi}} \int_0^{\eta} \exp(-t^2) dt. \quad (7)$$

Figure 3 depicts the graph of the relationship $\operatorname{erf}(\eta) = f(\eta)$, which can be used in calculations.

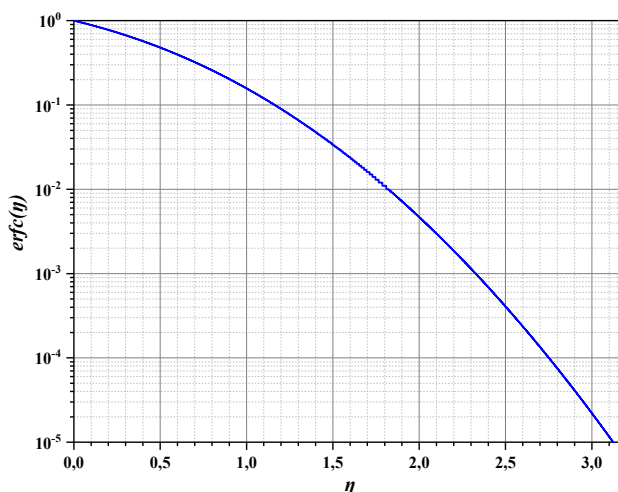


Figure 3. Gaussian error function ($\operatorname{erf}(\eta)$) as a function of its argument (η)

3. RESULTS OF THEORETICAL CALCULATION

In the works of the authors [18,19], the diffusion process of Mn impurity atoms into Si was carried out in the temperature range $T \sim 1000 \div 1100$ °C. Based on the above data, the diffusion distribution of Mn and Cr impurity atoms in Si was calculated in the temperature range $T \sim 950 \div 1150$ °C (Figure 5 and Figure 6).

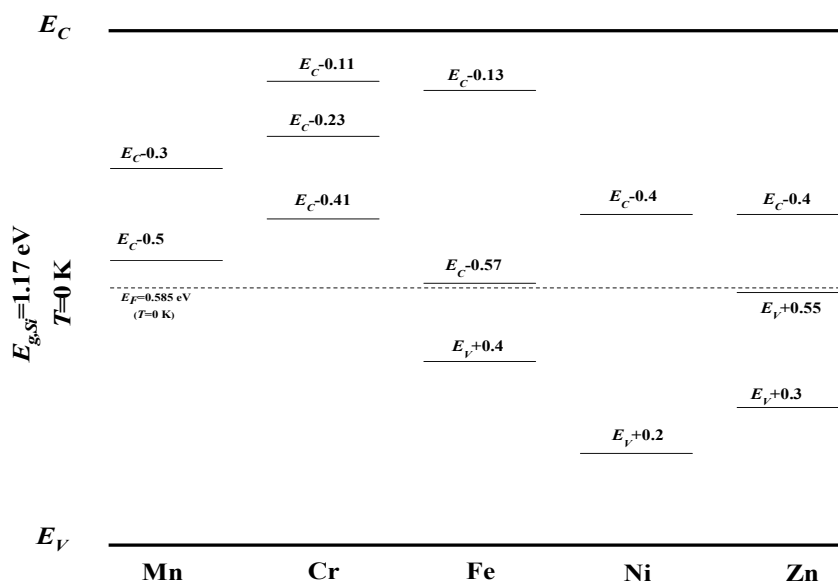


Figure 4. Energy levels of some elements in silicon.

It is known that Mn impurity atoms form two donor energy levels $E_C - 0.3$ eV and $E_C - 0.5$ eV in silicon [20] (see Figure 4). Cr impurity atoms form three donor energy levels in silicon, $E_C - 0.11$ eV, $E_C - 0.23$ eV, and $E_C - 0.41$ eV [20] (see Figure 4). As can be seen from figure 4, when a Mn impurity atom is placed at a node of a silicon single crystal, it will have three charge states: neutral-Mn⁰, one electron lost-Mn⁺, and two electrons lost-Mn²⁺. Similarly, if Cr

impurity atoms is placed at the node of a silicon single crystal, it will have four different charge states: neutral – Cr^0 , one electron lost – Cr^{+1} , two electrons lost – Cr^{+2} , and three electrons lost – Cr^{+3} .

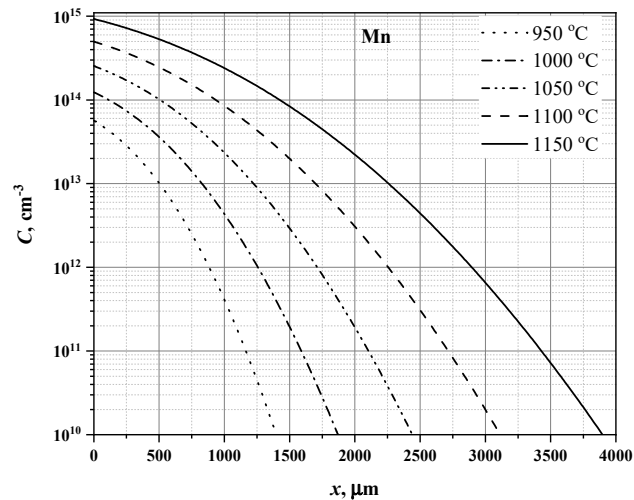


Figure 5. Diffusion distribution of Mn dopant atoms in silicon calculated using equations (2), (3) and (4)

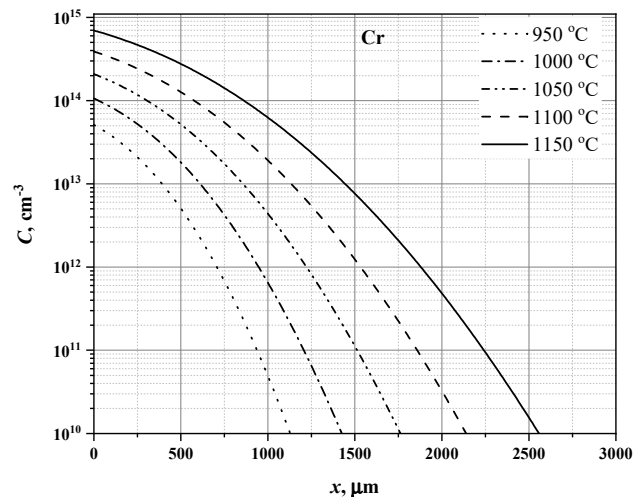


Figure 6. Diffusion distribution of Cr dopant atoms in silicon calculated using equations (2), (3) and (4)

4. CONCLUSION

Currently, many scientists have studied the magnetic properties of silicon doped with Mn [9-20] impurity atoms, while the magnetic properties of silicon doped with Cr [21] impurity atoms have been less studied. Theoretical calculations show that the diffusion coefficients of Mn and Cr impurity atoms in silicon (Figure 1) and maximum solubility (Figure 2) are very close to each other, but their electronic configurations and distribution in silicon (Figures 5 and 6) are slightly different. Therefore, it requires a lot of theoretical and practical research to study the electrical-physical, electromagnetic, magnetic, optical, photoelectric, and magneto-photon properties of a Si sample doped with Cr impurity atoms.

ORCID

Bobir O. Isakov, <https://orcid.org/0000-0002-6072-3695>; Zabarjad N. Umarkhodjaeva, <https://orcid.org/0009-0000-1488-6410>
Shakhzod I. Hamrokulov, <https://orcid.org/0009-0000-2701-4320>

REFERENCES

- [1] Kh.M. Iliev, S.V. Kovesnikov, B.O. Isakov, E.Zh. Kosbergenov, G.A. Kushiev, and Z.B. Khudoynazarov. "The Elemental Composition Investigation of Silicon Doped with Gallium and Antimony Atoms." *Surface Engineering and Applied Electrochemistry*, **60**(4), 633–639. (2024). <https://doi.org/10.3103/S106837552470025X>
- [2] Kh.M. Iliev, N.F. Zikrillayev, K.S. Ayupov, B.O. Isakov, B.A. Abdurakhmanov, Z.N. Umarkhodjaeva, and L.I. Isamididnova, "Effect of GaSb Compound on Silicon Bandgap Energy," *Journal of nano- and electronic physics*, **16**(2), 02004(4pp) (2024). [https://doi.org/10.21272/jnep.16\(2\).02004](https://doi.org/10.21272/jnep.16(2).02004)
- [3] N.F. Zikrillayev, S.B. Isamov, B.O. Isakov, T. Wumaier, Li wen Liang, J.X. Zhan, and T. Xiayimulati, "New Technological Solution for the Tailoring of Multilayer Silicon-based Systems with Binary Nanoclusters Involving Elements of Groups III and V," *Journal of nano- and electronic physics*, **15**(6), 06024 (2023). [https://doi.org/10.21272/jnep.15\(6\).06024](https://doi.org/10.21272/jnep.15(6).06024)

- [4] N.F. Zikrillae, M.K. Khakkulov, and B.O. Isakov, "The Mechanism of the formation of binary compounds between Zn and S impurity atoms in Si crystal lattice," East Eur. J. Phys. (4), 177-181 (2023). <https://doi.org/10.26565/2312-4334-2023-4-20>
- [5] M.K. Bakhadirkhanov, Z.T. Kenzhaev, Kh.S. Turekeev, B.O. Isakov, and A.A. Usmonov, "Gettering properties of nickel in silicon photocells," Technical Physics, **67**(14), (2022). <https://doi.org/10.21883/TP.2022.14.55221.99-21>
- [6] G.A. Kushiev, B.O. Isakov, and U.X. Mukhammadjonov, "The Prospects of Obtaining a New Material with a Hetero-Baric Structure $\text{Ge}_x\text{Si}_{1-x}\text{-Si}$ Based on Silicon for Photo Energy Applications," Journal of nano- and electronic physics, **16**(3), 03003 (2024). [https://doi.org/10.21272/jnep.16\(3\).03003](https://doi.org/10.21272/jnep.16(3).03003)
- [7] X.M. Iliyev, V.B. Odzhaev, S.B. Isamov, B.O. Isakov, B.K. Ismaylov, K.S. Ayupov, Sh.I. Hamrokulov, and S.O. Khasanbaeva, "X-ray diffraction and Raman spectroscopy analyses of GaSb-enriched Si surface formed by applying diffusion doping technique," East Eur. J. Phys. (3), 363-369 (2023). <https://doi.org/10.26565/2312-4334-2023-3-38>
- [8] X.M. Iliyev, S.B. Isamov, B.O. Isakov, U.X. Qurbonova, and S.A. Abduraxmonov, "A Surface study of Si doped simultaneously with Ga and Sb," East Eur. J. Phys. (3), 303-307 (2023). <https://doi.org/10.26565/2312-4334-2023-3-29>
- [9] N.F. Zikrillae, G.A. Kushiev, S.B. Isamov, B.A. Abdurakhmanov, and O.B. Tursunov, "Photovoltaic Properties of Silicon Doped with Manganese and Germanium," Journal of nano- and electronic physics, **15**(1), 01021 (2023). [https://doi.org/10.21272/jnep.15\(1\).01021](https://doi.org/10.21272/jnep.15(1).01021)
- [10] M.O. Tursunov, Kh.M. Iliev, and B.K. Ismaylov, "High-temperature analysis of silicon properties with manganese-oxygen binary complexes," Physical Sciences and Technology, **11**(1-2), 4-12 (2024). <https://doi.org/10.26577/phst2024v11i1a1>
- [11] X.M. Iliyev, Z.B. Khudoynazarov, B.O. Isakov, M.X. Madjitov, and A.A. Ganiyev, "Electrodiffusion of manganese atoms in silicon," East Eur. J. Phys. (2), 384-387 (2024). <https://doi.org/10.26565/2312-4334-2024-2-48>
- [12] M. Alawein, and H. Fariborzi, "Circuit Models for Spintronic Devices Subject to Electric and Magnetic Fields," Journal on Exploratory Solid-State Computational Devices and Circuits, **4**(2), (2018). <https://doi.org/10.1109/JXCDC.2018.2876456>
- [13] I. Zutic, J. Fabian, and S.D. Sarma, "Spintronics: Fundamentals and applications," Reviews of Modern Physics, **76**, (2004). <https://doi.org/10.1103/RevModPhys.76.323>
- [14] B. Behin-Aein, A. Sarkar, S. Srinivasan, and S. Datta, "Switching energydelay of all spin logic devices," Appl. Phys. Lett. **98**(12), 123510-1–123510-3 (2011). <https://doi.org/10.1063/1.3567772>
- [15] I.V. Krauklis, O.Yu. Podkopaeva, and Yu.V. Chizhov, "DFT Modeling of Mn Charged States in $\text{Ga}_{1-x}\text{Mn}_x\text{As}$ Diluted Ferromagnetic Semiconductors: the Cluster Approach," Semiconductors, **48**(8), 1010–1016 (2014). <https://doi.org/10.1134/S1063782614080168>
- [16] M. Takahashi, "Carrier States in Ferromagnetic Semiconductors and Diluted Magnetic Semiconductors—Coherent Potential Approach," Materials, **3**, 3740-3776 (2010). <https://doi.org/10.3390/ma3063740>
- [17] Glitzky and W. Merz, and K.H. Homann, "Single dopant diffusion in semiconductor technology," Math. Meth. Appl. Sci. **27**, 133-154 (2004). <https://doi.org/10.1002/mma.447>
- [18] M.K. Bakhadirkhanov, Kh.M. Iliev, S.A. Tachilin, S.S. Nasriddinov, and B.A. Abdurakhmanov, "Impurity Photovoltaic Effect in Silicon with Multicharge Mn Clusters," Applied Solar Energy, **44**(2), 132–134 (2008). <https://doi.org/10.3103/S0003701X08020151>
- [19] M.K. Bakhadirkhanov, S.B. Isamov, N.F. Zikrillae, Kh.M. Iliev, G.Kh. Mavlonov, S.V. Koveshnikov and Sh.N. Ibodullaev, "Functional Capabilities of Silicon with Nanoclusters of Manganese Atoms", Surface Engineering and Applied Electrochemistry, Vol. 56, No. 6, pp. 734–739. (2020). <https://doi.org/10.3103/S1068375520060046>
- [20] M.K. Bakhadirkhanov, Sh.I. Askarov and N. Norkulov, "Some Features of Chemical Interaction between a Fast Diffusing Impurity and a Group VI Element in Silicon," Phys. Stat. Sol. (a), **142**, 339 (1994). <https://doi.org/10.1002/PSSA.2211420206>
- [21] Y. Ezer, J. Harkonen, S. Arpiainen, V. Sokolov, P. Kuivalainen, J. Saarihahti, and J. Kaitila, "Diffusion Barrier Performance of thin Cr Films in the Cu/Cr/Si Structure", Physica Scripta **T79**, 228E231 (1999). [https://doi.org/10.1016/S0025-5408\(98\)00117-2](https://doi.org/10.1016/S0025-5408(98)00117-2)

ДИФУЗІЙНИЙ РОЗПОДІЛ ДОМІШКОВИХ АТОМІВ Cr ТА Mn У КРЕМНІЇ

Гійосіддін Х. Мавлонов^a, Хуршид Х. Уралбаєв^a, Бобір О. Ісаков^{a,b}, Забарджад Н. Умарходжаєва^a,
Шахзод І. Хамрокулов^a

^aТашкентський державний технічний університет, вул. Університетська, 2, 100095, Ташкент, Узбекистан

^bТашкентський державний технічний університет Кокандська філія, вул. Усмана Насіра, 66А, 150700, Фергана, Узбекистан

У роботі наведено теоретичні розрахунки коефіцієнта дифузії, розчинності та дифузійного розподілу домішкових атомів Mn і Cr у кремнії. Результати теоретичних досліджень показали, що розподіл атомів елемента Cr у кремнії дещо відрізняється від розподілу атомів елемента Mn у кремнії, а решта фізико-хімічних властивостей майже ідентичні. Крім того, якщо атом Mn помістити у вузол монокристалу кремнію, він матиме три зарядові стани: нейтральний – Mn^0 , один втрачений електрон – Mn^{+1} і два втрачені електрони – Mn^{+2} . Подібним чином, якщо атом Cr помістити у вузол монокристала кремнію, він матиме чотири різні стани заряду: нейтральний – Cr^0 , один втрачений електрон – Cr^{+1} , два втрачені електрони – Cr^{+2} і три втрачені електрони – Cr^{+3} . Тому актуальним є дослідження властивостей легованого кремнію домішковими атомами Cr.

Ключові слова: кремній; домішкові атоми; дифузія; марганець; хром; розподіл

EFFECT OF Cu \rightarrow Tm CATION-CATION SUBSTITUTIONS ON STRUCTURAL PROPERTIES OF Cu₂Se

Y.I. Aliyev^{a,b,*}, A.O. Dashdemirov^a, T.M. Ilyasli^c, S.R. Azimova^d, M.E. Aliyev^e, H.J. Huseynov^d

^aAzerbaijan State Pedagogical University, Baku, AZ-1000, Azerbaijan

^bWestern Caspian University, Baku, AZ-1001, Azerbaijan

^cBaku State University, Baku, AZ-1148, Azerbaijan

^dInstitute of Physics, Ministry of Science and Education, Baku, AZ-1143, Azerbaijan

^eNakhchivan State University, Nakhchivan, AZ-7012, Azerbaijan

Corresponding Author e-mail: yusifafshar@gmail.com

Received January 22, 2025; revise April 14, 2025; accepted May 1, 2025

Cu_{2-x}Tm_xSe ($x = 0.1, 0.2, 0.3$) system compounds were synthesized and their structural properties were studied. Research was carried out by X-ray diffraction method at room temperature. It was determined that the crystal structure of these compounds corresponds to rhombohedral symmetry with R-3m(166) space group. Lattice parameters and atomic coordinates were assigned for each compound. The difference between the crystallographic parameters of Cu_{1.9}Tm_{0.1}Se, Cu_{1.7}Tm_{0.3}Se and Cu_{1.5}Tm_{0.5}Se compounds was explained by the difference between the ionic radii of Cu and Tm atoms.

Keywords: Cu₂Se; Rare-earth element; Chalcogenide; X-ray diffraction

PACS: 74.62.bf; 61.05.C-

1. INTRODUCTION

It is very important to study the structure and physical properties of functional materials. Because the results obtained in the course of these studies determine the possibilities of their application. Therefore, recently, extensive research has been conducted to obtain, process and study the properties of new functional materials [1-5]. It is known that the physical and chemical properties of materials can change under the influence of temperature, pressure and ionizing radiation. For this reason, materials that can maintain their functions in areas exposed to external influences are considered more interesting. The processes occurring under external influences are studied at the atomic level using modern research methods [6-10].

Copper-containing chalcogenide semiconductors are materials with interesting physicochemical properties. Therefore, the physical properties of these materials are widely studied. It was determined that interesting thermal, optical and electrical properties are observed in these compounds [11-15]. When adding rare earth elements to chalcogenide compounds, changes in optical properties are observed. Therefore, optically active systems have recently been obtained by introducing Eu, Nd, and Gd into chalcogenide matrices [16-20]. Making these substitutions in copper chalcogenides can lead to new optical materials. Cu – Se systems can serve as a basis for obtaining such materials.

During the analysis of the crystal structures of the compounds of the Cu-Se system, it was found that the factor that most affects the crystal structures of these compounds is valence variation. In these compounds, Se chalcogen atoms show stable valency. It was determined that depending on the valence and concentration of copper atoms in the compound, Cu₂Se [21-24], CuSe [25], Cu_{1.78}Se [26], Cu_{0.87}Se [27], Cu₃Se₂ [28], CuSe₂ [29], Cu_{1.95}Se [30], Cu_{1.77}Se [24], Cu_{1.89}Se [24] and Cu_{1.8}S [31] are available. Obtaining these compounds depends on the synthesis conditions, including the stoichiometric amount of Cu and Se elements during the synthesis process. As a result of the classification of Cu-Se system compounds, it was found that the Cu₂Se compound is the most studied among these compounds. As a result of the analysis of the X-ray diffraction patterns by the Rietveld method, it was found that single crystals of the Cu₂Se compound have a monoclinic syngonium crystal structure with space group C2/c (15) under normal conditions and at room temperature. The parameters of the elementary core are: $a = 7.1379(4) \text{ \AA}$, $b = 12.3823(7) \text{ \AA}$, $c = 27.3904(9) \text{ \AA}$, $\beta = 94.308(5)^\circ$ and $V = 2414.0(4) \text{ \AA}^3$. Apparently, the crystal structure of the Cu₂Se compound does not have high symmetry. Therefore, each of the atoms that make up the crystal lattice stands in different crystallographic positions. Copper atoms occupy 12 and selenium atoms occupy 6 different positions [32]. The crystal structure of the Cu₂Se compound consists of the arrangement of CuSe₄ tetrahedra formed by selenium atoms along the c axis. Copper atoms are located in the centre of these tetrahedra. It is known that the physical properties of materials mainly depend on their crystal and electronic structures. The fact that these compounds have semiconducting properties mainly depends on the electronic configurations of the copper and selenium atoms included in their composition.

Different crystal structures can be obtained depending on the stoichiometric amount of metal and chalcogen elements included in Cu-Se compounds and synthesis conditions. The most widely studied of these compounds is the Cu₂Se compound. Because in this structure, copper atoms are in a monovalent state. Therefore, this system becomes more stable. Although many physical properties of the Cu₂Se compound have been studied, structural changes occurring during

Cu \rightarrow Tm cation-cation substitutions have not been studied. In this study, compounds $\text{Cu}_{1.9}\text{Tm}_{0.1}\text{Se}$, $\text{Cu}_{1.8}\text{Tm}_{0.2}\text{Se}$ and $\text{Cu}_{1.7}\text{Tm}_{0.3}\text{Se}$ were synthesized and their structural properties were studied.

2. EXPERIMENTS

The research objects $\text{Cu}_{2-x}\text{Tm}_x\text{Se}$ ($x = 0.1, 0.2, 0.3$) were synthesized in high-temperature stoves under high vacuum conditions by the standard method available for synthesizing chalcogenide semiconductors. Stoichiometric amounts of Cu, Tm and Se were taken according to the compounds. First, the furnace temperature was raised to $T = 400$ K. After keeping it at that temperature for $t = 4-5$ hours, it raised to $T = 1400$ K. Next keeping it at the specified temperature for $t = 4-5$ hours, the oven was cooled at a rate of 60 degrees/hour. Then the mixture is heated to the boiling point for about $t = 750$ hours at $T = 450$ K for homogenization of the mixture and further studies were carried out.

XRD (X-ray diffraction) is one of the modern methods for studying the crystal structure of solids. The crystal structure of the $\text{Cu}_{1.9}\text{Tm}_{0.1}\text{Se}$, $\text{Cu}_{1.8}\text{Tm}_{0.2}\text{Se}$ and $\text{Cu}_{1.7}\text{Tm}_{0.3}\text{Se}$ compounds at room temperature was studied by X-ray diffraction. For structural studies, we used a D8 Advance diffractometer (Bruker, Germany) with $\text{CuK}\alpha$ radiation, parameters: $\lambda = 1.5406$ Å, 40 kV, 40 mA. The experimental X-ray diffraction spectrum was analyzed by the Rietveld method in the Fullprof program.

3. RESULTS AND DISCUSSIONS

In order to study the crystal structures of $\text{Cu}_{2-x}\text{Tm}_x\text{Se}$ ($x = 0.1, 0.2, 0.3$) compounds, crystal studies were carried out. The X-ray diffraction spectrum obtained for the $\text{Cu}_{1.9}\text{Tm}_{0.1}\text{Se}$ compound is given in Figure 1.

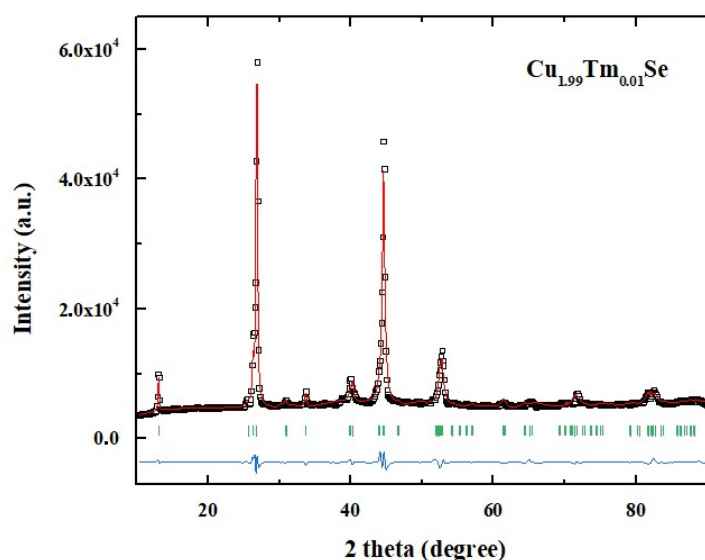


Figure 1. X-ray diffraction spectrum of compound $\text{Cu}_{1.9}\text{Tm}_{0.1}\text{Se}$.

It was determined from the analysis of the spectrum that the crystal structure of the $\text{Cu}_{1.9}\text{Tm}_{0.1}\text{Se}$ compound corresponds to the rhombohedral symmetry $R\bar{3}m$ (166) space group structure. The values of the lattice parameters are set to: $a = b = 4.06405(4)$ Å, $c = 20.32801(7)$ Å, $V = 290.78(5)$ Å³. The coordinates of copper and selenium atoms standing in different positions were also determined. The obtained values are given in Table 1.

Table 1. Atomic coordinates in the elementary lattice of compound $\text{Cu}_{1.9}\text{Tm}_{0.1}\text{Se}$.

Atom	<i>x</i>	<i>y</i>	<i>z</i>
Cu1	0.666(7)	0.333(3)	0.614(3)
Cu2	0.301(7)	0.488(4)	0.694(6)
Se1	0.666(7)	0.333(3)	0.157(5)
Se2	0.666(7)	0.333(3)	0.650(3)

Analyzing the data obtained on the crystal structure of the $\text{Cu}_{1.9}\text{Tm}_{0.1}\text{Se}$ compound, it was determined that the crystal structure of this compound has a higher symmetry compared to the Cu_2Se compound. This is due to the fact that when there are Tm elements inside the crystal, more arrangement occurs. Therefore, the symmetry of the crystal structure increases. In order to clarify the effect obtained in the crystal structure of $\text{Cu}_{1.9}\text{Tm}_{0.1}\text{Se}$ compound and the influence of Cu \rightarrow Tm substitutions, the crystal structure of $\text{Cu}_{1.8}\text{Tm}_{0.2}\text{Se}$ compound obtained with higher concentrations of Tm atoms was studied. The X-ray diffraction spectrum taken at room temperature is shown in Figure 2.

From the analysis of the spectrum given in Figure 2, it was determined that the crystal structure of the $\text{Cu}_{1.8}\text{Tm}_{0.2}\text{Se}$ compound corresponds to the $R\bar{3}m$ (166) space group structure with rhombohedral symmetry, as well as the crystal structure of the $\text{Cu}_{1.9}\text{Tm}_{0.1}\text{Se}$ compound. The values of the lattice parameters are set to: $a = b = 4.04116(4)$ Å, $c = 20.31306(2)$ Å, $V = 287.28(1)$ Å³. The coordinates of Cu and Se atoms are given in Table 2.

Table 2. Atomic coordinates in the elementary lattice of compound $\text{Cu}_{1.8}\text{Tm}_{0.2}\text{Se}$.

Atom	x	y	z
Cu1	0.666(7)	0.333(3)	0.530(7)
Cu2	0.421(7)	0.585(5)	0.654(3)
Se1	0.666(7)	0.333(3)	0.160(2)
Se2	0.666(7)	0.333(3)	0.629(6)

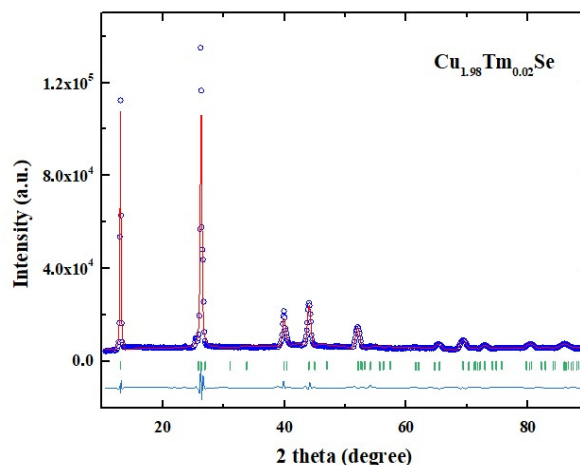


Figure 2. X-ray diffraction spectrum of compound $\text{Cu}_{1.8}\text{Tm}_{0.2}\text{Se}$

The analysis of the information obtained about the crystal structure of the $\text{Cu}_{1.8}\text{Tm}_{0.2}\text{Se}$ compound has shown that compared to the $\text{Cu}_{1.9}\text{Tm}_{0.1}\text{Se}$ compound, the volume of the elementary cell of this compound is smaller. It is known that the ion radius of Cu atoms is $R_{\text{Cu}} = 0.96 \text{ \AA}$, and the ion radius of Tm atoms is $R_{\text{Tm}} = 1.36 \text{ \AA}$ [33]. Therefore, an increase in the concentration of Tm elements should have led to an increase in the volume of the elementary cell. However, a decrease has been observed instead. This is related to the fact that as the concentration of Tm elements inside the crystal increases, it seems as if the vacancies inside the crystal are filled and a more compact arrangement occurs. In order to clarify this effect, the crystal structure of the $\text{Cu}_{1.7}\text{Tm}_{0.3}\text{Se}$ compound with higher concentrations of Tm atoms has also been investigated. The X-ray diffraction spectrum obtained at room temperature is shown in Figure 3.

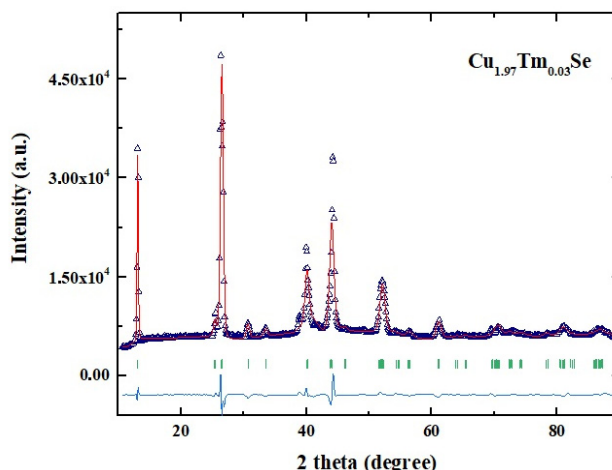


Figure 3. X-ray diffraction spectrum of the compound $\text{Cu}_{1.7}\text{Tm}_{0.3}\text{Se}$.

The analysis of the spectrum given in Figure 3 shows that the crystal structure of the $\text{Cu}_{1.7}\text{Tm}_{0.3}\text{Se}$ compound corresponds to the crystal structure of $\text{Cu}_{1.9}\text{Tm}_{0.1}\text{Se}$ and $\text{Cu}_{1.8}\text{Tm}_{0.2}\text{Se}$ compounds, which is in accordance with the rhombohedral symmetry $R\bar{3}m$ (166) phase group. The lattice parameters are determined as: $a = b = 4.01955(2) \text{ \AA}$, $c = 20.26288(1) \text{ \AA}$, $V = 283.51(3) \text{ \AA}^3$. The coordinates of Cu and Se atoms are given in Table 3.

Table 3. Atomic coordinates in the elementary lattice of compound $\text{Cu}_{1.7}\text{Tm}_{0.3}\text{Se}$.

Atom	x	y	z
Cu1	0.666(7)	0.333(3)	0.459(9)
Cu2	0.452(2)	0.639(9)	0.622(9)
Se1	0.666(7)	0.333(3)	0.167(8)
Se2	0.666(7)	0.333(3)	0.611(7)

The analysis of the crystal structure of the $\text{Cu}_{1.7}\text{Tm}_{0.3}\text{Se}$ alloy has revealed that compared to the $\text{Cu}_{1.9}\text{Tm}_{0.1}\text{Se}$ and $\text{Cu}_{1.8}\text{Tm}_{0.2}\text{Se}$ alloys, this alloy has a smaller volume of the elementary cell. This effect can be explained by the rearrangement of atoms inside the crystal as the concentration of Tm elements increases. Similar phenomena have been observed in other structures affected by rare earth elements in previous studies [33]. Figure 4 shows the dependence of the cell parameters and the volume of the elementary cell on the concentration of Tm atoms.

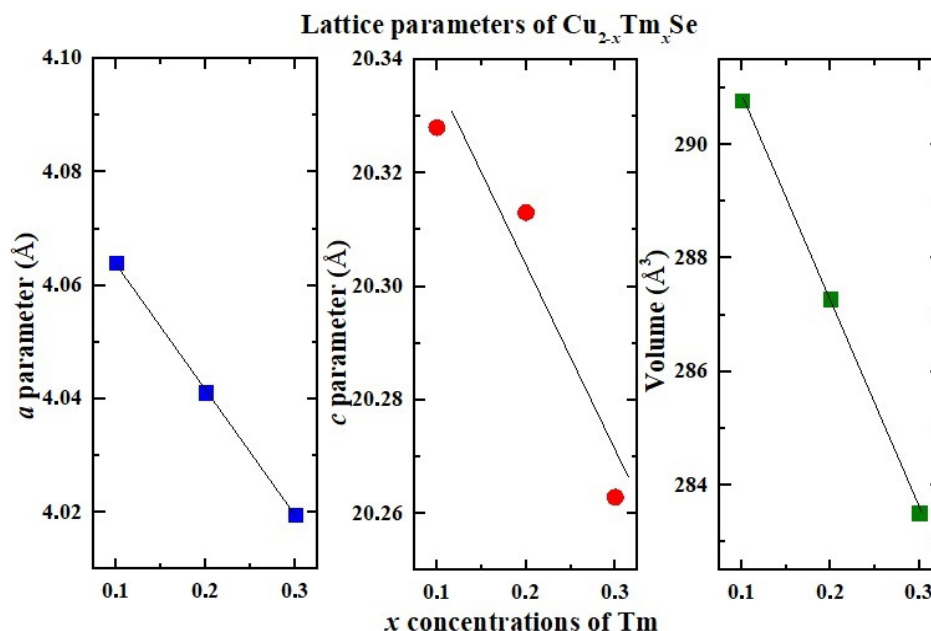


Figure 4. Dependence of lattice parameters of $\text{Cu}_{2-x}\text{Tm}_x\text{Se}$ compounds on the concentration of Tm atoms.

As can be seen from the dependencies shown in Figure 4, as the concentration of Tm atoms increases, both the values of lattice parameters and the volume of the elementary cell have decreased. The change in parameters has affected the c parameter the most. The mechanism of the change in the volume of $\text{Cu}_{2-x}\text{Tm}_x\text{Se}$ compounds depending on the concentration has occurred according to the law $\alpha = \frac{1}{V_0} \cdot \frac{dV}{dx}$. It has been determined that the decrease in volume in the interval $x = 0.1-0.3$ occurred with the coefficient $\alpha = -0.125$.

CONCLUSION

In the Cu_2Se compound, $\text{Cu} \rightarrow \text{Tm}$ cation-cation substitutions have been used to synthesize $\text{Cu}_{1.9}\text{Tm}_{0.1}\text{Se}$, $\text{Cu}_{1.8}\text{Tm}_{0.2}\text{Se}$, and $\text{Cu}_{1.7}\text{Tm}_{0.3}\text{Se}$ compounds, and their structures have been investigated. It has been determined that as the concentration of Tm atoms increases, the symmetry of the crystals increases and a more ordered arrangement occurs. Depending on the concentration, changes in lattice parameters have been observed, and it has been determined that the changes mainly occur along the c-axis. The volume change mechanism has been calculated depending on the concentration, and it has been determined that it occurs with an $\alpha = -0.125$ coefficient.

ORCID

Y.I. Aliyev, <https://orcid.org/0000-0001-8896-2180>; R.E. Huseynov, <https://orcid.org/0000-0003-0636-3948>

REFERENCES

- [1] H.J. Alasali, U. Rilwan, K.A. Mahmoud, T.A. Hanafy, and M.I. Sayyed, Nuclear Engineering and Technology, **56**(10), 4050 (2024). <https://doi.org/10.1016/j.net.2024.05.006>
- [2] E.M. Mahrous, A.M. Al-Baradi, Kh.S. Shaaban, A. Ashour, Sh.A.M. Issa, and H.M.H. Zakaly, Optical Materials, **157**(1), 116057 (2024). <https://doi.org/10.1016/j.optmat.2024.116057>
- [3] S.G. Asadullayeva, N.A. Ismayilova, and T.G. Naghiyev, Modern Physics Letters B, **37**(34), 2350166 (2023). <https://doi.org/10.1142/S021798492350166X>
- [4] Sh.A.M. Issa, A.M. Hassan, M. Algethami, and H.M.H. Zakaly, Ceramics International, **50**(20), 38281 (2024). <https://doi.org/10.1016/j.ceramint.2024.07.192>
- [5] Sh. Biradar, M.N. Chandrashekhara, Manjunatha, A. Dinkar, G.B. Devidas, A.S. Bennal, R. Rajaramakrishna, and M.I. Sayyed, Optical Materials, **155**, 115815 (2024). <https://doi.org/10.1016/j.optmat.2024.115815>
- [6] R.S. Madatov, A.S. Alekperov, F.N. Nurmammadova, N.A. Ismayilova, and S.H. Jabarov, East European Journal of Physics, (1), 322 (2024). <https://doi.org/10.26565/2312-4334-2024-1-29>
- [7] M. Papailiou, S. Dimitrova, E.S. Babayev, and H. Mavromichalaki, AIP Conference Proceedings, **1203**, 748 (2010). <https://doi.org/10.1063/1.3322548>
- [8] E.S. Babayev, in: 2007 Proceedings of the 3rd International Conference on Recent Advances in Space Technologies, (Istanbul, Turkey, 2007) 4284095 (2007), pp. 760-767. <https://doi.org/10.1109/RAST.2007.4284095>

- [9] Sh.B. Utamuradova, Sh.Kh. Daliev, D.A. Rakhmanov, A.S. Doroshkevich, V.A. Kinev, O.Yu. Ponomareva, *et al.*, Advanced Physical Research, **5**(2), 73 (2023). http://jomardpublishing.com/UploadFiles/Files/journals/APR/V5N2/Utamuradova_et_al.pdf
- [10] N.A. Ismayilova, Z.A. Jahangirli, and S.H. Jabarov, Journal of Superconductivity and Novel Magnetism, **36**, 1983 (2023). <https://doi.org/10.1007/s10948-023-06641-1>
- [11] Y.I. Aliyev, Y.G. Asadov, T.M. Ilyasli, F.M. Mammadov, T.G. Naghiyev, Z.A. Ismayilova, M.N. Mirzayev, *et al.*, Modern Physics Letters B, **34**(05), 2050066 (2020). <https://doi.org/10.1142/S0217984920500669>
- [12] G.M. Agamirzayeva, G.G. Huseynov, Y.I. Aliyev, T.T. Abdullayeva, and R.F. Novruzov, Advanced Physical Research, **5**(1), 19 (2023). http://jomardpublishing.com/UploadFiles/Files/journals/APR/V5N1/Agamirzayeva_et_al.pdf
- [13] S.R. Gosavi, N.G. Deshpande, Y.G. Gudage, and R. Sharma, Journal of Alloys and Compounds, **448**(1-2), 344 (2008). <https://doi.org/10.1016/j.jallcom.2007.03.068>
- [14] T.A. Darziyeva, E.Sh. Alekperov, S.H. Jabarov, and M.N. Mirzayev, Integrated Ferroelectrics, **232**(1), 127 (2023). <https://doi.org/10.1080/10584587.2023.2173447>
- [15] A.K. Nabiyeva, S.H. Jabarov, N.A. Ismayilova, and H.J. Huseynov, Ferroelectrics Letters Section, **51**(1-3), 9 (2024). <https://doi.org/10.1080/07315171.2023.2300594>
- [16] A.S. Alekperov, A.O. Dashdemirov, A.E. Shumskaya, and S.H. Jabarov, Crystallography Reports, **66**, 1322 (2021). <https://doi.org/10.1134/S1063774521070026>
- [17] B.G. Tagiyev, O.B. Tagiyev, A.I. Mammadov, V.X. Quang, T.G. Naghiyev, S.H. Jabarov, M.S. Leonenya, *et al.*, Physica B: Condensed Matter, **478**, 58 (2015). <https://doi.org/10.1016/j.physb.2015.08.061>
- [18] S.G. Asadullayeva, A.O. Dashdemirov, A.S. Alekperov, N.A. Ismayilova, A.A. Hadieva, A.N. Cafarova, and A.S. Abiyev, Adv. Phys. Res. **5**(1), 12 (2023). http://jomardpublishing.com/UploadFiles/Files/journals/APR/V5N1/Asadullayeva_et_al.pdf
- [19] R.Z. Ibaeva, G.B. Ibragimov, A.S. Alekperov, and R.E. Huseynov, East European Journal of Physics, (4), 360 (2024). <https://doi.org/10.26565/2312-4334-2024-4-41>
- [20] A.O. Dashdemirov, S.G. Asadullayeva, A.S. Alekperov, N.A. Ismayilova, and S.H. Jabarov, International Journal of Modern Physics B, **35**(30), 2150305 (2021). <https://doi.org/10.1142/S0217979221503057>
- [21] M. Oliveria, R.K. McMullan, and B.J. Wuensch, Solid State Ionics, **28**, 1332 (1988). [https://doi.org/10.1016/0167-2738\(88\)90382-7](https://doi.org/10.1016/0167-2738(88)90382-7)
- [22] P. Rahlfs, Zeitschrift fuer Physikalische Chemie, Abteilung B: Chemie der Elementarprozesse, Aufbau der Materie, **31**, 157 (1936). <https://doi.org/10.1515/zpch-1936-3114>
- [23] T. Sakuma, K. Sugiyama, E. Matsubara, and Y. Waseda, Materials Transactions, JIM, **30**, 365 (1989). <https://doi.org/10.2320/matertrans1989.30.365>
- [24] K.D. Machado, J.C. de Lima, T.A. Grandi, C.E.M. Campos, C.E. Maurmann, A.A.M. Gasperini, S.M. Souza, and A.F. Pimenta, Acta Crystallographica Section B, **60**, 282 (2004). <https://doi.org/10.1107/S0108768104007475>
- [25] V.K. Milman, Acta Crystallographica B, **58**, 437 (2002). <https://doi.org/10.1107/S0108768102003269>
- [26] S.A. Danilkin, A.N. Skomorokhov, V. Rajevac, A. Hoser, H. Fuess, and N.N. Bickulova, Journal of Alloys Compounds, **361**, 57 (2003). [https://doi.org/10.1016/S0925-8388\(03\)00439-0](https://doi.org/10.1016/S0925-8388(03)00439-0)
- [27] H. Effenberger, and F. Pertlik, Neues Jahrbuch fuer Mineralogie. Monatshefte, 1981, 197 (1981).
- [28] N. Morimoto, and K. Koto, Science, **153**, 345 (1966). <https://doi.org/10.1126/science.152.3720.345>
- [29] G. Gattow, Zeitschrift fuer Anorganische und Allgemeine Chemie, **340**, 312 (1965).
- [30] E. Eikeland, A.B. Blichfeld, K.A. Borup, K. Zhao, J. Overgaard, X. Shi, L. Chen, and B.B. Iversen, IUCrJ, **4**, 476 (2017). <https://doi.org/10.1107/S2052252517005553>
- [31] L. Gulay, M. Daszkiewicz, O. Strok, and A. Pietraszko, Chemistry of Metals and Alloys, **4**, 200 (2011). <https://doi.org/10.30970/cma4.0184>
- [32] L.T. Bugaenko, S.M. Ryabykh, and A.L. Bugaenko, Moscow University Chemistry Bulletin, **63**, 303 (2008). <https://doi.org/10.3103/S0027131408060011>
- [33] T.G. Naghiyev, U.R. Rzayev, E.M. Huseynov, I.T. Huseynov, and S.H. Jabarov, UNEC Journal of Engineering and Applied Sciences, **2**(1), 85 (2022). <https://unec-jeas.com/articles/volume-2-2012/effect-of-the-europium-doping-on-the-calcium-sulphide-structural-and-thermal-aspects>

ВПЛИВ КАТИОН-КАТИОННИХ ЗАМІЩЕНЬ Cu → Tm НА СТРУКТУРНІ ВЛАСТИВОСТІ Cu₂Se

Ю.І. Алієв^{a,b}, А.О. Дашдеміров^a, Т.М. Ільяслі^c, С.Р. Азімова^d, М.Е. Алієв^e, Г.Дж. Гусейнов^d

^aАзербайджанський державний педагогічний університет, Баку, AZ-1000, Азербайджан

^bЗахідно-Каспійський університет, Баку, AZ-1001, Азербайджан

^cБакинський державний університет, Баку, AZ-1148, Азербайджан

^dІнститут фізики, Міністерство науки і освіти, Баку, AZ-1143, Азербайджан

^eНахчіванський державний університет, Нахичевань, AZ-7012, Азербайджан

Синтезовано сполуки системи Cu_{2-x}Tm_xSe (x = 0.1, 0.2, 0.3) та вивчено їх структурні властивості. Дослідження проводилися методом рентгенівської дифракції за кімнатної температури. Було встановлено, що кристалічна структура цих сполук відповідає ромбоєдричній симетрії з просторовою групою R-3m(166). Для кожної сполуки було визначено параметри кристалічної решітки та атомні координати. Різниця між кристалографічними параметрами сполук Cu_{1.9}Tm_{0.1}Se, Cu_{1.7}Tm_{0.3}Se та Cu_{1.5}Tm_{0.5}Se була пояснена різницею між іонними радіусами атомів Cu та Tm.

Ключові слова: Cu₂Se; рідкісноземельний елемент; халькогенід; рентгенівська дифракція

TEMPERATURE AND INFRARED QUENCHING OF EQUILIBRIUM CONDUCTIVITY IN $\text{CdSe}_x\text{S}_{1-x}$ FILM

 Valijon T. Mirzaev,  Bozorboy J. Akhmadaliyev,  Iftikhorjon I. Yulchiev,

 Muminjon M. Madraximov,  Tokhirbek I. Rakhmonov*

Fergana State Technical University, Fergana, Uzbekistan

*Corresponding Author e-mail: radiofizik2014@gmail.com

Received January 29, revised March 17, 2025; accepted April 8, 2025

A method for obtaining CdSe , $\text{CdSe}_x\text{S}_{1-x}$ films with high photosensitivity has been developed. This method involves thermal treatment of freshly prepared films in vacuum and air in a specially prepared quasi-hermetic chamber in the presence of CdCl_2 or CuCl_2 , which ensures uniform diffusion of sensitizing substances. Experiments have shown that CdSe , $\text{CdSe}_x\text{S}_{1-x}$ films with stable and reproducible electrophysical properties are obtained by heating at the following temperatures: in air in the presence of CdCl_2 – 470°C; in the presence of CuCl_2 – 300°C; in vacuum – 480°C. Temperature and infrared quenching of equilibrium conductivity are observed only in optically photosensitive samples with both fast (τ) and slow (s) recombination centers and efficiently operating intercrystalline barriers. However, various external influences significantly affect the carrier motion, leading to the loss of high photosensitivity of the sample. Infrared quenching of equilibrium conductivity is observed at $T < 300\text{ K}$ and low infrared light intensities $I_{\text{IR}} < 10^{-1}\text{ lx}$ in the entrance spectral absorption range of $1.0 \div 3.0\mu\text{m}$, and a pronounced photoconductivity with a clearly defined entrance is observed at $I_{\text{IR}} \geq 10^{-1}\text{ lx}$.

Keywords: Photosensitivity; CdSe , $\text{CdSe}_x\text{S}_{1-x}$; Quasi-closed camera; Thermal treatment; Temperature and infrared quenching; Spatial charge field; Drift barriers; Grain size

PACS: 72.20.My, 73.50.Gr, 77.55.-g, 78.55.Et, 81.15.-z

INTRODUCTION

The anomalous temperature dependence of the electrical conductivity of photosensitive CdSe , $\text{CdSe}_x\text{S}_{1-x}$ thin films with infrared quenching of the equilibrium conductivity was determined. The results of measurements and analysis of the kinetic parameters σ_d , n , μ in the dark for $\text{CdSe}_x\text{S}_{1-x}:\text{Cd}:\text{Cu}:\text{Cl}$ samples with different thermal treatment methods in the range 300÷500 °C were carried out. It was found that the observed anomalous effects are associated with the excessive charge of bulk deep r -, s -centers in the spatial charge field and the modulation of this region and drift barriers at the grain boundaries upon heating or under the influence of infrared radiation. Previously, an anomalous temperature dependence of the electrical conductivity was found in a number of polycrystalline $\text{CdSe}_x\text{S}_{1-x}$ samples [1-2], which manifests itself in a sharp decrease in the dark current in a certain temperature range when the semiconductor is heated. In $\text{CdSe}_x\text{S}_{1-x}:\text{Cu}:\text{Cl}$ films, the decrease in dark conductivity reached 7 orders of magnitude in the temperature range 200÷300 K [2-3]. Various authors attribute the occurrence of this effect to the unbalanced filling of trapping centers, the influence of humidity [1-5], intercrystal reactions [1], macroscopic barriers [2], diffusion processes and oxygen chemisorption [4], and thermo-field migration of ions [6]. There is still no single comprehensive opinion about the mechanism of this anomalous phenomenon. Our goal is to study the temperature dependence of the dark conductivity of photosensitive thin $\text{CdSe}_x\text{S}_{1-x}$ films, depending on the production technology and under the influence of weak infrared radiation.

TECHNOLOGY AND MEASUREMENT METHODS

To obtain $\text{CdSe}_x\text{S}_{1-x}$ films, we used the method of thermal evaporation in vacuum. A vacuum unit was assembled based on an automatically controlled vacuum unit VUP-5M and a “VAKMA” 2NVR-5 DM type fore vacuum pump, which provides a pressure of $\sim 10^{-2}$ Pa and a “VAKMA” NVDM-160 vapor-oil diffusion pump (Figure 1). Polycrystalline $\text{CdSe}_x\text{S}_{1-x}$ films with dimensions of $5 \times 25\text{ mm}^2$ and a thickness of 5÷10 microns were obtained by evaporating a $\text{CdSe}_{0.8}\text{S}_{0.2}$ solid solution in a quasi-closed vacuum at a pressure of 10^{-2} Pa at a growth rate of 80÷100 Å/s, at an angle of 45° , from a crucible heated to 300÷500 °C at a height of 9 cm above a glass substrate. The substrate and crucible temperatures were monitored using a “Chromel-Alumel” thermocouple on a PeakTech 3340 DMM thermometer [15-18]. The obtained films were subjected to thermal treatment in three ways: in a vacuum of 10^{-2} Pa at a temperature of 480 °C, in air in the presence of CdCl_2 at a temperature of 470 °C, and in the presence of CuCl_2 vapor at a temperature of 300 °C (Figure 2). The films obtained in this way (dark conductivity $\sigma_d \approx 10^{-5} \div 10^{-6}\text{ }\Omega^{-1} \cdot \text{m}^{-1}$ at 300 K) were strongly compensated and had high photosensitivity $\sim 10^2\text{ lx}$ under natural light intensity).

RESULTS OF THE EXPERIMENT AND THEIR DISCUSSIONS

We were able to observe a sharp decrease in the dark conductivity σ_d , the temperature quenching of the dark conductivity (TQDC), in high-resistance ($R_{\text{film}} > 10^9\text{ }\Omega$) $\text{CdSe}_x\text{S}_{1-x}$ ($\text{Cd}:\text{Cu}:\text{Cl}$) films when the temperature was raised in the range of 150÷300 °C. Unlike the results presented in works [7-9], for the first time in these films, an inverse photoconductivity with an entrance character and infrared quenching of dark conductivity (IQDC) were identified. It was found that multiple heating-cooling cycles of films obtained in vacuum of 10^{-2} and 10^{-5} Torr and in air at $T=77\div 473\text{ K}$ in the dark for $t=30$ minutes do not affect the dependence of σ_d (T) and the spectrum (IQDC) $\sigma_d(\lambda)$. Moreover, measurements of σ_d after a year did not reveal any significant changes in the σ_d (T) and $\sigma_d(\lambda)$ spectra. The reproducibility of the observed effects is indicated by the balance of the re-measured σ_d value. Figure 3 shows the temperature dependence of the equilibrium conductivity for three samples: $\text{CdSe}_x\text{S}_{1-x}$ (curve 1) thermally treated in vacuum with a

residual gas pressure of 10^{-2} Pa, $\text{CdSe}_x\text{S}_{1-x}$ (CdCl) (2) and $\text{CdSe}_x\text{S}_{1-x}$ (CuCl) (3), treated in air in the presence of CdCl_2 and CuCl_2 vapor molecules, respectively.

It can be seen that all $\sigma_d(T)$ curves have two intervals of thermal quenching I and II. Within the measurement error, the "small" quenching (I) corresponds to the intervals $150 \div 230$ K and the "large" quenching (II) to the intervals $230 \div 300$ K for all samples. The activation energies determined from the slopes of curves 1-3 for section II are the same and equal to $E_r \approx 0.5$ eV, while for section I they differ slightly: 0.2 eV for CdSe (CdCl) and 0.3 eV for CdS (CdCl). However, it should be noted that these values do not accurately reflect the energy depth of the recombination centers responsible for the observed conductivity quenching [10-12]. In the temperature range $T=400$ K, a sharp increase in σ_d occurs with an activation energy of $1.5 \div 1.7$ eV, which means that in this case, the dark conductivity is associated with the thermal generation of carriers characteristic of the intrinsic conductivity region of the semiconductor.



Figure 1. Schematic diagram of the vacuum chamber for obtaining $\text{CdSe}_x\text{S}_{1-x}$ films
1-crucible (evaporator); 2-shield; 3-furnace and substrate; 4-thermocouple; 6-metal cover

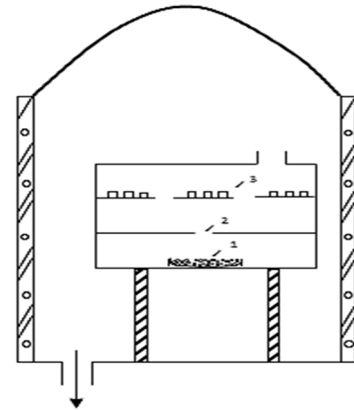


Figure 2. Schematic diagram of the chamber for increasing the sensitivity of $\text{CdSe}_x\text{S}_{1-x}$ films
1-crucibles; 2-slit for the entry of CdCl_2 or CuCl_2 vapors; 3-freshly prepared samples.

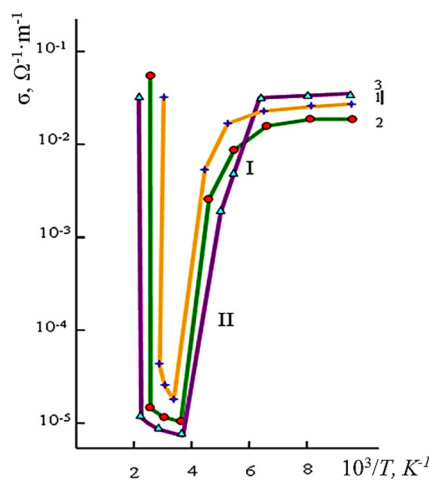


Figure 3. Temperature dependence of the equilibrium conductivity for three samples: $\text{CdSe}_x\text{S}_{1-x}$ (curve 1) thermally treated in vacuum with a residual gas pressure of 10^{-2} Pa, $\text{CdSe}_x\text{S}_{1-x}$ (CdCl) (2) and $\text{CdSe}_x\text{S}_{1-x}$ (CuCl) (3), treated in air in the presence of CdCl_2 and CuCl_2 vapor molecules, respectively.

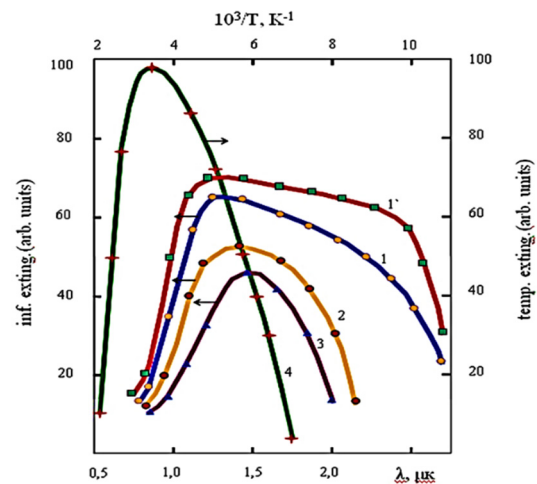


Figure 4. Infrared quenching spectra of the equilibrium conductivity Γ_{IR} of $\text{CdSe}_x\text{S}_{1-x}$ (CuCl) films thermally treated in air at temperatures T : 1-150 K, 2-200 K, 3-250 K. For comparison, the temperature dependence of the quenching magnitude of the equilibrium conductivity Γ_T (curve 4) and the infrared quenching spectrum of the photoconductivity Γ_{IR} (curve 1', $T=150$ K) are shown.

Figure 4 shows the infrared quenching spectra of the equilibrium conductivity of the films for three temperatures (curves 1-3). It is convenient to describe the quenching of the dark current (i.e. conductivity) by the relative value $\Gamma = \frac{j_0 - j}{j}$, where j_0 and j are the current densities without and with infrared radiation thermal quenching. As can be seen from the figure, with increasing temperature, the amplitude and half-width of the IQDC spectrum decrease and its red edge shifts significantly towards shorter wavelengths. At $T=150$ K, the IQDC spectrum, as well as the quenching spectrum of the infrared photoconductivity (curve 1'), reveals a doublet structure with red edges at $\lambda_{r'} = 2.8$ μm . This indicates that at a certain temperature, the equilibrium conductivity in the film is determined by the presence of two recombination centers, one of which has an activation energy of $E_r \approx 0.44$ eV. If we assume, as in the case of single crystals [13], that the E_r level is located close to the edge of the valence band and effectively exchanges carriers with this band, then the "small" TQDC (interval I in Figure 3) and the long-wavelength line of IQDC at low temperatures are associated with the generation or transfer of heat by the infrared radiation of carriers from the r' -center to the valence band. As the temperature increases, the r' -centers become filled and the equilibrium recombination current is captured by deeper centers. These deeper centers now

determine the capture time of electrons in the sample, and therefore define the larger quenching intervals of TQDC and the shorter wavelength line of TQDC. From the red edge of this line at $T=250$ K, we find $\lambda_r = 2 \mu\text{m}$ ($E_r \approx 0.62$ eV). For comparison, Figure 4 shows the temperature dependence of the quenching magnitude of the equilibrium conductivity Γ_T (curve 4). It can also be seen from the figure that infrared quenching was not observed at $T=300$ K.

To clarify the nature of the observed TQDC and IQDC phenomena, Hall measurements were performed on the studied $\text{CdSe}_x\text{S}_{1-x}$ films to determine the average mobility μ_H and electron concentration n in the dark (T). The temperature dependence of $\mu_H(T)$ and $n(T)$ is shown in Figure 5, where curves 1-3 are experimental curves corresponding to curves 1-3 in Figure 4, and curves 1'-3' are calculated using $\mu_H = R_H \sigma_d$, where R_H is the Hall coefficient. It is evident that all dependencies $\mu_H(T)$, $n(T)$, $\sigma_d(T)$ are similar at temperatures close to $T=300$ K. In the range $T=100\div150$ K, n , μ_H , and therefore σ_d are practically independent of temperature, which seems to correspond to the decrease in the donor and the tunnel mechanism of electrical conductivity in polycrystalline semiconductors.

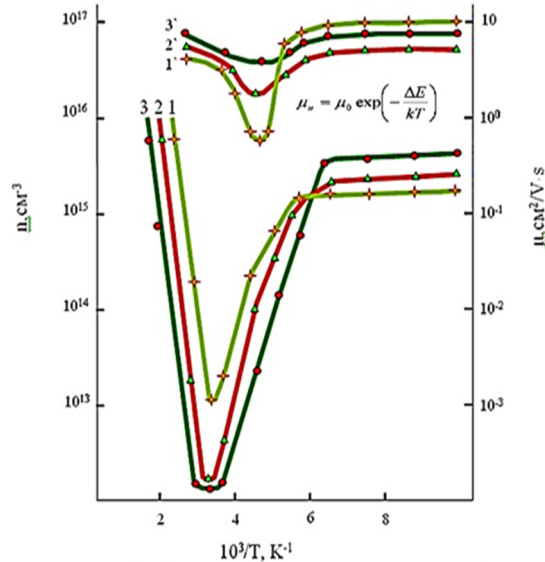


Figure 5. Temperature dependence of the Hall concentration of equilibrium electrons n (1-3) and mobility μ_H (1'-3'). Curves 1-3 and 1'-3' correspond to the description of the sample heating conditions in (Figure 3).

If the Hall mobility of equilibrium electrons μ_H is related to the average height of the drift barriers ΔE_μ

$$\mu_H = \mu_0 \exp \left(-\frac{\Delta E_\mu}{kT} \right),$$

Here, μ_H is the Hall mobility in a homogeneous sample, equal to $200 \text{ cm}^2/(\text{V s})$. Then, in the regions of curves 1'-3' in the temperature range $150\div300$ K, there is a temperature quenching (μ_H) (i.e., we have an anomalous dependence), and at $T>300$ K, ($d\Delta E_\mu/dT > 0$). Interestingly, for the sample $\text{CdSe}_x\text{S}_{1-x}$ (CuCl) in the quenching region, the mobility changes with temperature as $\mu \sim T^{-3/2}$, and after quenching, it increases exponentially according to the activation energy $\Delta E_\mu = 0.11$ eV. Furthermore, in all samples, small quenches in the $\mu_H \sim T^{-5/2}$ and $\mu_H \sim T^{-7}$ regions and large quenches in the $\mu_H \sim T^{-5/2}$ and $\mu_H \sim T^{-7}$ temperature ranges correspond to the $\text{CdSe}_x\text{S}_{1-x}$ (CdCl) and samples, respectively. For the second one, the Hall mobility at temperatures above 300 K first increases according to the laws $\mu_H \sim T^3$ and $\mu_H \sim T^5$, and then exponentially with activation energies of 0.13 and 10 eV. The complex temperature dependence of $\mu_H(T)$ around the temperature quenching naturally reflects the scattering mechanism of electrons at drift barriers. As the temperature increases, the significant decrease in electron concentration leads to the expansion, overlapping, and increase in height of neighboring potential barriers, as well as the emergence of new drift barriers. The sharp difference in temperature dependence of $\mu_H(T)$ in different samples is related to the different crystalline structures of the films, the impurities in them, and the specific defects. The effect of TQDC and IQDC studied cannot be explained using the model of photoconductivity of the same semiconductor containing two or more types of recombination centers [14]. The obtained experimental results also do not fit within the framework of the model in [3], where the negative temperature dependence of the equilibrium carrier concentration is calculated when there is a heterojunction between a low-resistance surface-near region and a high bulk resistance semiconductor. Although the above experimental results clearly indicate the role of volume recombination r -, r' -, s -centers and surface states in the correlation processes, as well as the thermal modulation of drift barriers associated with them, the mechanism of manifestation of these processes in TQDC and IQDC phenomena, at first glance, is not entirely clear within the framework of known models of photoconductivity quenching. Nevertheless, the observed effect can be qualitatively described as follows.

Let's consider a physical model of a bicrystal, corresponding to two adjacent grain boundary regions of a polycrystalline compensated semiconductor with n -type conductivity, containing fast (s) and slow (r) recombination volume centers (Figure 6). In equilibrium, due to the upward bending of energy levels near the interface of adjacent crystallites. Under the effective influence of surface acceptor levels, the recombination r -centers in the space charge region, unlike the quasineutral bulk, are partially filled, and the s -centers associated with doubly charged cadmium vacancies V_{Cd}'' become vacant and transform into a singly charged state V_{Cd}' (r -center), leading to an increase in the concentration of r -centers at the interface. In the space charge region, the absorption of phonons in TQDC or IQDC quanta can lead to the transition of IQDC electrons from the valence band to empty levels at r -centers. In this case, the generated free hole participates in recombination processes with free electrons of the conduction band either through r - and s -centers or through surface levels, resulting in a decrease in the average concentration of conduction band electrons and dark conductivity.

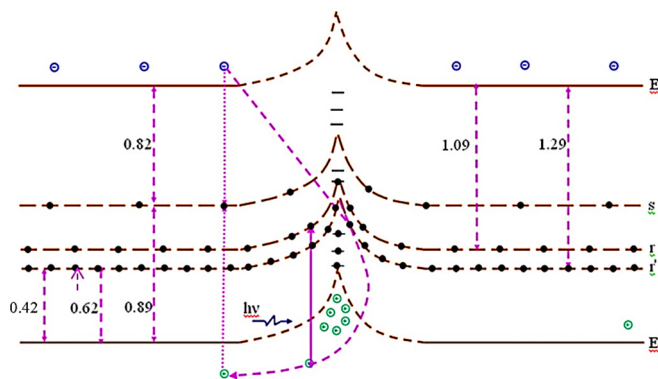


Figure 6. Schematic of a bicrystal model with volume r- and s-recombination centers, showing electron transitions that lead to quenching of dark conductivity with temperature or infrared irradiation.

CONCLUSION

The temperature and infrared quenching of equilibrium conductivity σ_d is observed only in optimally photosensitive samples with r and s recombination centers and effectively working inter-crystallite barriers. They are not observed in freshly evaporated films with a thin fine-grained structure and a thickness of less than 1 micron. It's interesting to note that the quenching of both equilibrium conductivity and photoconductivity occurs within almost identical temperature ($150 \div 300$ K) and spectral ($1.0 \div 3.0 \mu\text{m}$) ranges. The dependence $\sigma_d(T)$, as well as $\sigma_{ph}(T)$, consists of two parts: 1) a slow decrease with an activation energy $E_{rr} \sim 0.14 - 0.4$ eV ($150 \div 230$ K); 2) a sharp decrease with $E_{rr} \sim 0.6 - 1.0$ eV ($230 \div 300$ K).

The infrared quenching of equilibrium conductivity is observed at $T < 300$ K and low infrared light intensities $I_{IR} < 10^{-1}$ lx in the input spectral absorption range of $1.0 \div 3.0 \mu\text{m}$. However, with higher intensities $I_{IR} \geq 10^{-1}$ lx, a clear induced photoconductivity is observed.

It's interesting that no significant residual conductivity was found in the temperature quenching of dark conductivity within the samples. This could be attributed to the specific thermal treatment technology used, which might lead to a uniform spatial distribution of inter-crystal point barriers.

It's noteworthy that there was no significant decrease in the influence of TQDC and IQDC throughout the year. However, various external factors significantly impact the movement of charge carriers, leading to the loss of the sample's high photosensitivity. These factors include prolonged high-temperature, laser or ultrasonic treatment in different environments; mechanical deformations with sufficiently large amplitudes $\varepsilon > 10^{-2}$ and a large number of cycles $N > 500$.

It's worth noting that the studied polycrystalline $\text{CdSe}_{1-x}\text{(Cd:Cu:Cl)}$ samples can be used as thermal switches in the temperature range $T = 150 \div 300$ K and as weak IQ radiation detectors in the $\lambda = 1 \div 3 \mu\text{m}$ range at $T < 300$ K.

ORCID

Valijon T. Mirzaev, <https://orcid.org/0000-0002-8382-6750>; Bozorboy J. Akhmadaliyev, <https://orcid.org/0000-0003-1930-8649>
 Iftikhorjon I. Yulchiev, <https://orcid.org/0000-0001-9346-0441>; Muminjon M. Madraximov, <https://orcid.org/0000-0001-5435-1242>
 Tokhirbek I. Rakhmonov, <https://orcid.org/0000-0002-6080-6159>

REFERENCES

- [1] S.N. Moger, and M.G. Mahesha, "Investigation on spectroscopic and electrical properties of p-Si/CdS_xSe_{1-x} ($0 \leq x \leq 1$) heterostructures for photodetector applications," *Journal of Alloys and Compounds*, **870**, 159479 (2021). <https://doi.org/10.1016/j.jallcom.2021.159479>
- [2] P. Lv, Y. Sun, L. Sui, Z. Ma, K. Yuan, G. Wu, *et al.*, "Pressure-Tuned Core/Shell Configuration Transition of Shell Thickness-Dependent CdSe/CdS Nanocrystals," *The Journal of Physical Chemistry Letters*, **11**(3), 920-926 (2020). <https://pubs.acs.org/doi/10.1021/acs.jpclett.9b03650>
- [3] M. Ajibzhanov, M.A. Karimov, M.S. Saudov, and N.K. Yuldashev, "An anomalous temperature dependence and infrared extinction of equilibrium conductivity in polycrystalline CdSe films," *Fizika i tekhnika poluprovodnikov*, **30**(9), 1578-1584 (1996).
- [4] M.A. Karimov, and N.H. Yuldashev, "Obliquely deposited CdTe: In films with anomalous photovoltaic properties," *Bulletin of the Russian Academy of Sciences: Physics*, **71**, 1151-1153 (2007). <https://doi.org/10.3103/S1062873807080291>
- [5] N.K. Yuldashev, D.T. Mamadiyeva, V.T. Mirzaev, and D.S. Xidirov, "Effect of Heat Treatment Conditions on Photo sensitivity of CdSe_xS_{1-x} Polycrystalline Films," *Journal of Applied Mathematics and Physics*, **10**(10), 3208-3217 (2022). <https://doi.org/10.4236/jamp.2022.1010213>
- [6] Polvonov, B. Z., & Yuldashev, N. K. (2016). Spectra of low-temperature photoluminescence in thin polycrystalline CdTe films. *Semiconductors*, 50, 1001-1004. <https://doi.org/10.1134/S1063782616080194>
- [7] G. Lucovsky, "On the photoionization of deep impurity centers in semiconductors," *Solid state communications*, **88**(11-12), 879-882 (1993). [https://doi.org/10.1016/0038-1098\(93\)90261-K](https://doi.org/10.1016/0038-1098(93)90261-K)
- [8] A.S. Hassanien, and A.A. Akl, "Effect of Se addition on optical and electrical properties of chalcogenide CdSSe thin films," *Superlattices and Microstructures*, **89**, 153-169 (2016). <https://doi.org/10.1016/j.spmi.2015.10.044>
- [9] J. Sharma, G.S.S. Saini, N. Goyal, and S.K. Tripathi, "Thermally induced changes on the electrical and optical properties of nanocrystalline CdSe thin films," *Journal of optoelectronics and advanced materials*, **9**(10), 3194 (2007). <https://www.researchgate.net/publication/216691417>

- [10] P.K.C. Pillai, N. Shroff, N.N. Kumar, and A.K. Tripathi, "Photoconductivity and dark-conductivity studies of $\text{CdS}_{1-x}\text{Se}_x(\text{Cu})$ sintered layers," *Physical Review B*, **32**(12), 8228 (1985). <https://doi.org/10.1103/PhysRevB.32.8228>
- [11] M. Ayibzhanov, O. Mamatov, V. Mirzaev, and B. Tuychibaev, "Luminescence spectrum of cadmium chalcogenide photovoltaic film structures and their power enhancement," *E3S Web of Conferences*, **583**, 04003 (2024). <https://doi.org/10.1051/e3sconf/202458304003>
- [12] B. Akhmadaliyev, T. Rakhmonov, K. Sulaimonov, and O. Nurmatov, "Photocunductivity spectra of thin solid solution films $\text{CdSe}_x\text{S}_{1-x}$," *E3S Web of Conferences*, **583**, 04002 (2024). <https://doi.org/10.1051/e3sconf/202458304002>
- [13] Y.V. Trofimov, L.N. Survilo, E.F. Ostretsov, and M.S. Tivanov, "Physicochemical features of dielectrical nano-barrier layers in $\text{CdSe}_x\text{S}_{1-x}$ films formed by screen printing method," *Lithuanian Journal of Physics*, **52**(3), 219–223 (2012). <https://doi.org/10.3952/physics.v52i3.2473>
- [14] A.S. Abdinov, M.A. Jafarov, N.M. Mechtiyev, E.F. Nasirov, and H.M. Mamedov, "Photodetectors of IR radiation on the basis of $\text{CdS}_{1-x}\text{Se}_x$ films deposited from solution," in: *16th International Conference on Photoelectronics and Night Vision Devices*, vol. 4340, pp. 107-111 (2000). SPIE. <https://doi.org/10.1117/12.407716>
- [15] M.A. Karimov, and N.H. Yuldashev, "Obliquely deposited CdTe:In films with anomalous photovoltaic properties," *Bull. Russ. Acad. Sci. Phys.* **71**, 1151–1153 (2007). <https://doi.org/10.3103/S1062873807080291>
- [16] Z.X. Mirzajonov, K.A. Sulaymonov, T.I. Rakhmonov, F.T. Yusupov, D.Sh. Khidirov, and J.S. Rakhimjonov, "Advancements in Zinc Oxide (ZnO) thin films for photonic and optoelectronic applications: a focus on doping and annealing processes," *E3S Web of Conferences*, **549**, 03013 (2024). <https://doi.org/10.1051/e3sconf/202454903013>
- [17] B.Z. Akhmadaliev, N.K. Yuldashev, and I.I. Yulchiev, "Surface-Radiative Modes and Longitudinal Excitons in the Spectra of Exciton–Polariton Luminescence. Opt. Spectrosc." **125**, 343–352 (2018). <https://doi.org/10.1134/S0030400X18090023>
- [18] F.T. Yusupov, T.I. Rakhmonov, M.F. Akhmadjonov, M.M. Madrahimov, and S.S. Abdullayev, "Enhancing ZnO/Si Heterojunction Solar Cells: A Combined Experimental and Simulation Approach," *East European Journal of Physics*, (3), 425-434. <https://doi.org/10.26565/2312-4334-2024-3-51>

ТЕМПЕРАТУРА ТА ІНФРАЧЕРВОНЕ ГАСІННЯ РІВНОВАЖНОЇ ПРОВІДНОСТІ В ПЛІВЦІ $\text{CdSe}_x\text{S}_{1-x}$

Валіджон Т. Мірзасєв, Бозорбой Дж. Ахмадалієв, Іфтіхорджон І. Юлчієв, Мумінджон М. Мадраксимов,
Тохірбек І. Рахмонов

Ферганський державний технічний університет, Фергана, Узбекистан

Розроблено метод отримання CdSe , $\text{CdSe}_x\text{S}_{1-x}$ плівок з високою світлочутливістю. Цей метод передбачає термічну обробку свіжоприготованих плівок у вакуумі та на повітрі в спеціально підготовленій квазігерметичній камері в присутності CdCl_2 або CuCl_2 , що забезпечує рівномірну дифузію сенсibiliзуючих речовин. Експерименти показали, що CdSe , $\text{CdSe}_x\text{S}_{1-x}$ плівки зі стабільними та відтворюваними електрофізичними властивостями отримують шляхом нагрівання за таких температур: на повітрі в присутності CdCl_2 – 470°C; у присутності CuCl_2 – 300°C; у вакуумі – 480°C. Температурне та інфрачервоне гасіння рівноважної провідності спостерігається лише в оптимально світлочутливих зразках як з швидкими (r), так і з повільними (s) центрами рекомбінації та ефективно працюють міжкристалічні бар'єри. Однак різні зовнішні впливи істотно впливають на рух носіїв, що призводить до втрати високої світлочутливості зразка. Інфрачервоне гасіння рівноважної провідності спостерігається на $T < 300 \text{ K}$ і низькій інтенсивності інфрачервоного світла $I_{\text{IR}} < 10^{-1} \text{ lx}$ у вхідному діапазоні спектрального поглинання $1.0 \div 3.0 \text{ }\mu\text{m}$, а виражена фотопровідність з чітко визначеним входом спостерігається на $I_{\text{IR}} \geq 10^{-1} \text{ lx}$.

Ключові слова: фоточутливість; CdSe , $\text{CdSe}_x\text{S}_{1-x}$; квазізакрита камера; термообробка; температурне та інфрачервоне гасіння; поле просторового заряду; дрейфові бар'єри; розмір зерен

THE ROLE OF RECOMBINATION TYPES IN EFFICIENCY LIMITS OF RADIAL p-n JUNCTIONS BASED ON Si AND GaAs

 **Jo'shqin Sh. Abdullayev^{a*}**,  **Ibrokhim B. Sapaev^{a,b,d,e}**, **Sardor R. Kadirov^c**

^aNational Research University TILAME, Department of Physics and Chemistry, Tashkent, Uzbekistan

^bWestern Caspian University, Baku, Azerbaijan

^cUrgench State University, Urgench, Uzbekistan

^dBaku Eurasian University, Baku, AZ 1073, Azerbaijan

^eCentral Asian University in Tashkent, Uzbekistan

*Corresponding Author e-mail: j.sh.abdullayev6@gmail.com

Received March 1, 2025; revised March 21, 2025; accepted May 13, 2025

In this study, we analyze and model the recombination mechanisms in radial p-n junction structures composed of Si and GaAs over a temperature range of 250 K to 500 K, in 50 K increments. Using both analytical and computational modeling techniques, we examine the effects of doping concentration, core and shell radius, and external voltage on charge carrier behavior and recombination mechanisms. Our analysis focuses on core radii of 0.5 μm and 1 μm , with a total structure height of 4 μm . The external voltage varies from 0 to 2 V, and the doping levels are set to $p = 2 \times 10^{16} \text{ cm}^{-3}$ and $n = 2 \times 10^{17} \text{ cm}^{-3}$. A comparative analysis of Si and GaAs highlights their respective advantages in semiconductor applications: Si offers cost-effectiveness and stability, while GaAs exhibits superior electron mobility and radiative recombination efficiency. Additionally, we investigate the influence of external voltage on recombination mechanisms, revealing that GaAs has a higher rate of surface and radiative recombination compared to Si, which is more affected by Auger recombination at high doping levels. These findings provide valuable insights into optimizing material selection for high-performance optoelectronic and photovoltaic devices.

Keywords: Radial p-n junction; Light trap; External factors; Recombination; Doping concentration; Temperature

PACS: 73.40. Lq, 73.61.Cw, 73.61.Ey, 72.20.Jv

INTRODUCTION

In recent decades, significant research efforts have focused on developing advanced photovoltaic (PV) architectures to enhance energy conversion efficiency while minimizing fabrication costs. Among the various strategies employed, the integration of micro- and nanostructured materials in radial p-n junction configurations has emerged as a promising approach [1-2]. Compared to conventional planar structures, radial p-n junctions offer several advantages [3-5], including an increased junction area for charge separation [6,7], improved carrier transport due to shorter diffusion lengths [8,9], and enhanced internal and external quantum efficiency [10-12]. Additionally, the orthogonal alignment of light absorption and carrier transport in radial p-n junctions supports high-frequency operation [13,14], making them highly suitable for high-speed electronics [15,16] and wireless communication systems [17].

As a result, radial p-n junctions have been widely adopted in cutting-edge semiconductor technologies, including two-dimensional transistors [18], nanowires, and particularly radial p-n and p-i-n junction structures [19]. Over the past two decades, these junctions have gained increasing attention due to their superior optical and electronic properties, positioning them as ideal candidates for various applications such as photodiodes [20], optical sensors [21], thermal and photovoltaic detectors, and high-efficiency solar cells [22].

Despite their numerous advantages, the efficiency of radial p-n junctions is fundamentally constrained by recombination mechanisms, which play a pivotal role in charge carrier dynamics and overall device performance. However, while recombination processes have been extensively studied in planar and bulk semiconductor structures, their impact in radial p-n junctions remains relatively underexplored. A comprehensive understanding of these recombination pathways is essential for optimizing device efficiency and unlocking the full potential of radial p-n junction-based technologies.

METHODS AND MATERIAL

2.1 Materials and geometric parameters

In this study, we focus on core radii of 0.5 μm and 1 μm within the structure. The height of the structure, as shown in Figure 1, z is 4 μm . The temperature range is considered from 50 K to 500 K in increments of 50 K. An external voltage ranging from 0 to 2 V is applied, and the doping concentrations are set to $p = 2 \times 10^{16} \text{ cm}^{-3}$ and $n = 2 \times 10^{17} \text{ cm}^{-3}$. We selected Si and GaAs as the materials for this analysis due to their well-established use in semiconductor devices, this structure has been previously used in our research papers [31]. Si is widely utilized in microelectronics and solar cells because of its abundance, cost-effectiveness, and stable material properties. In contrast, GaAs offers superior electron mobility, direct bandgap properties, and high efficiency in optoelectronic applications such as LEDs, laser diodes, and

high-speed electronics. By comparing these two materials, we aim to evaluate their performance under different structural and temperature conditions. Where r denotes the radial dimension, $+$ and $-$ represents the densities of ionized N_D^+ donor and N_A^- acceptor atoms respectively, at the interface of the radial p-n junction within the depletion region. If full ionization case $N_D^+ = N_D$, $N_A^- = N_A$. In Figure 1 b), the interval $0 < r < r_p$ represents the p-type quasi-neutral region (QNR), the interval $r_p < r < r_n$ represents the depletion region in the radial p-n junction, the interval $r > r_n$ represents the n-type quasi-neutral region (QNR).

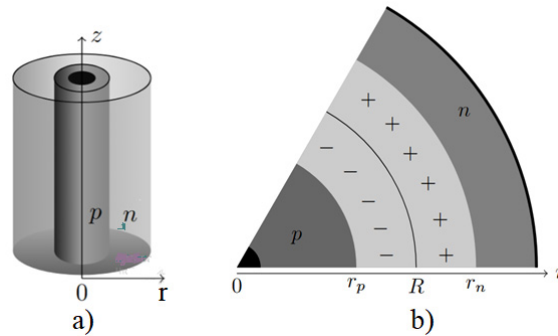


Figure 1. Schematic representation of the radial p-n junction: (a) 3D structure and (b) 2D cross-sectional view

2.2 Recombination models

The radial p-n junction structure has the potential to surpass the Shockley-Queisser limit due to its unique geometric configuration, which enhances charge carrier collection and light absorption compared to conventional planar p-n junctions. However, despite this theoretical advantage, efficiency can be significantly constrained by various recombination mechanisms. These recombination processes, such as Shockley-Read-Hall (SRH) recombination, surface recombination, radiative recombination, and Auger recombination, lead to carrier losses, thereby reducing the actual device performance below the theoretical maximum. A thorough understanding of these recombination pathways is crucial for optimizing the efficiency of radial p-n junction-based optoelectronic and photovoltaic devices.

In this work, we studied the main recombination effects, namely Auger recombination, Shockley-Read-Hall (SRH) recombination in the bulk, surface recombination, and optical generation/radiative recombination. These different recombination effects, along with total recombination, are related as follows (1):

$$R_{Total} = R_{SRH} + R_{Auger} + R_{Rad} + R_{Sur} . \quad (1)$$

If we consider $R \sim 1/\tau$, equation (1) can be expressed in terms of the lifetime (τ), obtaining a total effective lifetime (τ_{Total}) as follows (2):

$$\frac{1}{\tau_{Total}} = \frac{1}{\tau_{SRH}} + \underbrace{\frac{1}{\tau_{Auger}} + \frac{1}{\tau_{Rad}}}_{bulk} + \frac{1}{\tau_{Sur}} = \frac{1}{\tau_{bulk}} + \frac{1}{\tau_{Sur}} . \quad (2)$$

The carrier lifetime varies depending on the recombination mechanism. Radiative recombination lifetime is inversely proportional to carrier concentration and governed by the radiative recombination coefficient. SRH recombination depends on defect density and carrier capture cross-sections. Auger recombination lifetime decreases with increasing carrier concentration due to carrier-carrier interactions. Surface recombination is influenced by surface recombination velocity and material thickness. Understanding these mechanisms is crucial for optimizing semiconductor device performance. The band gap diagram of a semiconductor, illustrating different recombination mechanisms involving electrons and holes, is shown in Figure 2. Each recombination mechanism is explored in the following subsections. Additionally, the next subsection presents a brief overview of the recombination effects examined in this study, aiming to enhance the comprehension of the obtained results.

Table 1. Comparative Analysis of Si and GaAs in Radial p-n Junctions

Property	Si Radial p-n Junctions	GaAs Radial p-n Junctions
SRH Recombination	Moderate (depends on defects)	High (due to sensitivity to defects)
Auger Recombination	Significant at high doping	More dominant at high injection levels
Radiative Recombination	Negligible	Strong (due to direct bandgap)
Surface Recombination	Moderate	High (due to higher surface recombination velocity)

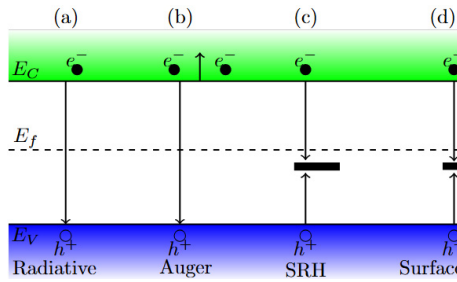


Figure 2. Possible recombination mechanisms in semiconductors include: (a) band-to-band radiative recombination, (b) nonradiative recombination through defect states (SRH recombination), (c) nonradiative Auger recombination, and (d) surface recombination

2.2.1 Shockley-Read-Hall and Surface recombination

In Shockley-Read-Hall (SRH) recombination, a charge carrier transitioning between energy bands is captured by a trap—an energy state introduced by a defect or a dopant. The trapped carrier then releases energy through phonon interactions. This process is predominant in indirect bandgap materials but can also become significant in direct bandgap semiconductors when a high density of traps is present.

For our simulations, we employed the SRH lifetime model, which accounts for concentration-dependent carrier lifetimes since it is also influenced by impurity concentration (Roulston et al., 1982; Law et al., 1991; Fossum and Lee, 1982). Based on this, SRH recombination is described by the following equation (Hall, n.d.):

$$R_{net}^{SRH} = \frac{p \cdot n - \gamma_n \cdot \gamma_p \cdot n_{i,eff}^2}{\tau_p \cdot (n + \gamma_n \cdot n_1) + \tau_n \cdot (p + \gamma_p \cdot p_1)}, \quad (3a)$$

$$R_{Sur,net}^{SRH} = \frac{p \cdot n - n_{i,eff}^2}{\frac{(n + n_1)}{S_p} + \frac{(p + p_1)}{S_n}}. \quad (3b)$$

Where, $\tau_n = 4.4 \cdot 10^{-4}$ s and $\tau_p = 2.2 \cdot 10^{-4}$ s life time for carrier charge, S_n and S_p surface recombination velocity.

2.2.2 Auger recombination

In this recombination process, an electron and a hole recombine without emitting a photon. Instead, the released energy is transferred to another electron, which is excited to a higher energy level. This excited electron subsequently relaxes back to the conduction band through thermal dissipation (Selberherr, 1984). This model becomes significant at high current densities and elevated carrier concentrations, such as those observed at UH levels. The standard Auger recombination is described by the following equation (Dziewor and Schmid, 1977):

$$R_{net}^{Auger} = (C_n \cdot n + C_p \cdot p)(p \cdot n - n_{i,eff}^2). \quad (4)$$

Where n and p represent the electron and hole concentrations, respectively, $n_{i,eff}$ is the intrinsic concentration, C_n and C_p are the Auger coefficients for electrons and holes, respectively.

2.2.3 Optical generation/radiative recombination

In this mechanism, photon transitions must be considered for generation and recombination processes. It is a direct process because it occurs in a single step. During radiative recombination, an electron loses energy and transitions from the conduction band to the valence band, emitting a photon with energy similar to the bandgap. In optical generation, an electron moves from the valence band to the conduction band. Radiative recombination is the dominant recombination mechanism in direct bandgap materials, such as GaAs, and in narrow-bandgap semiconductors. However, in indirect bandgap materials, this process is very weak and can often be neglected. This model, also known as band-to-band recombination, can be described by equation (5), where the total band-to-band generation/recombination is determined by the difference between the capture rate and the emission rate processes.

$$R_{net}^{Rad} = C_{Rad} \cdot (p \cdot n - n_{i,eff}^2). \quad (5)$$

Where, $C_{Rad} = 1.5 \cdot 10^{-10}$ cm³ / s means the capture rate. The analysis results for each of these recombination effects are presented in Table 1. In all recombinations $n_{i,eff} = 1.5 \cdot 10^{10}$ cm⁻³ for Si, $n_{i,eff} = 1.5 \cdot 10^{10}$ cm⁻³ for GaAs.

RESULTS AND DISCUSSION

The distribution of recombination rate in the radial direction obtained from the model developed for radial p-n junction structures made of Si and GaAs is presented and analyzed in Figure 3 and Figure 4 in this section. In Figure 3, for $R = 0.5 \mu\text{m}$, the external voltage is set to 0.2 V and 0.4 V, while the temperature is varied from 250K to 500K in steps of 50K. Thus, the model indicates that in Si material, the recombination process occurs both in the depletion region and the electrically neutral regions, but it is shown to proceed at a higher rate in the depletion region. In contrast, in GaAs material, the recombination rate remains low in the electrically neutral regions $0 < r < r_p$ and $r > r_n$. For radial p-n junctions made of Si and GaAs, the recombination rate is higher in the depletion region $r_p < r < r_n$ for both materials. However, GaAs exhibits a higher maximum recombination rate compared to Si.

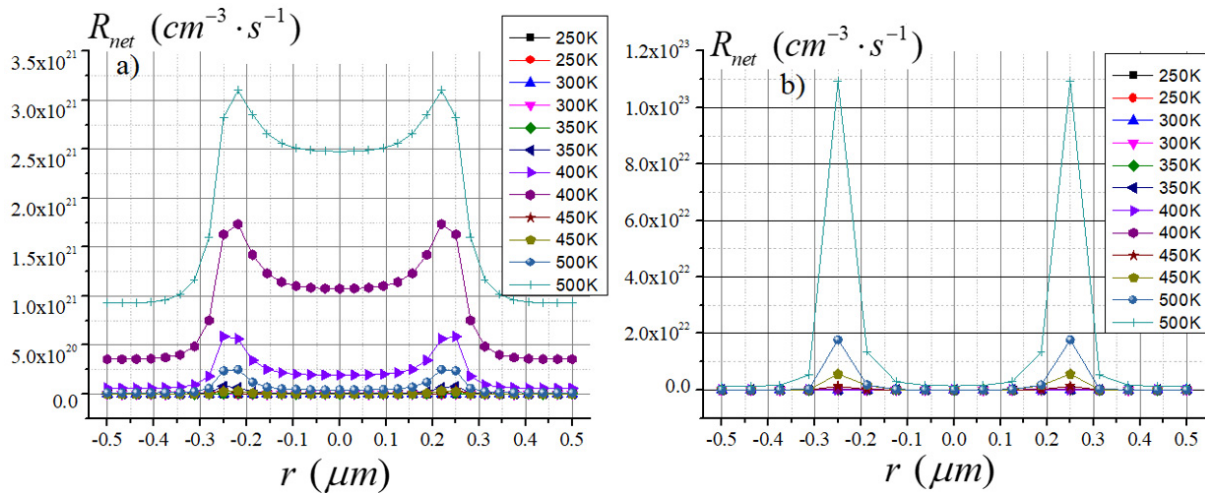


Figure 3. Recombination rate distributions as a function of radial dimension over a temperature range from 250 K to 500 K for (a) Si and (b) GaAs at $R=0.5 \mu\text{m}$

As the radius decreases, the core region becomes fully depleted, leading to a disruption of internal neutrality. As a result, the recombination rate increases due to the enhanced depletion effect in smaller-radius structures.

In this case, the performance of radial p-n junction structures can vary depending on their application field, as the recombination behavior is strongly influenced by the radius reduction. Figure 4 compares the recombination rates for $R = 1 \mu\text{m}$ in two cases: (a) for Si, (b) for GaAs

The results show that in both materials, the maximum recombination rate decreases as the radius decreases. This suggests that smaller-radius structures exhibit higher recombination rates, while larger-radius structures tend to have lower recombination peak values.

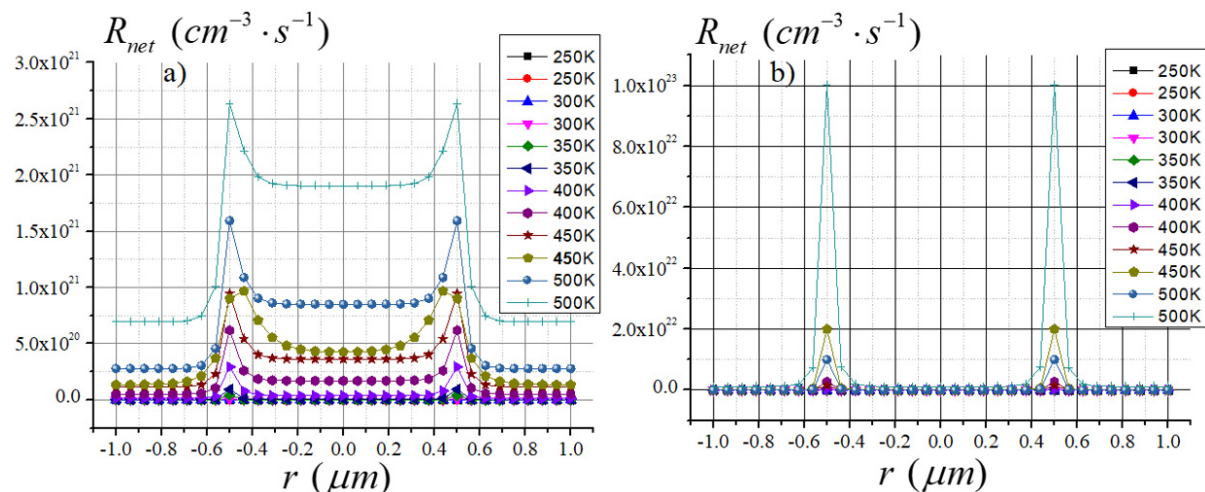


Figure 4. Recombination rate distributions as a function of radial dimension over a temperature range from 250 K to 500 K for (a) Si and (b) GaAs at $R=1 \mu\text{m}$

The analysis of recombination rate distribution in radial Si and GaAs p-n junction structures reveals the following key points. In Si material, recombination occurs in both the depletion and electrically neutral regions, but it is more dominant in the depletion region. In GaAs material, the recombination rate in the electrically neutral region is lower compared to the depletion region. The depletion region exhibits high recombination rates for both materials, but GaAs

shows a higher peak recombination rate than Si. As the radius decreases, the core region becomes fully depleted, leading to a loss of internal neutrality and an increase in the recombination rate. In Figure 4, for $R = 1 \mu\text{m}$, the recombination rates for Si and GaAs are compared, showing that as the radius decreases, the maximum recombination rate also decreases. These findings suggest that the performance of radial p-n junction structures depends on the application, as the recombination behavior varies with radius and material properties.

CONCLUSIONS

This study presents a detailed analysis of radial p-n junction structures based on Si and GaAs, emphasizing their distinct electrical and recombination characteristics. The temperature increase from 250 K to 500 K significantly influences charge storage and recombination dynamics, with GaAs exhibiting higher radiative and surface recombination rates due to its direct bandgap and elevated surface recombination velocity. In contrast, Si is more susceptible to Auger recombination at high doping levels. Furthermore, the effects of external voltage on recombination mechanisms underscore the necessity of carefully selecting material and structural parameters for specific semiconductor applications. These findings provide valuable insights for optimizing high-performance optoelectronic and photovoltaic devices, paving the way for advancements in material engineering and device design to enhance efficiency and reliability.

ORCID

Jo'shqin Sh. Abdullayev, <https://orcid.org/0000-0001-6110-6616>; Ibrokhim B. Sapaev, <https://orcid.org/0000-0003-2365-1554>

REFERENCES

- [1] R. Elbersen, R.M. Tiggelaar, A. Milbrat, G. Mul, H. Gardeniers, and J. Huskens, *Advanced Energy Materials*, **5**(6), 1401745 (2014). <https://doi.org/10.1002/aenm.201401745>
- [2] E. Gnani, A. Gnudi, S. Reggiani, and G. Baccarani, "Theory of the Junctionless Nanowire FET," *IEEE Trans. Electron Devices*, **58**(9), 2903 (2011). <https://doi.org/10.1109/TED.2011.2159608>
- [3] J.Sh. Abdullayev, and I.B. Sapaev, "Optimization of the Influence of Temperature on The Electrical Distribution of Structures with Radial p-n Junction Structures," *East European Journal of Physics*, (3), 344-349 (2024). <https://doi.org/10.26565/2312-4334-2024-3-39>
- [4] J.Sh. Abdullayev, and I.B. Sapaev, "Optimizing the Influence of Doping and Temperature on the Electrophysical Features o p-n and p-i-n Junction Structures," *Eurasian Physical Technical Journal*, **21**(3(49)), 21–28 (2024). <https://doi.org/10.31489/2024No3/21-28>
- [5] J.Sh. Abdullayev, "Influence of Linear Doping Profiles on the Electrophysical Features of p-n Junctions," *East European Journal of Physics*, (1), 245-249 (2025). <https://doi.org/10.26565/2312-4334-2025-1-26>
- [6] O.V. Pylypova, A.A. Evtukh, P.V. Parfenyuk, I.I. Ivanov, I.M. Korobchuk, O.O. Havryliuk, and O.Yu. Semchuk, "Electrical and optical properties of nanowires based solar cell with radial p-n junction," *Opto-Electronics Review*, **27**(2), 143 (2019). <https://doi.org/10.1016/j.opelre.2019.05.003>
- [7] R. Ragi, R.V.T. da Nobrega, U.R. Duarte, and M.A. Romero, "An Explicit Quantum-Mechanical Compact Model for the I-V Characteristics of Cylindrical Nanowire MOSFETs," *IEEE Trans. Nanotechnol.* **15**(4), 627 (2016). <https://doi.org/10.1109/TNANO.2016.2567323>
- [8] R.D. Trevisoli, R.T. Doria, M. de Souza, S. Das, I. Ferain, and M.A. Pavanello, "Surface-Potential-Based Drain Current Analytical Model for Triple-Gate Junctionless Nanowire Transistors," *IEEE Trans. Electron Devices*, **59**(12), 3510 (2012). <https://doi.org/10.1109/TED.2012.2219055>
- [9] N.D. Akhavan, I. Ferain, P. Razavi, R. Yu, and J.-P. Colinge, "Improvement of carrier ballisticity in junctionless nanowire transistors," *Appl. Phys. Lett.* **98**(10), 103510 (2011). <https://doi.org/10.1063/1.3559625>
- [10] J.Sh. Abdullayev, and I.B. Sapaev, "Modeling and calibration of electrical features of p-n junctions based on Si and GaAs," *Physical Sciences and Technology*, **11**(3-4), 39–48 (2024). <https://doi.org/10.26577/phst2024v11i2b05>
- [11] J.Sh. Abdullayev, and I.B. Sapaev, "Factors Influencing the Ideality Factor of Semiconductor p-n and p-i-n Junction Structures at Cryogenic Temperatures," *East European Journal of Physics*, (4), 329-333 (2024). <https://doi.org/10.26565/2312-4334-2024-4-37>
- [12] A.V. Babichev, H. Zhang, P. Lavenus, F.H. Julien, A.Y. Egorov, Y.T. Lin, and M. Tchernycheva, "GaN nanowire ultraviolet photodetector with a graphene transparent contact," *Applied Physics Letters*, **103**(20), 201103 (2013). <https://doi.org/10.1063/1.4829756>
- [13] D.H.K. Murthy, T. Xu, W.H. Chen, A.J. Houtepen, T.J. Savenije, L.D.A. Siebbeles, *et al.*, "Efficient photogeneration of charge carriers in silicon nanowires with a radial doping gradient," *Nanotechnology*, **22**(31), 315710 (2011). <https://doi.org/10.1088/0957-4484/22/31/315710>
- [14] I. Aberg, G. Vescovi, D. Asoli, U. Naseem, J.P. Gilboy, C. Sundvall, and L. Samuelson, "A GaAs Nanowire Array Solar Cell With 15.3% Efficiency at 1 Sun," *IEEE Journal of Photovoltaics*, **6**(1), 185 (2016). <https://doi.org/10.1109/JPHOTOV.2015.2484967>
- [15] J. Sh. Abdullayev, I. B. Sapaev, and Kh. N. Juraev, "Theoretical analysis of incomplete ionization on the electrical behavior of radial p-n junction structures," *Low Temp. Phys.* **51**, 60–64 (2025). (<https://doi.org/10.1063/10.0034646>)
- [16] J.Sh. Abdullayev, and I.B. Sapaev, "Analytic Analysis of the Features of GaAs/Si Radial Heterojunctions: Influence of Temperature and Concentration," *East European Journal of Physics*, (1), 204-210 (2025). <https://doi.org/10.26565/2312-4334-2025-1-21>
- [17] O. Toktarbaiuly, M. Baisariyev, A. Kaisha, T. Duisabayev, N. Ibrayev, T. Serikov, M. Ibraimov, *et al.*, "Enhancement of Power Conversion Efficiency of Dye-Sensitized Solar Cells Via Incorporation of Gan Semiconductor Material Synthesized in Hot-Wall Chemical Vapor Deposition Furnace," *Eurasian Physical Technical Journal*, **21**(4(50)), 131–139 (2024). <https://doi.org/10.31489/2024No4/131-139>
- [18] M.Sh. Isaev, A.I. Khudayberdieva, M.N. Mamatkulov, U.T. Asatov, and S.R. Kodirov, "The Surface Layer Morphology of Si<Cr> Samples," *East European Journal of Physics*, (4), 297–300 (2024). <https://doi.org/10.26565/2312-4334-2024-4-32>

- [19] I. Sapaev, I.B. Sapaev, *et. al.*, E3S Web Conf. **383**, 04022 (2023). <https://doi.org/10.1051/e3sconf/202338304022>
- [20] A.T. Mamadalimov, M.Sh. Isaev, M.N. Mamatkulov, S.R. Kodirov, and J.T. Abdurazzokov, "Study Of Silicide Formation In Large Diameter Monocrystalline Silicon," East European Journal of Physics, (2), 366–371 (2024). <https://doi.org/10.26565/2312-4334-2024-2-45>
- [21] M.S. Isaev, U.T. Asatov, M.A. Tulametov, S.R. Kodirov, and A.E. Rajabov, "Study of The Inhomogeneities of Overcompensated Silicon Samples Doped with Manganese," East European Journal of Physics, (2), 341–344 (2024). <https://doi.org/10.26565/2312-4334-2024-2-40>
- [22] B. Pal, K.J. Sarkar, and P. Banerji, Solar Energy Materials and Solar Cells, **204**, 110217 (2020). <https://doi.org/10.1016/j.solmat.2019.110217>

РОЛЬ ТИПІВ РЕКОМБІНАЦІЇ У МЕЖАХ ЕФЕКТИВНОСТІ РАДІАЛЬНИХ p-n ПЕРЕХОДІВ НА ОСНОВІ Si ТА GaAs

Джошкін Ш. Абдуллаєв^a, Іброхім Б. Сапаєв^{a,b,d,f}, Сардор Р. Кадиров^c

^aНаціональний дослідницький університет ТПAME, кафедра фізики та хімії, Ташкент, Узбекистан

^bЗахідно-Каспійський університет, Баку, Азербайджан

^cУргенчський державний університет, Ургенч, Узбекистан

^dБакинський Євразійський університет, Баку, Аризона 1073, Азербайджан

^eЦентральноазіатський університет у Ташкенті, Узбекистан

У цьому дослідженні ми аналізуємо та моделюємо механізми рекомбінації в радіальних p-n переходах, що складаються з Si та GaAs, у температурному діапазоні від 250 К до 500 К з кроком 50 К. Використовуючи як аналітичне, так і комп'ютерне моделювання, ми вивчаємо вплив концентрації домішок, радіуса ядра та оболонки, а також зовнішньої напруги на поведінку носіїв заряду та механізми рекомбінації. Наш аналіз фокусується на радіусах ядра 0,5 мкм і 1 мкм, при загальній висоті структури 4 мкм. Зовнішня напруга варіюється від 0 до 2 В, а рівні легування встановлені як $p = 2 \times 10^{16} \text{ см}^{-3}$ і $n = 2 \times 10^{17} \text{ см}^{-3}$. Порівняльний аналіз Si та GaAs висвітлює їхні відповідні переваги в напівпровідникових застосуваннях: Si забезпечує економічність і стабільність, тоді як GaAs демонструє кращу рухливість електронів і високу ефективність радіаційної рекомбінації. Додатково, ми досліджуємо вплив зовнішньої напруги на механізми рекомбінації, виявляючи, що GaAs має вищу швидкість поверхневої та радіаційної рекомбінації, тоді як Si більше схильний до Оже-рекомбінації при високих рівнях легування. Отримані результати надають цінну інформацію для оптимізації вибору матеріалів у високоефективних оптоелектронних і фотоелектричних пристроях.

Ключові слова: радіальний p-n перехід; світлова пастка; зовнішні фактори; рекомбінація; концентрація домішок; температура

i-ZnO AND CdS BUFFER LAYERS FOR IMPROVING THE EFFICIENCY OF COPPER TIN SULPHIDE QUANTUM DOT SENSITIZED SOLAR CELLS

 Maya Mathew*

Department of Physics, Carmel College (Autonomous), Mala, Thrissur, Kerala, India

*Corresponding Author Email: maya@carmelcollegemala.ac.in

Received February 24, 202; revised April 17, 2025; accepted April 30, 2025

The effect of layer defects as well as interface defects in copper tin sulphide quantum dot sensitized solar cells were investigated using SCAPS-1D software. Layer defects in the sensitizer and hole transporting layer were found to have no effect on the cell efficiency except at very high densities of 10^{19} cm^{-2} . The interface defect at CTS/ETL was also found to have no effect on the cell efficiency. Defects at the HTL/CTS interface decreased the cell efficiency significantly and so a buffer layer was introduced at this interface. Both i-ZnO and CdS buffer layer materials were found to have energy levels in alignment with the HTL enhancing charge transport. The cell efficiency increased from 17.86% to 18.37% with i-ZnO buffer layer while the cell efficiency rose to 18.61% when CdS was used as the buffer layer. Absorption of the solar spectrum in the blue-green region was enhanced when buffer layers were used in the cell.

Keywords: *Quantum dot sensitized solar cells; Buffer layer; SCAPS-1D; Charge carrier recombination; Quantum efficiency; Defects*

PACS: 61.46.+w., 61.72.Ww., 73.21.La., 73.50.Pz

1. INTRODUCTION

Quantum dot sensitized solar cells are being extensively researched now-a-days due to several characteristic phenomena in quantum dots such as quantum confinement, multiple electron generation, high absorption coefficient and cost effectiveness [1-3]. Quantum confinement is a quantum phenomenon in which the bandgap of the material can be tuned according to its size. This fine tuning of bandgap is possible only if the size of the particle is less than the Bohr radius of charge carriers, i.e., the average distance between the electron and a hole in an exciton [4-6]. Multiple electron generation is another quantum phenomenon in which a high energy photon can excite more than one electron. Quantum dots naturally have high absorption coefficients which make them potential candidates in solar cells [7-9]. Quantum dots are now being prepared by simple deposition techniques such as colloidal synthesis [10] and successive ionic layer adsorption and reaction techniques and that too at room temperature [11,12], which can bring down the cost of making a solar cell. This work is on copper tin sulphide (CTS) quantum dots sensitized solar cells where CTS is a ternary semiconductor with high absorption coefficient of 10^4 cm^{-1} . Quantum dots of CTS have been prepared by solvothermal, hydrothermal and ball milling techniques and cost effective and room temperature techniques too such as colloidal synthesis and SILAR techniques [13-18].

Quantum dot sensitized solar cells are similar to dye sensitized solar cells where the dye has been replaced by the sensitizer which are quantum dots. The quantum dots are usually coated onto a porous electron transporting layer (ETL) and transparent conducting oxides are the electrical contacts for taking the charge carriers out of the solar cell. The hole transporting layer (HTL) allows the extraction of holes from the sensitizer to the electrical contacts [19, 20].

Similar to the various types of defects present in solar cells leading to charge carrier recombination, QDSSCs also have various types of defects [21, 22]. There can be defects within the layers of sensitizer, affecting photon absorption, defects in the HTL, affecting hole transport and also interface defects where the recombination happens between different layers. Investigation on the effect of various defects in the solar cell is very important for improving the efficiency of the solar cell. Buffer layers are inserted between the layers where interface recombination is more and the cell efficiency is enhanced. Commonly used buffer layers are ZnS, ZnO, i-ZnO, CdS and CdSe. Buffer layers are so chosen that their valence band is in alignment with that of the HTL, facilitating the hole transport [23- 25].

ZnS buffer when used in CTS thin film solar cells, decreased the interface recombination and enhanced the cell efficiency by 1% compared to the CdS buffer layer [26]. Ag₂S quantum dots and also that in bulk were found to be good buffer layers in CIGS solar cells. It was found that not only the band alignment but also the opto-electrical properties of the buffer layer affect the efficiency of the solar cell. Higher bandgap and higher carrier concentration buffer layers improve the power conversion efficiency of the device [27]. Decrease in charge carrier recombination at the CdTe quantum dots absorber layer and the metal oxide layer were observed when ZnS buffer layer was used and the cell efficiency was found to improve by 2% [28].

In this work, the effect of layer as well interface defects in CTS QDSSCs are investigated and then a comparison between i-ZnO and CdS buffer layers have been made. This is a first approach made in the study of the effect of the buffer layer in CTS QDSSCs.

2. DESIGN AND SIMULATION

Copper Tin sulphide quantum dot sensitized solar cell having the structure ITO/TiO₂/CTS/CuSbS₂/Au was simulated where, ITO is the transparent conducting oxide, TiO₂ is the electron transporting layer, CTS quantum dots of bandgap 2.5 eV is the sensitizer layer, CuSbS₂ is the hole transporting layer and Au is the metal back contact with a workfunction of 5.1 eV. The schematic diagram of the solar cell as well as its band structure has been shown in Figures 1 and 2 respectively.

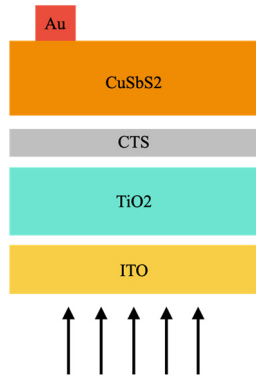


Figure 1. Solar cell structure used for simulation

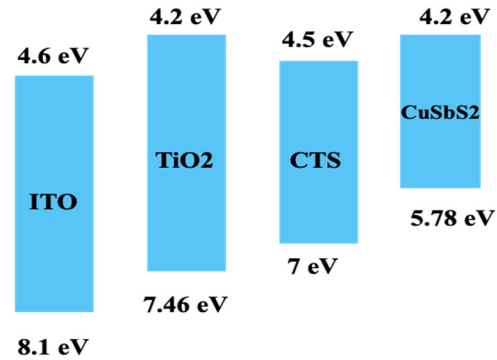


Figure 2. Band structure for the solar cell ITO/TiO₂/CTS/CuSbS₂/Au

This QDSSC was optimized previously for all the layer parameters and accordingly the layer thicknesses, doping densities and defect densities were taken. The layer parameters have been tabulated in Table 1.

Table 1. Layer parameters used in simulation of the solar cell structure

Parameters	ITO	TiO ₂	CTS	CuSbS ₂
Thickness (μm)	0.05	0.3	0.01	1
Bandgap E _g (eV)	3.5	3.26	2.5	1.58
Electron affinity (eV)	4.6	4.2	4.5	4.2
Dielectric constant (ε/ε ₀)	8.9	10	10	14.6
Density of state conduction band (cm ⁻³)	2.2×10 ¹⁸	2.0×10 ¹⁷	1×10 ¹⁹	2 × 10 ¹⁸
Density of state valence band (cm ⁻³)	1.8×10 ¹⁹	6×10 ¹⁷	1×10 ¹⁹	1 × 10 ¹⁸
Thermal velocity of electron V _e (cms ⁻¹)	1×10 ⁷	1×10 ⁷	1×10 ⁷	1×10 ⁷
Thermal velocity of holes V _h (cms ⁻¹)	1×10 ⁷	1×10 ⁷	1×10 ⁷	1×10 ⁷
electron mobility μ _e (cm ² /V.s)	10	100	100	49
hole mobility μ _h (cm ² /V.s)	10	250	25	49
Density of donor atom N _D (cm ⁻³)	1×10 ²¹	1×10 ²⁰	1×10 ¹⁹	0
Density of acceptor atom N _A (cm ⁻³)	0	0	0	1×10 ¹⁸
Defect density (cm ⁻³)	0	0	10 ¹⁰	10 ¹⁰

Other than these parameters, the rest have been taken from literature [29-31]. Defect densities in the HTL and sensitizer were taken as amphoteric type with defect density of 10¹⁰ cm⁻², at an energy level of 0.6 eV with respect to the highest valence band. Interface defect densities are also added at the HTL/CTS and TiO₂/CTS interfaces which are neutral type with defect density of 10¹⁰ cm⁻², at an energy level of 0.6 eV with respect to the highest valence band. All the simulations were performed at 300 K and under standard illumination of AM 1.5G (1 Sun).

The simulations were performed using SCAPS-1D software which was developed by Prof. Marc Burglemann and his team at Gent University. The software was initially developed for the simulation of CuInGaSe (Copper Indium Gallium Selenide) and CdTe (Cadmium Telluride) thin film solar cells but it is widely used for simulation of all types of solar cells including dye sensitized and quantum dot sensitized solar cells. The simulation works by solving the Poisson's and continuity equations for electrons and holes [30]. The continuity equations for electrons and holes are as follows:

$$\frac{dJ_n}{dx} = G - R, \quad (1)$$

$$\frac{dJ_p}{dx} = G - R. \quad (2)$$

Where, J_n and J_p are the current densities of electrons and holes, G is the generation rate and R is recombination rate. The Poisson's equation is given by:

$$\frac{d^2}{dx^2} \phi(x) = \frac{q}{\epsilon_0 \epsilon_r} \{p(x) - n(x) + N_D^+(x) - N_A^-(x) + p_t - n_t\}. \quad (3)$$

Where x indicates the distance in the solar cell, ϕ is the electrostatic potential, q is the electric charge, ϵ_0 is the permittivity of free space, ϵ_r is the relative permittivity, $p(x)$ is the concentration of free holes, $n(x)$ is the concentration of free electrons, $N_D^+(x)$ is the density of donor type charge impurities, $N_A^-(x)$ is the density of acceptor type charge impurities, p_t is the hole distribution and n_t is the electron distribution.

The simulation is done by first setting the layers of the solar cells using the “Set Problem” button where the layer parameters are given and then saved. Then “single shot calculation” is done for single simulation and “Calculate batch” for simulating a range of data. Current- Voltage curve, energy band diagram, graph of current densities, generation-recombination curves and quantum efficiency curve can be obtained after each simulation. Data on cell parameters such as the open circuit voltage (Voc), short circuit current density (Jsc), fill factor and efficiency can be obtained [32].

In the current work, an extensive evaluation is made on the defect densities of the sensitizer and hole transporting layer and their effects on the cell efficiency. Also, the effect of interface defect densities at TiO₂/CTS and CTS/HTL interfaces were also investigated. Cell efficiency was improved with the use of buffer layers of i-ZnO and CdS and the mechanism in which the cell efficiency is enhanced has also been discussed. The layer parameters of the buffer layers [27] have been tabulated in Table 2.

Table 2. Layer parameters of the buffer layers used

Buffer layer	i-ZnO	CdS
Thickness (nm)	1000	1000
Dielectric constant (ϵ/ϵ_0)	10	9
Electron mobility μ_e (cm ² /V.s)	50	100
Hole mobility μ_h (cm ² /V.s)	20	25
Acceptor concentration N_A (cm ⁻³)	0	0
Donor concentration N_D (cm ⁻³)	5×10^{17}	10^{18}
Bandgap E_g (eV)	3.4	2.4
Electron affinity (eV)	4.55	4.2
Density of state conduction band (cm ⁻³)	4×10^{18}	1.8×10^{18}
Density of state valence band (cm ⁻³)	9×10^{18}	2.4×10^{19}
Electron thermal velocity V_e (cms ⁻¹)	10^7	10^7
Hole thermal velocity V_h (cms ⁻¹)	10^7	10^7

3. RESULTS AND DISCUSSION

3.1. Effect of sensitizer defect density

The sensitizer defect density was varied from 10^{10} - 10^{19} cm⁻² and the variation in efficiency has been tabulated in Table 3. There is no significant change in the efficiency of the cell except at very high defect density of 10^{19} cm⁻², at which the efficiency drops by 0.39%.

Table 3. Variation of efficiency with sensitizer defect density

Sensitizer defect density (cm ⁻²)	Voc (V)	Jsc (mA/cm ²)	FF (%)	Efficiency (%)
10^{10}	1.034	21.04	82.14	17.86
10^{11}	1.034	21.04	82.14	17.86
10^{12}	1.034	21.04	82.14	17.86
10^{13}	1.034	21.04	82.14	17.86
10^{14}	1.034	21.04	82.14	17.86
10^{15}	1.034	21.04	82.14	17.86
10^{16}	1.034	21.04	82.14	17.86
10^{17}	1.034	21.04	82.14	17.86
10^{18}	1.034	21.04	82.14	17.85
10^{19}	1.034	21.02	81.99	17.46

The lower thickness of the sensitizer (10 nm) is one reason for the unchanged efficiency as the diffusion length of charge carriers is very less, decreasing the chance for recombination. The donor doping density of CTS is taken as 10^{19} cm⁻³, the optimized density, which also overcomes the effect of defect levels in the sensitizer. At very high defect density, the fill factor is found to decrease which indicates the increase in series resistance in the cell, owing to more recombinations leading to comparatively lower cell efficiency. The recombination rates of charge carriers in the solar cell at various defect densities were investigated as shown in Figure 3 and it can be seen that upto defect densities of 10^{13} cm⁻², the recombination rate in the sensitizer is minimal, of the order of 10^{16} /cm³s, generation rate being 10^{22} /cm³s. At very high defect densities, the recombination rate in the HTL is found to decrease and that at the sensitizer is found to increase. Higher defect densities cause recombination in the sensitizer and only a few holes manage to reach the HTL, decreasing the power conversion efficiency.

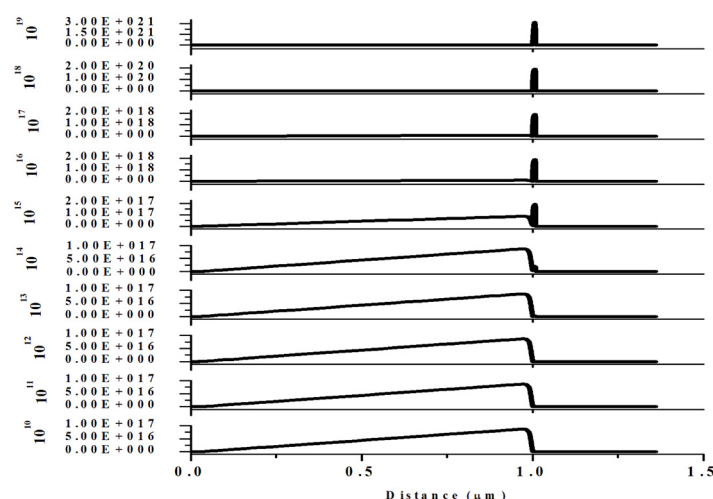


Figure 3. Recombination rates ($\text{cm}^{-3}\text{s}^{-1}$) of charge carriers at different defect densities of sensitizer

3.2. Effect of HTL defect density

Keeping the defect density of sensitizer at 10^{10} cm^{-2} , the defect density of CuSbS_2 , the hole transporting layer was varied from 10^{10} to 10^{19} cm^{-2} and the data has been tabulated in Table 4. Here the cell efficiency is found to be independent of the defect densities except at high values of 10^{17} cm^{-2} and above. High doping density of CuSbS_2 is the main reason for the constancy in cell efficiency at low to moderate defect densities. At higher defect densities, J_{sc} is found to decrease due to increased recombination. The fill factor is also found to decrease due to increased series cell resistance owing to recombination of charge carriers and by equation 4, the cell efficiency also decreases.

$$\eta = \frac{V_{oc} J_{sc} FF}{P_{in}} \quad (4)$$

Where, V_{oc} is the open circuit voltage, J_{sc} is the short circuit current density, FF is the fill factor, P_{in} is the input power and η is the solar cell efficiency.

Table 4. Variation of cell parameters at different HTL defect densities

CuSbS ₂ HTL defect density (cm^{-2})	V _{oc} (V)	J _{sc} (mA/cm^2)	FF (%)	Efficiency (%)
10^{10}	1.034	21.04	82.14	17.86
10^{11}	1.034	21.04	82.14	17.86
10^{12}	1.034	21.04	82.14	17.86
10^{13}	1.034	21.04	82.14	17.86
10^{14}	1.034	21.04	82.14	17.86
10^{15}	1.034	20.996	82.20	17.84
10^{16}	1.035	20.594	81.17	17.30
10^{17}	1.045	18.073	74.85	14.13
10^{18}	0.742	16.091	59.73	7.13
10^{19}	0.205	0.254	25.9	0.01

3.3. Effect of interface defect density at CTS/TiO₂ interface

The interface defect density at CTS/TiO₂ interface was varied from 10^{10} to 10^{19} cm^{-2} and the data showing the variation is tabulated in Table 5. Cell efficiency was found to be independent of the defects at the CTS/TiO₂ interface.

Table 5. Variation of cell parameters at different interface defect density for CTS/TiO₂ interface

CTS/TiO ₂ interface defect density (cm^{-2})	V _{oc} (V)	J _{sc} (mA/cm^2)	FF (%)	Efficiency (%)
10^{10}	1.034	21.04	82.14	17.86
10^{11}	1.034	21.04	82.14	17.86
10^{12}	1.034	21.04	82.14	17.86
10^{13}	1.034	21.04	82.14	17.86
10^{14}	1.034	21.04	82.14	17.86
10^{15}	1.034	21.04	82.14	17.86
10^{16}	1.034	21.04	82.14	17.86
10^{17}	1.0335	21.006	82.02	17.81
10^{18}	1.0334	20.814	81.72	17.58
10^{19}	1.033	20.581	81.79	17.39

Figure 4 shows the band structure of the solar cell at thermodynamic equilibrium and it can be seen that there is a positive band offset between the electron transporting layer (ETL) and the sensitizer, creating a spike at the interface. The electron fermi level is seen to be close to the conduction band minimum of the sensitizer due to which there is more band bending at the interface. This spike formation at the interface acts as a barrier to the free flow of electrons hence reducing the recombination rate. Lower recombination rates at this interface unaffected the cell efficiency. At very high defect densities, the recombination rate is comparatively higher, leading to a slight drop in cell efficiency. This phenomenon is evident from the short circuit current and fill factor values which remain unchanged.

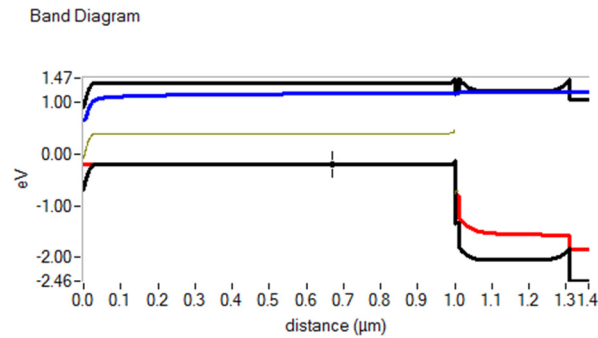


Figure 4. Band diagram of the solar cell structure at thermodynamic equilibrium

3.4. Effect of interface defect density at CuSbS₂/CTS interface

The defect densities at the CuSbS₂/CTS interface were varied from 10¹⁰ to 10¹⁴ cm⁻² and Table 6 shows the variation in cell parameters. The cell efficiency was found to be considerably affected by the defects at this interface. The recombination rate of charge carriers of the cell at this interface has been plotted in Figure 5. The band offsets for the solar cell are conducive for the holes formed at the sensitizer to easily diffuse into the HTL. At 10¹⁰ and 10¹¹ cm⁻² defect densities, there is more recombination in the HTL indicating a greater number of holes reaching the HTL from the sensitizer which indicates that lesser recombinations are happening at the interface. As the defect density at the interface increases from 10¹² to 10¹⁴ cm⁻², the recombination rate in the HTL drastically decreases signifying the drop in number of holes reaching the HTL which also signifies that more recombinations are taking place in the interface. So, at higher interface defect density at CuSbS₂/CTS interface, more recombinations take place at the interface, decreasing the number of holes at the electrical contacts causing the cell efficiency to significantly drop.

Table 6. Variation of cell parameters for different interface defect density at CuSbS₂/CTS interface

Interface defect density (cm ⁻²)	Voc	Jsc	FF	Efficiency
10 ¹⁰	1.034	21.04	82.14	17.86
10 ¹¹	1.0312	21.043	80.91	17.56
10 ¹²	1.0078	21.043	78.34	16.61
10 ¹³	0.9458	21.043	77.37	15.40
10 ¹⁴	0.8764	21.043	76.75	14.15

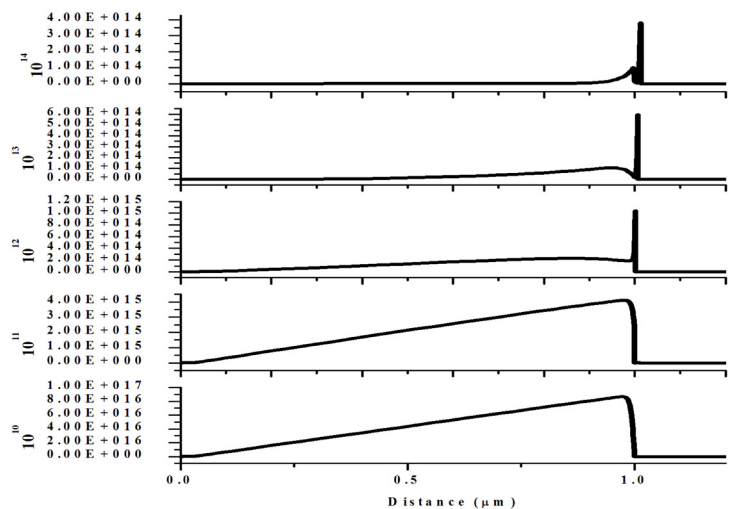


Figure 5. Recombination rate (/cm³s) of charge carriers in the cell at varying defect densities at the CuSbS₂/CTS interface

3.5. Effect of buffer layer i-ZnO on the performance of CTS QDSSC

Owing to the decrease in cell efficiency due to defect densities at the CTS/HTL interface, buffer layer was used to improve the efficiency. Buffer layer of i-ZnO was inserted between the HTL and CTS sensitizer and simulations were run with different thickness of the buffer layer in order to optimize the thickness of the buffer layer. Thickness of the buffer layer was varied from 100 nm to 1000 nm and their cell parameters were plotted as shown in Figures 6 and 7. With increasing thickness, all the cell parameters were found to increase and then saturate at 1000 nm and so the optimized thickness of i-ZnO buffer layer was taken as 1000 nm. Cell efficiency increased from 17.86% to 18.37% when this buffer layer was used.

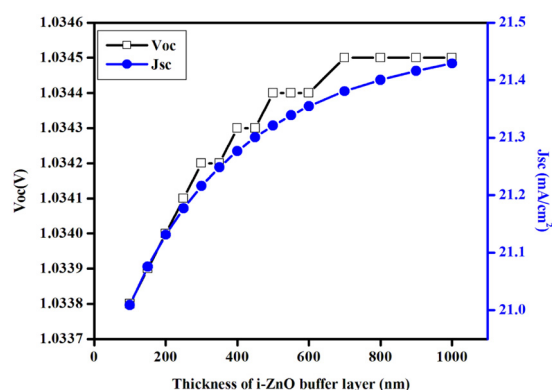


Figure 6. Variation of Voc and Jsc with increasing thickness of buffer layer

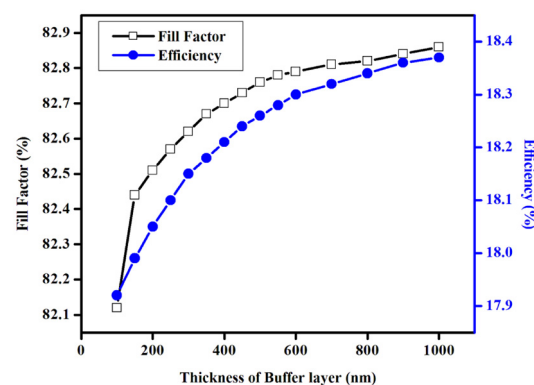


Figure 7. Variation of fill factor and efficiency with increasing thickness of buffer layer

Figure 8 shows the graph of recombination rates in the solar cell with and without the buffer layer. The recombination of charge carriers in the HTL increases by one order of magnitude when the buffer layer is used which indicates that a greater number of holes reach the HTL and there is lesser recombination at the interface. So i-ZnO is a good buffer layer which reduces the recombination at the HTL/CTS interface. The band structure of the solar cell with buffer layer has been shown in Figure 9; smooth transition of holes is possible with minimum recombination at the interfaces due to the favourable band offsets. Band structure at thermodynamic equilibrium has also been shown in Figure 10. The fermi level of electrons is found to be along the conduction band signifying higher electron density at the conduction band and higher electrical conductivity, enhancing the cell efficiency.

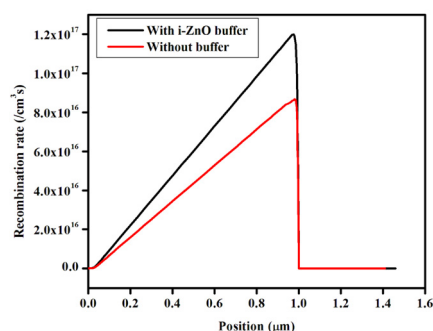


Figure 8. Recombination rates of solar cell with and without the i-ZnO buffer layer

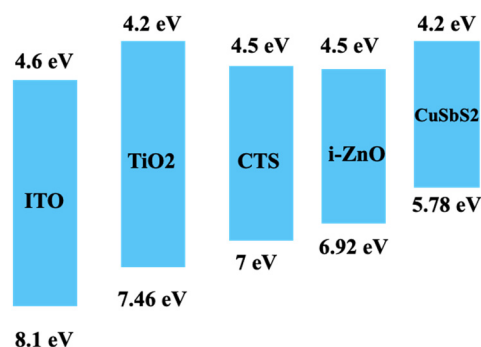


Figure 9. Band structure of the CTS QDSSC with buffer layer

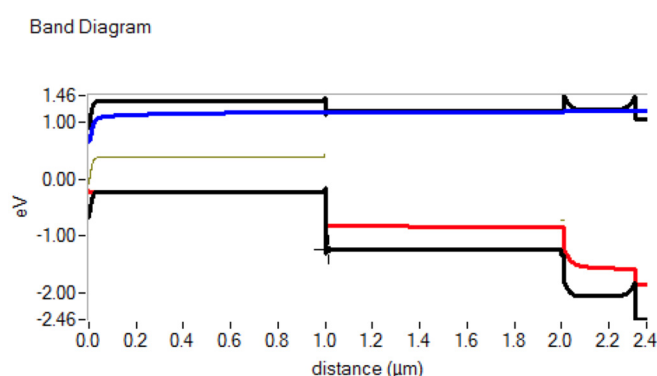


Figure 10. Band structure of the solar cell at thermodynamic equilibrium (with i-ZnO buffer)

3.6. Effect of CdS as buffer layer on the performance of CTS QDSSC

Inorder to optimise the material for buffer layer, CdS was also used in CTS QDSSC. Here too the band offsets are suitable for unhindered flow of holes and the band diagram at thermodynamic equilibrium (Figure 11) shows that the fermi level of electrons is along the conduction band facilitating electron transport and better electrical conductivity. The cell efficiency improved to 18.61% when CdS was used as a buffer layer in place of i-ZnO, the cell structure being ITO/TiO₂/CTS/CdS/CuSbS₂/Au. Higher fill factor was obtained as shown in Table 7, due to lower series resistance owing to lower recombination of charge carriers. The recombination rate of the solar cell with CdS buffer has been shown in Figure 12. The graph follows a gaussian curve indicating more recombination at the middle of the HTL rather than at the edges. Also, the recombination rate was found to be lower, 10¹³(cm⁻³ s⁻¹), compared to that when i-ZnO was used. Generation of charge carriers is higher here owing to increased absorption of the solar spectrum in the high energy blue-green regime.

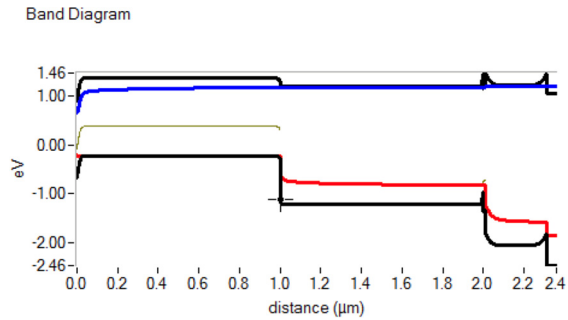


Figure 11. Energy band diagram at thermodynamic equilibrium- with CdS buffer

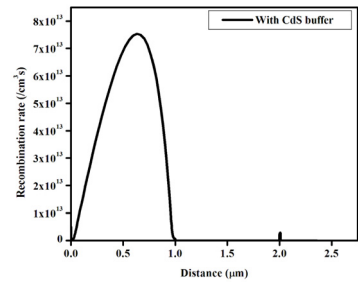


Figure 12. Recombination rate curve of solar cell when CdS is used as buffer

Table 7. Cell Parameters with CdS buffer layer

Buffer layer used	Voc (V)	Jsc (mA/cm ²)	FF (%)	Efficiency (%)
CdS	1.035	21.485	83.73	18.61

The quantum efficiency curves were plotted in all three cases, without buffer, with i-ZnO buffer and that with CdS buffer as shown in Figure 13. Absorption in the 350 nm to 500 nm is enhanced when the buffer layers are used. Solar cells with CdS buffer layer yielded higher quantum efficiency than i-ZnO, thus enhancing the cell efficiency.

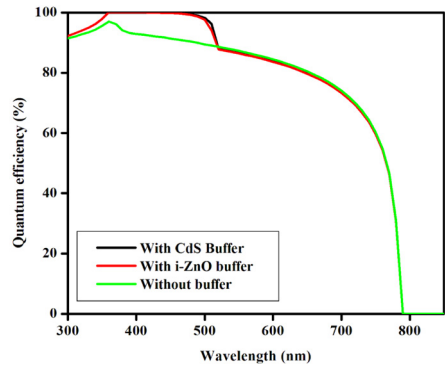


Figure 13. Quantum efficiency curves

CONCLUSIONS

Here simulation of CTS quantum dot sensitized solar cells were performed using SCAPS-1D software and an investigation was made on the effect of defects. HTL/CTS interface was found to have defects which affected the cell efficiency considerably and so buffer layers were introduced at this interface. CdS buffer layer was found to be better in performance compared to i-ZnO yielding cell efficiency of 18.61%.

Data Availability Statement

The data for the work is available with the corresponding author and can be produced upon request.

Declaration of Competing interests

The author declares that she has no known competing financial interests or personal relationships that could have appeared to influence the work reported in this paper.

Declaration of Generative AI and AI-assisted technologies in the writing process

No AI tools were used in the preparation of this manuscript.

Acknowledgements

The author would like to thank Marc Burglemann and his team for the SCAPS-1D software which is used in this work. Also, the author would like to thank Carmel College (Autonomous), Mala, Thrissur, Kerala, for the management fund for the successful completion of this work.

ORCID

Maya Mathew, <https://orcid.org/0000-0002-2088-4419>

REFERENCES

- [1] G. Konstantatos, editor, *Colloidal quantum dot optoelectronics and photovoltaics*, (Cambridge University Press; 2013).
- [2] G.H. Carey, A.L. Abdelhady, Z. Ning, S.M. Thon, O.M. Bakr, and E.H. Sargent, "Colloidal quantum dot solar cells," *Chemical reviews*, **115**(23), 12732-12763 (2015). <https://doi.org/10.1021/acs.chemrev.5b00063>
- [3] I.J. Kramer, and E.H. Sargent, "Colloidal quantum dot photovoltaics: a path forward," *ACS nano*, **5**(11), 8506-8514 (2011). <https://doi.org/10.1021/nn203438u>
- [4] N.M. Gabor, Z. Zhong, K. Bosnick, J. Park, and P.L. McEuen, "Extremely efficient multiple electron-hole pair generation in carbon nanotube photodiodes," *Science*, **325**(5946), 1367-1371 (2009). <https://doi.org/10.1126/science.1176112>
- [5] V.I. Klimov, editor, *Nanocrystal quantum dots*, (CRC press, 2017).
- [6] P.G. Prabhash, and S.S. Nair, "Synthesis of copper quantum dots by chemical reduction method and tailoring of its band gap," *AIP Advances*, **6**, 055003 (2016). <https://doi.org/10.1063/1.4948747>
- [7] Sahu, A. Garg, and A. Dixit, "A review on quantum dot sensitized solar cells: Past, present and future towards carrier multiplication with a possibility for higher efficiency," *Solar Energy*, **203**, 210-239 (2020). <https://doi.org/10.1016/j.solener.2020.04.044>
- [8] P. Bhambhani, "Quantum dot-sensitized solar cells: a review," *Bulletin of Electrical Engineering and Informatics*, **7**(1), 42-54 (2018). <https://doi.org/10.11591/eei.v7i1.841>
- [9] T.J. Ikyumbur, F. Gbaorun, A.A. McAsule, T.M. Aper, N.S. Akiiga, A.A. Gundu, and M.S. Shiada, "SCAPS-1D simulation of a high-efficiency quantum dot solar cell using Sb₂Se₃ as an absorber layer," *Next Research*, **1**(2), 100084 (2024). <https://doi.org/10.1016/j.nexres.2024.100084>
- [10] M. Mathew, and K.C. Preetha, "An exploration into the quantum confinement of CTS/natural dye core-shell quantum dots," *Physica B: Condensed Matter*, **579**, 411913 (2020). <https://doi.org/10.1016/j.physb.2019.411913>
- [11] M. Mathew, and K.C. Preetha, "Effect of Pelargonidin on carrier recombination lifetime of CTS quantum dots," *Optik*, **205**, 164275 (2020). <https://doi.org/10.1016/j.ijleo.2020.164275>
- [12] M. Mathew, and K.C. Preetha, "Mesoporous copper tin sulphide quantum dots as photoanode materials for efficient dye-sensitized solar cell," *Optik*, **224**, 165411 (2020). <https://doi.org/10.1016/j.ijleo.2020.165411>
- [13] A.C. Lokhande, P.T. Babar, V.C. Karade, M.G. Gang, V.C. Lokhande, C.D. Lokhande, and J.H. Kim, "The versatility of copper tin sulfide," *Journal of Materials Chemistry A*, **7**(29), 17118-17182 (2019). <https://doi.org/10.1039/C9TA00867E>
- [14] S. Dias, K. Kumawat, S. Biswas, and S.B. Krupanidhi, "Solvothermal synthesis of Cu₂SnS₃ quantum dots and their application in near-infrared photodetectors," *Inorganic chemistry*, **56**(4), 2198-2203 (2017). <https://doi.org/10.1021/acs.inorgchem.6b02832>
- [15] S.M. Yadav, and A. Pandey, "Low Cost Solvothermal Processed CTS QDs (0D)-Based Visible-NIR Photoconductor," *IEEE Sensors Journal*, **21**(18), 19978-19983 (2021). <https://doi.org/10.1109/JSEN.2021.3099059>
- [16] Y. Chen, L. Ma, Y. Yin, X. Qian, G. Zhou, X. Gu, W. Liu, *et al.*, "Strong quantum confinement effect in Cu₄SnS₄ quantum dots synthesized via an improved hydrothermal approach," *Journal of Alloys and Compounds*, **5**(672), 204-211 (2016). <https://doi.org/10.1016/j.jallcom.2016.02.135>
- [17] V. Maheskumar, and B. Vidhya, "Investigation on the morphology and photocatalytic activity of Cu₃SnS₄ synthesized by ball milling and solvothermal method," *Journal of Photochemistry and Photobiology A: Chemistry*, **356**, 521-529 (2018). <https://doi.org/10.1016/j.jphotochem.2017.12.026>
- [18] V. Maheskumar, I. Sheebha, B. Vidhya, J.P. Deebasree, T. Selvaraju, and S. Akash, "Enhanced electrocatalytic and photocatalytic activity of ball milled copper tin sulphide by incorporating GO and rGO," *Applied Surface Science*, **484**, 265-275 (2019). <https://doi.org/10.1016/j.apsusc.2019.03.241>
- [19] S. Rühle, M. Shalom, and A. Zaban, "Quantum-dot-sensitized solar cells," *ChemPhysChem*, **11**(11), 2290-2304 (2010). <https://doi.org/10.1002/cphc.201000069>
- [20] S. Emin, S.P. Singh, L. Han, N. Satoh, and A. Islam, "Colloidal quantum dot solar cells," *Solar Energy*, **85**(6), 1264-1282 (2011). <https://doi.org/10.1016/j.solener.2011.02.005>
- [21] X. Ma, X. Yang, M. Wang, R. Qin, D. Xu, C. Lan, K. Zhao, *et al.*, "Comprehensive Passivation on Different Charged Ions and Defects for High Efficiency and Stable Perovskite Solar Cells," *Advanced Energy Materials*, **15**(3), 2402814 (2025). <https://doi.org/10.1002/aenm.202402814>
- [22] Z. Yang, Y. Liu, and W. Chen, "A brief review of perovskite quantum dot solar cells: Synthesis, property and defect passivation," *ChemSusChem*, **18**(3), e202401587 (2025). <https://doi.org/10.1002/cssc.202401587>
- [23] T.K. Nideep, M. Ramya, and M. Kailasnath, "The influence of ZnS buffer layer on the size dependent efficiency of CdTe quantum dot sensitized solar cell," *Superlattices and Microstructures*, **130**, 175-181 (2019). <https://doi.org/10.1016/j.spmi.2019.04.034>
- [24] Manjeevan, and J. Bandara, "Systematic stacking of PbS/CdS/CdSe multi-layered quantum dots for the enhancement of solar cell efficiency by harvesting wide solar spectrum," *Electrochimica Acta*, **271**, 567-575 (2018). <https://doi.org/10.1016/j.electacta.2018.03.193>
- [25] M.A. Basit, M.A. Ali, Z. Masroor, Z. Tariq, and J.H. Bang, "Quantum dot-sensitized solar cells: a review on interfacial engineering strategies for boosting efficiency," *Journal of Industrial and Engineering Chemistry*, **120**, 1-26 (2023). <https://doi.org/10.1016/j.jiec.2022.12.016>
- [26] E. Laghchim, A. Raidou, A. Fahmi, and M. Fahoume, "The effect of ZnS buffer layer on Cu₂SnS₃ (CTS) thin film solar cells performance: numerical approach," *Micro and Nanostructures*, **165**, 207198 (2022). <https://doi.org/10.1016/j.micrna.2022.207198>

- [27] Z.R. Abdulghani, A.S. Najm, A.M. Holi, A.A. Al-Zahrani, K.S. Al-Zahrani, and H. Moria, "Numerical simulation of quantum dots as a buffer layer in CIGS solar cells: A comparative study. Scientific Reports, **12**(1), 8099 (2022). <https://doi.org/10.1038/s41598-022-12234-0>
- [28] T.K. Nideep, M. Ramya, and M. Kailasnath, "The influence of ZnS buffer layer on the size dependent efficiency of CdTe quantum dot sensitized solar cell," Superlattices and Microstructures, **130**, 175-181 (2019). <https://doi.org/10.1016/j.spmi.2019.04.034>
- [29] Siddique, M.N. Islam, H. Karmaker, A.A. Iqbal, A.A. Khan, M.A. Islam, and B.K. Das, "Numerical modelling and performance investigation of inorganic Copper-Tin-Sulfide (CTS) based perovskite solar cell with SCAPS-1D," Results in Optics, **16**, 100713 (2024). <https://doi.org/10.1016/j.rio.2024.100713>
- [30] E. Danladi, P.M. Gyuk, N.N. Tasie, A.C. Egbugha, D. Behera, I. Hossain, I.M. Bagudo, et al., "Impact of hole transport material on perovskite solar cells with different metal electrode: a SCAPS-1D simulation insight," Heliyon, **9**(6), e16838 (2023). <https://doi.org/10.1016/j.heliyon.2023.e16838>
- [31] S. Kumar, P. Bharti, and B. Pradhan, "Performance optimization of efficient PbS quantum dots solar cells through numerical simulation," Scientific Reports, **13**(1), 10511 (2023). <https://doi.org/10.1038/s41598-023-36769-y>
- [32] M. Burgelman, K. Decock, A. Niemegeers, J. Verschraegen, and S. Degrave, *SCAPS manual*, (University of Ghent, Ghent, Belgium, 2016).

**БУФЕРНІ ШАРИ $i\text{-ZnO}$ І CdS ДЛЯ ПІДВИЩЕННЯ ЕФЕКТИВНОСТІ СОНЯЧНИХ ЕЛЕМЕНТІВ,
СЕНСИБІЛІЗОВАНИХ КВАНТОВИМИ ТОЧКАМИ СУЛЬФІДУ МІДІ ТА ОЛОВА**

Майя Метью

Факультет фізики, Кармел коледж, (автономний), Мала, Тріссур, Керала, Індія

Вплив дефектів шару, а також дефектів інтерфейсу в сонячних елементах, чутливих до квантових точок із сульфиду міді та олова, досліджували за допомогою програмного забезпечення SCAPS-1D. Було виявлено, що дефекти шару сенсibilізатора та шару транспортування дірок не впливають на ефективність клітини, за винятком дуже високих щільностей 10^{19} см^{-2} . Було також виявлено, що дефект інтерфейсу в CTS/ETL не впливає на ефективність клітинки. Дефекти на інтерфейсі HTL/CTS значно знизили ефективність комірки, тому на цьому інтерфейсі було введено буферний шар. Було виявлено, що і матеріали буферного шару $i\text{-ZnO}$, і CdS мають рівні енергії, узгоджені з HTL, що посилює транспортування заряду. Ефективність елемента зросла з 17,86% до 18,37% з буферним шаром $i\text{-ZnO}$, тоді як ефективність елемента зросла до 18,61% при використанні CdS як буферного шару. Поглинання сонячного спектру в синьо-зеленій області посилювалося при використанні в комірці буферних шарів.

Ключові слова: сенсibilізовані квантовими точками сонячні елементи; буферний шар; SCAPS-1D; рекомбінація носіїв заряду; квантова ефективність; дефекти

ANALYSIS OF AC RESPONSE AND CHARGE TRANSPORT MECHANISMS IN DOUBLE-LAYER AND TRIPLE-LAYER SOLAR CELL ARCHITECTURES

 **Hmoud Al Dmour**

Department of Physics, Faculty of Science, Mu'tah University, Mu'tah 6170, Jordan

Corresponding Author e-mail: hmoud79@mutah.edu.jo

Received February 28, 2025 revised April 18, 2025; accepted April 28, 2025

This work investigates the effect of the ruthenium dye (Ru -dye) layer on electrical properties of solar cells based on the nc-TiO₂ semiconducting polymer heterojunction. In TLSCs (P3HT/Ru-dye/nc-TiO₂ solar cells), when the measurement frequency is decreased from 10 Hz to 0.1 Hz, a three-orders-of-magnitude increase in capacitance is observed. It is attributed to the dominance of diffusion capacitance the measurements, which indicates enhanced charge carrier dynamics and contribute to better performance and improved efficiency. In contrast, in the same frequency range, DLSCs (P3HT/nc-TiO₂ solar cells) exhibits a one-order-of-magnitude increase in capacitance, ascribed to the dominance of depletion capacitance. Thus, DLSCs likely suffer from low carrier injection, high recombination losses, and ultimately lower efficiency. The Cole-Cole curves are plotted for applied voltages ranging from 0 to 1.5 V and frequencies from 20 Hz to 1 MHz. At zero bias, while there is evidence of a relaxation process in TLSCs, this is not as clear for DLSCs. This is related to the effect of the Ru-dye inserted between the P3HT and nc-TiO₂ layers (TLSC), which facilitates better charge carrier generation and transport.

Keywords: *Solar Cells; Diffusion capacitance; Charge carreris; Efficiency; Interfaces*

PACS: 84.60.Jt , 73.40.kp , 84.37.q, 42.60.Lh. 72.20.Jv

1. INTRODUCTION

The performance of solar cells based on electron and hole transport materials is influenced by many factors [1-3]. One of the main factors is the quality of the interfacial layer formed between the components of solar cells. This interface plays a very important role in solar cells. In the case of inorganic solar cell semiconductors, extensive studies on this interface have provided valuable knowledge, leading the electronics industry to improve fabrication techniques and develop better-performing, longer-lasting integrated circuits [3]. For inorganic/organic solar cells, the interface is especially important as well, since it is commonly found that in organic devices, the same semiconductor behaves very differently depending on the dielectric material used and the interface thus formed, such as TiO₂ and P3HT [4,5]. Therefore, various organic and inorganic interface modifiers have been used to enhance the efficiency of hybrid TiO₂/P3HT solar cells in order to improve charge separation and molecular arrangement. Some of these modifiers include optimized fabrication, dopants, and tailored interfacial interactions, which further enhance charge transport and light absorption, advancing organic photovoltaics [6,7]. The interface between these components of solar cells influences solar cell efficiency, stability, and resilience in harsh weather conditions, such as heavy rain or snowstorms.

In this study, we present an investigation into the frequency and voltage dependence of the admittance in solar cells based on the nc-TiO₂ semiconducting polymer heterojunction. Section II outlines the theoretical framework of the conductance technique applied to solar cells. Section III details the experimental procedures for device fabrication and characterization. In Section IV, we analyze and discuss the experimental results in relation to the theoretical concepts introduced earlier. Our data analysis highlights the role of interface states and the impact of dye layers on device performance.

2. THEORTCAL SECTION

To understand the behavior of a heterojunction solar cell it is useful to consider the behavior of polar dielectric in an alternating electric field using these references (8-11). If a small sinusoidal voltage of angular frequency ω is applied to a parallel plate capacitor filled with such a material, then the capacitance, C , is given by

$$C = \frac{\epsilon_r \epsilon_0 A}{d} \quad (1)$$

where ϵ_r is the relative permittivity of the dielectric, ϵ_0 the permittivity of free space, A the place area and d the plate separation.

When measured over a wide range of frequencies from 10^2 to 10^{10} Hz, ϵ_r shows a strong frequency dependence, see Figure 1.

At low frequencies ϵ_r is essentially constant and equal to ϵ_s the static or low-frequency dielectric constant. As the frequency increase and permanent dipoles in the dielectric cease to be able to follow the voltage, then dispersion occurs

and ϵ_r decrease to ϵ_∞ , the high frequency dielectric constant, which reflects induced polarization corresponding to atomic and electron displacements in the alternating electric field. Also shown dotted at low frequency is a possible contribution from interfacial polarization. In our solar cells, this is an important contribution for interfaces formed between the components of devices.

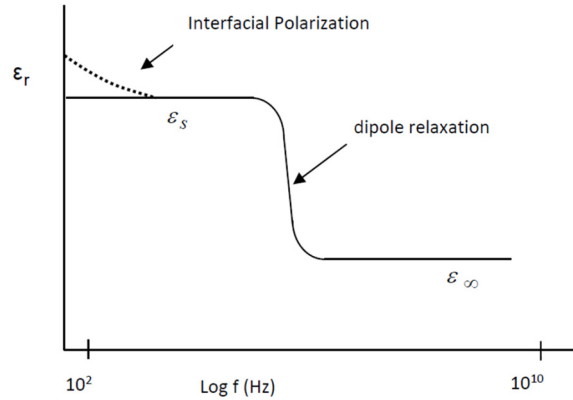


Figure 1. Frequency dependence of ϵ_r for a polar dielectric. The dotted curve shows the effect of interfacial polarization

● Interfacial polarization (Maxwell –Wagner Effect)

In a homogenous dielectric with conductivity σ and permittivity ϵ , the current density of the system is determined using Maxwell's equation

$$J = \sigma E + \epsilon \frac{dE}{dt} \quad (2)$$

where E is the electric field. For an alternating applied voltage $V = V_0 e^{j\omega t}$ and since $E = \frac{V}{d}$, equation (2) may be written as

$$J = j\omega \left(\epsilon - j\frac{\sigma}{\omega} \right) \frac{V}{d} \quad (3)$$

Hence the capacitor may be represented by a complex capacitance per unit area, C^* , where

$$C^* = \frac{\epsilon - j\frac{\sigma}{\omega}}{d} \quad (4)$$

If the capacitor consists of two different materials, they may be characterized by their thickness (d_1, d_2), conductivity (σ_1, σ_2) and permittivity (ϵ_1, ϵ_2) (Figure 2).

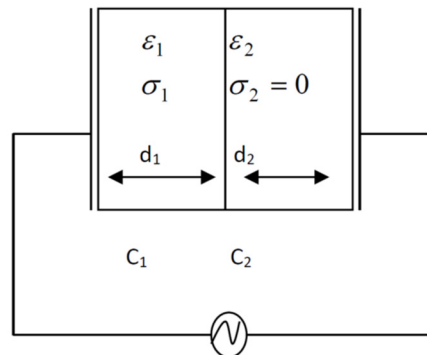


Figure 2. An inhomogenous capacitor formed from two different dielectrics

The two materials will have capacitances C_1 and C_2 in series and if $\sigma_2 = 0$, then

$$C_1 = \frac{\epsilon_1 - j\frac{\sigma}{\omega}}{d} \quad (5)$$

and

$$C_2 = \frac{\epsilon_2}{d_2} \quad (6)$$

so that the total capacitance C_T is given by

$$C_T^* = \frac{C_1 C_2}{C_1 + C_2} = \frac{\epsilon_T^*}{d_1 + d_2} \quad (7)$$

where ϵ_T^* is the apparent complex permittivity.

The apparent permittivity ϵ_T^* is given by

$$\epsilon_T^* = \frac{(\epsilon_1 - j\frac{\sigma}{\omega})\epsilon_2}{(\epsilon_1 - j\frac{\sigma}{\omega})f_2 + \epsilon_2 f_1} \quad (8)$$

where $f_1 = \frac{d_1}{d_1 + d_2}$ and $f_2 = \frac{d_2}{d_1 + d_2}$

When $\omega \rightarrow 0$, $\epsilon_T^* \rightarrow \epsilon_s$, the apparent value of the static permittivity

$$\epsilon_s = \frac{\epsilon_2}{f_2} \quad (9)$$

When $\omega \rightarrow \infty$, $\epsilon_T^* \rightarrow \epsilon_\infty$, the apparent value of the high frequency permittivity

$$\epsilon_\infty = \frac{\epsilon_2 \epsilon_1}{\epsilon_1 f_2 + \epsilon_2 f_1} \quad (10)$$

By substitution it can be shown that

$$\frac{\epsilon_T^* - \epsilon_\infty}{\epsilon_s - \epsilon_\infty} = \frac{-j\frac{\sigma}{\omega}}{\epsilon_1 f_2 + \epsilon_2 f_1 - j\frac{\sigma}{\omega} f_2} \quad (11)$$

or

$$\frac{\epsilon_T^* - \epsilon_\infty}{\epsilon_s - \epsilon_\infty} = \frac{1}{1 + j\omega\tau} \quad (12)$$

where $\tau = \frac{\epsilon_1 f_2 + \epsilon_2 f_1}{\sigma f_2}$. Here τ is the relaxation time of the double-layer capacitor structure. Rearranging equation (12)

then yields

$$\epsilon_T^* = \epsilon_\infty + \frac{\epsilon_s - \epsilon_\infty}{1 + j\omega\tau} \quad (13)$$

or

$$\epsilon_T^* = \epsilon_\infty + \frac{\epsilon_s - \epsilon_\infty}{1 + \omega^2 \tau^2} - \frac{j\omega\tau(\epsilon_s - \epsilon_\infty)}{1 + \omega^2 \tau^2} \quad (14)$$

Equation (14) may be simplified to

$$\epsilon_T^* = \epsilon' - j\epsilon'' \quad (15)$$

where the real part

$$\epsilon' = \epsilon_\infty + \frac{\epsilon_s - \epsilon_\infty}{1 + \omega^2 \tau^2} \quad (16)$$

And the imaginary part

$$\epsilon'' = \frac{\omega\tau(\epsilon_s - \epsilon_\infty)}{1 + \omega^2 \tau^2} \quad (17)$$

These represent exactly the format of the Debye equation for a single relaxation time process and show that ϵ' and ϵ'' are frequency dependent (Figure 3).

The Debye equation can be rearranged to eliminate ω , yielding

$$(\epsilon'(\omega) - \frac{\epsilon_s + \epsilon_\infty}{2})^2 + (\epsilon''(\omega))^2 = \frac{1}{4}(\epsilon'' - \epsilon_\infty)^2 \quad (18)$$

This is an equation for a circle when $\varepsilon''(\omega)$ is plotted against $\varepsilon'(\omega)$. Such a plot (Figure 4) is known as a Cole-Cole plot.

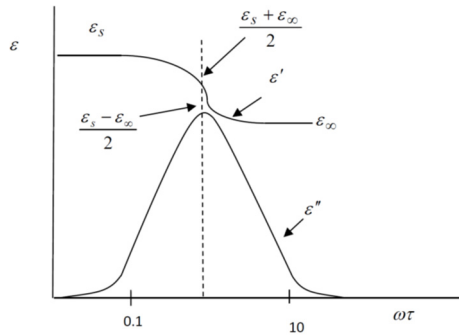


Figure 3. Relaxation spectrum of the inhomogeneous capacitor

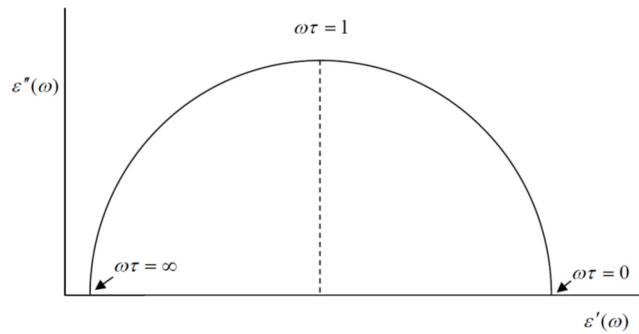


Figure 4. A Cole-Cole plot of $\varepsilon''(\omega)$ versus $\varepsilon'(\omega)$ of a single relaxation time process

If there are two semicircles in the Cole –Cole plot, then this provides evidence of two process occurring in the device (Figure 5).

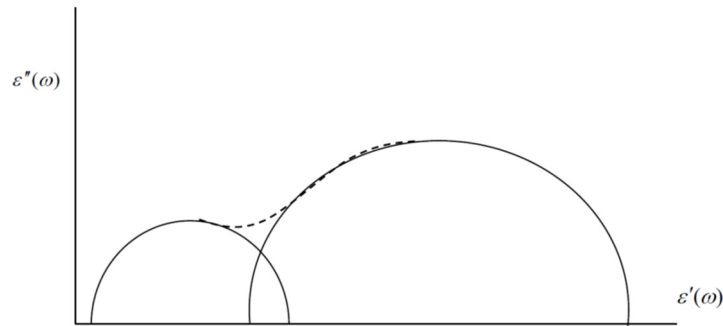


Figure 5. Cole-Cole plot of $\varepsilon''(\omega)$ versus $\varepsilon'(\omega)$ with two processes occurring in the device

In an interpenetrating system such as a bulk heterojunction solar cell, then the simple two-layer model breaks down and the device is likely to be characterized by a distribution of relaxation times. By analogy with polar dielectrics with a distribution of relation times we may now write the complex permittivity ε_T^* as

$$\varepsilon_T^* = \varepsilon_\infty + \frac{\varepsilon_s - \varepsilon_\infty}{1 + j\omega\tau^{(1-\alpha)}} \quad (19)$$

where α is a parameter describing the distribution. When $\alpha = 0$ the single relaxation time response is recovered. When $0 < \alpha < 1$, the effect of the distribution of relaxation times is to broaden and flatten the Cole-Cole plot as shown in Figure 6.

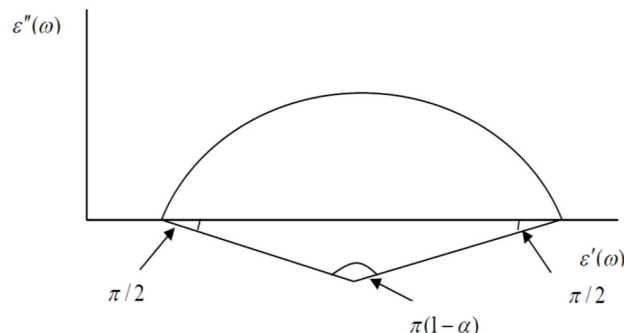


Figure 6. The effect of the distribution of relaxation time on the Cole-Cole plot

3. EXPERIMENTAL METHOD

Figure 7 shows the molecular structure of the materials used in our solar cells. The devices were made using fluorine-doped tin oxide ($\text{SnO}_2\text{:F}$) electrodes with a compact TiO_2 layer added by spray pyrolysis according to [7]. A nanocrystalline $\pi / 2$ TiO_2 (nc- TiO_2) paste acted as the active layer, sensitized with ruthenium dye ($\text{RuL}_2(\text{NCS})_2\text{:2 TBA}$) from Solaronix Co., Switzerland. The p-type semiconductor, P3HT, was from Sigma-Aldrich Ltd. Similar devices without the ruthenium dye were also fabricated for comparison. To fabricate the cells, the $\text{SnO}_2\text{:F}/\text{TiO}_2$ substrates were cleaned

thoroughly with Decon 90 soap, rinsed with tap, hot, and ultrapure water, and dried. The nc-TiO₂ paste was spread on the surface, dried in air, and heated to 450°C for 30 minutes to form a porous anatase layer about 2 μm thick. This layer was soaked in a ruthenium dye solution for 48 hours, then rinsed with ethanol and dried under nitrogen. The P3HT layer was applied on top by spin-coating a chloroform solution of P3HT at 1000 rpm. A gold layer (~50 nm thick) was deposited as the top electrode with a device area of 3 mm². Electrical testing was done using a Solartron 1260 Frequency analyzer. Capacitance and conductance were measured across frequencies from 100 Hz to 1 MHz at room temperature. Capacitance-voltage measurements were taken in the range of +2.5 V to -2.5 V at 0.1 V steps and a fixed frequency of 100 Hz. Voltage bias was applied to the SnO₂:F electrode, with forward bias from 0 V to -2.5 V and reverse bias from +2.5 V to 0 V.

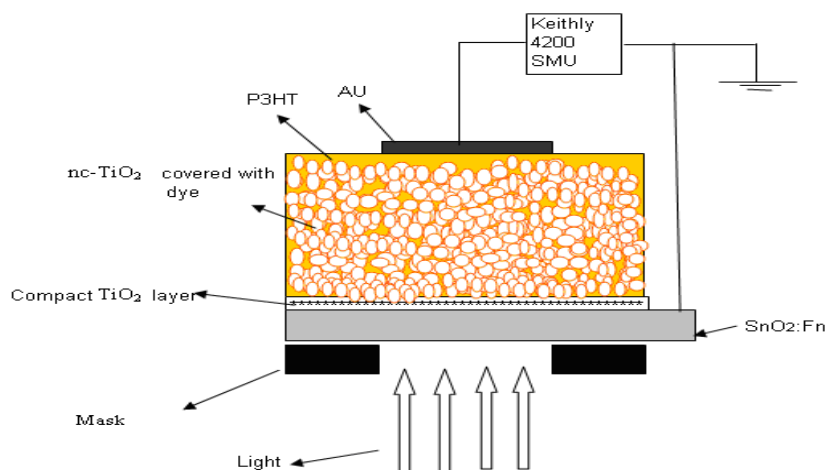


Figure 7. Schematic representation of the solar cell structure tested under illumination

4. RESULTS AND DISCUSSION

Figure 8 shows the difference in DC characteristics of TLSCs and DLSCs in both dark and illuminated conditions. In the dark, TLSCs have a strong rectification ratio of about 3000 at +1V, with a low reverse current, while DLSCs show a much lower rectification ratio of 10 at -0.8V.

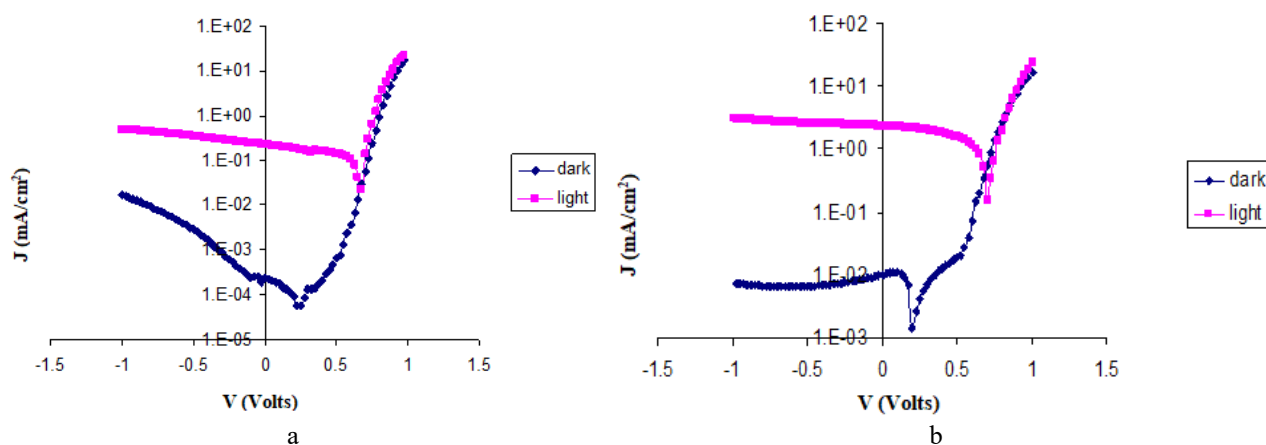


Figure 8. J–V characteristics of (a) DLSC and (b) TLSC device under illumination and dark conditions

Both types of devices turn on at around 0.65V, but TLSCs start conducting strongly at 0.65V, whereas DLSCs reach a high current (~10mA/cm²) at 0.8V. Under illumination with a halogen lamp, TLSCs produce a higher open-circuit voltage (V_{oc}) of 0.73V, a much greater short-circuit current density (J_{sc}) of 2.3mA/cm², a fill factor (FF) of 49%, and a power conversion efficiency (PCE) of 1.1%. In contrast, DLSCs achieve a V_{oc} of 0.68V, a significantly lower J_{sc} of 0.22mA/cm², an FF of 46%, and a PCE of just 0.09%. The higher J_{sc} in TLSCs suggests better charge collection efficiency. The DLSCs show some variation in V_{oc} (0.65V–0.68V), likely due to an electric field at the nc-TiO₂/P3HT interface, as previously reported for similar cells. Both device types show increased current under illumination at high forward bias, indicating photoconductivity. Overall, TLSCs outperform DLSCs in V_{oc}, J_{sc}, and PCE, making them a stronger choice for solar cell applications.

The capacitance versus frequency characteristics of DLSCs as a function of the applied voltage were presented in Figure 9. At high frequency (0.1MHz), the capacitance was ~188 pF and almost constant as the applied voltage increased. At low frequency, the loss appears to become almost constant capacitance was over 3 orders of magnitude greater and dependent on the voltage applied to the device. For an applied voltage of 0V, the capacitance measured at 1Hz was 156nF

and increased to 448 nF at -0.4V therefore remaining constant for further increases in forward bias. Figure 9-b shows the loss-frequency relationship for a DLSC with different voltages applied to the SnO₂:F electrode. With -0.8V applied, the loss at 0.1MHz was ~290pF, but increasing, following a law of the form $\omega^{-0.83}$, to ~1300nF at 1Hz. Similar behavior was observed for ~0.4V and 0V.

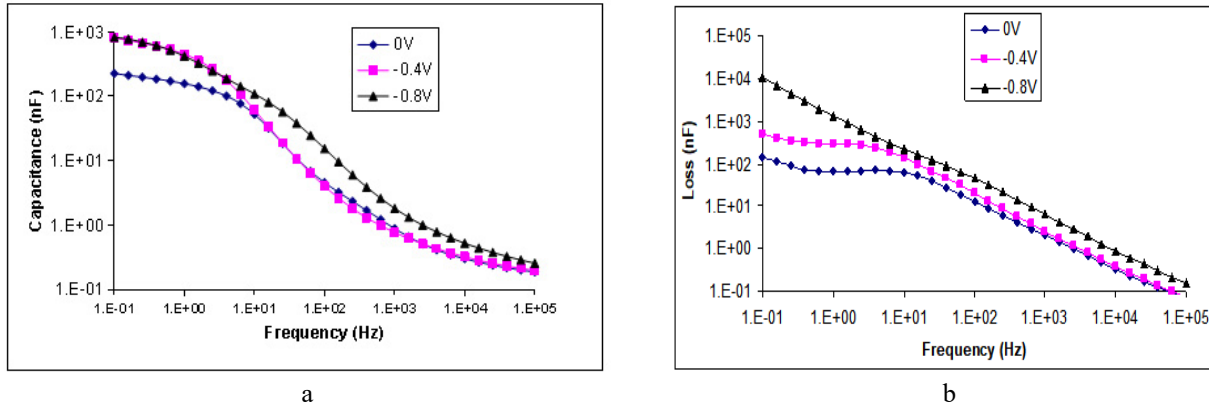


Figure 9. a) Logarithmic plot of capacitance and b) loss versus frequency characteristics of DLSC under different voltages applied to the SnO₂:F electrode

In Figures 10, the results presented in Figure 9 are replotted as Cole-Cole plot. Figure 10 shows the Cole-Cole plot of DLSC. In this figure, the curves show clear dispersion between about 1Hz and 100 Hz, corresponding to the region of almost constant loss in figure 9. At low frequency, a second process is observed which suggest additional dispersion although the almost constant capacitance in this region suggests that it arises from a DC loss in the device. This view is reinforced in Figure 10-b and 10-c where application of a forward voltage increases this component significantly. At the highest frequencies (100Hz TO 10kHz), there is a tendency for the plots to converge at a capacitance of 188pF, which corresponds to the device thickness.

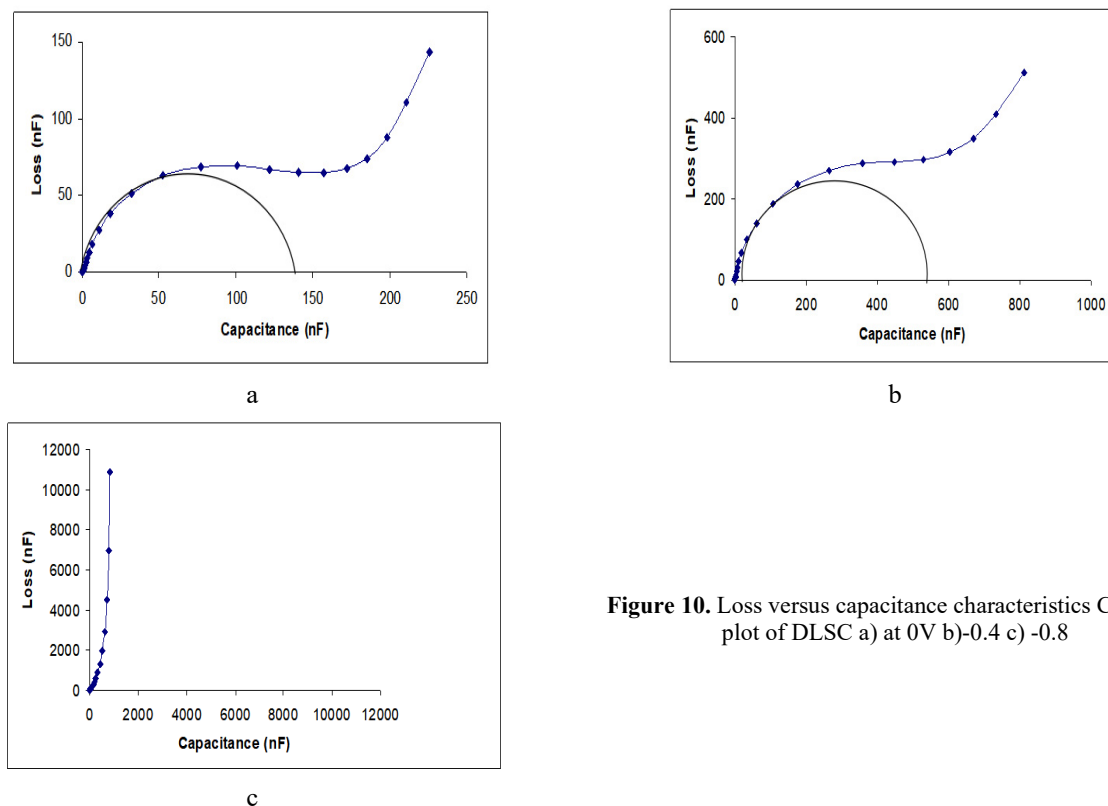


Figure 10. Loss versus capacitance characteristics Cole-Cle plot of DLSC a) at 0V b)-0.4 c)-0.8

The capacitance-voltage (C-V) characteristics of DLSCs were also measured at two different frequencies, namely 10 KHz and 1 Hz. The results are shown in Figures 11-a and 11-b respectively. As can be seen, capacitance was virtually independent of the applied voltage when the device was under reverse bias, but increased rapidly at -0.6V at high frequency and at -0.2V for the lower frequency. In both cases, this capacitance passes through a maximum and decreases rapidly for further increase in forward bias.

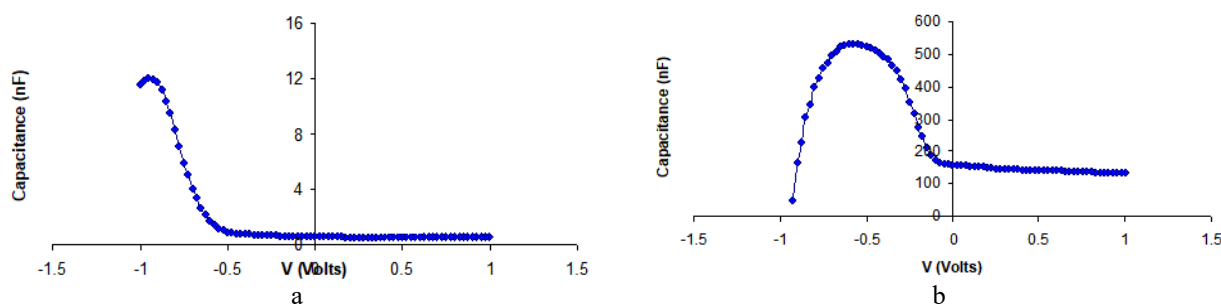


Figure 11. Capacitance-voltage characteristics of DLSC at (a) 10KHz and (b) 1Hz

Figure 12 shows capacitance versus frequency characterization of a TLSC as a function of the voltage applied to the $\text{SnO}_2\text{:F}$ electrode. For an applied voltage of 0V, the high frequency capacitance was ~ 189 pF for a frequency of 0.1 MHz which is similar to the high frequency capacitance of a DLSC. However, comparing Figure 9 and Figure 12-a, the high frequency capacitance of the TLSC was more strongly dependent on the applied voltage, especially at frequencies below 0.1 MHz. However, there was an increase in the low frequency capacitance compared to DLSCs as follows:

1. For an applied voltage of 0V, the capacitance of DLSC at 1Hz was ~ 157 nF in contrast to 42nF for TLSC.
2. For an applied voltage of -0.8V, the low frequency capacitance of TLSCs at 1Hz was ~ 3340 nF and hence significantly greater than ~ 471 nF for DLSCs.

Figure 12-b shows the loss-frequency characteristics of the TLSCs with different bias voltages applied to the $\text{SnO}_2\text{:F}$ electrode. At 0.1 MHz, the loss showed stronger voltage dependence in the TLSC compared with the DLSC. At 1Hz, this dependence was much more marked. The loss in the TLSCs increased by more than 3 orders of magnitude to $\sim 2.2 \times 10^4$ nF for an applied voltage of -0.8V.

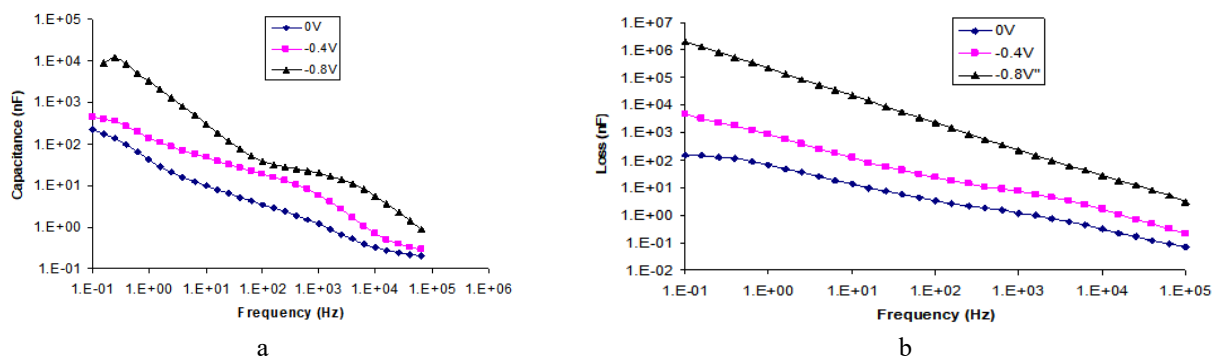


Figure 12. a) Logarithmic plot of (a) capacitance and b) loss versus frequency characteristics of TLSC versus frequency characteristics under different voltages applied to the $\text{SnO}_2\text{:F}$ electrode

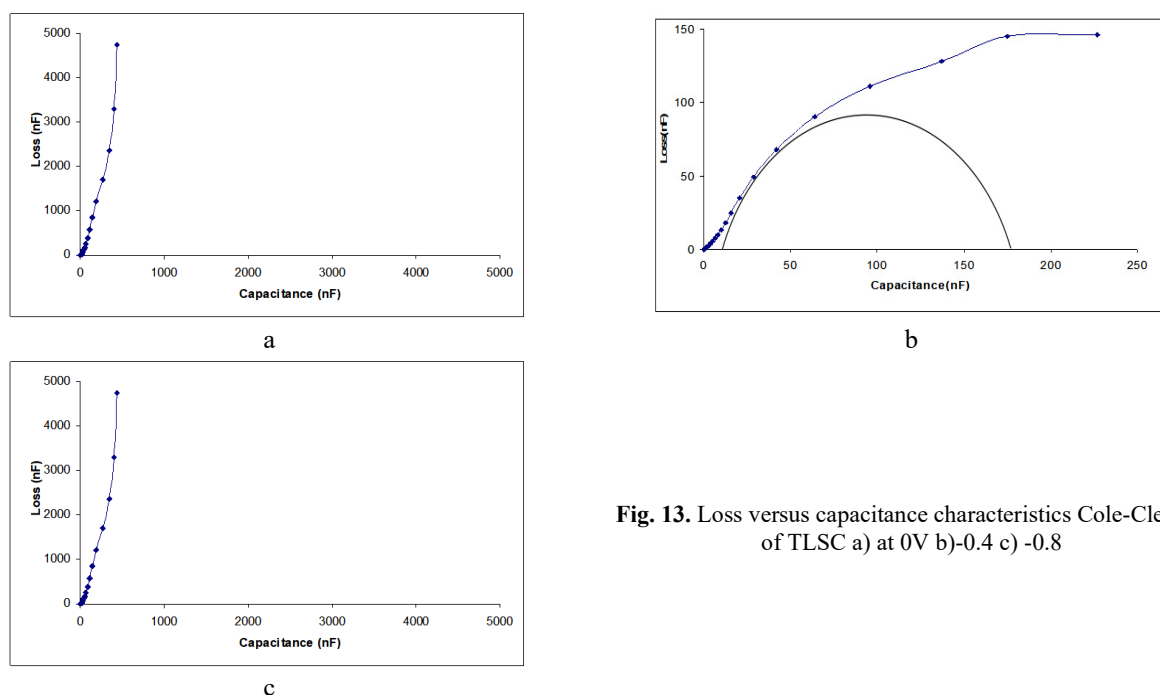


Fig. 13. Loss versus capacitance characteristics Cole-Cle plot of TLSC a) at 0V b) -0.4V c) -0.8V

Figures 13 show the Cole-Cole plots for the TLSCs with a different applied voltage. At zero bias, while there is evidence for a relaxation process, this is not so clear as for the DLSC. Here the DC loss is already beginning to dominate the dispersion and clearly does so when the voltage applied was increased from 0V to -0.4V and -0.8V. Figure 14 shows the C-V characteristic of a TLSC at two different frequencies, namely 10 KHz and 1 Hz. The capacitance was independent of the applied voltage when the device was in reverse bias, but increased rapidly to a maximum value in forward bias as seen in the DLSCs (figure 11). Interestingly in the TLSC, the maximum capacitance reached was lower than in DLSCs (~ 4 nF compared to 13 nF) and occurred at a lower voltage -0.85V. On other hand, Figure 14 shows capacitance-voltage measurements on a TLSC at 1Hz. The result behave a steadily increasing capacitance for increasing forward bias, reaching 1600nF at 0.5V and much higher, therefore, than observed in DLSC under corresponding conditions.

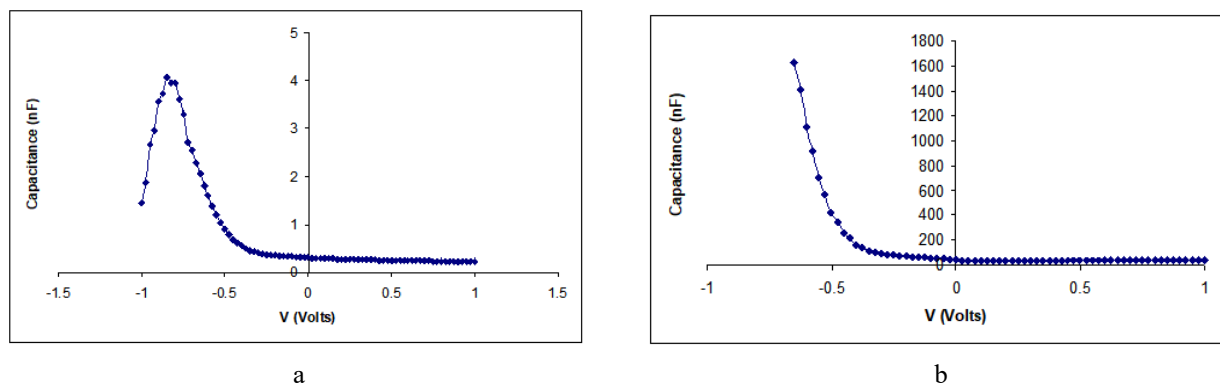


Figure 14. Capacitance-voltage characteristics of TLSC at (a) 10KHz and (b) 1Hz

5. DISCUSSION

The J-V characteristics (Figure 8) clearly show that TLSCs show better performance in comparison with DLSCs. Under illumination, TLSCs produce a V_{oc} of 0.73V, a J_{sc} of 2.3 mA/cm², and a PCE of 1.1%, while DLSCs produce a V_{oc} of 0.68V, a J_{sc} of 0.22 mA/cm², and a PCE of just 0.09%. The higher efficiency in TLSCs is attributed to the presence of the Ru-dye layer, which acts as a sensitizer and facilitates better charge carrier generation and transport. That is accompanied by higher J_{sc} and V_{oc} in TLSCs, indicating improved charge collection efficiency and reduced recombination losses at the interface [11-14]. In contrast, DLSCs suffer from poor charge separation and high recombination, leading to lower efficiency.

The AC results, including capacitance-frequency (C-f) measurements, loss-frequency characteristics, and Cole-Cole plots, provide further insights into the charge transport mechanisms and the role of the Ru-dye layer. At high frequencies (0.1 MHz), the capacitance is nearly constant (~ 188 pF for DLSCs and ~ 189 pF for TLSCs) and represents the geometric capacitance of the device, dominated by the bulk regions of P3HT and nc-TiO₂. However, at low frequencies (1 Hz), the capacitance behavior diverges significantly between DLSCs and TLSCs. In DLSCs, the capacitance increases with applied voltage, reflecting the dominance of depletion capacitance, which is associated with charge accumulation and recombination at the P3HT/nc-TiO₂ interface. This behavior is consistent with the poor charge separation and high recombination losses observed in the DC results. In contrast, TLSCs exhibit a much larger increase in capacitance at low frequencies, which is attributed to diffusion capacitance, indicating efficient charge carrier dynamics and reduced recombination. This is consistent with the improved charge collection efficiency and higher J_{sc} observed in the DC results. The capacitance-voltage (C-V) characteristics at different frequencies further support these findings. At 10 kHz, the capacitance in TLSCs reaches a maximum of ~ 4 nF at -0.85V, which is lower than the maximum capacitance observed in DLSCs (~ 13 nF). This indicates better charge control in TLSCs, consistent with the improved charge transport and reduced recombination observed in the DC results. At 1 Hz, the capacitance in TLSCs increases steadily with forward bias, reaching 1600 nF at 0.5V, which is significantly higher than in DLSCs. This reflects the dominance of diffusion capacitance in TLSCs due to improved charge carrier dynamics.

6. CONCLUSIONS

The DC and AC results are closely interrelated and provide complementary insights into the performance and charge transport mechanisms of the solar cells. The DC results demonstrate that TLSCs have better steady-state performance, with higher V_{oc} , J_{sc} , and PCE, while the AC results reveal that this improvement is due to better charge separation, reduced recombination, and more efficient charge transport facilitated by the Ru-dye layer. The Ru-dye acts as a sensitizer, enhancing charge injection into nc-TiO₂ and reducing recombination losses, which leads to superior charge carrier dynamics and overall device efficiency. The combination of DC and AC analysis provides a comprehensive understanding of the charge transport mechanisms and highlights the critical role of the Ru-dye layer in improving the performance of TLSCs. This integrated approach underscores the importance of interfacial modifications, such as the incorporation of a Ru-dye layer, in optimizing the performance of organic-inorganic hybrid solar cells.

ORCID

©Hmoud Al Dmour, <https://orcid.org/0000-0001-5680-5703>

7. REFERENCES

- [1] L. Bhattacharya, and M. Caspary, "Factors influencing charge transport at perovskite-charge transport layer interfaces: current strategies, challenges, and perspectives based on first-principles studies," J. Phys. D: Appl. Phys; **57**, 412001 (2024). <https://doi.org/10.1088/1361-6463/ad4dae>
- [2] H. Al-Dmour, and D.M Taylor, "Effect of properties of NC-TiO₂ grains on the performance of organic/inorganic solar cells," JOR, **19**, 587-596 (2023). <https://doi.org/10.15251/JOR.2023.195.587>
- [3] N. Dey, M. Reza, A. Ghosh, H. Al-Dmour, *et al.*, "Optimization of Sr₃NCI₃-based perovskite solar cell performance through the comparison of different electron and hole transport layers," J. Phys. Chem. Solids, **196**, 112386 (2025) <https://doi.org/10.1016/j.jpcs.2024.112386>
- [4] N. Juneja, *et al.*, "Sb₂S₃ solar cells with a cost-effective and dopant-free fluorene-based enamine as a hole transport material," Sustain Energy Fuels, **6**, 3220 (2022). <https://doi.org/10.1039/d2se00356b>
- [5] H. Al Dmour, and D. Taylor, "Small-signal response of nanocrystalline-titanium dioxide/poly(3-hexylthiophene) heterojunction solar cells," Thin solid Film, **519**(22), 8135-8138 (2011). <https://doi.org/10.1016/j.tsf.2011.06.009>
- [6] Z. Wang, C. Gong, C. Zhang, C. Zhao, T.-S. Su, H. Li, and H. Zhang, "Recent Advances in Interfacial Engineering for High-Efficiency Perovskite Photovoltaics," DeCarbon, 1-47 (2025) <https://doi.org/10.1016/j.decarb.2025.100107>
- [7] N. Saleh, S. Al-Trawneh, H. Al-Dmour, *et al.*, "Effect of Molecular-Level Insulation on the Performance of a Dye-Sensitized Solar Cell: Fluorescence Studies in Solid State," J. Fluoresc. **25**, 59–68 (2015). <https://doi.org/10.1007/s10895-014-1479-8>
- [8] S.M. Sze, *Physics of Semiconductor Devices*, 2nd edition, (Wiley-Interscience, 1981).
- [9] E.H. Nicollian, and J.R. Brews, *MOS (Metal Oxide Semiconductor) Physics and Technology*, (Wiley Interscience, Wiley Classics Library edition, 1981)
- [10] M. Madanat, A. Al-Tabbakh, M. Alsa'eed, H. Al-Dmour, and M. Mousa, "Application of Murphy – Good Plot Parameters Extraction Method on Electron Emission from Carbon Fibers," Ultramicroscopy, **234**, 113479 (2022). <https://doi.org/10.1016/j.ultramic.2022.113479>
- [11] H. Zhou, M. Aftabuzzaman, M. Masud, S. Kang, and H.K. Key, "Materials and Fabrication Strategies for High-Performance Dye-Sensitized Solar Cells: Comprehensive Comparison and Perspective," ACS Energy Letters, **10**(2), 881-895 (2025). <http://dx.doi.org/10.1021/acsenenergylett.4c03579>
- [12] N. Lal Dey, M. Reza, Av. Ghosh, H. Al-Dmour, *et al.*, "Optimization of Sr₃NCI₃-based perovskite solar cell performance through the comparison of different electron and hole transport layers," J. Fluoresc, **25**, 59–68 (2015). <https://doi.org/10.1007/s10895-014-1479-8>
- [13] N.L. Dey, Md.S. Reza, A. Ghosh, H. Al-Dmour, M. Moumita, Md.S. Reza, S. Sultana, *et al.*, "Optimization of Sr₃NCI₃-based perovskite solar cell performance through the comparison of different electron and hole transport layers," J. Phys. Chem. Solids, **96**, 112386 (2025). <https://doi.org/10.1016/j.jpcs.2024.112386>
- [14] H. Al Dmour, "Capacitance response of solar cells based on amorphous Titanium dioxide (A-TiO₂) semiconducting heterojunctions," AIMS Mater. Sci, **8**(2), 261-270 (2021). <https://doi.org/0.3934/matricsci.2021017>

АНАЛІЗ ВІДГУКУ ЗМІННОГО СТРУМУ І МЕХАНІЗМІВ ПЕРЕНОСУ ЗАРЯДУ В ДВОШАРОВІХ І ТРИШАРОВІХ АРХІТЕКТУРАХ СОНЯЧНИХ ЕЛЕМЕНТІВ

Хмуд Аль Дмур

Кафедра фізики, факультет природничих наук, Університет Мута, Мута 6170, Йорданія

У цій роботі досліджується вплив шару рутенієвого барвника (Ru-барвник) на електричні властивості сонячних елементів на основі напівпровідникового полімерного гетеропереходу nc-TiO₂. У TLSC (сонячні елементи РЗНТ/Ru-барвник/nc-TiO₂) при зменшенні частоти вимірювань з 10 Гц до 0,1 Гц спостерігається збільшення ємності на три порядки. Це пояснюється домінуванням дифузійної ємності у вимірюваннях, що вказує на покращену динаміку носіїв заряду та сприяє кращій продуктивності та підвищенню ефективності. На противагу цьому, в тому ж діапазоні частот, DLSC (сонячні елементи РЗНТ/nc-TiO₂) демонструють збільшення ємності на один порядок, що пояснюється домінуванням виснажливої ємності. Таким чином, DLSC, ймовірно, страждають від низької інжекції носіїв заряду, високих втрат на рекомбінацію та, зрештою, нижчої ефективності. Криві Коула-Коула побудовані для прикладених напруг в діапазоні від 0 до 1,5 В та частот від 20 Гц до 1 МГц. При нульовому зміщенні, хоча є ознаки процесу релаксації в TLSC, це не так очевидно для DLSC. Це пов'язано з ефектом Ru-барвника, вставленого між шарами РЗНТ та nc-TiO₂ (TLSC), що сприяє кращому генеруванню та транспорту носіїв заряду.

Ключові слова: сонячні елементи; дифузійна ємність; носії заряду; ефективність; інтерфейси

VIBRATIONAL FREQUENCIES OF DICHLORODIFLUOROMETHANE USING A LIE ALGEBRAIC FRAMEWORK

P. Suneetha^a, B.V.S.N. Hari Prasad^b,  J. Vijayasekhar^{c*}

^aDepartment of Mathematics, SAHE-Siddhartha Academy of Higher Education-Deemed to be University, Vijayawada, India

^bDepartment of Mathematics, Vasireddy Venkatadri Institute of Technology, Nambur, Guntur District, Andhra Pradesh, India

^cDepartment of Mathematics, GITAM (Deemed to be University), Hyderabad, India

*Corresponding Author e-mail: vijayjaliparthi@gmail.com

Received January 3, 2025; revised March 19, 2025; accepted March 26, 2025

This study introduces a symmetry-adapted Lie algebraic framework, a highly efficient tool for calculating vibrational frequencies in dichlorodifluoromethane (CCl_2F_2). With its C_{2v} point group symmetry, the molecule under consideration is particularly suited for this approach. By formulating carbon-hydrogen (C-H) and carbon-chlorine (C-Cl) bond structures in unitary Lie algebras, the determination of the vibrational quantum states of the molecule becomes remarkably straightforward. The Hamiltonian, including Casimir and Majorana invariant operators and fitted parameters, accurately reproduces the desired vibrational modes using fundamental and higher overtone frequencies. This approach, which compares modern and classical models, underscores the Lie algebraic techniques as efficient tools for modelling anharmonic interactions and transition dynamics on a molecular scale. Beyond its theoretical relevance, the model constructed provides a deep understanding of the vibrational aspects of molecules, a knowledge crucial for practical applications such as spectroscopic data interpretation, the design of materials with desired vibrational characteristics, or the study of molecules in complex environments. These practical applications enhance the versatility of the methodology and have enabled its successful application to molecular spectroscopy, chemical kinetics, and the design of energy-efficient materials and sensors, among other areas. This study provides experimentalists with confidence in the Lie algebraic approach and paves the way for further polyatomic molecule experiments. By significantly contributing to reducing the error margin in computational molecular physics, this methodology opens exciting possibilities for future research and development.

Keywords: Lie Algebraic Approach; Vibrational Hamiltonian; Casimir and Majorana Operators; Dichlorodifluoromethane; Anharmonic Vibrational Modes

PACS: 02.20.Qs, 31.15.Xf, 03.65.Fd, 33.20.Tp, 33.20.Ea

1. INTRODUCTION

Vibrational spectra are of great importance as they form the basis of molecular spectroscopy and are a valuable resource for depicting a molecule's structural, dynamic, and chemical aspects. The spectra are the result of the quantization of vibrational modes of molecular bonds and are valuable in understanding molecular behaviour, such as bond strength, structure, and energy interactions. These natural frequencies are associated with the vibrational spectra of molecules and serve as the basis for understanding inter and intra-molecular interaction and stability. Their accurate determination is important for various applications in science and industry, including the characterization of materials, monitoring of the environment, analysis of chemicals, and even drug design. Their prediction and analysis enable scientists to envisage the molecular properties under varied physical and chemical circumstances, which enhances the growth of both theoretical and experimental chemistry [1-3].

For a long time now, various means of computational geometry have existed to compute vibrational frequencies, each applying to scenarios and having flaws of their own. For example, the first approximation treats vibrations of molecules as harmonic oscillators, with the only caveat being a quadratic potential energy surface. This leads to having multiple overtones at one time; thus, considering anharmonic oscillations masks this model for a better chance of correctness while being overly simplistic when adjusting for vertical strength. As long as we narrow our scope to smaller molecules, there are quantum equations that allow such non-harmonics to work as expected, yet as the size of the molecule increases, so does the cost. Because of this, Ab initio seems infeasible, which leaves us with the now classical Density Functional Theory, which does have good scaling while providing correct values but does depend on the set basis chosen for the function, which raises their accuracy depending on the interactions at hand. A brute method and exact method are a popular combination because half the work done on the molecule allows for the rest to be narrowed down, so while being computationally less in demand, they still are limited [4-9].

To begin with, it must be pointed out that even though they are helpful, conventional strategies are faced with great difficulties when applying them to complex molecular systems. Such limitations encompass the difficulties in handling anharmonic vibrations, especially in excited states, and large computationally expensive molecules. In addition, too many conventional methods have the opportunity to account for transitions between the localized and delocalized vibrational modes, which is crucial for an adequate description of the molecular dynamics. All these disadvantages justify using different approaches, which have to specify molecular vibrations at specific but not-so-high computational expenses [10-14].

The Lie algebraic approach is a viable way to cope with such shortcomings. This method applies the mathematics of Lie algebras to the task of defining molecular vibrations in a symmetry-adapted form, which has certain benefits over the standard approach. The vibrational Hamiltonian, which encapsulates the energy of the molecules in terms of their vibrations, is written in the form of operators that include the system's characteristics regarding its vibrational aspects. These operators include Casimir operators that explain symmetry relations between the states of vibration and Majorana operators that describe an anharmonic relation between the vibration modes. The parameters connected with these operators are fitted to the experimental data, and the results obtained are used to predict the molecular vibrational characteristics. Unlike the conventional approaches, the Lie Algebraic approach automatically includes some anharmonicity and, therefore, is much more applicable when predicting higher overtones and the detail of molecular vibrations is required. In this case, the method primarily benefits from using the symmetry of molecules to substantially simplify and reduce the number of variables and operations required to perform a deep analysis of the Hamiltonian vibrational function. Lie algebraic model provides accurate, efficient calculations of molecular spectroscopic information that account for vibrational modes that are localized and delocalized. This model has applications that range from complex systems to diatomic molecules and encompasses all in between, thus proving to be quite versatile. Furthermore, this model alleviates the problems faced by traditional models that are primarily computational, such as dealing with nuclear and computational costs, which enhances its use for molecular spectroscopy [15-19].

This study calculates the vibrational frequencies of dichlorodifluoromethane using an integrated Lie algebraic approach. The vibrational spectrum of dichlorodifluoromethane helps assess computational methods due to its frequency range, making the molecule of both industrial and environmental significance. The molecule possesses overlapping stretching and bending vibrational modes and belongs to the C_{2v} symmetry point group, which validates the use of the Lie algebraic framework. The parameters of symmetry-adapted operators used in a molecule's vibrational Hamiltonian are adjusted to reduce the difference between theoretical predictions and experimental observations. This study has displayed that the system can accurately forecast the fundamental and higher over-tone frequencies while dealing with non-linear interactions.

The results of this research point out the benefits of utilizing the Lie algebraic approach compared to typical approaches. The approach's capability of accounting for anharmonic effects, cutting down the computation required, and conforming to the symmetry properties of molecules indicates that it has prospects for broader use in molecular spectroscopy. Apart from providing a thorough treatment of dichlorodifluoromethane's vibrational characteristics, this study also demonstrates the ability of the theory to deal with sophisticated molecular systems. The results demonstrate how the Lie algebraic approach fills in the important voids in vibrational analysis and provides an inexpensive and efficient substitute for the conventional computational methods.

The main goals of this study are to assess the shortcomings of the available approaches in estimating vibrational frequencies and display the inherent advantages of this Lie algebraic framework. Using dichlorodifluoromethane as an illustration, the present work seeks to validate the relevance of the method in dealing with problems on anharmonicity and offering further savings on computation time. It also targets bringing the foundations towards using the Lie algebraic technique on a larger scale and more complicated molecular structures, which can further enhance molecular spectroscopy methods. This study's results improve the vibrational dynamics of the molecule under investigation, dichlorodifluoromethane, and foster the use of such symmetry-adapted methods in studying molecular vibrations in other fields.

2. LIE ALGEBRAIC HAMILTONIAN FOR VIBRATIONAL ANALYSIS OF CCl_2F_2

The tetrahedral molecule known as Freon-12 or Dichlorodifluoromethane has a carbon atom which is bonded two each of two atoms, chlorine and two atoms of fluorine. It possesses C_{2v} symmetry which enables the vibrational modes to be divided into four unique symmetry species (A_1 , A_2 , B_1 , B_2). The components of A_1 include symmetric stretching and bending, the component of B_1 is asymmetric stretching whereas the component of B_2 is asymmetric bending that is oriented perpendicular to the molecular plane. Such symmetry classification aids in conducting vibrational analysis by estimating IR and Raman activity, besides classifying the molecular into other spectroscopic properties. Employing the Lie algebraic framework, this symmetry is applied to derive the vibrational Hamiltonian which describes in a good approximation both harmonic and anharmonic molecular interactions.

The vibrational Hamiltonian for CCl_2F_2 is expressed as [20-22]:

$$H = E_0 + \sum_{i=1}^n A_i C_i + \sum_{i<j}^n A_{ij} C_{ij} + \sum_{i<j}^n \lambda_{ij} M_{ij} \quad (1)$$

where E_0 represents the zero-point energy, $A_i, A_{ij}, \lambda_{ij}$ are algebraic parameters, C_i are Casimir operators for individual vibrational modes, C_{ij} represent coupled vibrational modes, and M_{ij} are Majorana operators capturing cross-mode interactions.

Casimir operators C_i quantify the anharmonicity of single vibrational modes with eigenvalues given by:

$$-4(N_i v_i - v_i^2) \quad (2)$$

where N_i is the vibron number, and v_i is the vibrational quantum number. For coupled modes, the operator C_{ij} has diagonal matrix elements:

$$\langle N_i, v_i; N_j, v_j | C_{ij} | N_i, v_i; N_j, v_j \rangle = 4 \left[(v_i + v_j)^2 - (v_i + v_j)(N_i + N_j) \right]. \quad (3)$$

The Majorana operator M_{ij} includes both diagonal and off-diagonal terms, representing energy exchange between coupled vibrational modes:

$$\langle N_i, v_i; N_j, v_j | M_{ij} | N_i, v_i; N_j, v_j \rangle = (N_i v_j + N_j v_i - 2v_i v_j). \quad (4)$$

Off-diagonal elements for vibrational transitions are given by:

$$\left. \begin{aligned} \langle N_i, v_i + 1; N_j, v_j - 1 | M_{ij} | N_i, v_i; N_j, v_j \rangle &= -[v_j(v_i + 1)(N_i - v_i)(N_j - v_j + 1)]^{1/2} \\ \langle N_i, v_i - 1; N_j, v_j + 1 | M_{ij} | N_i, v_i; N_j, v_j \rangle &= -[v_i(v_j + 1)(N_j - v_j)(N_i - v_i + 1)]^{1/2} \end{aligned} \right\} \quad (5)$$

The vibron numbers N_i , which quantify the anharmonicity of each bond, are calculated as:

$$N_i = \frac{(\omega_e)_i}{(\omega_e x_e)_i} - 1, \quad i = 1, 2, 3, 4, \quad (6)$$

where ω_e is the harmonic frequency, and $\omega_e x_e$ is the anharmonic constant obtained from spectroscopic data [23].

The initial estimates for algebraic parameters $A_i, A_{ij}, \lambda_{ij}$ are derived using fundamental vibrational energy relations. For the symmetric and asymmetric stretching modes:

$$\left. \begin{aligned} E^{C-F}(v=1) &= -4A_1(N_1 - 1) \\ E^{C-Cl}(v=1) &= -4A_2(N_2 - 1) \end{aligned} \right\} \quad (7)$$

The coupling parameters are estimated as:

$$\left. \begin{aligned} \lambda_{ij}^{C-F} &= \frac{|E^{C-F}(\text{Symmetric Stretch}) - E^{C-F}(\text{Asymmetric Stretch})|}{3N_1} \\ \lambda_{ij}^{C-Cl} &= \frac{|E^{C-Cl}(\text{Symmetric Stretch}) - E^{C-Cl}(\text{Asymmetric Stretch})|}{3N_2} \end{aligned} \right\} \quad (8)$$

Applying the least square numerical regression improves the parameters, in this way reducing the difference between computed and experimental frequencies. The Hamiltonian includes both the C-Cl bond and C-F bond contributions:

$$H = H^{C-F} + H^{C-Cl}, \quad (9)$$

where:

$$\left. \begin{aligned} H^{C-Cl} &= E_0^{C-Cl} + A_1 C_1 + A_2 C_2 + A_{12} C_{12} + \lambda_{12} M_{12} \\ H^{C-F} &= E_0^{C-F} + A_3 C_3 + A_4 C_4 + A_{34} C_{34} + \lambda_{34} M_{34} \end{aligned} \right\} \quad (10)$$

This model considers the bending and stretching vibrations of C-Cl and C-F bonds, and it portrays the vibration spectrum of CCl_2F_2 even more accurately. From the invariance group C_{2v} and the symmetry adapted operator's aid, the Lie algebraic model provides close estimates of the resonant and harmonic frequencies which makes it highly effective in analysing the molecular dynamics and the spectroscopic characteristics of the halogenated hydrocarbons.

3. RESULTS AND DISCUSSIONS

The vibrational Hamiltonian parameters were obtained by fitting to the fundamental vibrational frequency data of CCl_2F_2 , in order to determine a set of parameters such that the U(2) Lie algebraic approach for predicting the vibrational frequencies of CCl_2F_2 could be applied []. The fitted parameters are as follows:

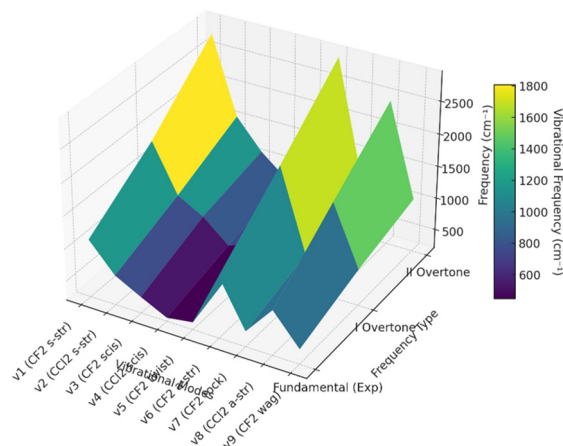
$$N_{C-F} = 118, N_{C-Cl} = 160, A_i^{C-F} = -2.35, A_i^{C-Cl} = -1.04, A_{ij}^{C-F} = 6.38, A_{ij}^{C-Cl} = 3.26, \lambda_{ij}^{C-F} = -0.16, \lambda_{ij}^{C-Cl} = -0.48$$

Table 1 below provides a comprehensive summary of the vibrational frequencies, symmetry species, and the corresponding vibrational modes within the molecule. These results highlight the distribution of vibrational energy across different modes, offering a detailed understanding of the molecular dynamics.

Further, these quantities are expressed graphically in the Figure which depicts the vibrational frequencies alongside specific symmetry species and modes graphs. This bi-presentation both integrates and enhances an analysis of the CCl_2F_2 vibrational behavior and deepens the understanding of the U(2) Lie algebraic framework effectiveness in capturing the molecular vibrational characteristics.

Table 1. Vibrational frequencies (in cm^{-1}) for CCl_2F_2

Vibrational Mode	Symmetry Species	Fundamental		I overtone	II overtone
		Experimental [24]	Calculated		
ν_1 (CF_2 s-str)	A_1	1101	1092.27	1822.31	2761.22
ν_2 (CCl_2 s-str)	A_1	667	669.14	1086.80	1561.11
ν_3 (CF_2 scis)	A_1	458	451.03	867.67	1109.37
ν_4 (CCl_2 scis)	A_1	262	255.61	527.83	783.99
ν_5 (CF_2 twist)	A_2	322	334.00	681.88	997.94
ν_6 (CF_2 a-str)	B_1	1159	1136.38	2005.03	2900.55
ν_7 (CF_2 rock)	B_1	446	432.77	753.32	1087.07
ν_8 (CCl_2 a-str)	B_1	902	900.29	1683.37	2446.42
ν_9 (CF_2 wag)	B_2	437	424.20	769.53	1033.30

**Figure.** Vibrational Frequencies Representation for CCl_2F_2

4. CONCLUSIONS

The findings of this paper demonstrate that the Lie algebraic framework applied in this research is a precise and accurate method for estimating the vibrational frequencies of CCl_2F_2 . The framework succeeds in calculating the fundamental frequencies close to the experimental value, resulting in a Root Mean Square (RMS) of 11.39 cm^{-1} , further illustrating the model's efficiency in accounting for anharmonic interactions. Both computational savings and flexibility substantiate it, and it works well for vibrational fundamental and overtone modes. The vibrational dynamics of the system have been successfully captured, which opens up new possibilities for using the framework and the associated techniques for broader applications like molecular dynamics and spectroscopy. This will be done by applying the developed method to more complex systems while ensuring that this work focuses on developing procedural integration with modern computational approaches.

Acknowledgments

On behalf of Vijayasekhar, special thanks are extended to the NIST Standard Reference Database 69: NIST Chemistry WebBook [webbook.nist.gov] for providing the experimental database utilized in this research.

ORCID

©J. Vijayasekhar, <https://orcid.org/0000-0002-2745-7401>

REFERENCES

- [1] J. Zhang, Y. Jing, M. Wan, J. Xue, J. Liu, J. Li, and Y. Du, "Investigation into polymorphism within ethenzamide-ethylmalonic acid cocrystal using Raman and terahertz vibrational spectroscopy," *Spectrochim. Acta Part A: Mol. Biomol. Spectrosc.* **305**, 123478 (2024). <https://doi.org/10.1016/j.saa.2023.123478>
- [2] P. Vennila, J. S. Al-Otaibi, G. Venkatesh, Y.S. Mary, V. Raj, N. Acharjee, and P. Tamilselvi, "Structural, spectral, molecular docking, and molecular dynamics simulations of phenylthiophene-2-carboxylate compounds as potential anticancer agents," *Polycycl. Aromat. Compd.* **44**(1), 238–260 (2023). <https://doi.org/10.1080/10406638.2023.2172052>
- [3] N. Elangovan, S. Sowrirajan, N. Arumugam, A.I. Almansour, M. Altaf, V. Viswanathan, and S.M. Mahalingam, "Computational investigation of molecular structure, spectral analysis, PES study, and molecular docking studies of 4-(butan-2-ylideneamino) benzenesulfonamide," *J. Mol. Struct.* **1298**(2), 137054 (2024). <https://doi.org/10.1016/j.molstruc.2023.137054>
- [4] M. Benaissa, A. Boukaoud, D. Sebbar, Y. Chiba, and A. Krid, "Periodic and non-periodic DFT studies of an organic semiconductor material: Structural, electronic, optical, and vibrational properties of ninhydrin," *Spectrochim. Acta Part A: Mol. Biomol. Spectrosc.* **307**, 123636 (2024). <https://doi.org/10.1016/j.saa.2023.123636>
- [5] M. Fusè, G. Mazzeo, G. Longhi, S. Abbate, Q. Yang, and J. Bloino, "Scaling-up VPT2: A feasible route to include anharmonic correction on large molecules," *Spectrochim. Acta Part A: Mol. Biomol. Spectrosc.* **311**, 123969 (2024). <https://doi.org/10.1016/j.saa.2024.123969>

- [6] M.M. Ayoob, and F.E. Hawaiz, "Synthesis, crystal structure, DFT calculation and Hirshfeld surface analysis of N-(4-methylphenyl)-2-(3-nitro-benzamido) benzamide," Bull. Chem. Soc. Ethiop. **38**(1), 229–239 (2024). <https://doi.org/10.4314/bcse.v38i1.17>
- [7] S. Ahmad, M. Kumar, Km. Garima, A. Ali, H. Arora, S. Muthu, and S. Javed, "DFT, molecular docking, molecular dynamics simulation, and Hirshfeld surface analysis of 2-phenylthioaniline," Polycycl. Aromat. Compd. **44**(9), 5876–5898 (2023). <https://doi.org/10.1080/10406638.2023.2270128>
- [8] Y. Dague, S.J. Koyambo-Konzapa, H. Nose, et al., "DFT investigation on the structural and vibrational behaviours of the non-protein amino acids in hybrid explicit/continuum solvent: a case of the zwitterions γ -aminobutyric and α -aminoisobutyric acids," J. Mol. Model. **30**, 17 (2024). <https://doi.org/10.1007/s00894-023-05817-9>
- [9] A. Zochedh, K. Chandran, A. Shunmuganarayanan, and A. B. Sultan, "Exploring the synergistic effect of tegafur-syringic acid adduct against breast cancer through DFT computation, spectroscopy, pharmacokinetics, and molecular docking simulation," Polycycl. Aromat. Compd. **44**(4), 2153–2187 (2023). <https://doi.org/10.1080/10406638.2023.2214281>
- [10] T. Valarmathi, R. Premkumar, E.J.J. Samuel, and A.M.F. Benial, "Spectroscopic characterization, quantum chemical, and molecular docking studies on 1-chloroanthraquinone: A novel oral squamous cell carcinoma drug," Polycycl. Aromat. Compd. **44**(3), 1816–1834 (2023). <https://doi.org/10.1080/10406638.2023.2209249>
- [11] Y. Syetov, "Thermal expansion and vibrational spectra of paratellurite in quasiharmonic approximation," Ukr. J. Phys. Opt. **26**(1), 01032–01039 (2025). <https://doi.org/10.3116/16091833/Ukr.J.Phys.Opt.2025.01032>
- [12] K. Smit, J. Matysik, P. Hildebrandt, and F. Mark, "Vibrational analysis of biliverdin dimethyl ester," J. Phys. Chem. **97**(46), 11887–11900 (1993). <https://doi.org/10.1021/j100148a009>
- [13] V.J. Esposito, P. Ferrari, W.J. Buma, C. Boersma, C.J. Mackie, A. Candian, R.C. Fortenberry, et al., "Anharmonicity and deuteration in the IR absorption and emission spectrum of phenylacetylene," Mol. Phys. **122**(7–8) (2023). <https://doi.org/10.1080/00268976.2023.2261570>
- [14] G. Pitsevidh, and A. Malevich, "Symmetry properties, tunneling splittings of some vibrational energy levels and torsional IR spectra of the trans- and cis-conformers of hydroquinone molecule," J. Mol. Spectrosc. **404**, 111937 (2024). <https://doi.org/10.1016/j.jms.2024.111937>
- [15] S. Nallagonda, and V. Jaliparthi, "Higher overtone vibrational frequencies in naphthalene using the Lie algebraic technique," Ukr. J. Phys. Opt. **25**(2), 02080–02085 (2024). <https://doi.org/10.3116/16091833/Ukr.J.Phys.Opt.2024.02080>
- [16] S. Teppala, and V. Jaliparthi, "Exploring cyclohexane vibrational dynamics through a Lie algebraic Hamiltonian framework," Ukr. J. Phys. Opt. **25**(3), 03093–03100 (2024). <https://doi.org/10.3116/16091833/Ukr.J.Phys.Opt.2024.03093>
- [17] S. Teppala, and V. Jaliparthi, "Vibrational frequencies of tetrachloroethylene using Lie algebraic framework," Momona Ethiop. J. Sci. (MEJS), **16**(2), 281–288 (2024). <https://doi.org/10.4314/mejs.v16i2.6>
- [18] K. Lavanya, M.P. Kumari, and J. Vijayasekhar, "Vibrational frequencies of phosphorus trichloride with the vibrational Hamiltonian," East Eur. J. Phys. (2), 407–410 (2024). <https://doi.org/10.26565/2312-4334-2024-2-52>
- [19] K. Lavanya, A.G. Rao, and J. Vijayasekhar, "Vibrational Hamiltonian of carbonyl sulphide and hydrogen cyanide," East Eur. J. Phys. (1), 432–435 (2024). <https://doi.org/10.26565/2312-4334-2024-1-46>
- [20] M.R. Balla, and V. Jaliparthi, "Vibrational Hamiltonian of methylene chloride using U(2) Lie algebra," Mol. Phys. **119**(5), (2020). <https://doi.org/10.1080/00268976.2020.1828634>
- [21] F. Iachello, and R.D. Levine, *Algebraic theory of molecules*, (Oxford University Press, Oxford, 1995).
- [22] S. Oss, "Algebraic models in molecular spectroscopy," Adv. Chem. Phys. **93**, 455–649 (1996).
- [23] K.K. Irikura, Erratum: Experimental Vibrational Zero-Point Energies: Diatomic Molecules [J. Phys. Chem. Ref. Data **36**, 389–397 (2007)]. J. Phys. Chem. Ref. Data, **38**(3), 749 (2009). <https://doi.org/10.1063/1.3167794>
- [24] T. Shimanouchi, Tables of Molecular Vibrational Frequencies Consolidated Volume II, J. Phys. Chem. Ref. Data, **6**(3), 993–1102 (1972).

КОЛИВАЛЬНІ ЧАСТОТИ ДИХЛОРИДФОРМЕТАНУ З ВИКОРИСТАННЯМ АЛГЕБРАІЧНОГО ПІДХОДУ ЛІ

П. Суніта^a, Б.В.С.Н. Харі Праса^b, Дж. Віджаясехар^c

^aКафедра математики, SANE-Академія вищої освіти Сіддхартхі-Вважасья Університетом, Віджаяяда, Індія

^bКафедра математики, Технологічний інститут Васіредді Венкатадрі, Намбур, округ Гунтур, Андхра-Прадеш, Індія

^cКафедра математики, GITAM (вважається Університетом), Хайдарабад, Індія

У цьому дослідженні представлено симетрійно-адаптований підхід Лі, високоефективний інструмент для розрахунку коливальних частот у дихлоридформетані (CCl_2F_2). Завдяки своїй точковій груповій симетрії C_{2v} , молекула, що розглядається, особливо підходить для цього підходу. Формулюючи структури зв'язків вуглець-водень (C-H) та вуглець-хлор (C-Cl) в унітарних алгебрах Лі, визначення коливальних квантових станів молекули стає надзвичайно простим. Гамільтоніан, включаючи інваріантні оператори Казимира та Майорани та підібрані параметри, точно відтворює бажані коливальні моди, використовуючи фундаментальні та вищі обертонові частоти. Цей підхід, який порівнює сучасні та класичні моделі, підкреслює алгебраїчні методи Лі як ефективні інструменти для моделювання ангармонічних взаємодій та динаміки переходів на молекулярному рівні. Окрім своєї теоретичної значущості, побудована модель забезпечує глибоке розуміння коливальних аспектів молекул, знання, що є критично важливим для практичних застосувань, таких як інтерпретація спектроскопічних даних, проектування матеріалів з бажаними коливальними характеристиками або вивчення молекул у складних середовищах. Ці практичні застосування підвищують універсальність методології та дозволили її успішно застосувати до молекулярної спектроскопії, хімічної кінетики та проектування енергоефективних матеріалів та сенсорів, серед інших галузей. Це дослідження надає експериментаторам впевненість у алгебраїчному підході Лі та прокладає шлях для подальших експериментів з поліатомними молекулами. Роблячи значний внесок у зменшення допустимої похибки в обчислювальній молекулярній фізиці, ця методологія відкриває захопливі можливості для майбутніх досліджень та розробок.

Ключові слова: алгебраїчний підхід Лі; коливальний гамільтоніан; оператори Казимира та Майорани; дихлоридформетан; ангармонічні коливальні моди

PHOTODETECTORS FOR X- AND γ -RAY SCINTILLATORS

 Mykola S. Kukurudziak*,  Ivan P. Koziarskyi,  Mykola S. Solodkyi,  Eduard V. Maistruk^a,
 Vasylyna V. Kopach^a,  Yurii O. Semeniuk^a,  Mykola M. Pavliuk^a

Yuriy Fedkovych Chernivtsi National University, Kotsyubyns'kogo str. 2, 58012, Chernivtsi, Ukraine

**Corresponding Author e-mail: mykola.kukurudzyak@gmail.com*

Received March 2, 2025; revised May 6, 2025 accepted May 13, 2025

The article analyzes X- and γ -ray detectors based on the ionizing and scintillation principles of operation. The effectiveness of using silicon *p-i-n* and *p-n* photodiodes in scintillation sensors for detecting visible photoluminescent radiation is investigated. The *p-i-n* detector was fabricated on the basis of *p*-type single crystal silicon with orientation [111] and resistivity 8-10 k Ω ·cm. The *p-n* photodiode was fabricated on the basis of *n*-type single crystalline silicon with orientation [111] and resistivity 200-300 Ω ·cm. It was found that *p-n* photodiodes have a much lower dark current than *p-i-n* photodiodes (although somewhat inferior in sensitivity), which provides their advantage in detectivity. However, if it is necessary to register short pulses of luminescent radiation, *p-i-n* photodiodes should be used, since they have a higher response speed. The increase in response speed is due to the fact that the process of diffusion of charge carriers in a *p-n* structure of a photodiode is replaced in the *p-i-n* structure by the drift of charge carriers through the *i*-region in a strong electric field.

Keywords: Photoluminescence; Zinc Selenide; Silicon; CdTe; Electrical Properties; Detectivity; Photodiodes

PACS: 61.72. Ji, 61.72. Lk, 85.60. Dw

Continuous scientific and technological progress will make it increasingly important to monitor and measure doses of ionizing radiation, in particular X-rays and γ -rays. These are high-energy types of radiation that can cause damage to cells and tissues of the body [1]. Therefore, controlling the level of these radiations is necessary to ensure the safety of people working in environments where these radiations may be present (e.g., medical facilities, nuclear power plants, industrial enterprises) [2]. Measurement of X-ray and gamma radiation levels is necessary to ensure the safe use of these methods in medical diagnostic procedures (radiography, computed tomography) and therapy (radiotherapy) [3]. When radioactive materials are used in industry, energy, or research, it is important to monitor the environment to detect and prevent radiation contamination in a timely manner. Measurements of X-rays and gamma rays are important in astrophysics, nuclear physics, and the study of cosmic phenomena, as these types of radiation are important indicators of various processes in the Universe, such as interaction with high energies.

Meeting these monitoring needs requires the development of new and improvement of existing approaches to the manufacture of ionizing radiation detectors. These approaches can be focused on improving sensitivity, accuracy, measurement speed, and ability to operate in difficult conditions.

The most common methods for detecting X- and γ -radiation that are being developed and improved are ionization and scintillation methods. The ionization method [4, 5] is based on measuring the ionization effect. It occurs in the sensitive volume of the detector when ionizing radiation interacts with it. Three types of ionization detectors are mainly used: a semiconductor detector, a pulsed ionization chamber with a grid, and a proportional counter [6]. However, semiconductor detectors are the most widely used. In a semiconductor detector, a sensitive region is created in which there are no free charge carriers. Once in this area, a charged particle causes ionization. Accordingly, holes appear in the valence band and electrons in the conduction band. Under the action of a voltage supplied to the electrodes deposited on the surface of the sensitive zone, the movement of holes and electrons occurs, which leads to the appearance of a current pulse. Devices for registering ionizing radiation are made both on the basis of elementary semiconductors and complex ones, including solid solutions. For example, spectrometers with silicon diffusion-drift detectors measure β -spectra, as well as X-ray and low-energy γ -ray spectra. Germanium detectors made it possible to create γ -spectrometers with high technical parameters. However, among the many complex semiconductors used for X- and γ -ray detectors at room temperature, such as halide perovskite semiconductors [7], thallium bromide [8], cadmium telluride-based detectors have been the most promising and studied compounds for many years [9-12]. At the same time, the most successful of the latter is CdZnTe [13-15]. However, due to the strict requirements for the properties of materials needed to operate at room temperature, they all have several critical problems. In particular, thallium bromide (TlBr) exhibits unresolved problems of contact deterioration and device polarization, although various solution approaches are being investigated [16]. The use of halide perovskite materials (CsPbBr₃) shows poor performance stability over time due to ion migration and defects under the influence of an electric field [17]. CdZnTe has some problems with Te inclusions, subgrain boundaries, and zinc segregation coefficient [18, 19]. Thus, the development of a nuclear detector based on a semiconductor that would have high performance and low cost at room temperature remains a significant challenge. An interesting fact is that the addition of impurities in the form of Mn

and Se results in the formation of solid solutions of the composition CdZnTeSe and CdMnTeSe, which exhibit improved electrophysical properties compared to CdTe [20, 21]. In particular, the addition of selenium leads to a sharp decrease in the density of dislocations and grain boundaries, and better compositional homogeneity [22]. The addition of manganese to CdTe can solve the problem of zinc segregation factor due to the more stable segregation property of manganese [23]. In [24], the suitability of CdMnTe and CdMnTeSe as materials for room temperature X-ray and γ -ray detectors was investigated and their crystal structures, mechanical and optical properties were studied.

However, the above are complex physical and technological problems that can be avoided by using scintillation detectors. These detectors use scintillation materials, materials that emit light when they absorb ionizing radiation. This light is converted into an electrical signal using photodiodes or photomultipliers [25].

The variety of scintillation materials is wide. For example, scintillation crystals based on ZnSe exhibit luminescence at $\lambda = 460\text{--}590$ nm when irradiated with X-rays [26, 27], scintillators based on polystyrene - $\lambda = 425\text{--}530$ nm [28, 29], bismuth germanate $\text{Bi}_4\text{Ge}_3\text{O}_{12}$ has a maximum luminescence at $\lambda = 480$ nm [30], yttrium aluminum garnet $\text{Y}_3\text{Al}_5\text{O}_{12}:\text{Ce}$ (YAG:Ce), lutetium aluminum garnet ($\text{Lu}_3\text{Al}_5\text{O}_{12}:\text{Ce}$, LuAG:Ce), and yttrium lutetium aluminum garnet mixed crystals ($(\text{Y,Lu})_3\text{Al}_5\text{O}_{12}$) have a scintillation wavelength of $\lambda = 530\text{--}550$ nm, which is ideal for matching with photodiodes and avalanche photodiodes [31,32].

As can be seen from the above list of scintillation materials, detectors sensitive to the visible spectral range are required to detect their luminescent radiation. The development and improvement of these detectors is an urgent scientific and technical task. These can be avalanche photodiodes [33], photomultipliers [34], or *p-i-n* photodiodes [35,36], as well as *p-n* photodiodes [37]. The most widespread are scintillation detectors based on silicon *p-i-n* and *p-n* photodiodes.

The market leader in the production of silicon photodetectors is Hamamatsu (Japan). The manufacturer offers a series of visible and near-infrared detectors for scintillators: S2744-08 [38], S2744-09 [39], S3204-08 [40], S3584-08 [41], S3590-18 [42] - *p-i-n* photodiodes of different areas are sensitive in the range of $\lambda = 340\text{--}1100$ nm with a maximum at $\lambda = 960$ nm and photosensitivity $S = 0.2\text{--}0.4$ A/W in the visible range; as well as S12497 [43] and S12498 [44] - *p-n* photodiodes are sensitive in the range of $\lambda = 400\text{--}1100$ nm with a maximum at $\lambda = 920$ nm and a photosensitivity of $S = 0.32\text{--}0.36$ A/W at $\lambda = 540$ nm.

As can be seen from the analysis of the detectors, their spectral maximum is shifted towards the near-infrared region, respectively, shifting the maximum towards shorter wavelengths may increase the sensitivity of the detectors in a given range. No less urgent is the need to reduce the dark currents of the detectors to ensure their significant detectivity. Accordingly, the aim of this work is to develop silicon *p-i-n* and *p-n* photodiodes for the visible range, to characterize them comparatively and to study the possibilities of increasing their detectivity and reducing the dark current (I_d) for effective use in scintillation detectors.

EXPERIMENTAL

Two types of single-element PDs of the same area, *p-i-n* and *p-n*, were fabricated for the detection of photoluminescent radiation in the visible range. The *p-i-n* detector was fabricated on the basis of *p*-type single crystal silicon with orientation [111] and resistivity $\rho \approx 8\text{--}10$ k $\Omega\cdot\text{cm}$ according to the technical regimes given in [45]. The structure of the PD crystal with a guard ring (GR) was used to prevent the influence of inversion layers at the Si-SiO₂ interface on the parameters of the PD and surface breakdown (Fig. 1a). The n^+ -type responsive element (RE) and GR were formed by phosphorus diffusion. The depth of the phosphorus impurity reached $x_{n+p} = 2\text{--}2.5$ μm . The p^+ -type ohmic contact on the reverse side of the crystal was formed by boron diffusion. The antireflective SiO₂ on the surface of the RE was formed by oxidation in a dry oxygen atmosphere and met the condition of minimum reflection [46]:

$$\frac{\lambda}{4} = nd_{\text{SiO}_2} \quad (1)$$

where λ is the working wavelength; n the refractive index of SiO₂; d_{SiO_2} is the thickness of the antireflective film.

Considering that the fabricated PDs are planned to be used for detecting wavelengths in the range of $\lambda = 400\text{--}780$ nm, in which the thickness of the antireflection oxide reaches $d_{\text{SiO}_2} = 70\text{--}140$ nm, we formed an intermediate thickness of the oxide film $d_{\text{SiO}_2} = 100\text{--}110$ nm.

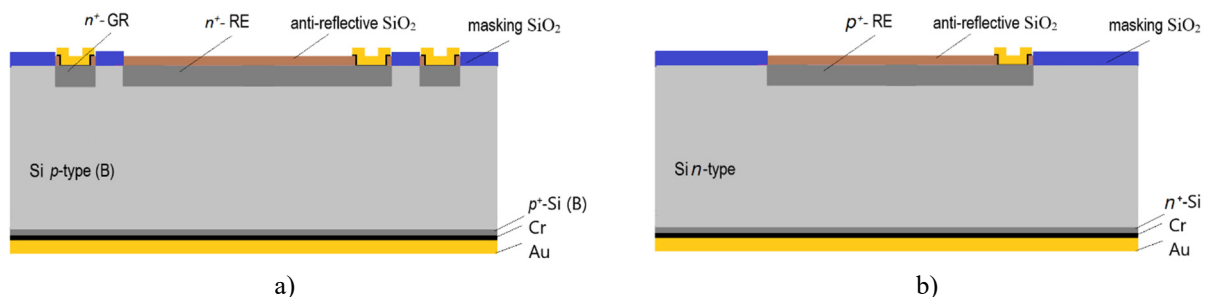


Figure 1. Schematic cross-section of *p-i-n* PD (a) and *p-n* PD (b)

The p - n PD was fabricated on the basis of n -type single crystalline silicon with orientation [111] and resistivity $\rho \approx 200$ -300 $\Omega \cdot \text{cm}$ (Fig. 1b). The topology without GR was used. The p -type RE was formed by boron diffusion ($x_{p+} = 2$ -2.5 μm). The n -type ohmic contact on the back side of the crystal was formed by phosphorus diffusion.

The parameters of the obtained PDs were compared.

RESULTS OF THE RESEARCH AND THEIR DISCUSSION

From the dark I - V -characteristics of the studied samples, it can be seen (Fig. 2) that the p - n PD has a significantly lower dark current than the p - i - n PD. This can be explained by considering the components of the dark current. The dark current of the PD is determined by the sum of the diffusion current in the neutral region (I_{dif}) (1) and the generation current in the depleted region (I_G) (2) [47].

$$I_{dif} = e \left(n_p \cdot \sqrt{\frac{D_n}{\tau_n}} + p_n \cdot \sqrt{\frac{D_p}{\tau_p}} \right) \quad (2)$$

where e is the electron charge, n_p and p_n are the concentrations of electrons and holes in the p - and n -layers, respectively, D_n and D_p are the diffusion coefficients of electrons and holes, respectively, τ_p and τ_n are the lifetimes of electrons and holes as minor charge carriers, respectively.

$$I_G = e \frac{n_i}{2\tau} W_i A_{RE} \quad (3)$$

where n_i is intrinsic concentration of charge carriers in the substrate; W_i is width of the space charge region, A_{RE} is the area of RE, τ is the effective lifetime of minor charge carriers.

The main contribution to the value of the PD dark current is made by the generation component, which is proportional to the width of the spatial charge region (SCR), which in turn is directly proportional to the reverse bias voltage [48]:

$$W_i = \left(\frac{2\epsilon\epsilon_0 (\phi_c - U_{bias})}{eN_A} \right)^{\frac{1}{2}} \quad (4)$$

where ϵ , ϵ_0 are dielectric constants for silicon and vacuum, respectively; ϕ_c is contact potential difference.

If we calculate W_i for p - i - n PD and p - n PD, for example, at $|10 \text{ V}|$, we obtain $W_i = 95$ -105 μm in p - i - n PD and $W_i = 15$ -20 μm in p - n PD. Accordingly, the generation dark current of p - i - n PD is much higher than that of p - n PD. Also, we note that the dependence of the dark current on the voltage in the p - i - n structure is stronger.

It is worth noting that in the case of manufacturing p -Si-based PDs (especially high-resistance ones), a surface component of the dark current (I_d^{surf}) is added (5), which characterizes the generation of charge carriers on the silicon-silicon oxide interface and in the region of the p - n junction exit to the crystal surface. It is the GR that is the element of the PD crystal that limits the surface component of the dark current, since in the presence of inversion layers at the Si-SiO₂ interface, the p - n junction area increases, and, accordingly, I_d increases (Fig. 2 inset) [49].

$$I_d^{surf} = \frac{eN_{ss}v\sigma_{ss}A_{p-n}}{2} \quad (5)$$

where σ_{ss} is the cross section of the capture, N_{ss} is the density of surface states, v – is the average relative velocity of thermal charge carriers, A_{p-n} is the area of the p - n junction.

The use of the GR in the design of the PD crystal requires control of the insulation resistance between the GR and the RE [49]. In the investigated case, it reached about 1-2 M Ω .

The light I - V -characteristic of the PDs at $\lambda = 405 \text{ nm}$, $\lambda = 646 \text{ nm}$, $\lambda = 780 \text{ nm}$ (Fig. 3) were obtained and their sensitivity (S) was determined by formula (6) [50].

$$S = (I_{ph} - I_d)/P_{opt} \quad (6)$$

where I_{ph} is the light current of the PD, P_{opt} is the power of the radiation.

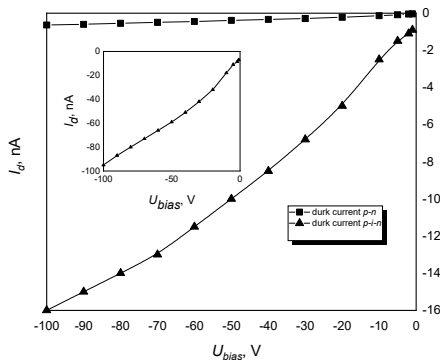


Figure 2. Reverse dark I - V -characteristics of PDs (insert is the dark I - V -characteristics of p - i - n PD without the connected GR)

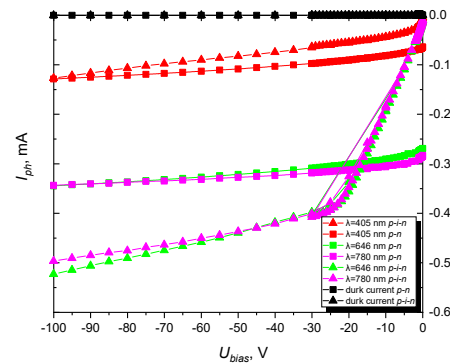


Figure 3. Reverse light I - V -characteristics of PDs ($P_{opt} = 5 \text{ mW}$)

In both cases, with an increase in the radiation wavelength, the photocurrent and sensitivity of the PDs increased, since the maximum of their spectral characteristics was shifted to longer wavelengths.

The absorption coefficient of the wave $\lambda = 405$ nm in silicon is $\alpha = 10^5 \text{ cm}^{-1}$ [51], respectively, the intensity of radiation with this wavelength, according to the Bouguer-Lambert-Beer law [52], decreases by a factor of e in the thickness of silicon about $1 \mu\text{m}$ (we assume that it is absorbed). Accordingly, in both studied samples, this radiation is absorbed in the doped layer, so the expansion of the SCR does not affect the collection of photogenerated charge carriers. Photogenerated charge carriers, in the described case, reach the p - n junction by diffusion due to the concentration gradient.

From the light I - V -characteristics of the PDs and the dependence of $S(U_{bias})$ (Fig. 4) at $\lambda = 646$ nm, $\lambda = 780$ nm, it is clear that the photocurrent and sensitivity of the p - n PD depend on the reverse voltage applied minimally, since its SCR changes minimally when the voltage is changed due to the low resistivity of the base material. It is known [53] that the p - n junction is reached only by those charge carriers that are photogenerated at a distance of the sum of the SCR width and the diffusion length of minor charge carriers from the p - n junction. Given that the SCR in this case changes minimally, and the diffusion length of the charge carriers is constant, the increase in photosensitivity with an increase in the reverse voltage is minimal.

In the case of p - i - n PDs, a slightly higher value of the photocurrent and sensitivity and a stronger dependence on voltage (at $\lambda = 646$ nm, $\lambda = 780$ nm) were observed due to an increase in W_i . At a reverse bias of 20-25 V, the photosensitivity of the PD reaches quasi-saturation, which indicates the complete collection of photogenerated charge carriers at this voltage.

In order to evaluate the photodetectors, their detectivity (D^*) was quantified using formula (7) [50], and the dependence $D^*(U_{bias})$ was obtained (Fig. 5).

$$D^* = \sqrt{\frac{A R E}{2 e I_d}} S \quad (7)$$

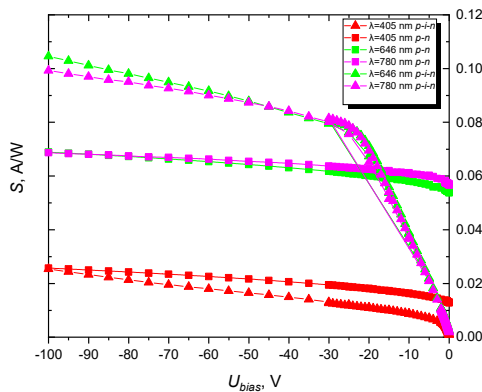


Figure 4. Dependence of the $S(U_{bias})$ of PDs

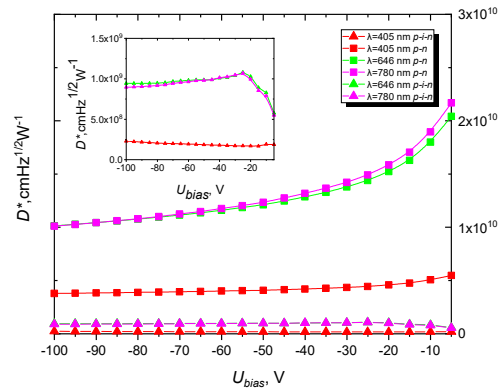


Figure 5. Dependence of the $D^*(U_{bias})$ of PDs (insert dependence of the $D^*(U_{bias})$ of p - i - n PD)

As can be seen from Fig. 5, p - n PD have much higher detectivity than p - i - n PD due to much lower dark currents, and thus this class of PD can be effectively used in scintillators where there is a need to detect weak optical signals. However, it should be noted that sometimes there is a need to register short pulses of photoluminescent radiation [54], in which case p - i - n PDs, although inferior in detectivity, are superior in response speed. The increase in speed is due to the fact that the process of diffusion of charge carriers in a conventional p - n structure of a photodiode is replaced in the p - i - n structure by the drift of carriers through the i -region in a strong electric field [55]. The drift time of electrons t_{dr} through the i -region with a width W_i and electric field intensity E is [48]:

$$t_{dr} = \frac{W_i}{v_n} = \frac{W_i}{\mu_n E} \quad (8)$$

where $v_n = \mu_n E$ is the speed of electron drift in an electric field, μ_n is the mobility of electrons.

The ratio of the electron drift time through the i -region to the diffusion time through the base of the p - n PD (t_{dif}) can be represented as:

$$\frac{t_{dr}}{t_{dif}} = \frac{W_i / \mu_n E}{W_i^2 / 2 D_n} = \frac{W_i^2 / \mu_n U_{bias}}{W_i^2 / 2 D_n} = \frac{2 \phi}{U_{bias}} \quad (9)$$

Since $D_n / \mu_n = kT/q = \phi$, where k is the Boltzmann constant and T is the temperature.

CONCLUSIONS

The analysis of ionizing radiation detectors based on semiconductor structures and scintillators is carried out. It is possible to avoid the technological difficulties of obtaining perfect semiconductor detectors based on CdTe compounds by using scintillators. The possibilities of using silicon p - i - n and p - n photodiodes to register the visible luminescent

radiation of scintillation detectors are investigated. It was found that the p - n photodiodes have a significantly lower dark current than p - i - n photodiodes (by about an order of magnitude), which ensures their higher detectivity. However, p - i - n photodiodes have an advantage in response speed.

Acknowledgments

This work was partially supported by Ministry of Education and Science of Ukraine (grant number 0125U000832, authors M.S. Kukurudziak and M.S. Solodkyi, V.V. Kopach).

ORCID

Mykola S. Kukurudziak, <https://orcid.org/0000-0002-0059-1387>; Ivan P. Koziarskyi, <https://orcid.org/0000-0002-4984-4349>
 Mykola S. Solodkyi, <https://orcid.org/0000-0001-7432-9202>; Eduard V. Maistruk, <https://orcid.org/0000-0002-9025-6485>
 Vasylyna V. Kopach, <https://orcid.org/0009-0004-7927-983X>; Yuri O. Semeniuk, <https://orcid.org/0009-0003-4900-7334>
 Mykola M. Pavliuk, <https://orcid.org/0009-0008-4578-7288>

REFERENCES

- [1] T.B. Feldman, M.A. Yakovleva, and M.A. Ostrovsky, *Experimental Eye Research*, **252**, 110270 (2025). <https://doi.org/10.1016/j.exer.2025.110270>
- [2] B. Huang, Y. Liu, X. Sun, L. Huang, S. Dong, and L. Mao, *National Science Open*, **4**(1), 20240021 (2025). <https://doi.org/10.1360/nso/20240021>
- [3] D.P. Frush, et al., *Journal of Applied Clinical Medical Physics*, **e70022**, 1-11 (2025). <https://doi.org/10.1002/acm2.70022>
- [4] N. Tsoulfanidis, and S. Landsberger, *Measurement and Detection of Radiation* (CRC Press, 2021). <https://doi.org/10.1201/9781003009849>
- [5] Y. He, I. Hadar, and M.G. Kanatzidis, *Nature Photonics*, **16**(1), 14-26 (2022). <https://doi.org/10.1038/s41566-021-00909-5>
- [6] R.V. Berestov, and N.Ye. Hots, *Visnyk Cherkaskoho derzhavnoho tekhnolohichnoho universytetu. Tekhnichni nauky*, **3**, 14-23 (2021). <https://doi.org/10.24025/2306-4412.3.2021.243580> (in Ukrainian)
- [7] Y. He, et al., *Nature Photonics*, **15**, 36-42 (2021). <https://doi.org/10.1038/s41566-020-00727-1>
- [8] A. Datta, et al., *Applied Physics Letters Materials*, **5**, 106109 (2017). <https://doi.org/10.1063/1.5001181>
- [9] N. Vyhnan, and Y. Khalavka, *Luminescence*, **29**(7), 952-954 (2014). <https://doi.org/10.1002/bio.2600>
- [10] I. Fodchuk, et al., *Proceedings of SPIE*, **11369**, 113691H (2020). <https://doi.org/10.1117/12.2553970>
- [11] D. Vorontsov, et al., *CrystEngComm*, **19**(45), 6804-6810 (2017). <https://doi.org/10.1039/C7CE01688C>
- [12] I. Fodchuk, et al., *Physics and Chemistry of Solid State*, **23**(1), 144-149 (2022). <https://doi.org/10.15330/pccs.23.1.144-149>
- [13] E.V. Maistruk, et al., *Engineering Research Express*, **2**(3), 035037 (2020). <https://doi.org/10.1088/2631-8695/abb7e5>
- [14] E.V. Maistruk, et al., *Journal of Nano- and Electronic Physics*, **11**(2), 02007 (2019). [https://doi.org/10.21272/jnep.11\(2\).02007](https://doi.org/10.21272/jnep.11(2).02007)
- [15] I.G. Orletskyi, et al., *Materials Research Express*, **8**(1), 015905 (2021). <https://doi.org/10.1088/2053-1591/abdbf8>
- [16] K. Takagi, et al., in: *IEEE Transactions on Nuclear Science*, **68**(9), 2435-2439 (2021). <https://doi.org/10.1109/TNS.2021.3078448>
- [17] B.B. Zhang, et al., *Applied Physics Letters*, **116**, 063505 (2020). <https://doi.org/10.1063/1.5134108>
- [18] A.E. Bolotnikov, et al., in: *2007 IEEE Nuclear Science Symposium Conference Record*, 1788-1797, (2007). <https://doi.org/10.1109/NSSMIC.2007.4436507>
- [19] A.E. Bolotnikov, et al., *Journal of Crystal Growth*, **379**, 46-56 (2013). <https://doi.org/10.1016/j.jcrysgro.2013.01.048>
- [20] O. Kopach, et al., *Journal of Phase Equilibria and Diffusion*, **45**, 612-620 (2024). <https://doi.org/10.1007/s11669-024-01116-9>
- [21] V. Kopach, et al., in: *Proc. SPIE. Hard X-Ray, Gamma-Ray, and Neutron Detector Physics XXIII*, **11838**, 1183819, 155-161 (2021). <https://doi.org/10.1117/12.2594545>
- [22] U.N. Roy, et al., *Sci. Rep.*, **9**, 7303 (2019). <https://doi.org/10.1038/s41598-019-43778-3>
- [23] S.U. Egarievwe et al. "Advances in CdMnTe Nuclear Radiation Detectors Development", *IEEE Nuclear Science Symposium and Medical Imaging Conference Proceedings (NSS/MIC)*, Sydney, NSW, Australia, pp. 1-3 (2018).
- [24] A. Masłowska, et al., *Sensors*, **24**(2), 345 (2024). <https://doi.org/10.3390/s24020345>
- [25] W.W. Moses, *Nuclear Instruments and Methods in Physics Research Section A: Accelerators, Spectrometers, Detectors and Associated Equipment*, **487**(1-2), 123-128 (2002). [https://doi.org/10.1016/S0168-9002\(02\)00955-5](https://doi.org/10.1016/S0168-9002(02)00955-5)
- [26] M.A. Jafarov, and S. A. Jahangirova, *Phys. Solid State*, **67**, 207-213 (2025). <https://doi.org/10.1134/S106378342460211X>
- [27] O.H. Trubayeva, et al., *Tekhnologiya i Konstruirovaniye v Elektronnoi Apparature*, **3**, 43-49 (2018). <http://dx.doi.org/10.15222/TKEA2018.3.43> (in Ukrainian)
- [28] S. Bhatnagar, arXiv preprint arXiv:2401.14706 (2024). <https://doi.org/10.48550/arXiv.2401.14706>
- [29] Y.L. Yan, et al., *J. Polym. Res.*, **32**, 19 (2025). <https://doi.org/10.1007/s10965-024-04206-x>
- [30] I.L. Matos, et al., *Int. J. Appl. Ceram. Technol.*, **22**(1), e14911 (2025). <https://doi.org/10.1111/ijac.14911>
- [31] P. Roos, in: *Handbook of Nuclear Medicine and Molecular Imaging for Physicists* (ed. by M. Ljungberg) (CRC Press, 107-128, 2022). <https://doi.org/10.1201/9780429489556>
- [32] N. Cichocka, et al., *Nanotechnology*, **33**(3), 035702 (2021). <https://doi.org/10.1088/1361-6528/ac2e74>
- [33] J. Jegal, H.W. Park, and H.J. Kim, *IEEE Transactions on Nuclear Science*, **68**(6), 1304-1308 (2021). <https://doi.org/10.1109/TNS.2021.3070040>
- [34] S.J. van der Sar, S.E. Brunner, and D.R. Schaart, *Medical Physics*, **48**(10), 6324-6338 (2021). <https://doi.org/10.1002/mp.14886>
- [35] M.S. Kukurudziak, and E.V. Maistruk, in: *Fifteenth International Conference on Correlation Optics*, 121261V (SPIE, Chernivtsi, 2021). <https://doi.org/10.1117/12.2616170>
- [36] S.A. Canazza, et al., in: *2021 International Nuclear Atlantic Conference – INAC 2021 Virtual meeting*, (2021). <http://repositorio.ipen.br/handle/123456789/32524>
- [37] Z.W. Bell, *Scintillators and Scintillation Detectors*, in: *Handbook of Particle Detection and Imaging*, (Springer, Cham. 413-449, 2021). https://doi.org/10.1007/978-3-319-93785-4_15

- [38] Passport data Si PIN photodiodes S2744/S3588-08, -09, Electronic resource https://www.hamamatsu.com/content/dam/hamamatsu-photonics/sites/documents/99_SALES_LIBRARY/ssd/s2744-08_etc_kpin1049e.pdf
- [39] Passport data Si PIN photodiodes S2744-09, <https://www.hamamatsu.com/jp/en/product/optical-sensors/photodiodes/si-photodiodes/S2744-09.html>
- [40] Passport data Si PIN photodiode S3204-08, <https://www.hamamatsu.com/jp/en/product/optical-sensors/photodiodes/si-photodiodes/S3204-08.html>
- [41] Passport data Si PIN photodiode S3584-08, <https://www.hamamatsu.com/jp/en/product/optical-sensors/photodiodes/si-photodiodes/S3584-08.html>
- [42] Passport data Si PIN photodiode S3590-18, <https://www.hamamatsu.com/jp/en/product/optical-sensors/photodiodes/si-photodiodes/S3590-18.html>
- [43] Passport data Si photodiode S12497, <https://www.hamamatsu.com/jp/en/product/optical-sensors/photodiodes/si-photodiodes/S12497.html>
- [44] Passport data Si photodiode S12498, <https://www.hamamatsu.com/jp/en/product/optical-sensors/photodiodes/si-photodiodes/S12498.html>
- [45] M.S. Kukurudziak, Journal of nano- and electronic physics, **14**(1), 01023 (2022). [https://doi.org/10.21272/jnep.14\(1\).01023](https://doi.org/10.21272/jnep.14(1).01023)
- [46] S.B. Khan, S. Irfan, Z. Zhuanghao and S.L. Lee, Materials, **12**(9), 1483 (2019). <https://doi.org/10.3390/ma12091483>
- [47] K.V. Ravi, *Imperfections and impurities in semiconductor silicon*, (Wiley, New York, 1981).
- [48] N.M. Tugov, B.A. Glebov, and N. Charykov, *Semiconductor devices: Textbook for universities*, edited by V.A. Labuntsov, (Energoatomizdat, Moscow, 1990). (in Russian)
- [49] M.S. Kukurudziak, Journal of Instrumentation, **19**(09), P09006 (2024). <https://doi.org/10.1088/1748-0221/19/09/P09006>
- [50] S.N. Moger, and M. Mahesha, Sensors and Actuators A: Physical, **315**, 112294 (2020). <https://doi.org/10.1016/j.sna.2020.112294>
- [51] S.M. Sze, and K.K. Ng, *Physics of semiconductor devices*, (Wiley, 2006).
- [52] A.V. Igo, Opt. Spectrosc. **128**, 1125 (2020). <https://doi.org/10.1134/S0030400X20080135>
- [53] M.S. Kukurudziak, and E.V. Maistruk, East Eur. J. Phys. **1**, 386 (2024). <https://doi.org/10.26565/2312-4334-2024-1-39>
- [54] J.J. van Blaaderen, et. al., Chemistry of Materials, **37**(5), 1716-1740 (2025) <https://doi.org/10.1021/acs.chemmater.4c03437>
- [55] A. Rawat, and M.S. Islam, in: *Physics and Simulation of Optoelectronic Devices XXXII*. SPIE, 12880, 128800Q (2024). <https://doi.org/10.1117/12.3003413>

ФОТОПРИЙМАЧІ ДЛЯ СЦИНТИЛЯТОРІВ РЕНТГЕНІВСЬКОГО ТА γ -ВИПРОМІНЮВАННЯ†



Микола С. Кукурудзяк, Іван П. Козярьський, Микола С. Солодкий, Едуард В. Майстрок, Василина В. Копач,
Юрій О. Семенюк, Микола М. Павлюк

Чернівецький національний університет імені Юрія Федьковича, 58002, м. Чернівці, вул. Коцюбинського, 2, Україна

У статті проаналізовано детектори рентгенівського та γ -випромінювання на основі іонізаційного та сцинтиляційного принципів дії. Досліджено ефективність використання кремнієвих p - i - n і p - n фотодіодів у сцинтиляційних сенсорах для детектування видимого фотолюмінесцентного випромінювання. Детектор на основі p - i - n -структури виготовлено на основі монокристалічного кремнію p -типу з орієнтацією [111] та питомим опором 8-10 кОм·см. Фотодіод на основі p - n -структури виготовлявся на основі монокристалічного кремнію n -типу з орієнтацією [111] та питомим опором 200-300 Ом·см. Встановлено, що p - n фотодіоди мають значно менший темновий струм, ніж p - i - n фотодіоди (хоча дещо поступаються за чутливістю), що забезпечує їх перевагу в детективності. Однак, якщо необхідно реєструвати короткі імпульси люмінесцентного випромінювання, слід використовувати p - i - n фотодіоди, оскільки вони мають вищу швидкість. Збільшення швидкості відгуку пов'язано з тим, що процес дифузії носіїв заряду в p - n структурі фотодіода замінюється в p - i - n структурі дрейфом носіїв заряду через i -область в сильному електричному полі.

Ключові слова: фотолюмінесценція; селенід цинку; кремній; CdTe; електричні властивості; детектування; фотодіоди

TEMPERATURE RESPONSE CURVE OF SILICON DIODE TEMPERATURE SENSORS

 **Damir B. Istamov**^{a*},  **Oybek A. Abdulkhayev**^a, **Shukurullo M. Kuliye**^a, **Nuraddin Abdullayev**^b, **Shamshidin A. Ashirov**^c, **Dilbara M. Yodgorova**^a

^aPhysical-Technical Institute of Uzbekistan Academy of Sciences, Tashkent 100084, Uzbekistan

^bNational University of Uzbekistan, University St.4, Tashkent 100174, Uzbekistan

^cGulistan State University, 4 micro districts, 120100, Gulistan, Uzbekistan

*Corresponding Author e-mail: istamov@uzsci.net

Received March 1, 2025; revised May 12, 2025; accepted May 20, 2025

In this paper the results of the development of a semi-analytical model of the temperature response curve of silicon temperature diode sensors for the case of an arbitrary current transport mechanism, and a physical model that allows for high-precision determination of the temperature response curve for the case of diffusion-dominated current transport are presented. The results obtained using calculations based on this model were compared with experimental data, which showed their correspondence over the entire temperature range.

Keywords: Diode temperature sensor; Temperature response curve; Silicon; $p - n$ junction; Saturation Current; Built-in potential

PACS: 73.40.Lq, 73.61.Cw, 73.61.Ey, 72.20.Jv

INTRODUCTION

Currently, temperature sensors are effectively used in various fields of technology, such as personal computers, mobile phones, vehicles, medical devices, industrial installations, power plants, and many others. In recent years, with the widespread adoption of concepts such as the "Internet of Things" and "smart technologies," various sensors, including temperature sensors, have been utilized even more actively [1]-[6]. Additionally, temperature sensors are also used as a key component of other types of sensors, such as pressure sensors, humidity sensors, mass flow gas sensors, bolometers, and many others [7]-[9].

To meet the new demands arising from all these applications, research is being conducted on the development of new temperature sensors based on various principles and made from different materials [10]-[16]. However, in order to take temperature sensor technology to the next level and establish large-scale production, it is necessary to study the impact of technological and structural parameters on their working principles. In other words, it is essential to answer the question of how sensitive sensor parameters are to processes at each stage of their manufacturing technology. The most effective way to achieve this is through modeling.

First and foremost, for the correct interpretation of the sensor's working principle, it is crucial to create a model that closely reflects reality. That is, such a model should not require precise data on material properties but should accurately reflect the primary physical characteristics of the sensor. During the design phase, it is more important to correctly describe how relative changes in input variables affect the sensor's operation than to precisely calculate absolute values.

Thus, the main objective of this work is to develop an optimal physical model for silicon diode temperature sensors.

RESEARCH METHODOLOGY

In this section, a physical model of silicon diode temperature sensors is proposed, allowing the determination of the temperature dependence of sensitivity for any current transport mechanism through the sensor.

As is well known, the process of current flow in diodes based on a $p - n$ junction can generally be expressed as follows:

$$I = I_s \left[\exp\left(\frac{qV}{nkT}\right) - 1 \right], \quad (1)$$

where: I_s is the saturation current, q is the charge of an electron, V is the voltage applied to the diode's $p - n$ junction, k is Boltzmann's constant, T is the absolute temperature, and n is the ideality factor.

We introduce the following notation:

$$I_s^* = I_s \exp\left(\frac{qV_k}{nkT}\right), \quad (2)$$

where: V_k is the built-in potential.

Considering equation (2), equation (1) can be rewritten as:

$$I = I_s^* \left\{ \exp\left(-\frac{q(V_k - V)}{kT}\right) - \exp\left(-\frac{qV_k}{kT}\right) \right\} \quad (3)$$

At room temperature, $V_k \gg \frac{kT}{q}$, since $V_k \sim 0.6 \div 0.8 \text{ V}$ and $\frac{kT}{q} \approx 0.026 \text{ V}$, so the second term in equation (3) can be neglected. Under forward bias and with the voltage equal to V_k , the first term inside the brackets in equation (3) will be equal to 1, and the current through the diode will be I_s^* . Thus, the physical meaning of I_s^* is the saturation current under forward bias, while I_s represents the saturation current under reverse bias. These cases are graphically illustrated in Fig. 1, showing the dynamics of charge carrier movement in the $p-n$ junction.

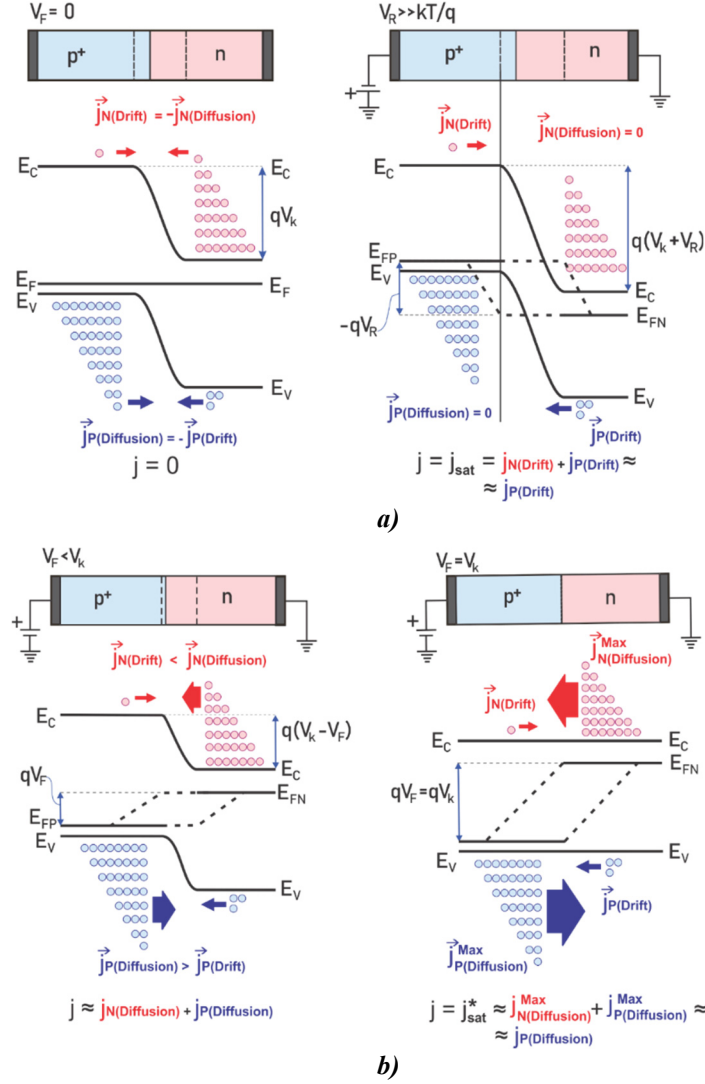


Figure 1. Dynamics of charge carrier movement in a $p-n$ junction:
a) drift and diffusion currents under reverse bias, and b) forward bias

From Figure 1a, under reverse bias, the electron concentration in the p -region is equal to n_i^2/N_A , where N_A is the acceptor concentration, which, in the first approximation, does not depend on temperature, while n_i (the intrinsic carrier concentration) is temperature-dependent. As the temperature increases, the concentration of minority charge carriers rises, indicating that the reverse saturation current I_s depends on temperature. From Fig. 1b, under forward bias, the electron concentration in the n -region depends on the doping level N_D and does not change with temperature. Therefore, it can be concluded that I_s^* , in the first approximation, is temperature-independent for any current transport mechanism.

Thus, I_s^* defines the saturation current under forward bias and does not depend on temperature, while I_s is the saturation current under reverse bias and is highly temperature-dependent.

From equation (1), the voltage across the $p-n$ junction can be determined as:

$$V = V_k - \frac{nkT}{q} \ln \frac{I_s^*}{I} + \frac{nkT}{q} \ln \left(1 + \frac{I_s}{I} \right) \quad (4)$$

To eliminate the term I_s^* , which depends on technological parameters, we can use the voltage $V(T_0)$ determined at a reference temperature T_0 :

$$V(T_0) = V_k(T_0) - \frac{nkT_0}{q} \ln \frac{I_s^*}{I} + \frac{nkT_0}{q} \ln \left(1 + \frac{I_s(T_0)}{I} \right) \quad (5)$$

Substituting the term $\ln \frac{I_s^*}{I}$, determined from equation (5), into equation (4), we can derive the following equation:

$$V(T) = V_k(T) - \frac{T}{T_0} (V_k(T_0) - V(T_0; I)) + \frac{nkT}{q} \ln \left(\frac{I + I_s(T)}{I + I_s(T_0)} \right) \quad (6)$$

This expression, being a semi-empirical model, allows for the determination of the temperature response curve of diode sensors for any current transport mechanism.

To construct a complete analytical model in this work, we consider the diffusion mechanism ($n = 1$), which is typically the dominant current transport mechanism in diode temperature sensors. It is known that for the diffusion mechanism, the saturation current I_s , the contact potential difference V_k , and the effective saturation current I_s^* are expressed as follows:

$$I_s = qAn_i^2 \left(\frac{\left(\frac{kT}{q} \mu_p \right)}{L_p N_D} + \frac{\left(\frac{kT}{q} \mu_n \right)}{L_n N_A} \right) \quad (7)$$

$$V_k = \frac{E_g}{q} - \frac{kT}{q} \ln \left(\frac{N_V N_C}{N_A N_D} \right) \quad (8)$$

$$I_s^* = q \left(\frac{L_p N_A}{\tau_p} + \frac{L_n N_D}{\tau_n} \right) \quad (9)$$

Considering expressions (7)-(9), equation (4) can be represented as:

$$V(T) = \frac{E_g(T)}{q} - \frac{kT}{q} \ln \left(\frac{N_V(T) N_C(T)}{N_A(T) N_D(T)} \right) - \frac{kT}{q} \ln \frac{q \left(\frac{L_p(T) N_A(T)}{\tau_p(T)} + \frac{L_n(T) N_D(T)}{\tau_n(T)} \right)}{I} + \frac{kT}{q} \ln \left(1 + \frac{qAn_i^2(T)}{I} \left(\frac{\left(\frac{kT}{q} \mu_p(T) \right)}{L_p(T) N_D(T)} + \frac{\left(\frac{kT}{q} \mu_n(T) \right)}{L_n(T) N_A(T)} \right) \right) \quad (10)$$

From this expression, it is clear that the voltage-temperature dependence in a forward-biased diode is determined by many variables. In particular, the primary temperature-dependent parameters are the lifetime of minority carriers τ , carrier mobility μ , and the bandgap E_g . Typically, in the first approximation, the temperature dependence of τ , μ and E_g is considered negligible, and only the temperature dependence of the intrinsic carrier concentration n_i in semiconductors is considered [17]-[19].

In this work, we aim to develop an analytical model of diode temperature sensors that considers the temperature dependence of all physical quantities (n_i , τ , μ , E_g , N_b). To achieve this, we used models from studies [20], [21] to determine carrier mobility and lifetime. It is known that in this model, the lifetime changes due to additional deep levels are not considered, and for such cases, the lifetime is assumed to be independent of or weakly dependent on temperature. For the temperature and doping dependence of the bandgap width, we used the model from study [22]. The proposed model also considers the temperature dependence of the ionized impurity concentration.

RESULTS AND DISCUSSION

This section presents the calculations performed based on the proposed model, their comparison with experimental results, and general conclusions. Figure 2 shows a comparison of the voltage dependence on temperature, calculated using the developed analytical model, with experimental data. From the figure, it can be seen that there is good agreement between the experimental data and the analytical calculations across almost the entire temperature range. However, it should be noted that this analytical model is applicable only when the diffusion mechanism of current transport is dominant. In cases where the experimental results do not align with the analytical model's predictions, it is recommended to use a semi-empirical model based on formula (5).

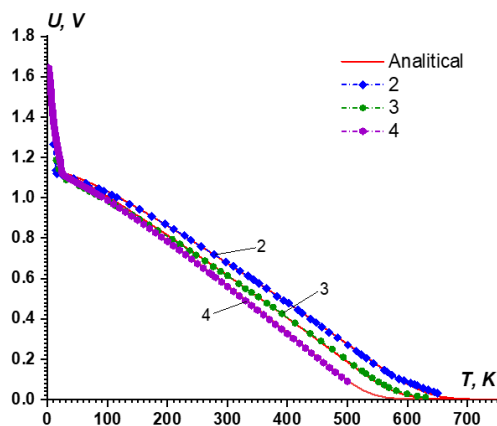


Figure 2. Temperature response curves for silicon diodes: 1 – analytical model (9); experimental data: 2, 3 – [23], 4 – [24].

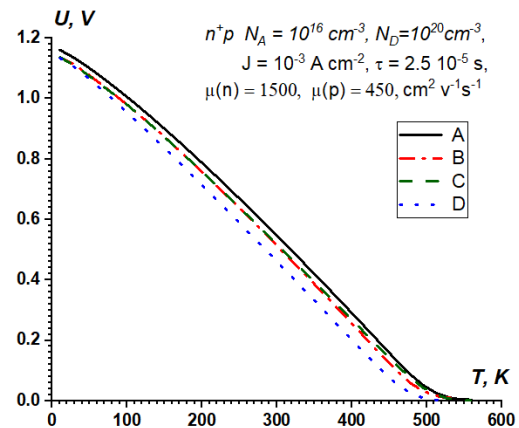


Figure 3. Temperature response curves for Cases A, B, C, and D.

Thus, using the analytical model that describes the temperature dependence of the voltage across a forward-biased diode, calculations were performed for the following cases: when only the temperature dependence of n_i was considered, while the temperature dependence of the parameters N_b , τ , μ , and E_g was not considered (*Case A*); when the temperature dependences of n_i , N_b and E_g were considered, but the temperature dependences of τ and μ were not (*Case B*); when the temperature dependences of n_i , N_b , E_g and μ , were considered, but the temperature dependence of τ was not (*Case C*); and when the temperature dependences of all parameters were considered (*Case D*) (Figure 3).

Figure 3 illustrates the differences between these cases, showing that ignoring parameters such as the concentration of partially ionized impurities, bandgap width, carrier mobility, and carrier lifetime is not always appropriate. Furthermore, it can be observed that in *Case D*, the temperature sensitivity curve is steeper compared to the other cases. This indicates higher temperature sensitivity for this case.

CONCLUSIONS

In this work, a semi-empirical model of the operation of a $p^+ - n$ diode was developed, showing the behavior of the structure without considering the ideality factor, i.e., assuming independence of the processes in the diode from current transport effects in the structure. Additionally, a complete model of a working diode was built, which considers the effects of incomplete impurity ionization, narrowing of the bandgap, total mobility of free carriers and lattice mobility, as well as the deviation of carrier lifetime depending on temperature. The consideration of the models mentioned above allowed for the graphical determination of the electro-physical and structural parameters in the form of temperature response curves.

Considering all parameters that play a crucial role in determining the diode's performance limits, the proposed complete model was studied based on four cases (*A, B, C, D*). Depending on the application areas, the optimal cases were identified. Determining the optimal variant by selecting materials and technological parameters during the production process is important for improving product quality and ensuring the reliability of manufacturing processes. The smaller the model error, the faster and more reliably the optimal variant can be determined and the correct operation of the diode evaluated.

ORCID

● Damir B. Istamov, <https://orcid.org/0009-0007-4654-1880>

● Oybek A. Abdulkhayev, <https://orcid.org/0000-0002-8822-1187>

REFERENCES

- [1] S. Kumar, P. Tiwari, and M. Zymbler, "Internet of Things is a revolutionary approach for future technology enhancement: a review," *J. Big Data*, **6**(111), (2019). <https://doi.org/10.1186/s40537-019-0268-2>
- [2] N. Cvar, J. Trilar, A. Kos, M. Volk, and E. Stojmenova Duh, "The Use of IoT Technology in Smart Cities and Smart Villages: Similarities, Differences, and Future Prospects," *Sensors*, **20**(14), 3897 (2020). <https://doi.org/10.3390/s20143897>
- [3] W.-T. Sung and S.-J. Hsiao, "The application of thermal comfort control based on Smart House System of IoT," *Measurement*, **149**, 106997 (2020). <https://doi.org/10.1016/j.measurement.2019.106997>
- [4] S. Awadallah, D. Moure, and P. Torres-González, "An Internet of Things (IoT) Application on Volcano Monitoring," *Sensors*, **19**(21), 4651 (2019). <https://doi.org/10.3390/s19214651>
- [5] R.G. Zakirov, O.A. Abdulhaev, A.A. Khakimov, A.Z. Rahmatov, D.M. Yodgorova, D.B. Istamov, and Sh.M. Kuliyeu, "Human body temperature monitoring wireless system," *E3S Web of Conferences* **401**, 04054 (2023). <https://doi.org/10.1051/e3sconf/202340104054>
- [6] R.R. Bebitov, O.A. Abdulhaev, D.M. Yodgorova, D.B. Istamov, G.M. Khamdamov, A.A. Khakimov, A.Z. Rakhmatov, *et al.*, "Potential distribution across the p-n junction diode temperature sensors with arbitrary doping of base region," *E3S Web of Conferences*, **401**, 03062 (2023). <https://doi.org/10.1051/e3sconf/202340103062>
- [7] Y. Zhang, and Y. Jiang, "An All-Sapphire Fiber Diaphragm-Free Extrinsic Fabry-Perot Interferometric Sensor for the Measurement of Gas Pressure at Ultrahigh Temperature," *IEEE Sensors Journal*, **23**(6), 5718-5823 (2023). <https://doi.org/10.1109/JSEN.2023.3240417>
- [8] L. Ribeiro, O. Saotome, R. d'Amore, and R. de Oliveira Hansen, "High-Speed and High-Temperature Calorimetric Solid-State Thermal Mass Flow Sensor for Aerospace Application: A Sensitivity Analysis," *Sensors*, **22**, 3484 (2022). <https://doi.org/10.3390/s22093484>
- [9] X. Xue, H. Xiong, Zh. Song, Y. Du, D. Wu, L. Pan, and Zh. Wang, "Silicon Diode Uncooled FPA With Three-Dimensional Integrated CMOS Readout Circuits," *IEEE Sensors J.*, **19**(2), 426-434 (2019). <https://doi.org/10.1109/JSEN.2018.2878098>
- [10] J.Sh. Abdullayev, and I.B. Sapaev, "Optimization of The Influence of Temperature on The Electrical Distribution of Structures with Radial P-N Junction Structures," *East Eur. J. Phys.* (3), pp. 344-349 (2024). <https://doi.org/10.26565/2312-4334-2024-3-39>
- [11] J.Sh. Abdullayev, and I.B. Sapaev, "Optimizing the Influence of Doping and Temperature on the Electrophysical Features of p-n and p-i-n Junction Structures," *Eurasian Physical Technical Journal*, **21**(3(49)), 21-28 (2024). <https://doi.org/10.31489/2024No3/21-28>
- [12] J.Sh. Abdullayev, I.B. Sapaev, and Kh.N. Juraev, "Theoretical analysis of incomplete ionization on the electrical behavior of radial p-n junction structures," *Low Temp. Phys.* **51**, 60-64 (2025). <https://doi.org/10.1063/10.0034646>
- [13] J.Sh. Abdullayev, and I.B. Sapaev, "Factors Influencing the Ideality Factor of Semiconductor p-n and p-i-n Junction Structures at Cryogenic Temperatures," *East Eur. J. Phys.* (4), 329-333 (2024). <https://doi.org/10.26565/2312-4334-2024-4-37>
- [14] J.Sh. Abdullayev, and I.B. Sapaev, "Modeling and calibration of electrical features of p-n junctions based on Si and GaAs," *Physical Sciences and Technology (Phys. sci. technol.)* **11**(3-4), 39-48 (2024). <https://doi.org/10.26577/phst2024v11i2b05>

- [15] S. Rao, G. Pangallo, and F.G. Della Corte, "4H-SiC pin diode as highly linear temperature sensor," IEEE Trans. Electron Devices, **63**(1), 414–418 (2016). <https://doi.org/10.1109/TED.2015.2496913>
- [16] G. Pangallo, S. Rao, G. Adinolfi, G. Graditi, and F. G. Della Corte, "Power MOSFET intrinsic diode as a highly linear junction temperature sensor," IEEE Sensors Journal, **19**(23), 11034–11040 (2019). <https://doi.org/10.1109/JSEN.2019.2935550>
- [17] R.R. Bebitov, O.A. Abdulkhaev, D.M. Yodgorova, D.B. Istamov, Sh.M. Kuliyeu, A.A. Khakimov, A.B. Bobonazarov, *et al.*, "Distribution of impurities in base-depleted region of diode temperature sensor," Low Temperature Physics, **50**(5), 418–424 (2024). <https://doi.org/10.1063/10.0025635>
- [18] M. Mansoor, I. Haneef, S. Akhtar, A. De Luca, and F. Udre, "Silicon diode temperature sensors - A review of applications," Sensors Actuators, A Phys. **232**, 63–74 (2015). <https://doi.org/10.1016/j.sna.2015.04.022>
- [19] R.R. Bebitov, O.A. Abdulkhaev, D.M. Yodgorova, D.B. Istamov, Khamdamov G.M., Sh.M. Kuliyeu, A.A. Khakimov, *et al.*, "Dependence of the accuracy of the silicon diode temperature sensors for cryogenic thermometry on the spread of their parameters," Low Temperature Physics, **49**(2), 256–260 (2023). <https://doi.org/10.1063/10.0016843>
- [20] D.B.M. Klaassen, "A unified mobility model for device Simulation-I. Model equations and Concentration dependence," Solid State Electron. **35**(7), 953–959 (1992). [https://doi.org/10.1016/0038-1101\(92\)90325-7](https://doi.org/10.1016/0038-1101(92)90325-7)
- [21] D.B.M. Klaassen, "A unified mobility model for device Simulation-II. Temperature dependence of carrier mobility and lifetime," Solid State Electr. **35**(7), 961–967 (1992). [https://doi.org/10.1016/0038-1101\(92\)90326-8](https://doi.org/10.1016/0038-1101(92)90326-8)
- [22] A. Schenk, "Finite-temperature full random-phase approximation model of band gap narrowing for silicon device simulation," J. Appl. Phys. **84**(7), 3684–3695 (1998). <https://doi.org/10.1063/1.368545>
- [23] Y.M. Shwarts, V.L. Borblik, N.R. Kulish, E.F. Venger, and V.N. Sokolov, "Limiting characteristics of diode temperature sensors," Sensors Actuators, A Phys. **86**(3), 197–205 (2000). [https://doi.org/10.1016/S0924-4247\(00\)00445-3](https://doi.org/10.1016/S0924-4247(00)00445-3)
- [24] S.S. Courts, "A standardized diode cryogenic temperature sensor for aerospace applications," Cryogenics, **74**, 172–179 (2016). <https://doi.org/10.1016/j.cryogenics.2015.09.006>

ХАРАКТЕРИСТИКА ТЕМПЕРАТУРНОГО ВІДГУКУ КРЕМНІЄВИХ ДІОДНИХ ДАТЧИКІВ ТЕМПЕРАТУРИ
**Дамір Б. Істамов^a, Ойбек А. Абдулхасєв^a, Шукуролло М. Кулієв^a, Нураддін Абдуллаєв^b, Шамшидін А. Аширов^c,
 Ділбара М. Йодгорова^a**

^aФізико-технічний інститут Академії наук Узбекистану, Ташкент 100084, Узбекистан

^bНаціональний університет Узбекистану, вул. Університетська, 4, Ташкент 100174, Узбекистан

^cГулістанський державний університет, 120100, Гулістан, Узбекистан

У цій роботі представлено результати розробки напіваналітичної моделі температурної відгуквої характеристики кремнієвих діодних температурних датчиків для випадку довільного механізму перенесення струму, а також фізичної моделі, яка дозволяє з високою точністю визначати температурну відгуккову характеристику для випадку дифузійно домінованого перенесення струму. Отримані результати, розраховані на основі цієї моделі, були порівняні з експериментальними даними, що показало їх відповідність у всьому діапазоні температур.

Ключові слова: діодний температурний датчик; температурна характеристика відгуку; кремній; p-n перехід; струм насичення; вбудований потенціал

STUDY OF THE FORMATION OF LOW-DIMENSIONAL DEFECT STATES IN SINGLE-CRYSTAL SILICON WITH THE PARTICIPATION OF OXYGEN

 Akramjon Y. Boboev,  Biloliddin M. Ergashev,  Nuritdin Y. Yunusaliyev, Murodiljon M. Xotamov

Andijan state university named after Z.M. Babur, Andijan, Uzbekistan

*Corresponding Author e-mail: aboboevscp@gmail.com

Received March 1, 2025; revised April 25, 2025; accepted May 15, 2025

This study investigates the formation of low-dimensional defect states in monocrystalline silicon involving oxygen, focusing on structural inhomogeneities and their impact on material properties. Monocrystalline silicon, a cornerstone of modern nanoelectronics, is primarily produced using the Czochralski method, which often introduces oxygen impurities. These impurities form oxide inclusions (SiO_x) and complexes (Si-O_n) during thermal treatments at 400–800°C, leading to defects that affect electrical and structural properties. The research employs X-ray diffraction to analyze p-type silicon samples grown by the Czochralski method, with thermal treatments at 950°C, 1050°C, and 1150°C. Results reveal that thermal processing redistributes atoms and defects, increasing lattice parameters and crystallinity, peaking at 1050°C. Subcrystalline sizes vary with temperature, reaching maximum stability at 1050°C. Oxygen and boron interactions form SiO_2 and B_2O_3 crystallites, with sizes ranging from 21–25 nm and 55 nm, respectively. Additionally, small clusters (1.6–2 nm) of SiO_x form in surface regions, indicating unsaturated silicon bonds and localized microdefects. The study also identifies SiB_6 crystallites (71–95 nm) on the surface, growing through Ostwald ripening at higher temperatures. These findings highlight the complex interplay between oxygen impurities, thermal treatments, and defect formation in silicon crystals. The research provides insights into optimizing silicon production processes to minimize defects and enhance material performance for advanced electronic applications. The results underscore the importance of controlling oxygen content and thermal processing conditions to achieve high-quality monocrystalline silicon with tailored properties. This work contributes to a deeper understanding of defect dynamics in silicon, offering practical implications for improving semiconductor manufacturing techniques. By addressing the challenges posed by oxygen impurities, the study paves the way for developing more efficient and reliable silicon-based devices in the nanoelectronics industry.

Keywords: Monocrystalline silicon; Czochralski method; Defect states; X-ray diffraction; Crystallographic orientation; Subcrystalline structures; Microdefects; Cluster formation

PACS: 78.30.Am

INTRODUCTION

Modern nanoelectronics requires high-purity and perfect semiconductor crystals, among which monocrystalline silicon occupies one of the leading positions due to mature technologies and low cost [1-3]. The main methods of industrial production of Si are the Czochralski method and crucible-free zone melting, with the Czochralski method being used in about 80% of cases. When growing single crystal silicon, it is important to minimise the amount of uncontrolled impurities, as their excess leads to distortion of the crystal lattice and the formation of defects that affect the properties of the material. One of such impurities is oxygen, which during crystallisation from the melt passes into silicon, partially dissolving in it and forming oxide inclusions SiO_x with the size from 1 to 50 microns [4]. During heat treatment of silicon in the temperature range of 400-800°C, supersaturated oxygen forms various complexes of Si-O_n type ($n = 1-4$). Part of these complexes decomposes with the release of SiO_2 or is deposited in the interstitial spaces of the Si crystal lattice in electrically neutral states. This causes the formation of defect states that affect the electrical properties of silicon [5].

The shape, type and size of such microformations depend on the technological conditions of single crystal growth and subsequent heat treatment. This problem remains unsolved until now, as it affects not only the electrophysical characteristics, but also the structural parameters of the crystal. Analysis of literature data shows that oxygen can form non-stoichiometric layers of SiO_x , microunits of precipitate type and amorphous SiO_2 particles, which significantly complicates the study of the structure and behaviour of oxygen in a silicon crystal [6-8]. The main method to investigate such characteristics of oxygen in single crystal silicon is X-ray diffraction analysis. In connection with the above, the aim of the present work is to investigate the structural inhomogeneities formed by the participation of oxygen in single-crystal silicon grown by the Czochralskii method [8].

MATERIALS AND METHODS

The object of the study was p-type single-crystalline silicon grown by the Czochralskii method with resistivity $\rho \approx 3 \div 10 \text{ } \Omega\text{-cm}$, boron impurity concentration $N_p \approx 2 \cdot 10^{15} \text{ cm}^{-3}$, dislocation density $N_d \geq 10^{13} \text{ cm}^{-2}$ and oxygen concentration $N_o \approx 2 \cdot 10^{17} \text{ cm}^{-3}$. Samples with dimensions of $1.4 \times 4 \times 22 \text{ mm}^3$ were fabricated from cut wafers of single-crystalline silicon.

Control of structural and phase states, O in Si of the studied samples was carried out on the third generation X-ray diffractometer types Empyrean Malvern PANalytical L.T.D. The OriginPro2022 programme was used to determine the

peak maximum [9]. X-ray diffraction measurements were carried out in Bragg - Brentano beam geometry in the range $2\theta_B = 15^\circ$ to 140° continuously at a scanning speed of 0.33 deg/min and an angular step of 0.0200 (deg).

RESULTS AND DISCUSSION

Thermal treatments of single-crystalline $p\text{-Si}\langle B \rangle$ (control samples) were carried out at temperatures of 950°C, 1050°C and 1150°C for 5 hours. Figure 1 shows the X-ray diffraction patterns of these samples. It can be seen from the X-ray radiographs that diffraction reflections corresponding to the $(111)_{\text{Si}}$ crystallographic orientation are observed at scattering angles $2\theta = 28.53^\circ$, 28.5° and 28.45° , possessing high intensity ($I_{\text{Si}(950^\circ\text{C})} = 3 \times 10^6$ imp/s, $I_{\text{Si}(1050^\circ\text{C})} = 4.7 \times 10^6$ imp/s and $I_{\text{Si}(1150^\circ\text{C})} = 1.4 \times 10^6$ imp/s) and a pronounced selective character. This indicates that the surface of the control silicon samples has a crystallographic orientation (111). Also note that with increasing processing temperature, the diffraction peaks shift towards smaller angles (from 28.53° to 28.45°) and their intensity first increases by a factor of 1.6 (at 1050°C) and then decreases by a factor of 2.1 (at 1150°C). This indicates that the heat treatment for 5 hours results in the redistribution of atoms and a decrease in the number of defects in the crystal and an increase in the silicon lattice parameter: $a_{\text{Si}(950^\circ\text{C})} = 0.534$ nm, $a_{\text{Si}(1050^\circ\text{C})} = 0.535$ nm and $a_{\text{Si}(1150^\circ\text{C})} = 0.536$ nm. Thus, the maximum degree of crystallinity is reached at 1050°C and a decrease is observed at 1150°C. In addition, diffraction reflections corresponding to $(333)_{\text{Si}}$ crystallographic orientation were recorded at scattering angles $2\theta = 94.95^\circ$, 94.94° and 94.98° , with intensities $I_{\text{Si}(950^\circ\text{C})} = 2.3 \times 10^4$ imp/s, $I_{\text{Si}(1050^\circ\text{C})} = 8.9 \times 10^4$ imp/s and $I_{\text{Si}(1150^\circ\text{C})} = 4.5 \times 10^5$ imp/s. In the range of scattering angles 10° – 60° , a non-monotonic character of the inelastic background level can be observed. The structural reflections of $(111)_{\text{Si}}$ are weakly separated into α_1 and α_2 components, whereas $(333)_{\text{Si}}$ shows a marked separation of these components. This indicates that the heat treatment at 950°C, 1050°C and 1150°C results in the formation of microstresses (dislocations or other defects) in the surface regions of the samples, whereas in the inner volume of the crystal lattice their stabilisation occurs [10]. In addition, at scattering angles $2\theta = 25.7^\circ$ and $2\theta = 83.3^\circ$, β components of the first-order $(111)_{\text{Si}}$ and third-order $(333)_{\text{Si}}$ reflections are observed (see Figs. 2 a and 2 c).

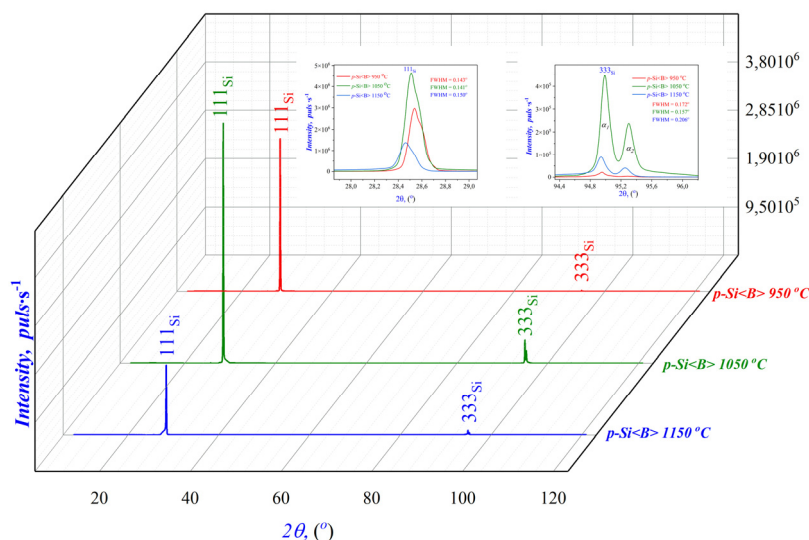


Figure 1. X-ray images of $p\text{-Si}\langle B \rangle$ samples subjected to heat treatment at 950°C, 1050°C, and 1150°C

According to experimental results on the diffraction reflections of $(111)_{\text{Si}}$, it was found that the subcrystallite sizes in silicon control samples, subjected to thermal treatment for 5 hours at 950°C, 1050°C, and 1150°C, were 59.7 nm, 61.1 nm, and 57.4 nm, respectively. This suggests that at 950°C, due to the relatively low diffusion temperature, the state of the subcrystallites did not undergo significant changes. At 1050°C, the size of the peak increased due to the process of recrystallization, through the attachment of subcrystallites. At 1150°C, the intensity of the peak decreased due to the activation of processes involving the removal and subsequent formation of subcrystallites. Additionally, X-ray diffraction patterns at scattering angles of $2\theta = 63.2^\circ$ and 105.1° reveal structural reflections corresponding to $(220)_{\text{Si}}$ and $(440)_{\text{Si}}$, indicating the presence of polycrystalline regions of various sizes (ranging from 11 nm to 87 nm) distributed on the surface and within the samples.

In addition, structural reflections corresponding to the $(222)_{\text{Si}}$ crystallographic orientation are observed at scattering angles $2\theta = 58.8^\circ$, 59.0° and 58.9° in the X-ray diffraction patterns of silicon control samples heat treated for 5 h at temperatures of 950°C, 1050°C and 1150°C (see Fig. 2c). As a rule, such structural reflections are not observed in the X-ray radiograph of silicon with a crystal lattice free from various microdistortions. That is, their appearance indicates the presence of micro-distortions in the crystal lattice. There is a possibility of quantitative determination of such micro-distortions, for which the ratio of the intensity of structural reflection $(222)_{\text{Si}}$ to the intensity of the main structural reflection $(111)_{\text{Si}}$, i.e. $I_{(222)_{\text{Si}}}/I_{(111)_{\text{Si}}}$, is used. In our case, these values are: 3.8×10^{-4} at 950°C, 5.4×10^{-4} at 1050°C, and 6.5×10^{-4} at 1150°C. These values exceed 10^{-4} , which is characteristic of crystal lattices with a diamond-like structure in which the atoms are uniformly distributed. This, in turn, indicates that mechanical stresses in localised regions of the silicon crystal

lattice increase with increasing heat treatment temperature. This effect is due to the non-uniform distribution of oxygen entering the crystal from background impurities. This is most likely due to the difference in ionic radii of silicon and oxygen, as well as to small stresses arising during crystal growth due to the temperature gradient. Due to the difference in ionic radius, oxygen atoms are located near crystal lattice boundaries, at the interfaces of silicon subcrystallites, and in displaced lattice nodes. In doing so, they compensate for the unsaturated silicon bonds [11,12]. This, in turn, shows that silicon atoms are predominantly located in the crystal volume and this structure has high symmetry, while oxygen atoms can spontaneously form asymmetric crystallites at subcrystallite interfaces.

The X-ray diffraction analysis of the *p*-Si sample revealed the presence of structural reflections corresponding to SiO_2 and B_2O_3 phases. For SiO_2 , the reflections were observed at scattering angles $2\theta = 20.2^\circ, 39.1^\circ, 42.6^\circ, 90.8^\circ$, and 91.9° , corresponding to the crystallographic orientations (100), (102), (200), (400), and (401). The analysis of the full width at half maximum (FWHM) values indicated the formation of SiO_2 crystallites with sizes ranging from 21 to 25 nm. The crystalline parameters for SiO_2 were determined to be $a_{\text{exp}} = b_{\text{exp}} = 0.5031$ nm and $c_{\text{exp}} = 0.5527$ nm, with a trigonal unit cell of space group P3221. Additionally, for B_2O_3 , a structural reflection was observed at scattering angles $2\theta = 23.0^\circ$ to 23.6° , indicating the presence of B_2O_3 crystallites with a size of 55 nm and a trigonal unit cell with lattice parameters $a_{\text{exp}} = b_{\text{exp}} = 0.4415$ nm and $c_{\text{exp}} = 0.8812$ nm. These findings suggest the coexistence of SiO_2 and B_2O_3 phases in the *p*-Si sample.

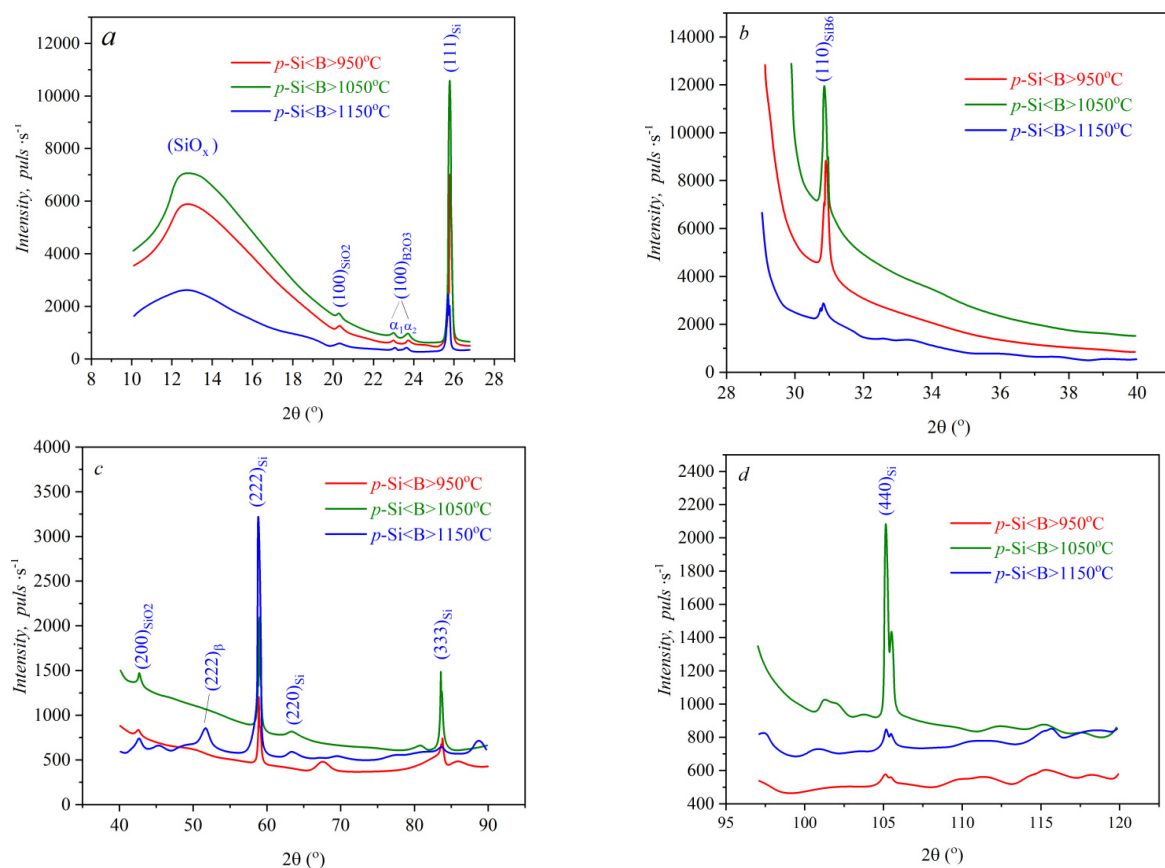


Figure 2. Variation in the inelastic background level of the X-ray image for the *p*-Si sample at small, medium, and large scattering angles, along with the shapes of the observed structural reflections.

Moreover, in the X-ray images of silicon control samples subjected to thermal treatment for 5 hours at temperatures of 950°C , 1050°C , and 1150°C , diffuse reflections associated with the SiO_x phase are observed in the small-angle scattering region ($2\theta \approx 13^\circ$) (see Fig. 2a). An analysis of the full width at half maximum (FWHM) values reveals the following: $\text{FWHM}(950^\circ\text{C}) = 7,2 \times 10^{-2}$ rad, $\text{FWHM}(1050^\circ\text{C}) = 8,7 \times 10^{-2}$ rad, $\text{FWHM}(1150^\circ\text{C}) = 8,4 \times 10^{-2}$ rad. Based on these values, it is established that these structures are not crystallites but rather small fragments with sizes of 2 nm at 950°C , 1.6 nm at 1050°C , and 1.7 nm at 1150°C . These fragments primarily form in the near-surface regions of silicon and indicate the presence of unsaturated bonds between silicon atoms. Additionally, their small size suggests the absence of long-range order in the arrangement of silicon and oxygen atoms. Therefore, these formations are not nanocrystallites but rather clusters [13]. Since similar clusters partially form in different regions of the silicon control samples at 950°C , 1050°C , and 1150°C , variations in the inelastic background of the X-ray images are observed across small, medium, and large scattering angles. This, in turn, indicates the formation of additional microdefects in the silicon crystal lattice.

In the X-ray radiographs of silicon control samples heat treated for 5 h at temperatures of 950°C , 1050°C and 1150°C , a structural reflection is observed at a scattering angle of $2\theta = 30.8^\circ$ referring to the SiB_6 (silicon hexaboride)

phase with crystallographic orientation (110) at a scattering angle of $2\theta = 30.8^\circ$ (see Fig. 2 b). This phase is formed by cubic unit cells with lattice parameters: $a_{\text{exp}} = 0.4156$ nm. The crystallite size corresponding to this phase is: 75 nm at 950°C , 71 nm at 1050°C and 95 nm at 1150°C . This, in turn, indicates the following processes: at 950°C , crystallite formation and growth occur; at 1050°C , reorganization and fragmentation are observed, which leads to a temporary decrease in their size; at 1150°C , atomic mobility increases and crystallite enlargement occurs due to the intensification of the Ostwald Ripening mechanism.

CONCLUSION

Based on the X-ray structural analysis of single-crystal p-Si samples, the following conclusions have been drawn:

It has been established that the surface of the p-Si single-crystal samples corresponds to the crystallographic orientation (111). Through thermal treatment at 950°C , 1050°C , and 1150°C , there is a redistribution of atoms and defects, leading to an increase in the lattice parameter: $a_{\text{Si}(950^\circ\text{C})} = 0,534$ nm $a_{\text{Si}(1050^\circ\text{C})} = 0,535$ nm and $a_{\text{Si}(1150^\circ\text{C})} = 0,536$ nm. Furthermore, the crystal perfection is increased at 1050°C and decreased at 1150°C .

During the thermal treatment at 950°C , 1050°C , and 1150°C , micro-stresses (dislocations and other defects) are formed in the surface areas of the samples, while their stabilization occurs within the bulk of the samples.

It has been found that at 950°C , due to the relatively low diffusion temperature, sub-crystals (59.7 nm) do not undergo significant changes. At 1050°C , a recrystallization process takes place, resulting in their enlargement to 61.1 nm. At 1150°C , due to the destruction and subsequent reformation of sub-crystals, their size is reduced to 57.4 nm.

The interaction of silicon, boron, and oxygen atoms results in the formation of crystallites SiO_2 and B_2O_3 , belonging to the trigonal elementary cell with spatial group $P3_221$. The dimensions of the SiO_2 crystallites are $a_{\text{exp}} = b_{\text{exp}} = 0,5031$ nm and $c_{\text{exp}} = 0,5527$ nm, with a size of 21–25 nm. The B_2O_3 crystallites have dimensions $a_{\text{exp}} = b_{\text{exp}} = 0,4415$ nm, $c_{\text{exp}} = 0,8812$ nm, and a size of 55 nm.

After thermal treatment at 950°C , 1050°C , and 1150°C , clusters with sizes of 2 nm, 1.6 nm, and 1.7 nm are formed in the surface regions of monocrystalline p-Si samples. These clusters are formed due to unsaturated silicon-oxygen (SiO_x) bonds, leading to the formation of additional microdefects in the crystal lattice.

Furthermore, thermal treatment at the same temperatures leads to the formation of nanocrystallites with sizes of 75 nm, 71 nm, and 95 nm on the surface of p-Si samples. These nanocrystallites consist of cubic elementary cells with lattice parameters $a_{\text{exp}} = 0.4156$ nm.

Funding

The present research work was financed under the project FZ-292154210 granted by the Ministry of Innovative Development of the Republic of Uzbekistan

ORCID

✉ Akramjon Y. Boboev, <https://orcid.org/0000-0002-3963-708X>; ✉ Biloliddin M. Ergashev, <https://orcid.org/0009-0007-9392-6548>
✉ Nuritdin Y. Yunusaliyev, <https://orcid.org/0000-0003-3766-5420>

REFERENCES

- [1] S. Simakov, N.A. Vinogradova, and O. Nikitushkina, "Irradiation of Monocrystalline Silicon with a High-Power Pulsed Beam of Carbon Ions and Protons," *Inorganic Materials: Applied Research*, **15**, 649–653 (2024). <https://doi.org/10.1134/S2075113324700072>
- [2] Jia-he CHEN, *et al.*, "Monocrystalline silicon used for integrated circuits: still on the way," *Front. Mater. Sci. China*, **2**(4) 335–344 (2008). <https://doi.org/10.1007/s11706-008-0062-0>
- [3] X. Yu, D. Yang, X. Ma, *et al.*, "Grown-in defects in nitrogendoped Czochralski silicon," *Journal of Applied Physics*, **92**(1), 188–194 (2002). <https://doi.org/10.1063/1.1481190>
- [4] X. Huang, T. Taishi, I. Yonenaga, *et al.*, "Dislocation-free Czochralski Si crystal growth without dash necking using a heavily B and Ge codoped Si seed," *Japanese Journal of Applied Physics*, **39**, 115–119 (2000). <https://doi.org/10.1143/JJAP.39.L1115>
- [5] N.Y. Yunusaliyev, "The Gas-Sensitive Properties of Tin Dioxide Films," *East Eur. J. Phys.* (4), 439–442 (2024). <https://doi.org/10.26565/2312-4334-2024-4-52>
- [6] S.Z. Zaynabidinov, Sh.U. Yuldashev, A.Y. Boboev, and N.Y. Yunusaliyev, "X-ray diffraction and electron microscopic studies of the ZnO(S) metal oxide films obtained by the ultrasonic spray pyrolysis method," *Herald of the Bauman Moscow State Technical University, Series Natural Sciences*, **1**(112), 78–92 (2024). <https://doi.org/10.18698/1812-3368-2024-1-78-92>
- [7] Sh.B. Utamuradova, Kh.J. Matchonov, J.J. Khamdamov, and Kh.Y. Utemuratova, "X-ray diffraction study of the phase state of silicon single crystals doped with manganese," *New Materials, Compounds and Applications*, **7**(2), 93–99 (2023). http://jomardpublishing.com/UploadFiles/Files/journals/NMCA/v7n2/Utamuradova_et_al.pdf
- [8] S.Z. Zainabidinov, A.Y. Boboev, M.B. Rasulova, and N.Y. Yunusaliyev, "X-ray diffraction analysis, optical characteristics, and electro-physical properties of the n-ZnO/p-NiO structure grown by the spray pyrolysis method," *New Materials, Compounds and Applications*, **8**(3), 411–421 (2024). <https://doi.org/10.62476/nmca83411>
- [9] G.T. Imanova, A.I. Kamardin, and I.R. Bekpulatov, "Investigation of Coatings Formed by Thermal Oxidation on Monocrystalline Silicon," *Integrated Ferroelectrics*, **240**(1), 53–63 (2024). <https://doi.org/10.1080/10584587.2023.2296317>
- [10] B.D. Igamov, A.I. Kamardin, D.Kh. Nabiev, I.R. Bekpulatov, *et al.*, "Study of the physical nature of Mn4Si7 crystals formed by the diffusion method using an X-ray diffraction," *Journal of Crystal Growth*, **649**, 27–32 (2025). <https://doi.org/10.1016/j.jcrysgro.2024.127932>

- [11] A.Y. Boboev, "Photoelectric characteristics of the heterojunction n-GaAs-p-(GaAs)_{1-x-y}(Ge₂)_x(ZnSe)_y," East European Journal of Physics, (3), 298-302 (2024) <https://doi.org/10.26565/2312-4334-2024-3-31>
- [12] M.K. Karimov, Kh.J. Matchonov, K.U. Otaboeva, and M.U. Otaboev, "Computer Simulation of Scattering Xe⁺ Ions from InP(001)<110> Surface at Grazing Incidence," e-Journal of Surface Science and Nanotechnology **17**, 179-183 (2019). <https://doi.org/10.1380/ejsnt.2019.179>
- [13] M. Li, Y. Liu, Y. Zhang, X. Han, T. Zhang, Y. Zuo, C. Xie, et al., "Effect of the Annealing Atmosphere on Crystal Phase and Thermoelectric Properties of Copper Sulfide," ACS Nano, **15**(3), 4967-4978 (2021). <https://doi.org/10.1021/acsnano.0c09866>

ДОСЛІДЖЕННЯ ФОРМУВАННЯ НИЗЬКОВИМІРНИХ ДЕФЕКТНИХ СТАНІВ В МОНОКРИСТАЛІЧНОМУ КРЕМНІІ ЗА УЧАСТЮ КИСНЮ

Акрамжон Ю. Бобоев, Білолідін М. Ергашев, Нурітдин Ю. Юнусалієв, Муродільжон М. Хотамов

Андижанський державний університет імені З.М. Бабура, Андижан, Узбекистан

В цій роботі досліджується формування низьковимірних дефектних станів у монокристалічному кремнії за участю кисню, зосереджуючись на структурних неоднорідностях та їхньому впливі на властивості матеріалу. Монокристалічний кремній, нарізний камінь сучасної напівелектроніки, виробляється переважно методом Чохральського, який часто вводить домішки кисню. Ці домішки утворюють оксидні включення (SiO_x) та комплекси (Si-On) під час термічної обробки при 400–800°C, що призводить до дефектів, які впливають на електричні та структурні властивості. У дослідженні використовується рентгенівська дифракція для аналізу зразків кремнію р-типу, вирощених методом Чохральського, з термічною обробкою при 950°C, 1050°C та 1150°C. Результати показують, що термічна обробка перерозподіляє атоми та дефекти, збільшуючи параметри решітки та кристалічність, досягаючи піку при 1050°C. Розміри субкристалічних структур змінюються з температурою, досягаючи максимальної стабільності при 1050°C. Взаємодія кисню та бору утворює кристаліти SiO₂ та B₂O₃ розмірами від 21 до 25 нм та 55 нм відповідно. Крім того, в поверхневих областях утворюються невеликі кластери (1,6–2 нм) SiO_x, що вказує на ненасичені кремнієві зв'язки та локалізовані мікродефекти. У дослідженні також виявлено кристаліти SiB₆ (71–95 нм) на поверхні, що ростуть шляхом дозрівання Оствальда за вищих температур. Ці результати підкреслюють складну взаємодію між домішками кисню, термічною обробкою та утворенням дефектів у кристалах кремнію. Дослідження дає уявлення про оптимізацію процесів виробництва кремнію для мінімізації дефектів та підвищення характеристик матеріалу для передових електронних застосувань. Результати підкреслюють важливість контролю вмісту кисню та умов термічної обробки для досягнення високоякісного монокристалічного кремнію з індивідуальними властивостями. Ця робота сприяє глибшому розумінню динаміки дефектів у кремнії, пропонуючи практичні наслідки для вдосконалення технологій виробництва напівпровідників. Вирішуючи проблеми, що виникають через домішки кисню, дослідження прокладає шлях для розробки більш ефективних та надійних пристроїв на основі кремнію в напівелектронній промисловості.

Ключові слова: монокристалічний кремній; метод Чохральського; дефектні стани; рентгенівська дифракція; кристалографічна орієнтація; субкристалічні структури; мікродефекти; утворення кластерів

EFFECT OF DEPOSITION CONDITIONS ON MICROSTRUCTURE AND COMPOSITION OF NITRIDE MONOLAYER AND CARBIDE-NITRIDE MULTILAYER COATINGS BASED ON W AND Nb

O.V. Maksakova^{a,b}, V.M. Beresnev^b, S.V. Lytovchenko^b, D.V. Horokh^b, B.O. Mazilin^b,
I.O. Afanasieva^b, M. Čaplovičová^c, M. Sahul^a

^a*Institute of Materials Science, Slovak University of Technology in Bratislava, 25, Jána Bottu Str., 917 24 Trnava, Slovakia*

^b*V.N. Karazin Kharkiv National University, 4, Svobody Sq., 61000 Kharkiv, Ukraine*

^c*Centre for Nanodiagnostics of Materials, Slovak University of Technology in Bratislava, Vazovova 5, 812 43 Bratislava, Slovakia*

^{*}*Corresponding Author e-mail: s.lytovchenko@karazin.ua*

Received March 5, 2025; revised April 27, accepted May 19, 2025

This study investigates the structural and compositional evolution of monolayer WNbN and multilayer WNbN/WNbC coatings deposited by the cathodic arc evaporation. The effects of substrate bias voltage (–50 V to –200 V) and cathode arc current (130 – 150 A for W, 110 – 120 A for Nb) were systematically studied to tailor coating morphology, phase formation, and elemental distribution. Cross-sectional microstructural analysis revealed pseudo-multilayer structures within monolayers due to substrate rotation and limited interdiffusion. Increasing bias voltage promoted densification, grain refinement, and improved adhesion, but also enhanced the re-sputtering of nitrogen, affecting stoichiometry and deposition rates. Multilayer coatings showed well-defined alternations between nitride and carbide layers, with morphology and crystallinity strongly influenced by ion energy and metal ion flux. The structural analysis confirmed the dominance of cubic solid solutions based on WNbN and WNbC, with minor hexagonal W₂N and Nb₂N detected. Grain sizes ranged from 6 to 15 nm, depending on deposition parameters. Optimal structure was achieved at moderate bias (–120 V) and high W arc current, yielding uniform layers, balanced composition, and enhanced crystallinity. The results demonstrate how controlled process parameters enable the design of high-performance nanocomposite coatings with tunable microstructure and phase composition, suitable for protective applications.

Keywords: Multilayer coatings; Nitrides; Carbides; Niobium; Tungsten; Microstructure; Composition

PACS: 68.55.Jk, 68.65.Ac

INTRODUCTION

To improve the quality, durability, and performance of metal products, various options are employed to alter their bulk structure and phase state while also modifying the surface for strengthening, enhancing thermal stability, and mitigating corrosion or friction. One of the most common and advanced methods for ensuring the desired operational properties of metal product surfaces is the application of functional films and coatings. Utilizing coatings increases the chemical stability of products and enhances mechanical and other properties, which significantly impacts their performance and service life, particularly under challenging conditions (thermobaric loads, friction, chemically active environments, etc.).

Among the various functional coatings, a distinct category consists of those designed to protect and enhance the operational qualities of cutting tools. Numerous cutting operations are prevalent in metalworking technologies across various sectors of mechanical engineering and other industries. The wear and premature failure of cutting tools pose a significant challenge, as they directly influence the efficiency and cost-effectiveness of their use, service life, and machining accuracy.

Among several methods for forming functional coatings, physical and chemical deposition technologies hold a significant position, particularly plasma technologies, which include processes like vacuum-arc evaporation or magnetron sputtering of metal targets and the deposition of condensate films. By adjusting the technological parameters of deposition (such as the composition of cathodes-evaporators, vacuum or gas environment, displacement potential on the substrate, geometry of the evaporators and substrates, and dynamic or static modes), it is possible to regulate the structural and phase state as well as the structure and architecture of coatings.

Protective two-element (binary) coatings of the first generation based on nitrides and carbides of titanium and zirconium (or those containing these compounds) have found widespread application due to properties such as high hardness, strong adhesion to the base, and resistance to wear, oxidation, and corrosion. Thus, coatings with TiC particles protect various components of mechanical systems [1], significantly increasing the wear resistance and hardness of parts. Coatings with TiN nitride are employed to modify and strengthen steel products [2, 3]. Zirconium nitride films are characterized by extraordinary overall stability, with excellent thermal and mechanical properties, high chemical inertness, and wear resistance, making them attractive for protecting a wide range of materials [4–6]. Alongside high hardness, toughness, and Young's modulus, niobium carbide (NbC) possesses an extremely high melting point, enabling the creation of coatings that provide material protection in high-temperature environments [7–10].

The aforementioned coatings have also found application in protecting cutting tools [11, 12], yet it became evident that binary nitride and carbide coatings have significant disadvantages, specifically low fracture toughness, high brittleness, and a tendency for microcrack formation [13]. This prompted the search for new methods to develop wear-resistant coatings that meet high standards of both hardness and strength.

One of these methods involves adding specific metals to binary compounds based on Ti, Nb, and Zr, resulting in the formation of ternary coatings with enhanced performance characteristics [14]. For instance, in [15], calculations of the microproperties of carbides (NbM)C, where M = V, Mo, W, and Cr (stability, mechanical parameters, and bonding structures) were conducted, demonstrating that the incorporation of V, Mo, W, and Cr atoms increases the hardness of carbides and reduces the mismatch between them and the matrix. The addition of TiC to WC [16] produces a significant hardness increase (> 3500 VHN) with nearly zero porosity, and its high melting point enables the use of such material in developing high-temperature resistant thermal protective coatings. The impact of molybdenum alloying on the microstructure and mechanical properties of transition metal carbides and nitrides for further enhancing the characteristics of these hard but brittle materials is illustrated by the examples of the compounds $(\text{Nb}_x\text{Mo}_{1-x})\text{C}$ [17] and $\text{M}_3\text{Mo}_3\text{N}$ and $\text{M}_2\text{Mo}_4\text{N}$ (M = Fe, Co, Ni) [18]. Triple thin films based on nitrides, particularly TiMN, where M=V, Al, Mo, Cu, Mg, Zr, provide a combination of high hardness and wear resistance in coatings, a low coefficient of friction, and adequate corrosion protection compared to binary nitride compounds [19] [20]. The requirements of modern technology and industry for coating strength have led to the development of a new stage in improving coating quality: the creation of multilayer coatings, whose hardness often exceeds the individual hardness of the materials involved [21-23]. Many theoretical works are dedicated to explaining this phenomenon [24-26], which explore various mechanisms that lead to a significant increase in the hardness and strength of multilayer coatings compared to monolayer ones. Generally, hardness increases with a greater number of layers and a decreased thickness until reaching a maximum value in the nanometer range. For example, multilayer TiCN/TiNbCN coatings exhibit a direct relationship between an increase in the number of bilayers and a decrease in residual stress, along with changes in mechanical properties and fracture toughness [27]. In addition to improved strength, hardness, and wear resistance, the use of multilayer coatings addresses the issue of compatibility – meeting fundamentally different requirements for the part on one hand and for the coating/substrate on the other. It is challenging to satisfy these conflicting requirements with a single-layer coating, unlike a multilayer coating system [28].

The combination of carbide and nitride compounds in nanoscale multilayer coatings represents a scientifically compelling and practically valuable research direction. Previous studies, such as those involving TiN/SiC multilayers, have demonstrated that alternating nanoscale layers of two distinct ceramic phases can achieve superior hardness and wear resistance compared to their monolithic counterparts of equal total thickness [29]. This performance enhancement stems from the superlattice effect, interface strengthening, and restricted dislocation motion across compositional boundaries. Extending this concept to tungsten-based systems, which are less explored yet highly promising, introduces a new level of novelty. Tungsten nitride (WN) offers excellent thermal stability and hardness, while tungsten carbide (WC) is renowned for its wear resistance and oxidation tolerance at elevated temperatures. The integration of these two phases into a multilayer architecture could result in a universal protective material applicable across diverse industrial domains, including aerospace, energy, cutting tools, and electronics. Evidence from related systems supports this potential. In [30], Ti-WN/Ti-WC multilayers exhibited the lowest corrosion rate and the highest dielectric response when structured as high-period ($n = 40$) multilayers, confirming that finely tuned layer stacking significantly enhances performance. Furthermore, the synthesis of superlattice nc-TiN/a-(W,Ti) $\text{C}_{0.83}$ nanocomposites demonstrated superhardness, reduced friction, and outstanding high-temperature wear resistance [31].

Given these insights, multilayer coatings that combine tungsten-based nitrides and carbides present a novel and underexplored class of materials [32]. Their potential for tailoring mechanical, tribological, and electrochemical properties through structural engineering, such as alloying with elements from the group IV-VI, on a nanoscale, makes them an exciting frontier in advanced coating technologies. Investigating such systems will fill a knowledge gap in current materials science and open pathways to designing next-generation coatings for extreme environments. Utilizing the vacuum-arc PVD technique with a recently developed two-channel control device – “evaporator-injector,” we have successfully synthesized carbide/nitride multilayer coatings based on W and Nb in a dynamically changing atmosphere of nitrogen and acetylene gases [33]. We reported on the deposition strategy of the multilayer with nanometer layer thicknesses and preliminarily assessed the microstructure, proving the formation of nanoscale multilayer coatings on a stainless-steel substrate.

This study investigated the structural and compositional evolution of monolayer WNbN and multilayer WNbN/WNbC coatings, deposited using cathodic arc evaporation (CAE-PVD). The influence of key deposition parameters – specifically the substrate bias voltage (-50 V to -200 V) and cathode arc current ($130 - 150$ A for W and $110 - 120$ A for Nb) – was systematically explored. This work emphasized how controlled process tuning can be used to tailor the microstructure, phase constitution, and elemental distribution of these coatings, paving the way for multifunctional applications in demanding environments such as cutting tools or plasma-facing components.

EXPERIMENTAL DETAILS

Substrate Preparation

The main goal of preparing the substrate is to enhance its receptiveness to the coating layer, which is crucial for effective interfacial bonding. This process includes steps to remove contaminants from substrate preprocessing and

address surface defects through proper profiling. Figure 1 vividly depicts the sequence of these essential processes, highlighting their importance in achieving a superior finish.

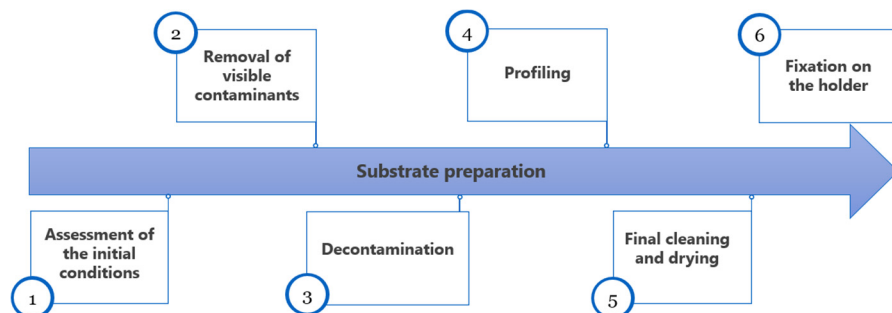


Figure 1. Steps for preparing substrates for coating deposition via the CAE-PVD method

Initially, an evaluation of the surface condition of the substrate was conducted to identify the presence of visible loose oxide layers, such as metallic rust species commonly found in tool steels, as well as dust particles and organic contaminants. Any accumulated dust was effectively eliminated using air blowing techniques. Subsequently, the substrate underwent a decontamination procedure, which is specifically designed to eliminate various contaminants, including grease, oils, chlorides, oxides, and hydrocarbons, from the substrate's surface. The presence of these contaminants, even in trace amounts, can significantly impair both the adhesion of coatings and the resultant properties of the substrate. The decontamination of the substrate was performed utilizing ultrasonic cleaning processes with alcohol. It is pertinent to note that even with the use of high-purity decontaminants, it remains impossible to achieve a completely contaminant-free substrate, primarily due to the existence of oxygen-containing species within the atmosphere. These oxide contaminants possess elevated surface energy and have a tendency to absorb additional contaminants with lower energy levels, particularly hydrocarbons, as a mechanism to reduce their surface energy. Nevertheless, these contaminants were subsequently removed through an etching process prior to the deposition of the coating. Figure 2 illustrates a typical decontamination process of the substrate surface prior to its fixation on the holder inside the deposition chamber.

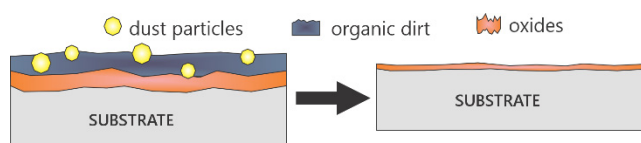


Figure 2. Decontamination process of the substrate surface for coating deposition via the CAE-PVD method

The subsequent step involves profiling the decontaminated substrate. This phase is critical in determining the degree of mechanical interlocking and chemical bonding of the coating to the substrate. The profiling of the substrate was accomplished through mechanical grinding and polishing methodologies. It utilized SiC grinding papers and polishing with a suitable medium, such as diamond suspensions with different particle sizes. Consequently, the resulting substrate profile was contingent upon the grit size of the SiC papers and the particle size of the polishing media. Mechanical profiling primarily focuses on achieving a face profile with minimal surface defects, including micro-cracks. Furthermore, it is imperative to exercise caution to prevent the induction of additional residual stresses in the substrate, as these can adversely affect the adhesion of the coating. Upon completion of substrate profiling, it is necessary to perform an additional cleaning of the substrates to remove any contaminants from the profiling process. The ultrasonic cleaning with a detergent, followed by thorough rinsing with deionized water, were applied. Finally, ensuring the substrate was dried before coating deposition is of utmost importance to mitigate the formation of pinholes.

Deposition Process

The series of operations involved in the deposition of coatings via the CAE-PVD method is illustrated in Figure 3. A comprehensive understanding of the sequence of processes and the principles underlying the deposition technique is crucial for enhancing coating quality and optimizing the resultant tribological performance. The process was initiated by loading appropriately prepared substrates into the deposition chamber. The distance maintained between the cathodes and substrates was 250 mm, thereby minimizing the impact of radiant heating during the evaporation process. Subsequently, the ramp-up stage commenced. It involved the preparation of the vacuum chamber for the cleaning process, elevating the temperature, and ultimately proceeding to the deposition stage. The chamber evacuation is imperative to inhibit gaseous contamination during the coating deposition. Consequently, a vacuum range of ($10^{-3} \div 10^{-4}$) Pa was established within the chamber. This stage was succeeded by heating to temperatures reaching 500 °C, serving as a precursor to the etching process.

The pre-treatment stage involved the removal of substrates' contaminants, which may be present, through a process known as plasma etching, where ions are utilized for bombardment. During the etching and subsequent coating deposition

stages, it is imperative to rotate the substrates to ensure uniformity in these processes. The primary objective of the etching procedure is to eliminate residue contaminants resulting from the decontamination process. This etching was executed using metal ion plasma. In this context, a high-speed plasma comprising metal ions from the targets was directed towards a highly negatively biased substrate (1000 V) for 5 minutes. This procedure induced the sputtering of surface contaminants and activated a superficial layer on the substrates' surfaces. The heating applied during this process is intended to facilitate the transport of etching species. At the same time, the high substrate biasing promoted the sputtering of surface contaminants and prevented the incorporation of the etching species within the substrate. In addition to decontamination, this process also led to roughening the substrate's surface, thereby enhancing the interlocking between the coating and the substrate. Following the etching process, the evacuation of gaseous contaminants occurred, and the vacuum conditions were re-established in preparation for the deposition of the coatings.

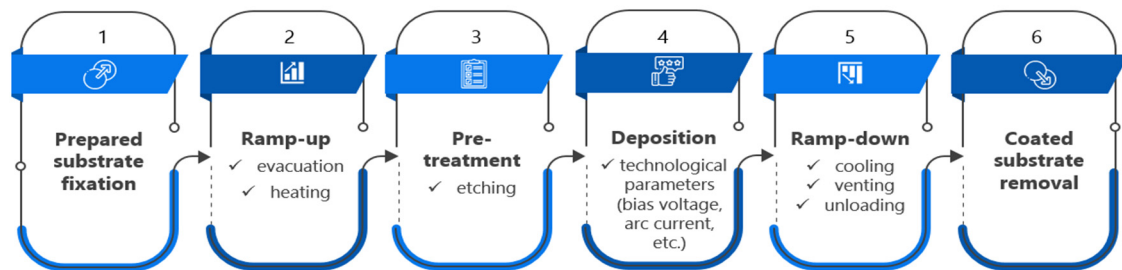


Figure 3. Operations in coating deposition via the CAE-PVD method.

Figure 4 illustrates the configuration of the CAE-PVD unit employed for deposition the coatings in this study. The monolayer and multilayer coatings were deposited by alternating technological parameters, as shown in Table 1. The deposition process was initiated with the evaporation of coating atoms from the target, achieved by initiating an arc on the cathode. The arc initiation was facilitated through a trigger arc generated by applying high voltage to an auxiliary electrode, which is typically positioned near the cathode surface. The behavior of the arc was influenced by various properties of the cathode, including its geometry, material composition, and purity level. Concentrated on the surface of the cathode, the generated arc gave rise to non-stationary micro-spots, referred to as cathode spots, on the target.

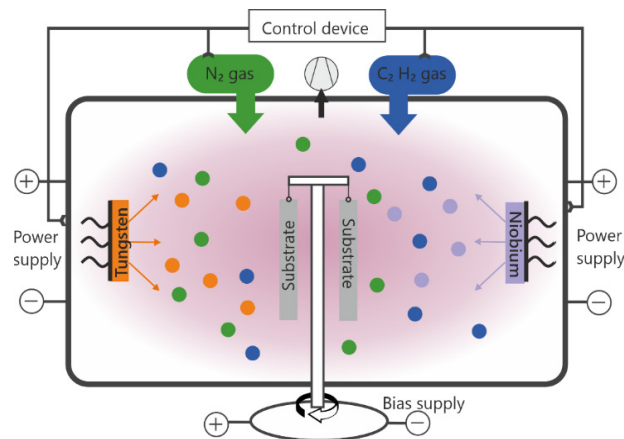


Figure 4. Schematic representation of the CAE-PVD unit used for coating deposition

Table 1. Deposition parameters of the experimental coatings.

Cathodes material	Substrate material	Coating	Arc current <i>I</i> _d , A	Bias voltage <i>U</i> _b , V	Gas composition	Gas pressure <i>P</i> , Pa
W 99.97 wt. % Nb 98.2 wt. %	12X18H9T (15 × 15 × 2.5 mm)	1-WNbN/WNbC	130/120	−200	N ₂ /C ₂ H ₂	0.4
		2-WNbN/WNbC	150/110			
		3-WNbN/WNbC	150/115			
		1-WNbN	120/90	−200	N ₂	
		2-WNbN	130/130	−100		
		3-WNbN	130/120	−50		

The elevated current density observed at the cathode spot induces erosion, resulting in localized melting, ionization, and evaporation of the cathode materials. The reactive gases, namely nitrogen and acetylene, introduced into the deposition chamber, underwent activation by the plasma, leading to their dissociation into ions and additional electrons. Subsequently, the plasma was transported to the substrate. The particles within the plasma traversed at varying velocities,

contingent upon their atomic mass and energy. Upon reaching the surface of the substrate, the plasma volume adjacent to the substrate experienced a depletion of plasma species. Due to the superior mobility of electrons, they were lost at a comparatively accelerated rate, consequently establishing a potential difference between the substrate and the plasma. This phenomenon necessitated the implementation of a negative substrate bias to expedite the acceleration of positive coating ions toward the substrate, thereby enhancing the deposition rate. Following this process, the plasma species condensed onto the surface of the substrate. The ramp-down stage followed this. It entailed cooling and the safe unloading of the machine, ensuring that neither the film nor the desired substrate hardness was compromised. Furthermore, the chamber required cooling facilitated by cold water. Ultimately, the coated substrates were removed from the deposition chamber, and venting was employed to restore the vacuum chamber to ambient pressure.

RESULTS

Microstructural Evolution

Understanding the microstructural evolution processes in coatings deposited by the CAE-PVD method is crucial for enhancing tribological performance. This process begins with mobile coating atom species, known as adatoms, condensing on the substrate surface, leading to nucleation, nuclei growth, the establishment of the "coating–substrate" interface, and ongoing film growth. Figure 5 illustrates these stages. Initially, adatoms condense on the substrate surface. During this condensation, the adatoms lose energy from colliding with others, forming chemical bonds with the substrate's surface atoms, or impacting adatoms already bonded to the substrate. Preferential sites for incoming adatoms typically include surface defects or impurities. At this phase, the movement of adatoms is primarily influenced by bond strength. After condensation, nucleation occurs, with each condensing adatom acting as a site for further coating growth. The nucleation of coating atoms is significantly affected by the substrate's crystal structure, binding energy of adatoms, contaminants, and surface profile. Following nucleation, the growth of nuclei involves bonding between formed nuclei and incoming adatoms or pre-existing condensed adatoms via surface diffusion. This growth results in the creation of randomly oriented islands, which subsequently coalesce to form the interfacial region.

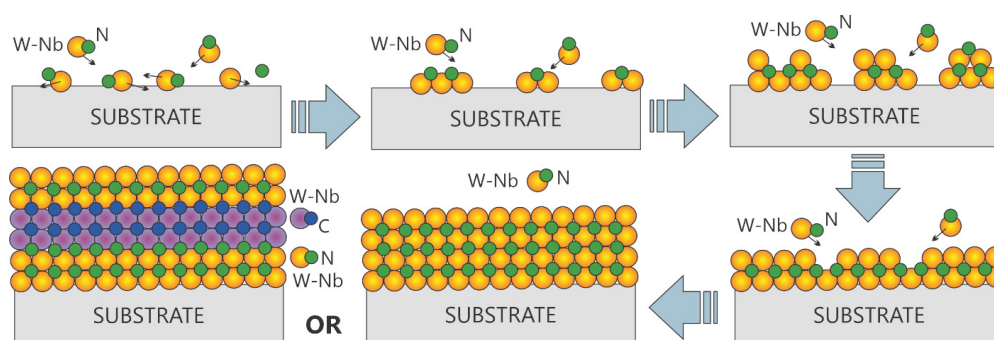


Figure 5. Schematic diagram depicting the microstructural evolution during the formation of the coatings via CAE-PVD method: adatom condensation → nucleation → nucleus growth → interface development → continuous film formation

Subsequent to the formation of the interface, the phase of continuous film growth commenced. This phase is characterized by the ongoing nucleation of the condensing adatoms at the interface, accompanied by perpetual growth, wherein previously deposited coating species are consistently enveloped by incoming ones. Throughout this process, grain coarsening occurs, as evidenced by the coalescence of the islands. The primary impetus for the migration of island boundaries is the imperative to minimize edge and surface energies, whereby islands with lower energy densities assimilate those with higher densities. This process is highly competitive, as crystallographic planes exhibiting higher densities are favored, resulting in accelerated growth compared to less dense planes. The disparity in growth rates among various crystallographic planes engenders a nonuniform coating surface morphology, thereby contributing to the increased surface roughness of the deposited coating. This phenomenon is particularly pronounced when the flux of incoming adatoms is oblique or when the adatoms possess low energy. Under these specific conditions, the influence of geometric shadowing becomes significantly pronounced, with the peaks of the rapidly growing planes capturing the entirety of the incoming adatoms, consequently overshadowing the valleys of the slower-growing planes. The resultant microstructure of the experimental coatings is illustrated in Figure 6 and Figure 7.

Figure 6 showcases the cross-sectional views of the monolayer WNbN coatings. The high-resolution images reveal a periodic nanostructure, which may arise from several contributing factors. The first factor pertains to the substrate rotation mode occurring in front of the two cathodes (W and Nb), resulting in alternating W and Nb fluxes during the deposition process. This behavior engenders periodic variations in composition (W-rich ↔ Nb-rich), even within a single monolayer deposition run. The second factor relates to limited interdiffusion, which is attributed to the low substrate temperature. Cathodic arc deposition typically transpires at moderate substrate temperatures. The restricted thermal diffusion inhibits the complete mixing of W and Nb layers during deposition, thereby preserving the compositional modulations resulting from the rotation cycles. This phenomenon further enhances the appearance of a "pseudo-multilayer" structure, despite the deposition being technically classified as monolayer. The third factor involves

high ionization and directionality. During CAE-PVD process, metal ions impinge upon the substrate with high energies and directed patterns. This characteristic can amplify the effects of angular flux discrepancies caused by rotation, contributing to the oscillating composition as deposition progresses. Conversely, SEM observations disclosed noticeable alterations in the microstructure of the WNbN coatings corresponding to decreases in substrate bias voltage. At the lowest applied bias of -50 V, the coating exhibits a distinctly layered structure characterized by sharp and well-defined interfaces, which remain discernible even at relatively low magnification. Columnar features are not prominent, and there is an absence of macroparticles or defects. At this reduced bias voltage, ion bombardment is minimized, resulting in decreased damage and intermixing. This environment facilitates the development of a highly ordered and periodic nanostructure, albeit with reduced density, culminating in a total thickness of 4.4 microns. As the bias voltage was elevated to -100 V, the coating exhibited moderate density accompanied by a smoother periodic nanostructure devoid of visible defects. The emergence of columnar growth was not observed. Re-sputtering effects began to affect the net deposition rate, culminating in a coating thickness of 2.3 microns. At the highest applied bias of -200 V, the morphology of the coating revealed a relatively dense and compact structure with fine, featureless contrast in the low-magnification image, indicative of high atomic packing density. The intense ion bombardment at this bias supplied sufficient energy to facilitate continuous re-nucleation and surface reorganization, resulting in enhanced packing density and superior structural cohesion. However, this energetic environment also induced significant re-sputtering of lighter elements, such as nitrogen, which diminished the overall deposition rate. Consequently, the final observed coating thickness was 3.2 microns. The interface between the coating and the substrate appeared sharply defined due to enhanced surface activation and improved adhesion under conditions of high-energy ion irradiation.

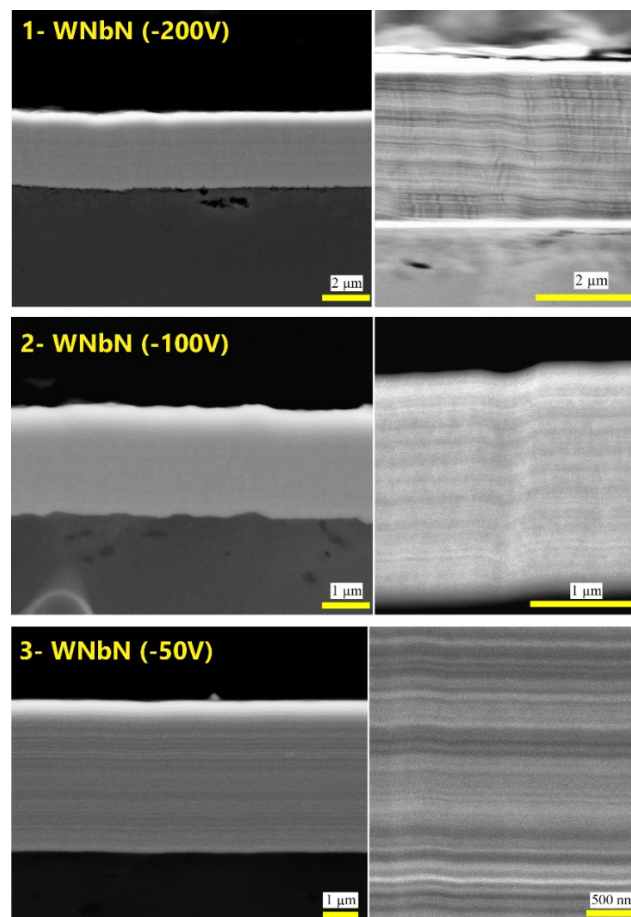


Figure 6. The cross-section structures of the monolayer WNbN coatings

Figure 7 illustrates the images depicting the surface morphology and cross-sectional architecture of the multilayer WNbN/WNbC coatings. All coatings demonstrate well-defined multilayer structures, which indicate successful modulation between the WNbN and WNbC layers. The periodicity and continuity of the layers were maintained under all deposition conditions, despite variations in arc current and bias voltage. The implementation of substrate rotation facilitated consistent deposition coverage and minimized shadowing effects. In the case of the multilayer 1-WNbN/WNbC coating, the surface reveals a relatively rough texture. The presence of structural defects such as cracks or delamination is not prominent, suggesting acceptable coating adhesion. While the multilayer architecture is discernible, it is less regular compared to alternative coatings. The total thickness of the multilayer region is approximately 423 nanometers. Some localized intermixing at the interfaces may be attributed to the lower W cathode current and the elevated Nb content. The

application of a higher bias voltage (-200 V) results in a denser structure but an increase in surface roughness due to intense ion bombardment and re-sputtering effects. In contrast, the multilayer 2-WNbN/WNbC coating exhibits a smoother surface than the previous coating, with fewer surface defects. This may be ascribed to the higher W cathode current, which promotes ionization and deposition uniformity. A highly regular multilayer structure is observed, with distinctly defined alternating layers and a total measured thickness of approximately 855 nanometers. The interfaces between the layers are sharper, indicating enhanced phase separation between nitride and carbide phases. The elevated W current of 150 A, in conjunction with intense ion bombardment, encourages a columnar, compact structure characterized by well-formed layer periodicity. This implies improved kinetic energy and momentum transfer during the alternating deposition cycles. The multilayer 3-WNbN/WNbC coating exhibits a refined structure characterized by large polygonal salients observable across the surface. The formation of droplets is less conspicuous, and the surface presents a more compact and smooth appearance, signifying diminished ion-induced surface damage attributed to the reduced bias voltage of -100 V. A distinctly ordered multilayer structure is apparent, with well-defined layer boundaries and a total measured thickness of approximately 583.5 nm. The layers appear thinner and more uniform, indicating controlled deposition occurring under moderate ion energies. The reduction in bias voltage from -200 V to -100 V leads to diminished re-sputtering and more precise layer formation. The elevated tungsten content, resulting from the 150 A arc current, is anticipated to slightly exceed that of niobium, while the structural modulation remains periodic and stable.

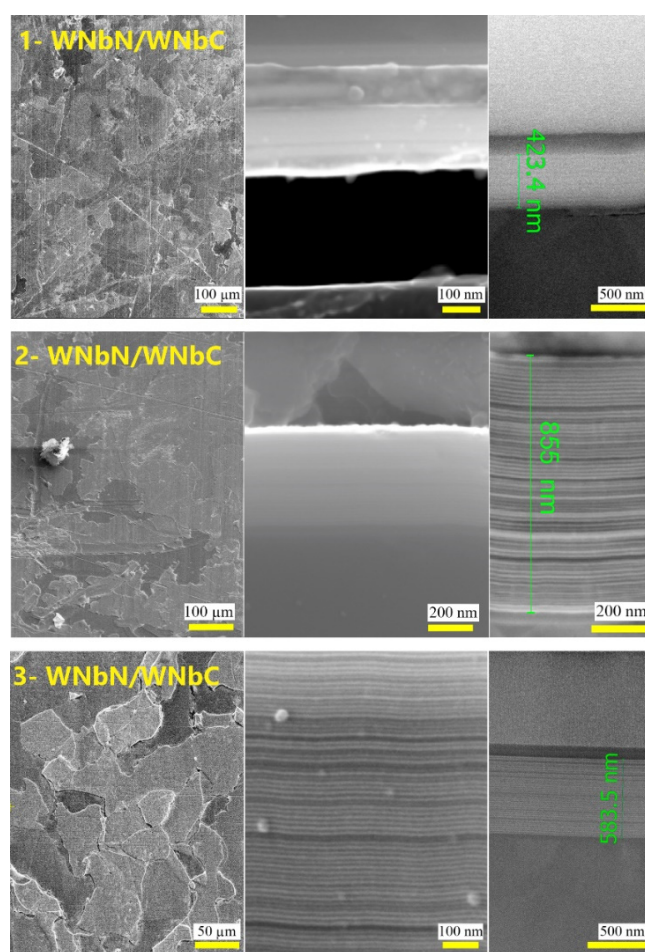


Figure 7. The surface and cross-section structures of the multilayer WNbN/WNbC coatings

These observations emphasize the critical importance of substrate bias in modulating the microstructural evolution of monolayer WNbN and multilayer WNbN/WNbC coatings during the CAE-PVD deposition. Adjusting the ion energy makes it feasible to attain an optimal equilibrium between coating density, grain refinement, and stoichiometry, achieving targeted functional performance.

Elemental Composition

The elemental composition of the multilayer WNbN/WNbC coatings is significantly influenced by the deposition parameters utilized during the CAE-PVD process. Comparative diagrams illustrating the elemental concentration in the multilayer WNbN/WNbC coatings are presented in Figure 8. It is apparent that the relative abundance of nitrogen in relation to carbon within the multilayer structure is primarily dictated by the ion bombardment energy, which is influenced by the substrate bias voltage.

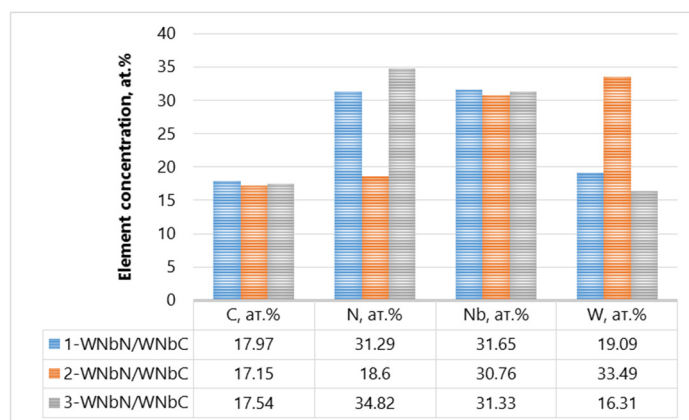


Figure 8. Elemental concentration diagrams of the multilayer WNbN/WNbC coatings

At an elevated bias voltage of -200 V, the increased ion energy facilitates the re-sputtering of lighter elements such as nitrogen and carbon. Although nitrogen atoms possess a lower atomic mass and higher volatility compared to carbon, rendering them more prone to re-sputtering, the deposition duration for the nitride layer was substantially longer than that for the carbide layers ($N_2 = (55 \div 90)$ s, $C_2H_2 = (5 \div 10)$ s). Consequently, under these conditions, it is anticipated that nitrogen will dominate over carbon in the multilayer structure. Upon the reduction of the bias voltage to -120 V, there is a notable decrease in the intensity of ion bombardment, which facilitates an enhanced retention of nitrogen, especially within the WNbN layers. Consequently, although carbon is anticipated to be more predominant overall, the relative nitrogen content is expected to rise as the bias voltage decreases as a result of diminished re-sputtering losses.

The relative concentrations of tungsten (W) and niobium (Nb) are significantly affected by both their respective arc current settings and inherent properties, including atomic mass and ionization efficiency. At an elevated arc current of 150 A for the W cathode, as opposed to 130 A, the W ion flux exhibits a substantial increase, facilitating elevated tungsten deposition rates. Concurrently, the arc current applied to the Nb cathode is comparatively lower, either 110 A or 120 A, which diminishes the niobium ion density within the plasma. Notably, the observed Nb concentration is remarkably high, ranging from 30.76 to 31.65 at. %, in relation to W (16.31 and 19.09 at. %). This phenomenon can be explicated by two principal factors: increased macroparticle emission and the interplay of tungsten's ionization energy and ion charge states. The first factor posits that the W cathode is recognized for its propensity to emit a greater volume of macroparticles (i.e., droplets) owing to its higher melting point and unique vaporization behavior. These macroparticles typically fail to integrate into the developing coating and may adhere to the chamber walls or accumulate within the system, consequently resulting in a net depletion of W content in the deposited coating when juxtaposed with Nb. The second factor underscores that tungsten possesses a higher ionization energy than niobium; in cathodic arc scenarios, this disparity can lead to a reduced fraction of multiply charged W ions. Consequently, Nb ions, being less heavy and more readily ionized, may prevail in the plasma and reach the substrate with greater efficiency, particularly when the substrate bias applied is insufficient to attract the heavier, less mobile W ions.

A trade-off outcome is observed for the multilayer 2-WNbN/WNbC coating. The tungsten ions possess greater mass and momentum, resulting in a higher probability of incorporation into the film, particularly under elevated substrate bias conditions of -200 V, which increases ion impact energy. This advantage is further enhanced by the higher arc current applied to the tungsten cathode. Consequently, under both bias conditions, especially at -200 V and an arc current of 150 A, tungsten (33.49 atomic percent) predominates over niobium (30.76 atomic percent) in the coating composition.

The elemental composition of monolayer WNbN coatings was found to be significantly affected by the applied substrate bias voltage. Monocoatings were deposited in a rotational substrate mode using dual metallic cathodes (tungsten and niobium) in the presence of nitrogen as the reactive gas. The substrate bias voltage was varied between -200 V, -100 V, and -50 V to examine its influence on the resulting coating composition. Comparative diagrams illustrating the elemental concentration in the monolayer WNbN coatings are shown in Figure 9.

At a higher bias voltage of -200 V, the intensified ion bombardment led to substantial re-sputtering of lighter elements such as nitrogen and carbon from the coating surface. This phenomenon resulted in metal-rich coatings with a potential shift toward sub-stoichiometric compositions, particularly in nitrogen-deficient $WNbN_x$ phases. Although a higher substrate bias (-200 V) is typically associated with enhanced incorporation of heavier elements like tungsten due to increased ion momentum, the observed composition of the WNbN coating shows a higher Nb content. This discrepancy is likely attributed to a combination of factors, including the higher ion flux and better ionization efficiency of Nb under cathodic arc conditions, greater erosion rate of Nb cathodes, and possibly less efficient incorporation or greater re-sputtering of tungsten ions. Additionally, geometric factors such as substrate positioning and the relative plasma exposure during rotation may have further favored Nb accumulation. These effects, taken together, resulted in the Nb-rich WNbN coating despite the applied high bias voltage.

Upon the reduction of the bias voltage to -100 V, the re-sputtering effect diminished significantly, thereby enhancing the retention of nitrogen within the developing coating. This condition facilitated the formation of coatings that are closer

to stoichiometric compositions, characterized by a more balanced ratio of metal to nonmetal. The relative incorporation of niobium increased as the disparity in ion kinetic energies between tungsten (W) and niobium (Nb) decreased.

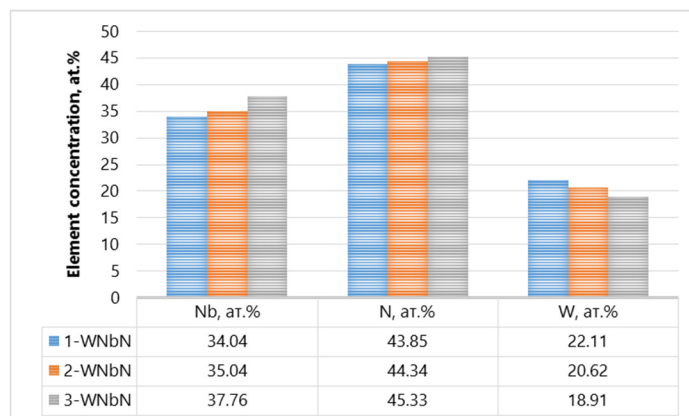


Figure 9. Elemental concentration diagrams of the monolayer WNbN coatings

At the minimal bias voltage of -50 V, the bombardment of ions was reduced, leading to the highest levels of nitrogen incorporation across all examined technological conditions. Although this promoted nearly ideal stoichiometry, it concurrently heightened the risks associated with the over-saturation of the non-metallic element. In the case of WNbN coatings, this may result in the development of nitrogen-rich amorphous regions or secondary nitride phases. Furthermore, a decrease in the incorporation of tungsten was noted, attributed to the diminished contribution of heavy metal ions within this lower ion energy regime.

In summary, increasing the substrate bias voltage leads to metal-enriched coatings with higher Nb content and reduced nitrogen concentration, while lower bias values promote more stoichiometric compositions and higher niobium content. These compositional variations are expected to strongly influence the resulting structural properties of the coatings, as discussed in the abovementioned sections.

Phase Evolution

Figure 10 presents the X-ray diffraction patterns of the monolayer WNbN coatings. All diffraction patterns exhibit broad peaks in the 2θ range of $30^\circ - 80^\circ$, indicating nanocrystalline or fine-grained structures.

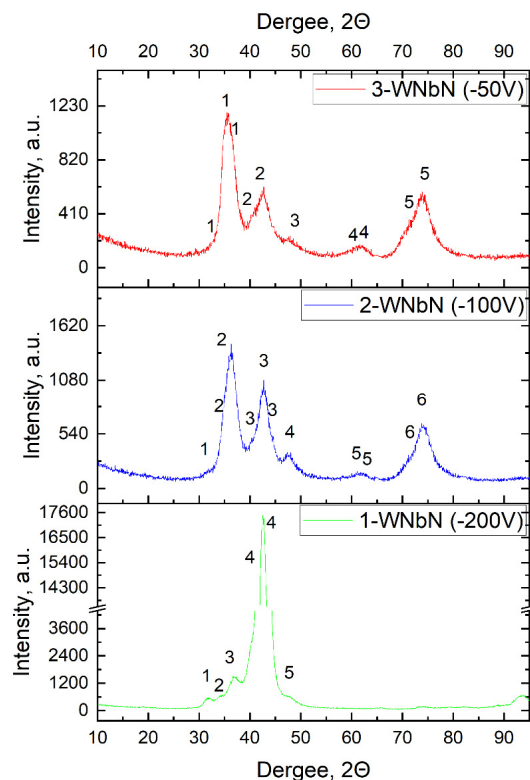


Figure 10. Diffraction patterns of the monolayer WNbN coatings

The most intense peaks are located around $\sim 36.5 - 37^\circ$ (2 θ), $\sim 42.5 - 43^\circ$ (2 θ), $\sim 62.5 - 63^\circ$ (2 θ), and $\sim 70 - 80^\circ$ (2 θ) (see Table 2). These peaks can be attributed to the face-centered cubic WNbN phase (NaCl-type structure), which is consistent with δ -WN (PDF #25-1257) and δ -NbN (PDF #38-1155). The presence of peaks in the range $\sim 31.6 - 33.6^\circ$ (2 θ), $\sim 46.8 - 47.4^\circ$ (2 θ), and $\sim 60.38^\circ$ (2 θ) suggests the formation of minor hexagonal nitride phase W_2N and/or Nb_2N , which is consistent with hexagonal W_2N (PDF #25-1256) and hexagonal Nb_2N (PDF #17-0381).

Table 2. Peak list and identification for the monolayer WNbN coatings.

	Peak no.	Position 2 θ (°)	Phase	Crystal System	Plane (hkl)	d-spacing
1-WNbN (–200 V)	1	31.77	W_2N / Nb_2N	hex	(100)	2.8136
	2	33.63	W_2N / Nb_2N	hex	(101)	2.6622
	3	37.01	WNbN solid solution (W-rich)	cubic	(111)	2.4266
	4	39.90	W_2N or Nb_2N	hex	(102)	2.2574
	4	42.50	WNbN solid solution (W-rich)	cubic	(200)	2.1252
	5	46.80	W_2N / Nb_2N	hex	(103)	1.9388
2-WNbN (–100 V)	1	31.64	W_2N / Nb_2N	hex	(100)	2.8250
	2	34.95	WNbN solid solution (Nb-rich)	cubic	(111)	2.5650
	2	36.37	WNbN solid solution (W-rich)	cubic	(111)	2.4680
	3	40.15	WNbN solid solution (Nb-rich)	cubic	(200)	2.2436
	3	42.60	WNbN solid solution (W-rich)	cubic	(200)	2.1204
	3	44.37	WNbN solid solution	cubic	(210)	2.0395
	4	47.45	Nb_2N / W_2N	hex	(104)	1.9144
	5	60.38	Nb_2N / W_2N	hex	(110)	1.5316
	5	62.01	WNbN	cubic	(220)	1.4955
	6	70.78	WNbN solid solution (Nb-rich)	cubic	(311)	1.3298
	6	74.00	WNbN solid solution (W-rich)	cubic	(311)	1.2798
3-WNbN (–50 V)	1	34.75	NbN	cubic	(111)	2.5793
	1	35.65	Nb_2N / W_2N	hex	(101)	2.5162
	1	36.90	WNbN solid solution (W-rich)	cubic	(111)	2.4338
	2	40.04	WNbN solid solution (Nb-rich)	cubic	(200)	2.2496
	2	42.40	WNbN solid solution (W-rich)	cubic	(200)	2.1299
	3	47.73	Nb_2N / W_2N	hex	(104)	1.9036
	4	60.35	Nb_2N / W_2N	hex	(110)	1.5323
	4	62.23	WNbN (solid solution)	cubic	(220)	1.4904
	5	70.32	WNbN solid solution (Nb-rich)	cubic	(311)	1.3375
	5	73.75	WNbN solid solution (W-rich)	cubic	(311)	1.2836

The substrate bias voltage is crucial in determining the crystalline quality and grain size of monolayer WNbN coatings obtained using CAE-PVD. The low bias of –50 V results in lower energy ion bombardment, leading to lower adatom mobility and less recrystallization, producing a fine-grained (nanocrystalline) structure of the monolayer 3-WNbN coating. The first broad peak with overlapping contributions in the region of 34.75° , 35.65° , and 36.9° (2 θ) suggests the presence of multiple overlapping crystallographic planes from different phases or orientations. This is very common in nanocrystalline and multiphase nitride coatings, especially those produced by CAE-PVD. The peak at 34.75° (2 θ) is assigned to the (111) plane of cubic NbN. It suggests the presence of Nb-rich cubic domains within the WNbN solid solution or a segregated cubic NbN phase forming at Nb-dominant growth points (due to arc rotation or target flux variation). The main peak at 35.65° (2 θ) refers to hexagonal Nb_2N or W_2N with (100) reflection. The peak at 36.9° (2 θ) corresponds to the (111) plane of cubic WN and suggests the W-rich domain in the WNbN solid solution. Another broad but less intensive peak centered around 40.04° and 42.4° (2 θ) is a superposition of (200) reflections from both W-rich and Nb-rich regions in the cubic WNbN solid solution. The peak at $\sim 40.04^\circ$ (2 θ) strongly refers to (200) reflection of cubic NbN or a region of the WNbN solid solution that is locally enriched in Nb. The peak at $\sim 42.4^\circ$ (2 θ) is strongly assigned to the (200) reflection of cubic WN or W-rich region within the cubic WNbN solid solution. The peak at

47.73° (2 θ) refers to minor hexagonal Nb₂N or W₂N (104), which may form in N-deficient regions. A broad and least intensive peak in the 60.3° to 62.2° (2 θ) range is a key signature of overlapping reflections from cubic WNbN and potentially minor hexagonal nitride phases. The peak at 60.35° (2 θ) is most likely hexagonal W₂N or Nb₂N (110). The peak at 62.23° (2 θ) is strongly assigned to the cubic WNbN solid solution with (220) reflection. The broad peak between 70.32° and 73.75° (2 θ) is a composite peak, most likely originating from overlapping reflections of cubic and hexagonal phases. The peak at 70.32° (2 θ) refers to cubic NbN (311) or a Nb-rich region in the WNbN solid solution. The peak at 73.75° (2 θ) corresponds to cubic WN (311) or a W-rich region in the WNbN solid solution.

The increase of bias voltage to -100 V causes a slightly higher ion bombardment, enhancing surface diffusion, promoting crystal growth, and increasing grain size. Therefore, the monolayer 2-WNbN coating formed with improved crystallinity with more defined peaks. The small peak positioned at 31.64° (2 θ) indicates the formation of minor hexagonal W₂N or Nb₂N phases with (100) reflection. The main broad peak consists of two overlapping contributions in the region of 34.95° and 36.97° (2 θ). The peak at 34.95° (2 θ) strongly corresponds to cubic (111) WNbN solid solution enriched with Nb. The peak at 36.97° (2 θ) refers to cubic (111) WNbN solid solution enriched with W. Another broad but less intensive peak centered around 40.15° and 42.60° (2 θ) is a superposition of (200) reflections from both W-rich and Nb-rich regions in the cubic WNbN solid solution. The peak at 44.37° (2 θ) is the (210) reflection of cubic WNbN solid solution, typical in highly oriented or dense coatings. The peak at 47.45° (2 θ) refers to minor hexagonal Nb₂N or W₂N phases with (104) reflection. Its presence supports the presence of small amounts of secondary phases or that finer structural details are being resolved. A broad peak in the 60.38° to 62.01° (2 θ) range is composed of the overlapping reflections from cubic and potentially minor hexagonal nitride phases. The peak at 60.38° (2 θ) refers to the hexagonal W₂N or Nb₂N (110). The peak at 62.01° (2 θ) is strongly assigned with cubic WNbN (220). The broad peak between 70.78° – 74.0° (2 θ) refers to WNbN solid solution with (311) reflection, which is consistent with other major reflections (111), (200), (220), and broaden by the composition (Nb- and W-rich regions).

At high bias voltage of -200 V, the intense ion bombardment may cause the densification and possibly stress-induced recrystallization. It results in larger grains and sharper diffraction peaks. The extremely high intensity may also be influenced by preferred orientation effects (texture). The diffraction peak at ~31.77° (2 θ) indicates the formation of hexagonal W₂N (or Nb₂N) as a minor phase in the monolayer 1-WNbN coating. These phases can both exhibit peaks in the 31 – 32° (2 θ) range, specifically, W₂N (100) → ~31.6 – 31.8° (2 θ) and Nb₂N (100) → ~31.5 – 31.7° (2 θ), and may form as secondary or surface-stabilized phases in nitrogen-deficient regions, especially under high-energy deposition conditions typical for CAE-PVD process. The peak at 33.63° (2 θ) also supports the earlier assumption of minor hexagonal phase presence with (101) reflection. The peak at 37.01° (2 θ) is highly consistent with the (111) reflection of a cubic WNbN solid solution phase, where W and Nb are substitutional, and the lattice parameter lies between that of WN and NbN. The peak at 39.9° (2 θ) refers to the presence of the hexagonal phase with (102) reflection. The main peak between at 42.5° (2 θ) is the (200) peak of the cubic WNbN solid solution. The peak at 46.8° (2 θ) assigned to hexagonal nitride with (103) reflection, supporting the presence of minor W₂N/Nb₂N phases.

Based on the (111)/(200) reflections at ~36.5° – 43° (2 θ), a qualitative trend in grain size was estimated as follows. The monolayer 3-WNbN coating has the smallest grain size in the range of ~5 – 7 nm, the monolayer 2-WNbN coating has moderate grain growth with sizes of ~10 – 12 nm and the monolayer 1-WNbN coating has the largest grain size ranging between ~15–20 nm.

Thus, the monolayer 3-WNbN and 2-WNbN coatings strongly supports the presence of a cubic NaCl-type WNbN structure, with minor hexagonal contributions that may reflect local composition variation or grain boundary effects. The deposition of the coatings at low (-50 V) and moderate (-100 V) bias voltage results in nanocomposite structures of the coatings with nanocrystalline nitride grains (~5 – 12 nm). The monolayer 1-WNbN coating is dominantly cubic WNbN with bigger contributions from hexagonal phases, indicating possible formation of W₂N or Nb₂N in local regions – potentially from N-deficient zones, or interfacial effects during high-energy deposition. The increase of bias voltage to -200 V produce the grains growth to larger sizes of ~20 nm and formation of the strong texture.

Figure 11 presents the X-ray diffraction patterns of the multilayer WNbN/WNbC coatings. All diffraction patterns exhibit distinct broadening and overlapping peaks in the 2 θ range of 30° – 80°, indicating the presence of nanocrystalline and multiphase structures. The most intense peaks are located at ~36 – 38° (2 θ), 43 – 44.5° (2 θ), 62–64° (2 θ), and 70–80° (2 θ) (see Table 3). The observed peaks can be ascribed to the cubic WNbN phase (NaCl-type structure), which aligns with cubic WN (PDF #25-1257) and cubic NbN (PDF #38-1155), along with the WNbC phase, which likely exhibits a cubic B1-type structure (cubic WC - PDF #89-2868 and cubic NbC - PDF #38-1364). Additionally, low-intensity or broad peaks located near 31.6°, 33.6°, and 37.0° (2 θ) may suggest the existence of hexagonal W₂N and Nb₂N as secondary phases, corresponding with hexagonal W₂N (PDF #25-1256) and hexagonal Nb₂N (PDF #17-0381). This phenomenon is particularly pronounced for the 3-WNbN/WNbC coating obtained under reduced bias conditions, where diminished ion energy is conducive to mixed-phase formation.

Lower arc currents (130/120 A) and a high bias voltage (-200 V) facilitate the formation of fine grains through enhanced re-sputtering and densification processes for the multilayer 1-WNbN/WNbC coating. The peak occurring at 31.55° (2 θ) is ascribed to the (100) reflection of hexagonal W₂N or Nb₂N, indicating the existence of under-stoichiometric nitride phases at specific interfaces or resulting from localized nitrogen deficiency during the deposition cycle. The peak observed at 35.69° (2 θ) corresponds to the (111) reflection of cubic NbC or cubic WC, suggesting the development of

carbides during the acetylene-assisted segments of the deposition. Given the slightly lower W arc current in this sample, it is anticipated that the NbC contribution will predominate. A broad peak at 39.70° (2θ) is associated with the (111) plane of a cubic WNbN solid solution with a high Nb content, which embodies the predominant structure of the nitride layers. This NaCl-type phase is indicative of transition metal nitrides formed under energetic deposition conditions. The weak reflection at 42.95° (2θ) likely encompasses contributions from (200) reflection of cubic WNbN solid solution with a high W content, reinforcing the existence of the cubic nitride phase in conjunction with the (111) reflection. The broadness of the peak is attributed to nanocrystallinity. The peak at 44.75° (2θ) aligns with the (200) reflection of cubic NbC or WC phases, further supporting the formation of well-structured carbide layers. At 47.63° (2θ), the (200) reflection of minor hexagonal Nb₂N or W₂N phases with (104) reflection.

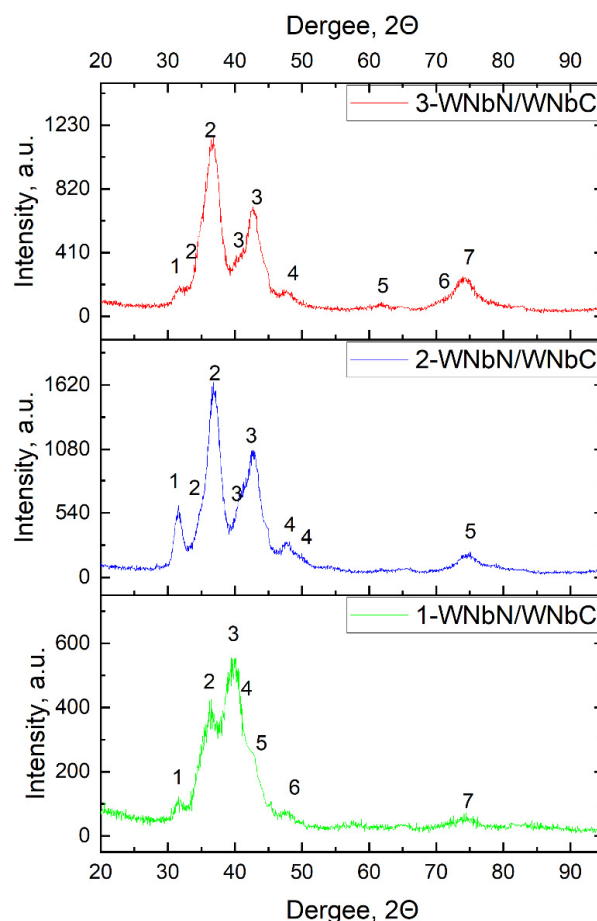


Figure 11. Diffraction patterns of the multilayer WNbN/WNbC coatings

The overall peak broadness indicates a nanocrystalline structure, with crystallite sizes estimated to be in the 6–8 nm range using the Scherrer equation. The relatively lower W arc current (130 A) may have contributed to a slightly reduced metal flux, which limits adatom mobility and suppresses grain growth. Meanwhile, the high substrate bias (–200 V) enhances surface densification and re-sputtering, promoting finer grain sizes and more uniform layer interfaces, albeit at the cost of increased compressive stress and peak broadening.

Table 3. Peak list and identification for the multilayer WNbN/WNbC coatings.

	Peak no.	Position 2θ ($^\circ$)	Phase	Crystal System	Plane (hkl)	d-spacing
1-WNbN/WNbC	1	31.55	Nb ₂ N / W ₂ N	hex	(100)	2.8332
	2	35.69	NbC / WC	cubic	(111)	2.5135
	3	39.70	WNbN solid solution (Nb-rich)	cubic	(111)	2.2683
	4	42.95	WNbN solid solution (W-rich)	cubic	(200)	2.1041
	5	44.75	NbC / WC	cubic	(200)	2.0234
	6	47.63	Nb ₂ N / W ₂ N	hex	(104)	1.9074
	7	74.42	WNbN solid solution	cubic	(220)	1.2731

	Peak no.	Position 2θ (°)	Phase	Crystal System	Plane (hkl)	d-spacing
2-WNbN/WNbC	1	31.45	Nb ₂ N / W ₂ N	hex	(100)	2.8420
	2	34.50	NbC / WC	cubic	(111)	2.5973
	2	36.80	Nb ₂ N / W ₂ N	hex	(101)	2.4402
	3	40.60	WNbN solid solution (Nb-rich)	cubic	(111)	2.2201
	3	42.65	WNbN solid solution (W-rich)	cubic	(200)	2.1180
	4	47.64	Nb ₂ N / W ₂ N	hex	(104)	1.9071
	4	49.80	Nb ₂ N / W ₂ N	hex	(110)	1.8292
	5	74.47	WNbN solid solution	cubic	(220)	1.2729
3-WNbN/WNbC	1	31.75	W ₂ N / Nb ₂ N	hex	(100)	2.8150
	2	34.65	NbC / WC	cubic	(111)	2.5865
	2	36.65	Nb ₂ N / W ₂ N	hex	(101)	2.4498
	3	40.19	WNbN solid solution (Nb-rich)	cubic	(111)	2.2415
	3	42.55	WNbN solid solution (W-rich)	cubic	(200)	2.1228
	4	47.52	Nb ₂ N / W ₂ N	hex	(104)	1.9115
	5	61.63	WNbN	cubic	(220)	1.5034
	6	70.28	WNbN solid solution (Nb-rich)	cubic	(311)	1.3382
	7	74.15	WNbN solid solution (W-rich)	cubic	(311)	1.2776

An increase in tungsten arc current to 150 A coupled with a reduction in niobium arc current to 110 A for the multilayer 2-WNbN/WNbC coating results in the diffraction peaks becoming sharper and more intense. The peak observed at 31.45° (2θ) corresponds to the (100) reflection of hexagonal W₂N or Nb₂N. This peak is indicative of under-stoichiometric or early-stage nitride phases and suggests localized nitrogen-deficient growth, potentially occurring at nitride-carbide interfaces. The reflection located at 34.50° (2θ) likely arises from overlapping contributions from cubic WC or cubic NbC, corresponding to the (111) plane. The formation of these carbides is associated with the acetylene-assisted deposition stages and is enhanced by the elevated W arc current. The prominent peak centered around 36.80° (2θ) is attributed to the (101) reflection of hexagonal W₂N/Nb₂N, although contributions from W₂C cannot be dismissed. This region typically reflects overlapping nitride and carbide signals, particularly within nanostructured multilayers. A weak reflection at 40.60° (2θ) is ascribed to the (111) plane of the cubic WNbN solid solution enriched with Nb, representing the primary signature of a cubic NaCl-type structure, which is common to transition metal nitrides deposited by arc evaporation. The adjacent peak at 42.65° (2θ) can be indexed to the (200) reflection of the cubic WNbN solid solution, thereby confirming the continuity of the cubic nitride structure across multiple stack layers. The peak at 47.64° (2θ) corresponds to the minor hexagonal Nb₂N or W₂N (104), which may form in N-deficient regions. A reflection at 49.80° (2θ) is attributed to the (110) plane of hexagonal Nb₂N or W₂N, further corroborating the presence of hexagonal domains within the coating. These may develop in regions where nitrogen incorporation is kinetically limited or disrupted during gas switching. Lastly, the high-angle reflection at 74.47° (2θ) aligns with the (220) plane of the cubic WNbN solid solution. The discernibility of this peak, despite its typically low intensity, indicates a well-aligned and crystalline cubic nitride phase within specific domains of the multilayer.

The observed peak widths suggest a significant broadening characteristic of nanocrystalline materials. This broadening likely results from a combination of small grain sizes (estimated to be in the range of 10 – 12 nm according to the Scherrer equation), internal microstrain, and the complex chemical modulation intrinsic to multilayer architectures. The elevated arc current on the W cathode (150 A) enhances the flux of metal ions, facilitating denser and more crystalline growth, particularly within the carbide layers. Concurrently, the implementation of a high substrate bias (–200 V) promotes densification and restricts adatom mobility, thus suppressing excessive grain growth while simultaneously increasing compressive stress, which may induce a slight shift in peak positions.

The reduction of the bias voltage to –120 V results in a decrease in ion bombardment intensity, which subsequently limits re-sputtering and fosters grain growth, culminating in an enhancement of crystallinity within both nitride and carbide phases. A series of pronounced yet comparatively broad peaks were detected for the multilayer 3-WNbN/WNbC coating. Specifically, the peak positioned at 31.75° (2θ) is attributed to the (100) reflection of hexagonal W₂N or Nb₂N. This phase indicates under-stoichiometric nitride domains, which may develop during the initial stages of nitride layer formation or within areas of diminished nitrogen activity occurring between gas switching intervals. The reflection observed at 34.65° (2θ) correlates with the (111) or (101) planes of cubic NbC or WC, respectively. These phases typically emerge during the acetylene-assisted deposition phases, particularly under elevated metal ion flux conditions, as

facilitated by the increased W arc current. The peak recorded at 36.65° (2θ) corresponds to the (101) plane of hexagonal W_2N or Nb_2N , potentially overlapping with faint reflections originating from W_2C . Its presence further reinforces the coexistence of minor hexagonal phases, often more stable at lower ion energies. A prominent peak at 40.19° (2θ) aligns with the (111) reflection of the cubic $WNbN$ phase, which characterizes a NaCl-type solid solution comprising WN and NbN . This peak signifies the primary orientation of the nitride phase within the multilayer stack. The peak at 42.55° (2θ) correlates with the (200) reflection of the cubic $WNbN$ solid solution, thereby confirming the existence of a continuous and well-crystallized B1-type structure across the multilayers. The peak at 47.52° (2θ) is interpreted as the minor hexagonal Nb_2N or W_2N phase exhibiting a (104) reflection. The peak at 61.63° (2θ) constitutes a continuation of the cubic series, aligning with the (220) reflection of cubic $WNbN$ (with minor contributions from $WNbC$), thereby reinforcing the observation of a predominant NaCl-type structure throughout the multilayer stack. The reflection noted at 70.28° (2θ) is attributed to the (311) plane of cubic NbN , suggesting the presence of Nb-rich domains within the $WNbN$ solid solution layers or localized segregation resulting from slight fluctuations in plasma composition. Finally, the peak at 74.15° (2θ) corresponds to the (311) plane of cubic WN or $WNbN$, thereby further substantiating the establishment of a well-defined cubic structure and the existence of W-rich zones, potentially influenced by the relatively high W arc current.

The observed diffraction peaks exhibit greater breadth compared to those of bulk materials, while remaining sharper than those present in coatings deposited at increased bias voltages (e.g., 1- $WNbN/WNbC$ and 2- $WNbN/WNbC$). This observation suggests a nanocrystalline structure characterized by enhanced grain growth, which is facilitated by the moderately diminished bias voltage (-120 V). The decrease in ion bombardment energy has permitted increased adatom mobility, subsequently leading to larger crystallite sizes and more distinct phase separation. The average crystallite size, as estimated utilizing the Scherrer equation, falls within the range of $10 - 15$ nm.

The multilayer 1- $WNbN/WNbC$ coating features a mixed-phase nanocrystalline structure primarily composed of cubic $WNbN$ and NbC phases, with smaller amounts of hexagonal W_2N/Nb_2N . The deposition conditions lead to a dense, fine-grained multilayer with overlapping phase domains, resulting in a broad and diffuse XRD profile. The high bias voltage results in densification and stress-induced peak shifts, while moderate arc currents facilitate balanced phase formation throughout the multilayer stack. There is a minor presence of hexagonal phases. The multilayer 2- $WNbN/WNbC$ multilayer coating combines cubic and hexagonal nitride phases. The dominant cubic $WNbN$ and $WNbC/NbC$ forms are substantiated by distinct (111), (200), and (220) reflections, while weaker peaks associated with hexagonal W_2N , and Nb_2N indicate minor phase segregation or localized composition variations. These findings highlight the intricate nature of phase formation in reactive arc-deposited multilayer systems and demonstrate how deposition parameters like arc current, reactive gas switching, and bias voltage affect structural evolution. An increased occurrence of hexagonal phase peaks suggests a reduced energy barrier for non-cubic phases. The multilayer 3- $WNbN/WNbC$ coating displays a well-defined nanocrystalline multilayer structure, dominated by cubic $WNbN$ and $WNbC$ phases (NaCl-type structure), with minor hexagonal W_2N/Nb_2N phases. A moderate bias voltage (-120 V) and high W arc current enhanced grain growth, crystallinity, and phase stability while limiting excessive re-sputtering and decreasing structural defects. There is a minor presence of hexagonal phases. These properties render this coating the most crystalline and structurally coherent among the three $WNbN/WNbC$ multilayer systems studied.

CONCLUSIONS

This study explores the microstructural, compositional, and phase evolution characteristics of both monolayer $WNbN$ and multilayer $WNbN/WNbC$ coatings, which were deposited via cathodic arc evaporation under different process conditions. Three distinct monolayer $WNbN$ coatings and three multilayer $WNbN/WNbC$ coatings were synthesized utilizing dual-metallic cathodes (W and Nb), with nitrogen and acetylene serving as reactive gases. The essential deposition parameters, namely substrate bias voltage and cathode arc current, were methodically altered to investigate their impact on the coating structure, morphology, elemental distribution, and phase composition.

The microstructural analysis of monolayer $WNbN$ coatings demonstrates a significant effect of substrate bias voltage on their evolution during cathodic arc evaporation. A clear pseudo-multilayer structure was observed in all samples, resulting from the interactions between substrate rotation, angular deposition flux from dual cathodes, and limited interdiffusion at moderate deposition temperatures. With low bias (-50 V), the coatings showcased distinct periodic layering, exhibiting minimal columnar growth and high structural order, although with lower density. As the bias increased to -100 V and -200 V, the morphology transitioned to denser, more compact structures, with the highest bias facilitating continuous re-nucleation, enhanced atomic packing, and improved interfacial adhesion. However, higher ion energies led to marked re-sputtering effects, which diminished net deposition rates and slightly affected stoichiometry. These findings underscore the pivotal role of bias voltage in balancing coating morphology, density, and composition – a vital element for optimizing monolayer $WNbN$ coatings for advanced functional uses.

The characterization of multilayer $WNbN/WNbC$ coatings at the morphological and microstructural levels confirmed the effective creation of periodic multilayer structures. The coatings displayed clear alternations between nitride and carbide layers, achieved through substrate rotation and precise gas pulsing. Factors such as arc current and bias voltage impacted layer definition, thickness uniformity, and the sharpness of interfaces. With a -200 V bias, the multilayer 1- $WNbN/WNbC$ and 2- $WNbN/WNbC$ coatings exhibited denser microstructures, though the multilayer

1-WNbN/WNbC had increased surface roughness and interfacial intermixing attributed to a lower W arc current (130 A). Conversely, the multilayer 2-WNbN/WNbC coating, which utilized a higher W arc current (150 A), demonstrated improved phase separation and structural order. On the other hand, the multilayer 3-WNbN/WNbC coating deposited at -120 V showed a smoother surface with well-defined, thinner multilayers, thanks to reduced re-sputtering and enhanced adatom incorporation. Elemental analysis supported these observations, indicating that tungsten content rose with arc current, while nitrogen retention was better at lower bias voltages. Notably, the Nb content consistently surpassed W at lower W arc currents due to greater ionization efficiency and effective plasma transport of Nb atoms.

The structural analysis of monolayer WNbN coatings indicated that the substrate bias voltage significantly influences grain size, phase formation, and the coatings' chemical composition. A low bias voltage of -50 V encouraged the development of nanocrystalline, fine-grained structures, minimizing re-sputtering and enhancing nitrogen incorporation. Consequently, the resulting monolayer WNbN coatings had nearly stoichiometric compositions with slight contributions from hexagonal secondary phases. Increasing the substrate bias to -100 V led to improved crystallinity in the monolayer WNbN coating, as evidenced by sharper, more distinct XRD peaks. The increased surface diffusion from moderate ion bombardment fostered grain growth, revealing a more defined cubic NaCl-type structure, along with recognizable phase separation between W-rich and Nb-rich areas. Although minor hexagonal phase peaks remained, they were less obvious than those observed at lower bias levels. At the extreme bias voltage of -200 V, the intense ion bombardment greatly enhanced film densification, increased re-nucleation frequency, and contributed to surface reorganization. This resulted in the formation of larger grains ($15 - 20$ nm), a well-textured cubic WNbN phase, and a noticeable reduction in nitrogen content due to re-sputtering effects. The occurrence of hexagonal W_2N/Nb_2N became more apparent under these conditions, indicating nitrogen deficiency at elevated ion energies. Furthermore, despite tungsten's substantial atomic mass, Nb-rich compositions were commonly identified, attributed to superior ionization efficiency of Nb, mobility, and angular plasma exposure.

The structural analysis of the multilayer WNbN/WNbC coatings revealed that all coatings predominantly consisted of cubic phases (WNbN and WNbC/NbC), exhibiting NaCl-type B1 structures. Major reflections at (111), (200), (220), and (311) confirmed the formation of well-crystallized cubic domains. The presence of overlapping or broad peaks was attributed to grain size reduction, stress effects, and minor contributions from the hexagonal phase. In the multilayer 1-WNbN/WNbC coating, the high bias and lower W arc current led to the formation of fine-grained, nanocrystalline structures with significant peak broadening and a noticeable hexagonal phase presence. The multilayer 2-WNbN/WNbC coating benefited from increased W ion flux, yielding improved crystalline quality and stronger cubic phase reflections. The multilayer 3-WNbN/WNbC coating demonstrated the most refined multilayer architecture, marked by enhanced crystallinity, reduced stress, and diminished hexagonal phase content, owing to the optimal combination of high W arc current and moderate bias voltage.

This comprehensive investigation highlights the versatility of cathodic arc evaporation for engineering high-performance WNbN/WNbC nanocomposite coatings. The ability to fine-tune bias voltage and arc current provides a powerful mechanism to control morphology, grain size, phase formation, and elemental distribution. These insights establish a solid foundation for optimizing multilayer coating architectures for advanced applications, including protective, diffusion barrier, or thermal shielding layers in extreme environments.

Acknowledgments

This project has received funding through the EURIZON project, which is funded by the European Union under grant agreement No.871072. Additional funding was received from the EU NextGenerationEU through the Recovery and Resilience Plan for Slovakia under the project No. 09I03-03-V01-00028 and VEGA – Scientific Grant Agency of the Ministry of Education, Research, Development and Youth of the Slovak Republic and the Slovak Academy of Sciences, grant number 1/0345/22.

ORCID

Olga V. Maksakova, <https://orcid.org/0000-0002-0646-6704>; Vyacheslav M. Beresnev, <https://orcid.org/0000-0002-4623-3243>;
 Serhiy V. Lytovchenko, <https://orcid.org/0000-0002-3292-5468>; Denis V. Horokh, <https://orcid.org/0000-0002-6222-4574>;
 Bohdan O. Mazilin, <https://orcid.org/0000-0003-1576-0590>; Inna Afanasieva, <https://orcid.org/0000-0002-9523-9780>;
 Mária Čaplovičová, <https://orcid.org/0000-0003-4767-8823>; Martin Sahul, <https://orcid.org/0000-0001-9472-500X>.

REFERENCES

- [1] Z. Zhang, X. Wang, Q. Zhang, Y. Liang, L. Ren, and X. Li, *Opt. Laser Technol.* **119**, 105622 (2019). <https://doi.org/10.1016/j.optlastec.2019.105622>
- [2] O. Kessler, T. Herding, F. Hoffmann, and P. Mayr, *Surface and Coatings Technology*, **182**(2-3), 184 (2004). <https://doi.org/10.1016/j.surfcoat.2003.08.054>
- [3] Y. Zhao, T. Yu, C. Guan, J. Sun, and X. Tan, *Ceramics International*, **45**(16), 20824 (2019). <https://doi.org/10.1016/j.ceramint.2019.07.070>
- [4] J. Deng, J. Liu, Z. Ding, and M. Niu, *Materials & Design*, **29**(9), 1828 (2008). <https://doi.org/10.1016/j.matdes.2008.03.007>
- [5] E. Atar, E.S. Kayali, and H. Cimenoglu, *Tribology International*, **39**(4), 297 (2006). <https://doi.org/10.1016/j.triboint.2005.01.038>
- [6] H.J. Ramos, and N.B. Valmoria, *Vacuum*, **73**(3-4), 549(2004). <https://doi.org/10.1016/j.vacuum.2003.12.158>

- [7] A. Bendavid, P.J. Martin, T.J. Kinder, and E.W. Preston, *Surface and Coatings Technology*, **163-164**, 347 (2003). [https://doi.org/10.1016/S0257-8972\(02\)00623-0](https://doi.org/10.1016/S0257-8972(02)00623-0)
- [8] T. Zhang, J.H. Song, X.B. Tian, P.K. Chu, and I.G. Brown, *J. Vac. Sci. Technol.* **A19**, 2048 (2001). <https://doi.org/10.1116/1.1372896>
- [9] K.-W. Kim, B.J. Kim, S.H. Lee, T. Nasir, H.K. Lim, I.J. Choi, B.J. Jeong, *et al.*, *Coatings*, **8**(11), 379 (2018). <https://doi.org/10.3390/coatings8110379>
- [10] B.-R. Kim, K.-D. Woo, J.-K. Yoon, J.-M. Doh, and I.-J. Shon, *Journal of Alloys and Compounds*, **481**(1-2), 573 (2009). <https://doi.org/10.1016/j.jallcom.2009.03.036>
- [11] D.T. Quinto, in: *50th Annual Technical Conference Proceedings*, 5-11 (2007), pp. 5-11. https://www.svc.org/clientuploads/directory/resource_library/07_005.pdf
- [12] J. Ratajski, W. Gulbiński, J. Staśkiewicz, *et al.*, *Journal of Achievements in Materials and Manufacturing Engineering*, **37**(2), 668 (2009). http://jamme.acmsse.h2.pl/papers_vol37_2/37263.pdf
- [13] N. Nedfors, O.E. Tengstrand, E. Lewin, *et al.*, *Surface & Coatings Technology*, **206**(2-3), 354 (2011). <https://doi.org/10.1016/j.surfcoat.2011.07.021>
- [14] K. Bobzin, N. Bagcivan, P. Immich, *et al.*, *Thin Solid Films*, **517**(3), 1251 (2008). <https://doi.org/10.1016/j.tsf.2008.06.050>
- [15] C. Zhao, X. Xing, J. Guo, Z. Shi, Y. Zhou, X. Ren, and Q. Yang, *Journal of Alloys and Compounds*, **788**, 852 (2019). <https://doi.org/10.1016/j.jallcom.2019.02.284>
- [16] T. Dash, and B.B. Nayak, *Ceramics International*, **45**(4), 4771 (2018). <https://doi.org/10.1016/j.ceramint.2018.11.170>
- [17] B. Osinger, O. Donzel-Gargand, S. Fritze, U. Jansson, and E. Lewin, *Vacuum*, **224**, 113146 (2024). <https://doi.org/10.1016/j.vacuum.2024.113146>
- [18] Y. Chen, J. Shen, and N. Chen, *Solid State Communications*, **149**(3-4), 121 (2009). <https://doi.org/10.1016/j.ssc.2008.11.004>
- [19] K.V. Chauhan, and S.K. Rawal, *Procedia Technology*, **14**, 430 (2014). <https://doi.org/10.1016/j.protec.2014.08.055>
- [20] M. Ghufuran, G.M. Uddin, S.M. Arafat, M. Jawad, and A. Rehman, *Proceedings of the Institution of Mechanical Engineers, Part J: Journal of Engineering Tribology*, **235**(1), 196 (2020). <https://doi.org/10.1177/1350650120933412>
- [21] R. Haubner, M. Lessiak, R. Pitonak, A. Köpf, and R. Weissenbacher, *International Journal of Refractory Metals and Hard Materials*, **62B**, 210 (2017). <https://doi.org/10.1016/j.ijrmhm.2016.05.009>
- [22] A.R. Naghashzadeh, A. Shafyei, and F. Sourani, *J. of Mater. Eng. and Perform.* **31**, 4335 (2022). <https://doi.org/10.1007/s11665-021-06533-2>
- [23] A. Pogrebniak, K. Smyrнова, and O. Bondar, *Coatings*, **9**(3), 155, (2019). <https://doi.org/10.3390/coatings9030155>
- [24] J.S. Koehler, *Physical Review B*, **2**, 547 (1970). <https://doi.org/10.1103/PhysRevB.2.547>
- [25] X. Junhua, G. Mingyuan, and L. Geyang, *Journal of Materials Science*, **35**, 3535 (2000). <https://doi.org/10.1023/A:1004853211220>
- [26] P.M. Anderson, T. Foecke, and P.M. Hazzledine, *MRS Bulletin*, **24**, 27 (1999). <https://doi.org/10.1557/S0883769400051514>
- [27] J.C. Caicedo, A. Guerrero, and W. Aperador, *Vacuum*, **143**, 217 (2017). <https://doi.org/10.1016/j.vacuum.2017.06.015>
- [28] Y. Li, Q. Ye, Y. Zhu, *et al.*, *Surface and Coatings Technology*, **362**, 27 (2019). <https://doi.org/10.1016/j.surfcoat.2019.01.091>
- [29] A.D. Pogrebniak, V.I. Ivashchenko, P.L. Skrynysky, *et al.*, *Composites Part B: Engineering*, **142**, 85 (2018). <https://doi.org/10.1016/j.compositesb.2018.01.004>
- [30] A. González-Hernández, A.B. Morales-Cepeda, M. Flores, *et al.*, *Coatings*, **11**(7), 797 (2021). <https://doi.org/10.3390/coatings11070797>
- [31] S. Zhang, E. Byon, M. Li, *et al.*, *Thin Solid Films*, **519**(6), 1901 (2011). <https://doi.org/10.1016/j.tsf.2010.10.024>
- [32] I. V. Serdyuk, V. O. Stolbovyi, A. V. Dolomanov, and V. M. Domnych, *Metallofiz. Noveishie Tekhnol.* **44**(4), 547 (2022). (in Ukrainian). <https://doi.org/10.15407/mfint.44.04.0547>
- [33] O.V. Maksakova, V.M. Beresnev, S.V. Lytovchenko *et al.*, *East European Journal of Physics*, (1), 396 (2025). <https://doi.org/10.26565/2312-4334-2025-1-49>

ВПЛИВ УМОВ ОСАДЖЕННЯ НА МІКРОСТРУКТУРУ ТА СКЛАД МОНОШАРОВИХ НІТРИДНИХ ТА КАРБІДНО-НІТРИДНИХ МУЛЬТИШАРОВИХ ПОКРИТТІВ НА ОСНОВІ W ТА Nb

О.В. Максакова^{a,b}, В.М. Береснев^b, С.В. Литовченко^b, Д.В. Горох^b, Б.О. Мазілін^b, І.О. Афанасьєва^{b,d},
М. Чапловичова^c, М. Сахула^a

^aІнститут матеріалознавства, Словацький технологічний університет у Братиславі,
вул. Яна Ботта 25, 917 24, Трнава, Словаччина

^bВ.Н. Харківський національний університет імені Каразіна, пл. Свободи, 4, 61000 Харків, Україна

^cЦентр нанодіагностики матеріалів, Словацький технологічний університет у Братиславі,
Вазовова 5, 812 43, Братислава, Словаччина

У роботі досліджено структурну та композиційну еволюцію моношарових покриттів WNbN та багатошарових покриттів WNbN/WNbC, осаджених методом катодного дугового випаровування. Вплив напруги зміщення підкладки (від -50 В до -200 В) і струму катодної дуги (130 - 150 А для W, 110 - 120 А для Nb) систематично вивчався з метою адаптації морфології покриттів, фазоутворення та розподілу елементів. Мікроструктурний аналіз поперечного перерізу виявив псевдобагатошарову структуру всередині моношарів через обертання підкладки та обмежену взаємодифузію. Збільшення напруги зміщення сприяло ущільненню, подрібненню зерен і покращенню адгезії, але також посилювало повторне розпилення азоту, впливаючи на стехіометрію і швидкість осадження. Багатошарові покриття демонстрували чітке чергування шарів нітридів і карбідів, причому на морфологію і кристалічність сильно впливала енергія іонів і утворений потік іонів металу. Структурний аналіз підтвердив домінування кубічних твердих розчинів на основі WNbN і WNbC з незначною кількістю гексагональних W₂N і Nb₂N. Розмір зерен коливався від 6 до 15 нм в залежності від параметрів осадження. Оптимальна структура була досягнута при помірному зміщенні (-120 В) і високому струмі дуги W, що дозволило отримати однорідні шари, збалансований склад і підвищену кристалічність. Результати демонструють, як контрольовані параметри процесу дозволяють створювати високоефективні нанокомпозитні покриття з регульованою мікроструктурою і фазовим складом, придатні для захисних застосувань.

Ключові слова: багатошарові покриття; нітриди; карбіди; ніобій; вольфрам; мікроструктура; склад

A NEW APPROACH OF OBTAINING SODIUM METASILICATE FROM DEALUMINATED KAOLIN FOR THE SYNTHESIS OF AMORPHOUS SILICON DIOXIDE NANOPARTICLES

 D.B. Puzer, A.C.K. Amuzu,  A. Abandoh,  I. Nkrumah*,  B. Kwakye-Awuah,
 F.K. Ampong,  R.K. Nkum, F. Boakye

Department of Physics, Kwame Nkrumah University of Science and Technology, Kumasi, Ghana

**Corresponding Author email: inkrumah.sci@knust.edu.gh*

Received December 24, 2024; revised March 20, 2025; accepted April 3, 2025

Silicon Dioxide nanoparticles of high purity were synthesized using a novel technique of obtaining sodium metasilicate from dealuminated metakaolin. The process involved taking the dealuminated metakaolin through several recrystallization steps to form sodium metasilicate. This was then converted into silicon dioxide nanoparticles using the sol-gel technique. The nanoparticles were studied by X-ray diffraction, scanning electron microscopy, energy dispersive X-ray analysis, thermogravimetric analysis, Fourier transform infrared spectroscopy and UV-visible optical absorption spectroscopy. The results from all the characterization techniques confirmed that the synthesized product was amorphous silicon dioxide nanoparticles with a high level of purity. This study gives an alternate pathway for obtaining sodium metasilicate from dealuminated metakaolin to synthesize amorphous silicon dioxide nanoparticles for industrial applications.

Keywords: *Amorphous silica; Sol-gel synthesis; Nanoparticles; Characterization; Metakaolin; Sodium metasilicate*

PACS: 61.43.Dq, 81.15.-z, 68.55.-a, 81.07.-b

INTRODUCTION

Silicon dioxide (SiO_2) can be found in nature in both crystalline and amorphous forms. Silica in its crystalline form occurs naturally in three polymorphic phases namely tridymite, quartz, and cristobalite [1-2]. Silica is the primary component of sand and the second most abundant mineral compound on the earth crust [3-4]. Several research works have proven interesting properties associated with nano silica, from their high porosity, thermal stability, tunable size, low toxicity to their higher specific surface area ($500\text{-}700\text{ m}^2/\text{g}$) [3, 5]. The economic importance of silica nanoparticles is evidenced by its widespread inclusion in various industrial applications such as anti-reflection coatings, photovoltaics, thermal energy storage, sensors, piezoelectric devices, photocatalysis and mixture of concrete [6-9]. As a result of these applications, amorphous silica has been projected to hold a significant share in silica production and is expected to increase in 2022–2030, due to its rising demand from the aforementioned industries [7, 10].

A cursory review of available literature shows that there are several techniques available for the synthesis of silicon dioxide (SiO_2) nanoparticles for a range of industrial applications [11-12]. These include, hydrothermal processes [13], vapor-phase reactions [14] chemical precipitation [15], hydrolysis and condensation reactions [16] and the sol-gel process [17-18]. The conventional industrial method involves a fusing reaction between soda ash and quartz at high temperatures ($1700\text{ to }2000\text{ }^\circ\text{C}$) for sodium silicate production, which is then precipitated with sulfuric acid to recover silicon dioxide. This process releases a large amount of greenhouse gases into the atmosphere, notably carbon dioxide contributing to greenhouse gas emissions [19]. It is evident that the conventional processes are environmentally unsustainable and energy-intensive [20-21].

Precursors employed for the production of silicon dioxide may either be synthetic silica from inorganic alkaline silicates or organic silicates such as tetramethyl orthosilicate (TMOS) and tetraethyl orthosilicate (TEOS) [4, 22]. However, these precursors are neither cost-effective nor ecologically friendly due to their high cost and toxicity [23]. Consequently, scholars are currently investigating substitute green precursor sources for synthetic silicon dioxide due to the environmental issues and substantial energy usage linked with these techniques [24-25]. Many researchers have produced silica synthetically using green precursors such as biomass including rice husk, sugarcane bagasse, palm kernel shell, sorghum bagasse, maize leaves and bamboo leaves [18, 26-29].

Meanwhile, the use of inorganic materials like kaolinite clay as a raw material to make sodium silicate as silica precursor has, rarely been reported in literature [24, 25]. Kaolin is an aluminosilicate soft powder clayed mineral containing mainly kaolinite with some trace minerals and impurities. Kaolin, when taken through a dehydroxylation reaction at temperatures between $650\text{--}800^\circ\text{C}$ results in formation of amorphous product known as metakaolin [30]. When the metakaolin is completely dealuminated, the resultant residue contains $> 95\%$ amorphous silica and quartz with relatively low impurities of metal oxides [31-32]. Sodium silicate solution (SSS) obtained from metakaolin offers typical advantages including refined and uniform particle size along with the high concentration of silica nanoparticles [33]. In our view, this makes it a likely starting material for the production of synthetic silica.

Hence this research work examines for the first time the synthesis of amorphous silica nanoparticles (AS – NPs) from de-aluminated metakaolin which is converted into sodium metasilicate and taken through a multi-step recrystallization process before acid hydrolysis and precipitation. The precipitated silica is then further purified through hydrothermal acid purification into amorphous silicon dioxide.

MATERIALS AND METHODS

Materials

Kaolin was obtained from the Ghana Bauxite Company located at Awaso in the western north part of Ghana. Sodium hydroxide (NaOH) pellets (99 wt% purity) and ethanol (98 wt%) were purchased from Analar Normapur, UK, whilst Sulphuric acid (H₂SO₄ 95 wt%) and Hydrochloric acid (HCl, 35 wt% and Whatman filter paper (No 1) were purchased from Sigma-Aldrich, Germany. Deionized water (WES laboratory, KNUST) served as solvent and used in the solution preparations. Without additional purification, all of the reagents were employed in their original form.

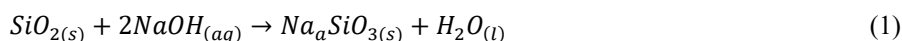
Methods

Preparation of de-aluminated Metakaolin

The metakaolin was obtained by thermal treatment of kaolinite clay. First, the kaolin clay was physically beneficiated using water to remove unwanted particles including quartz, then decanted and centrifuged to further remove residual quartz particles, dried and calcined at 850 °C for 60 minutes to obtain a more reactive phase of kaolin known as metakaolin; which was then leached using 2 M HCl at 105 °C for 2 hours to obtain de-aluminated metakaolin.

Preparation of Sodium Metasilicate

Sodium metasilicate solution was prepared by weighing 133.14 g of NaOH and adding it to 100.00 g of dealuminated metakaolin in a 1-litre Teflon beaker and mixed thoroughly. 500 g of H₂O was then gently added to the mixture which results in a spontaneous exothermic reaction thereby causing up to 80 % dissolution of the dealuminated metakaolin. The resultant solution was boiled for a while and then gradually cooled down and subsequently transferred into a Teflon bottle placed in an electric oven at 150 °C for approximately 90 minutes to allow for the reaction to complete. The reaction product was recovered at the end of the predetermined time, filtered to separate any unreacted residue from the sodium silicate solution. The sodium silicate solution was kept under normal ambient conditions for 24 hours to crystallize into sodium metasilicate after which it was recovered and filtered to separate it from the mother liquor. The chemical reactions occurring in the synthesis process is stated in Equation 1.

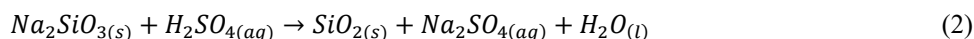


Conversion of Sodium Metasilicate to Sodium silicate solution

After the recrystallization process, the sodium metasilicate was then converted to precipitated silica via acid base neutralization and precipitation reactions. This was done by preparing 2 M of H₂SO₄ solution and used to neutralize and precipitate silica from an aliquot of a solution of the crystallized sodium metasilicate in a 1000 ml borosilicate glass beaker. The whole process was done under continuous stirring using a magnetic stirrer at 120 rpm at ambient temperature. The acid was added dropwise while the stirring continued and the pH of the mixture monitored until the pH reached a neutral point where a white precipitate of silica was obtained and at this point the temperature of the mixture reached 95°C, the stirring was then halted and the beaker covered to allow the mixture of the precipitate and the mother liquor to cool to near ambient temperature.

Obtaining Silicon Dioxide from Sodium Silicate Solution

The precipitated silica was recovered by filtration, washed with aqueous ethanol solution then copiously with distilled water. The sample was subsequently dried at 105 °C in an electric oven overnight; recovered, then ground into fine powder using agate mortar and pestle and then stored in zip lock bag for characterizations. The chemical reactions occurring in the synthesis process is stated in Equations 2.



RESULTS AND DISCUSSION

Chemical composition of De-aluminated metakaolin and as-prepared Sodium silicate

The chemical composition of the de-aluminated kaolin has shown clearly that, it is a suitable precursor for the synthesis of silica due to the fact that it contains over 93 % silicon oxides which readily solubilized in caustic soda solution at relatively low temperature. The precursor according to the XRF analysis contains some impurities of metallic oxides with some significant weight percent as shown in Table 1.

The chemical compositions of the sodium metasilicate obtained from the de-aluminated metakaolin is also shown in Table 1. The data in Table 1 shows that sodium metasilicate contains silicon and sodium oxides as the major chemical

constituents and impurities of metallic oxides derived from the de-aluminated metakaolin. It further shows that the yield of Na_2SiO_3 contained high concentrations of silicon dioxide (63 %) which makes it a good precursor for the synthesis of high purity silica nanoparticles. The recrystallized Na_2SiO_3 inherently exhibited impurities such as oxides of sodium, calcium, aluminum and iron which are characteristics of its precursor, and obviously emanated from the de-aluminated kaolin. The level of purity observed in the sodium silicate obtained in this study are much higher than those obtained in works by [34,16, 35, 36] who synthesised sodium silicate from quartz sand.

Table 1. XRF analysis showing the oxides present in De-aluminated metakaolin and Sodium metasilicate hydrate with their percentage weights

SAMPLES	Oxides/(wt%)				
	SiO_2	Na_2O	CaO	Fe_2O_3	Others
DE-ALMTK	93.573	0.854	0.112	0.235	5.226
S-SLCT	63.000	35.300	0.235	0.198	1.267

DE-ALMTK – De-aluminate metakaolin, S – SLCT – Sodium metasilicate

Structural characteristics of AS – NPs

The structure of the synthesised product was studied by Powder X-Ray Diffraction measurements using a Shimadzu XRD-6000 diffractometer, with Cu-K α radiation ($\lambda = 0.15408$ nm), The equipment was operated at 40 mA and 45 kV for phase analysis using the Bragg-Brentano geometry in the 2θ range 10 to 70 °, scan step of 0.05°. The X-ray diffraction pattern of amorphous silicon dioxide nano particles synthesised from kaolin-based metasilicate is illustrated in Figure 1.

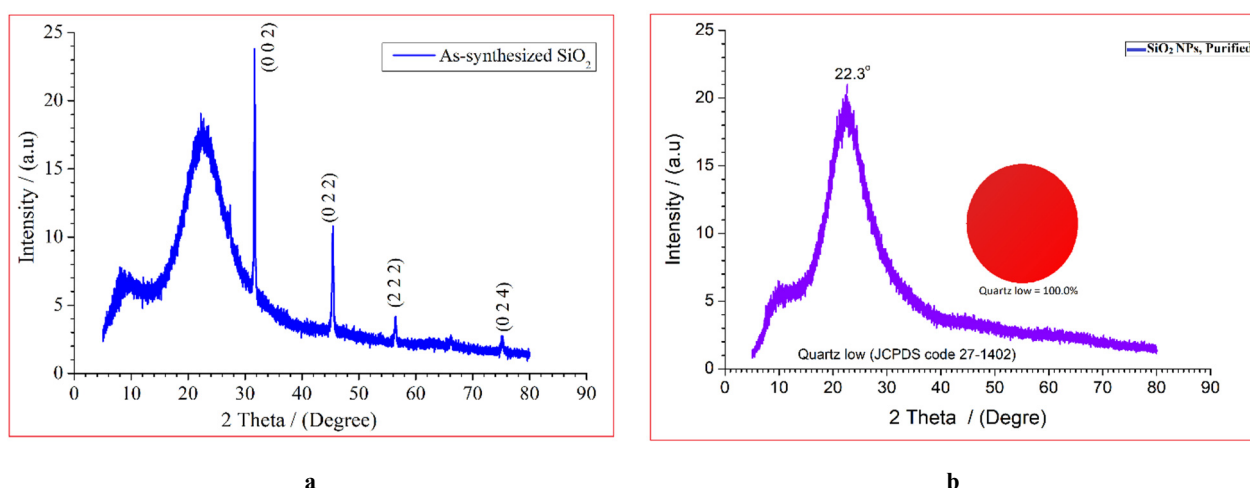


Figure 1. XRD patterns of amorphous SiO_2 nanoparticles (a) as-synthesised (b) purified

The XRD pattern of the as-synthesised and purified silicon dioxide nanoparticles are shown in Figures 1a and 1b. The pattern in Figure 1a shows a broad peak in the 2θ from 22.3° to 28.0° which is distinctive of amorphous solid, confirms the formation of amorphous silica [26, 37]. This observation is also in direct accordance with JCPDS 47-0715. The pattern of prominent peaks at positions 31.667, 45.412, 56.404 and 75.175° are indexed to reflections from the (002), (022), (222) and (024) planes of NaCl halite structure (Ref. COD 9008678), which is present as a contaminant. These peaks disappear completely after repeated washings as shown in Figure 1b, leaving behind what appears to be a pure phase of amorphous silicon dioxide. Figure 1b shows a pure phase of amorphous silica with no discernable peaks indexed to impurities.

Morphological and compositional analysis of amorphous SiO_2 nanoparticles

The morphology and elemental composition of synthesised product was studied using a Phenom Pro Desktop FEI Quanta FEG 200 High Resolution Scanning Electron Microscope, integrated with EDS.

SEM and EDX analysis

The micrograph from the SEM analysis of the as-synthesised silicon dioxide is displayed in Figure 2(d) and the corresponding EDS spectrum is depicted in 2(c). As exhibited in Figure 2, it is evident that the morphology shows that, sample consists of a rough surface composed of agglomerates of extremely tiny particles which exhibit irregular shapes and sizes with angular and sharp edges. The EDX spectrum presented in Figure 2 (c) shows that the silicon dioxide contains silicon at 40.63 % and oxygen at 59.37 % with traces of Na, Cl and C elements as impurities for the as-synthesised silica, while Figure 2(b) confirms the purity of the purified silica as it reveals the presence of only Si and O elements having significant intensities. This supports the observations made in the XRD analysis.

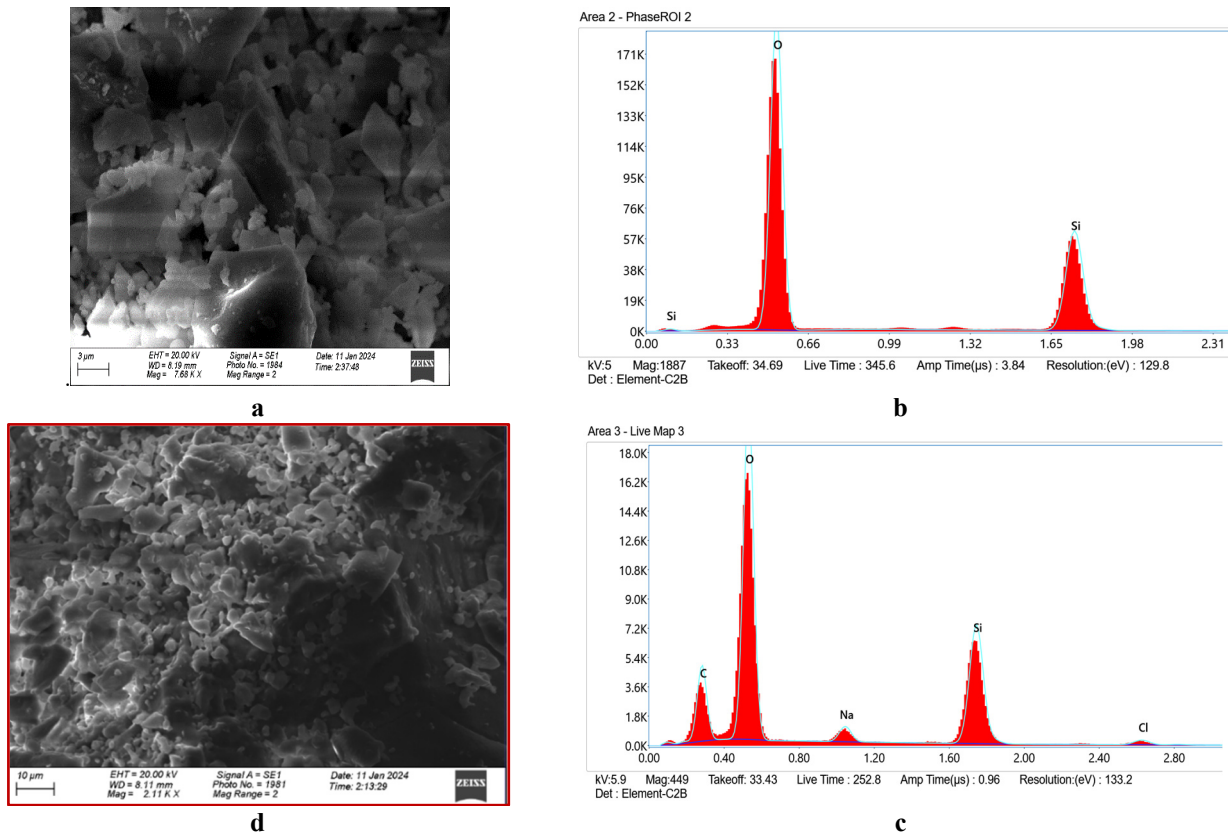


Figure 2. SEM micrograph (d and a) and EDS spectrum (c and b) of the as-synthesised silica and as-purified silica respectively

Thermal Analysis of the synthesised amorphous SiO_2 nanoparticles

To evaluate the thermal stability and phase transition temperature of the prepared SiO_2 nanoparticles, a thermogravimetric study (TGA) was conducted with a TA instrument (SDT Q600 V20.9 Build 20), under the following experimental conditions: temperature ranging from 25 to 1200 °C; speed of heating 10 °C/min; sample mass 4.0 mg; under an argon environment; material carrier – ceramic pot. The TGA profile of as-synthesised SiO_2 nanoparticles are depicted in Figure 3.

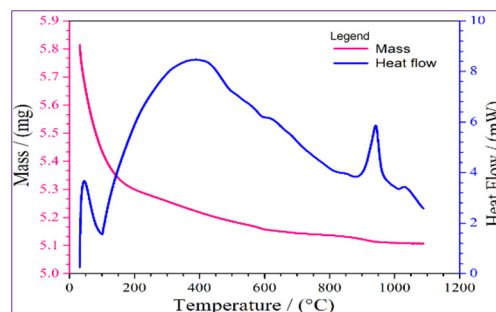


Figure 3. TG/DTA curves of the synthesised pure amorphous silicon dioxide nanoparticles

The thermogravimetric analysis conducted in a temperature range of 25 – 1200 °C, produced two curves that showed mass lost (in pink) and heat flow (in blue) over time as functions of temperature. The noticeable mass loss from 30 – 150 °C may be attributable to the evaporation of the absorbed moisture including water of crystallization which gets evaporated and volatile organic compounds present on the surface of the produced nano-silicon dioxide [38]. This initial mass loss indicates the presence of physically absorbed water on the open pore structure and possibly some loosely bound water molecules, which occurs on the silica particle's surface [39]. This suggests quite well that the synthesised silica nanoparticles are stronger absorbers of the surrounding moisture. Some reports have suggested that mass loss due to the presence of physical water is an indication of the porous nature of the material [38, 40]. At temperatures above 1000 °C, the mass loss curve flattens out, indicating no significant further loss in mass. This suggests that all volatile components have been removed, and the remaining material is thermally stable silicon dioxide [34]. Distinct exothermic peaks are also observed at around 800 – 1000 °C, which may indicate phase transitions or crystallization process within the silicon dioxide nanoparticles. El-didamony et al. (2019) explained that these peaks suggest structural rearrangements that release heat.

Optical analysis of the synthesised amorphous SiO₂ nanoparticles

FTIR Analysis

Fourier transform infrared (FTIR) spectra for the as-synthesised nanoparticles were evaluated via PerkinElmer Spectrum Two photometer (PerkinElmer, USA). The synthesized samples were prepared and placed in a holder constructed of KBr ionic materials and the spectrum is obtained in the wave number range of 400 – 4000 cm⁻¹. A background spectrum was run and subtracted from the compound spectrum. Structural functional group characteristics of the synthesised silica is presented in Figure 4.

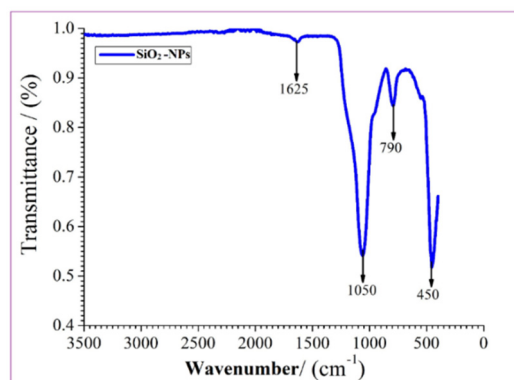


Figure 4. FTIR spectrum of the synthesised silicon dioxide nanoparticles using sodium metasilicate as precursor

The characteristic vibrational functional groups observed in the analyzed spectrum are Si – O – Si, Si – OH and O – Si – O. The synthesized silicon dioxide nanoparticles also exhibited H – O – H groups showing the presence of absorbed molecular water within the sample. The intensities of the peaks in the spectrum characterize the phase purity of the silicon dioxide, thereby corroborating with the EDS data and the XRD results which demonstrated that the silicon dioxide is composed of 100 % quartz low. The asymmetric vibrational mode due to Si – O in the SiO₂ groups occurred at 1050 cm⁻¹ while symmetric stretching mode due to Si – Si or Si – O – Si occurred at 790 cm⁻¹. The band at 450 cm⁻¹ was due to the bending mode of Si – O – Si or O – Si – O. The observed functional groups in this research are consistent with the reported results in literature [35, 37]. From the FTIR graphs, all peaks relevant to silicon dioxide nanoparticles are observed, thus, further confirming the synthesis of silicon dioxide nanoparticles.

Optical analysis of the synthesised amorphous SiO₂ nanoparticles

UV-Vis absorption spectroscopy

The optical absorption characteristics of the synthesised silicon dioxide nanoparticles at room temperature were studied by UV-Vis spectrophotometer (UV-1800, Shimadzu, Japan). 5.0 mg of each sample was measured into 1:1 ethanol solution to form a colloid. For the measurement of absorbance, the colloid sample was placed in a cuvette with a fixed 1 mm path-length. NaOH solution was utilised as reference to prepare a blank. An illuminated visible light source from the monochromator of constant intensity and low noise over the 200 – 700 nm wavelength range was employed to run through the colloid samples contained in the cuvette.

UV-Vis absorbance spectra of the amorphous SiO₂ were analyzed by plotting $(\alpha h\nu)^2$ as a function of photon energy $(h\nu)$ based on Tauc's relation in the wavelength range of 200 – 700 nm. It can be observed from Figure 5 that the absorbance value was around 385 nm indicating the onset of the fundamental absorption edge.

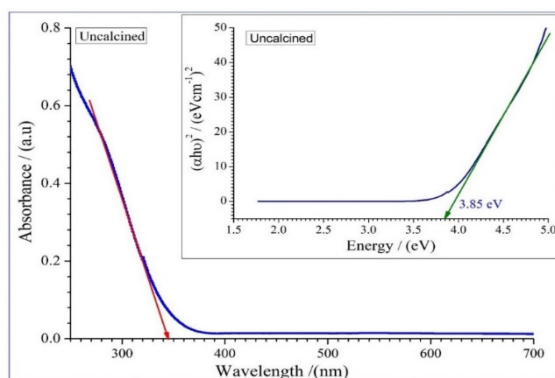


Figure 5. Absorbance spectra of as-synthesized amorphous silicon dioxide nanoparticles.

Figure 5, shows the optical absorbance spectra of the as-synthesised amorphous SiO₂ nanoparticles. It can be observed that the nanoparticles have very low absorbance in the visible range making them almost transparent to visible light. This is an inherent characteristic of amorphous silicon dioxide.

Optical Energy Band Gap (E_g) of the synthesized amorphous SiO₂ nanoparticles

The optical band gap shown inset of Figure 5 is obtained from the absorbance spectra by plotting $(ah\nu)^2$ against photon energy ($h\nu$). The band gap is obtained by drawing a line of best fit, and extrapolating that line to intersect the $h\nu$ axis where $(ah\nu)^2$ tends to zero [41]. The point of intersection gives the band gap. From the inset of Figure 5, the energy band gap is 3.85 eV. This high energy band gap is consistent with values reported in previous studies [42, 34]. This observed high band gap energy value shows that the absorption of the silicon dioxide sample is near UV-Vis region, clearly confirming the transparent nature of the synthesised amorphous silicon dioxide nanoparticles.

CONCLUSION

An alternate route for obtaining sodium metasilicate from de-aluminated Kaolin for the synthesis of amorphous silicon dioxide nanoparticles has been established. The physical, structural and thermal characteristics of the synthesized nanoparticles were all authenticated by the XRD, FTIR, SEM, TG/DTA results which were largely congruous with results reported in literature. The findings of the current work show that kaolinite-based clays are prospective alternative precursor for high purity synthesis of amorphous silicon dioxide nanoparticles for potential industrial applications.

Acknowledgements

Authors would like to express their profound gratitude to ZEOTEC Limited Company - Ghana for the provision of instruments and expertise in this research work. We greatly acknowledge the department of Earth Science, University of Ghana, Legon for allowing us to use their TGA machines and RWESCK for their XRD, SEM and EDS characterization tools.

ORCID

©D.B. Puzer, <https://orcid.org/0009-0001-4470-681X>; ©A. Abandoh, <https://orcid.org/0009-0004-2465-8277>
©I. Nkrumah, <https://orcid.org/0000-0003-4030-7931>; ©B. Kwakye-Awuah, <https://orcid.org/0000-0002-8842-681X>
©F.K. Ampomg, <https://orcid.org/0000-0003-3562-8183>; ©R.K. Nkum, <https://orcid.org/0000-0003-0404-760X>

References

- [1] R.S. Dubey, Y.B.R.D. Rajesh, and M.A. Mor, *Materials Today*, **2** (4-5), 3575 (2015). <https://doi.org/10.1016/j.matpr.2015.07.098>
- [2] M. Unasir, T. Riwikantoro, M.O.Z. Ainuri, and D. Arminto, *Materials Science*, **33** (1), 47 (2015). <https://doi.org/10.1515/msp-2015-0008>
- [3] H. Lin, M. Yang, X. Ru, G. Wang, S. Yin, F. Peng, C. Hong, *et al.*, *Nature Energy*, **8**(8), 789 (2023). <https://doi.org/10.1038/s41560-023-01255-2>
- [4] C.P. Faizul, C. Abdullah, and B. Fazlul, *Advanced Materials Research*, **626**, 997 (2013). <https://doi.org/10.4028/www.scientific.net/AMR.626.997>
- [5] F. Akhter, A. Atta, R. Mahmood, N. Abbasi, S. Ahmed, W. Mukhtiar, and A. Mallah, *Silicon*, **14** 8295 (2022). <https://doi.org/10.1007/s12633-021-01611-5>
- [6] T. Mizutani, K. Arai, M. Miyamoto, and Y. Kimura, *Progress in Organic Coatings*, **55**(3), 276 (2006). <https://doi.org/10.1016/j.porgcoat.2005.12.001>
- [7] S.S. Owuoye, S.M. Abegunde, and B. Oji, *Nano-Structures & Nano-Objects*, **25**, 100625 (2021). <https://doi.org/10.1016/j.nanoso.2020.100625>
- [8] M. Heikal, H. El-didamony, T.M. Sokkary, and I.A. Ahmed, *Construction and Building Materials*, **38**, 1180 (2013). <https://doi.org/10.1016/j.conbuildmat.2012.09.069>
- [9] N. Meftah, A. Hani, and A. Merdas, *Chemistry Africa*, **6**(6), 3039 (2023). <https://doi.org/10.1007/s42250-023-00688-2>
- [10] D. Bokov, A.T. Jalil, S. Chupradit, W. Suksatan, M.J. Ansari, I.H. Shewael, G.H. Valley, *et al.*, *Advances in Materials Science and Engineering*, **2021**(1), 5102014 (2021). <https://doi.org/10.1155/2021/5102014>
- [11] F. Farirai, M. Ozonoh, T.C. Aniokete, O. Eterigho-ikelegbe, M. Mupa, and B. Zeyi, *International Journal of Sustainable Engineering*, **14**(1), 57 (2021). <https://doi.org/10.1080/19397038.2020.1720854>
- [12] V. Zarei, M. Mirzaasadi, A. Davarpanah, A. Nasiri, and M. Valizadeh, *Processes*, **9**(2), 334 (2021). <https://doi.org/doi.org/10.3390/pr9020334>
- [13] F. Qi, G. Zhu, and Y. Zhang, X. Hou, S. Li, J. Zhang and H. Li, *Journal of American Ceramic Society*, **104**(1), 535 (2020). <https://doi.org/10.1111/jace.17440>
- [14] P.S. Utama, R. Yamsaengsung, and C. Sangwichien, *Brazilian Journal of Chemical Engineering*, **36**(1), 523 (2019). <https://doi.org/10.1590/0104-6632.20190361s20170458>
- [15] G.J. Croissant, K.S. Butler, J.I. Zink, and C.J. Brinker, *Nature Reviews Materials*, **5**(12), 886 (2020). <https://doi.org/10.1038/s41578-020-0230-0>
- [16] Z. Li, D. Wang, F. Lv, J. Chen, C. Wu, Y. Li, J. Shen, and Y. Li, *Materials*, **15**(3), 970 (2022). <https://doi.org/10.3390/ma15030970>
- [17] S. Rezaei, I. Manoucheri, R. Moradian, and B. Pourabbas, *Chemical Engineering Journal*, **252**, 11 (2014). <https://doi.org/10.1016/j.cej.2014.04.100>
- [18] U. Zulfikar, T. Subhani, and S.W. Husain, *Journal of Asian Ceramic Societies*, **4**(1), 91 (2016). <https://doi.org/10.1016/j.jascer.2015.12.001>
- [19] J. Tao, *Cement and Concrete Research*, **35**(10), 1943 (2005). <https://doi.org/10.1016/j.cemconres.2005.07.004>
- [20] C.P. Faizul, C. Abdullah, and B. Fazlul, *Advanced Materials Research*, **626**, 997 (2013). <https://doi.org/10.4028/www.scientific.net/AMR.626.997>
- [21] N.N. Maseko, D. Enke, S.A. Iwarere, O.S. Oluwafemi, and J. Pocock, *Sustainability*, **15**(5), 4626 (2023). <https://doi.org/10.3390/su15054626>

- [22] G. Zhu, H. Li, X. Wang, S. Li, X. Hou, W. Wu, and Q. Tang, The American Ceramic Society, **99**(8), 2778 (2016). <https://doi.org/10.1111/jace.14242>
- [23] P. Sharma, J. Prakash, R. Kaushal, Environmental Research, **212**, 113328 (2022). <https://doi.org/10.1016/j.envres.2022.113328>
- [24] J.A. Adebisi, J.O. Agunsoye, I.I. Ahmed, S.A. Bello, M. Haris, M.M. Ramakokovhu, and S.B. Hassan, Materials Today: Proceedings, **38**, 669 (2020). <https://doi.org/10.1016/j.matpr.2020.03.658>
- [25] G. Falk, G.P. Shinhe, L.B. Teixeira, E.G. Moraes, and A.P. Navaes de Oliveira, Ceramics International, **45**(17), 21618 (2019). <https://doi.org/10.1016/j.ceramint.2019.07.157>
- [26] P.E. Imoisili, K.O. Ukoba, and T. Jen, Boletín de La Sociedad Española de Cerámica y Vidrio, **59**(4), 159 (2020). <https://doi.org/10.1016/j.bsecv.2019.09.006>
- [27] E. Rafiee, S. Shahebrahimi, M. Feyzi, and M. Shaterzadeh, International Nano Letters, **2**, 29 (2012). <https://doi.org/10.1186/2228-5326-2-29>
- [28] G. Tchanang, C. Njiomou, C. Fon, D. Laure, M. Moukouri, and P. Blanchart, Applied Clay Science, **207**, 106087 (2021). <https://doi.org/10.1016/j.clay.2021.106087>
- [29] V. Vaibhav, U. Vijayalakshmi, and S.M. Roopan, Spectrochimica Acta Part A: Molecular And Biomolecular Spectroscopy, **139**, 515 (2015). <https://doi.org/10.1016/j.saa.2014.12.083>
- [30] B. Kwakye, A. Eric, K. Kyeh, A. Baah, S. Ntiri, I. Nkrumah, and E.V. Kiti, Journal of Thermal Analysis and Calorimetry, **146**, 1991 (2021). <https://doi.org/10.1007/s10973-021-10710-9>
- [31] S.G. Bawa, A.S. Ahmed, and P.C. Okonkwo, Nigerian Journal of Basic And Applied Science, **24**(2), 66 (2016). <https://doi.org/10.4314/njbas.v24i2.10>
- [32] A.B. Eldeeb, V.N. Brichkin, R.V. Kurtenkov, and I.S. Bormotov, Applied Clay Science, **172**, 146 (2018). <https://doi.org/10.1016/j.clay.2019.03.008>
- [33] O. Weichold, B. Tigges, M. Bertmer, and M. Möller, Journal of Colloid and Interface Science, **324**(1-2), 105 (2008). <https://doi.org/10.1016/j.jcis.2008.04.060>
- [34] A. Boualem, L. Leonite, S.A.G. Lopera, and S. Hamzaoui, Silicon, **14**(10), 5231 (2022). <https://doi.org/10.1007/s12633-021-01306-x>
- [35] N. Meftah, A. Hani, and A. Merdas, Chemistry Africa, **6**, 3039 (2023). <https://doi.org/10.1007/s42250-023-00688-2>
- [36] A.B. Prasetyo, I. Agency, M. Handayani, and E. Febrian, Journal of Ceramic Processing Research, **24**(1), 103 (2023). <https://doi.org/10.36410/jcpr.2023.24.1.103>
- [37] N. K. Mohd, N. Nur, A. Nik, and A.A. Azmi, American Institute of Physics, **1885**(1), 020123 (2017). <https://doi.org/10.1063/1.5002317>
- [38] H. El-Didamony, E. El-Fadaly, A.A. Amer, and I.H. Abazeed, Boletín de La Sociedad Española de Cerámica y Vidrio, **9**(1), 31 (2020). <https://doi.org/10.1016/j.bsecv.2019.06.004>
- [39] Q. Han, P. Zhang, J. Wu, Y. Jing, D. Zhang, and T. Zhang, Nanotechnology Reviews, **11**(1), 1478 (2022). <https://doi.org/10.1515/ntrev-2022-0092>
- [40] R.K. Kankala, Y. Han, J. Na, C. Lee, Z. Sun, S. Wang, T. Kimura, *et al.*, Advanced Materials, **32**(23), 1907035 (2020). <https://doi.org/10.1002/adma.201907035>
- [41] A.Y. Oral, E. Mensur, M.H. Aslan, and E. Basaran, Materials Chemistry and Physics, **83**(1), 140 (2004). <https://doi.org/10.1016/j.matchemphys.2003.09.015>
- [42] M.F. Anuar, Y.W. Fen, M.H.M. Zaid, K.A. Matori, and R.E.M. Khaidir, Applied Sciences, **10**(6) 2128 (2020). <https://doi.org/10.3390/app10062128>

НОВИЙ ПІДХІД ОТРИМАННЯ МЕТАСИЛКАТУ НАТРІЮ З ДЕАЛЮМІНІСНОВАНОГО КАОЛІНУ ДЛЯ СИНТЕЗУ НАНОЧАСТИНОК АМОРФНОГО ДІОКСИДУ КРЕМНІЮ

Д.Б. Пузер, А.Ч.К. Амузу, А. Абандо, І. Нкрума, Б. Квакі-Авуа, Ф.К. Ампонг, Р.К. Нкум, Ф. Боак'є

Факультет фізики, Університет науки і технологій Кваме Нкрума, Кумасі, Гана

Наночастинки діоксиду кремнію високої чистоти були синтезовані за допомогою нової методики отримання метасилікату натрію з деалюмінованого метакаоліну. Процес передбачав проходження деалюмінованого метакаоліну через кілька етапів перекристалізації з утворенням метасилікату натрію. Потім це було перетворено в наночастинки діоксиду кремнію за допомогою золь-гель техніки. Наночастинки були досліджені за допомогою рентгенівської дифракції, скануючої електронної мікроскопії, енергодисперсійного рентгенівського аналізу, термогравіметричного аналізу, інфрачервоної спектроскопії з перетворенням Фур'є та спектроскопії оптичного поглинання в УФ-видимому діапазоні. Результати всіх методів визначення характеристик підтвердили, що синтезований продукт являв собою аморфні наночастинки діоксиду кремнію з високим рівнем чистоти. Це дослідження пропонує альтернативний шлях отримання метасилікату натрію з деалюмінованого метакаоліну для синтезу наночастинок аморфного діоксиду кремнію для промислового застосування.

Ключові слова: аморфний кремнезем; золь-гель синтез; наночастинки; характеристикація; метакаолін; метасилікат натрію

STUDIES OF IMPLANTATION OF O⁺ IONS INTO SiO₂(001) FILMS AT THE SMALL-ANGLE ION BOMBARDMENT

U.O. Kutliev^a, A.S. Ashirov^{a*}, G.X. Allayarova^b, A. Saidova^a

^aUrgench State University, Urgench, Uzbekistan

^bKarshi State University, Ko'chabog st., Karshi, Uzbekistan

*Corresponding Author e-mail: atabeks.ashirov@gmail.com

Received January 22, 2025; revised April 2, 2025; accepted April 30, 2025

We have studied the process of ion implantation at small-angle ion bombardment of SiO₂(001) film at low values of initial energy (up to 5 keV). Along with scattered O⁺ ions ion implantation is observed. It has shown that the geometric parameters of the surface semichannel affect the bombardment angle, which initiates the implantation process. It was found that in the case of a shallow semichannel, the implantation process is observed more than a deep semichannel at one value of the angle of incidence of ions. The dependence of implanted ions on the angle of their bombardment is obtained. It is found that few bombarding ions were implanted into the deep surface semichannel. This is explained by the influence of the second atomic row of the semichannel. The results obtained are of great interest in studying the ion implantation process.

Keywords: Implantation; Ion bombardment; Computer modeling; Ion scattering; Focusing

PACS: 34.50.-s

INTRODUCTION

During ion bombardment of a solid surface, many processes are observed that can be described both experimentally and theoretically [1-5]. Along with these processes, there is also the process of ion scattering and their implantation on surface areas. It is known that ion scattering spectroscopy (ISS) is an analytical method based on the study of the interaction of ions with the surface of materials. The main focus is on the analysis of the surface composition, structure and properties of thin layers and nanomaterials [6-8]. This method allows one to study the atomic composition, chemical state and surface topography with high sensitivity to the outer atomic layers. This method is successfully used along with many other methods for studying processes occurring on and near the surface. With this method, one can also study the ion implantation process and the characteristic trajectories of implanted ions [9-11].

Silicon dioxide (SiO₂), also known as silica, is widely used in various industries due to its unique properties, such as high chemical inertness, hardness and heat resistance. It is used to create insulating layers in microcircuits and other electronic devices, and is also used to obtain high-purity silicon required for solar panels. Therefore, the study of its structure and composition is of great interest. Artificial oxidation (implantation) of silicon is usually carried out in oxidizing furnaces similar to those used for diffusion in a carrier gas flow at high temperature (1000-1200°C). The basis of such furnaces, as in diffusion, is a quartz tube with silicon plates, heated either by high-frequency currents or in some other way [12-13]. In this work, the implantation of oxygen ions under small-angle bombardment with small values of initial energy was calculated using computer modeling. Trajectories were plotted and the number of implanted oxygen ions was calculated.

METHOD AND DISCUSSION OF RESULTS

In this work, the binary collision approximation method was used to describe the ion-atom interaction. For further development of mathematical modeling of the scattering process of medium and low energy ions in a wide range of incidence and scattering angles, we used the collision patterns of two heavy particles. Thus, we will consider the scattering of an ion beam from the surface of a monocrystal sample based on the model of paired single, double, etc. multiple collisions [14-15].

The pair collision approximation is the basis of two basic programs, with the help of which a wide range of processes caused by the bombardment of solids by accelerated particles are modeled: the program MARLOWE and the program TRIM [16, 17]. Both programs are based on practically the same formalism. The difference between these programs is that the first initially operates with crystalline targets, while the second with amorphous ones. To estimate the inelastic energy loss in an elementary collision act, we used the modified Kishinevski potential [18]:

$$\varepsilon(E_0, P) = \frac{0,310^{-7} v Z_1 (Z_1^{1/2} + Z_2^{1/2}) (Z_1^{1/6} + Z_2^{1/6})}{(1 + \frac{0,67 \sqrt{Z_1} r_0}{a_f (Z_1^{1/6} + Z_2^{1/6})})} + (1 - 0,68) \frac{V(r_c)}{E_r}$$

where, $a_{\text{tr}} = 0.468 \text{ \AA}$, v and E_r - are the relative velocity and energy of the atom, Z_1 and Z_2 are the charge of the colliding ions and atoms, v - cm/s, E_r - eV, r_{min} in angstroms.

In our calculations, we considered 200 trajectories of bombarding oxygen ions separately for the $\langle 110 \rangle$ and $\langle \bar{1}10 \rangle$ directions of the SiO₂(001) film surface. The structure of the surface semichannels formed by SiO₂(001) $\langle 110 \rangle$ and SiO₂(001) $\langle \bar{1}10 \rangle$ is shown in Fig. 1a and Fig. 1b, respectively. The width of the semichannel formed in the $\langle 110 \rangle$ direction is 5.063 Å and the depth is 1.64 Å. And the width and depth of the semichannel formed in the $\langle \bar{1}10 \rangle$ direction are 5.063 Å and 2.46 Å, respectively.

It is known that some of the ions are reflected from the film, and some of them remain inside the film (implanted). To study this issue, we obtained the dependence of the reflected particles on the angle of incidence of the bombarding O⁺ ions to find out what part of the ions remains inside the SiO₂(001) film at low values of the initial energy (up to 5 keV). This dependence makes it possible to determine the percentage of implanted ions in the film. We calculated the scattering and implanted ions with low-angle ion bombardment. This work presents calculations exclusively of implanted ions. It should be noted that the width of the semichannel in SiO₂(001) $\langle 110 \rangle$ is 5.063 Å, and the depth is 1.64 Å. In the direction of SiO₂(001) $\langle \bar{1}10 \rangle$, the width of the semichannel is also 5.063 Å, and the depth is 2.46 Å.



Figure 1. Structure of the surface semichannel of the SiO₂(001) film in the directions $\langle 110 \rangle$ (a) and $\langle \bar{1}10 \rangle$ (b)

Figure 2 shows the dependence of the number of implanted O⁺ ions in SiO₂(001) $\langle 110 \rangle$ films on the angle of incidence. We selected the values of the angle of incidence in the range of 1-30°. This is due to the fact that small-angle implantation of ions on thin films. From the dependence it is evident that ions with an initial energy of $E_0 = 1$ keV to the value of the angle of incidence at $\psi \geq 9^\circ$ begin to penetrate into the film (black line). In this case, a small number of O⁺ ions penetrate into the film and a large number of ions reflecting from the film was observed. At the initial energy value $E_0 = 2$ keV, the ions penetrate into the film in $\psi \geq 6^\circ$ (red line). Our calculations showed that at $E_0 = 3$ keV, ions penetrate into the film at $\psi \geq 5^\circ$ (pink line). And $E_0 = 4$ keV, ions penetrate into the film at $\psi \geq 4^\circ$ (blue line). At values of $E_0 = 5$ keV, ions penetrate into the film at $\psi \geq 4^\circ$ (violet line).

At the next increase in the value of the angle of incidence of ions in all values of the initial energy, the number of implanted ions begin to increase. After the growth of the number of implanted particles, a small decline in the dependence is observed, which is located in the range $\psi = 12^\circ - 17^\circ$. Analysis of the particle trajectory showed that the decrease in the number of implanted ions is explained by the fact that in this value of the initial energy and angle of incidence of particles, the effect of ion focusing is observed. That is, what part of the ions are focused in the surface semichannels. After this decline, an increase in the number of implanted particles is observed and again the number of these particles decreases, which is explained by a decrease in the collision of ions with the surface atomic row and the wall of the semichannel.

Fig.3. shows the dependence of the number of implanted O⁺ ions in SiO₂(001) $\langle \bar{1}10 \rangle$ films on the angle of incidence. It is evident from the dependence that the process of implantation of ions with an initial energy of $E_0 = 1$ keV begins to penetrate into the film $\psi \geq 2^\circ$ (black line). Moreover, at other values of the initial energy, the ions penetrate with $\psi \geq 1^\circ$. This is because the geometric parameters semichannels are large. For this semichannel, a two-peak structure is also observed. And a decrease in the number of implanted ions is observed with the ion focusing effect. Comparison of these two dependencies presented in Fig.2 and Fig.3. shows that with an increase in the number of atomic rows of the surface semichannel, the number of implanted ions increases. Our calculations showed that there is a decrease in the number of implanted ions when bombarded at the $\psi = 12^\circ - 15^\circ$ in the direction of SiO₂(001) $\langle \bar{1}10 \rangle$. The process of ion focusing explains this decrease in the number of implanted ions.

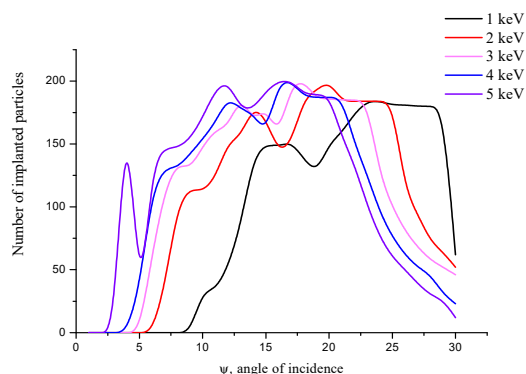


Figure 2. Dependence of the number of implanted O⁺ ions in SiO₂(001) $\langle 110 \rangle$ films on the angle of incidence

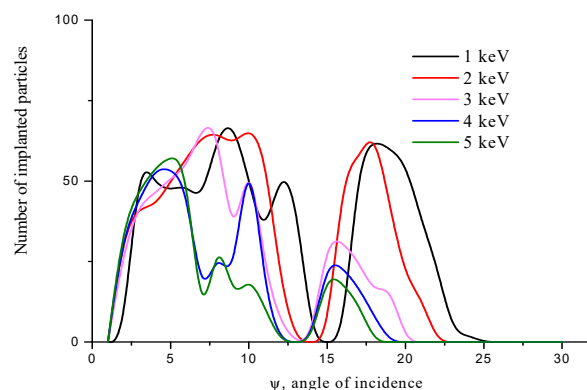


Figure 3. Dependence of the number of implanted O⁺ ions in SiO₂(001) $\langle \bar{1}10 \rangle$ films on the angle of incidence

For the study, we will consider two trajectories obtained for the $\text{SiO}_2(001)$ film in the $\langle 110 \rangle$ and $\langle \bar{1}10 \rangle$ directions. Fig. 4 and Fig. 5 show several trajectories of implanted ions for the $\langle 110 \rangle$ and $\langle \bar{1}10 \rangle$ directions, respectively, at an incidence angle $\psi = 10^\circ$ and with an initial energy of $E_0 = 1 \text{ keV}$. It is evident from the trajectory shown in Fig. 4 that two trajectories (1 and 2) penetrated into adjacent semichannels and remain in the film as an implanted particle. And trajectory 3 shows that this ion is scattered from the surface semichannel. When bombarded in the $\langle \bar{1}10 \rangle$ direction by O^+ ions, straight and zigzag trajectories are also observed before implantation of ions (Fig. 5).

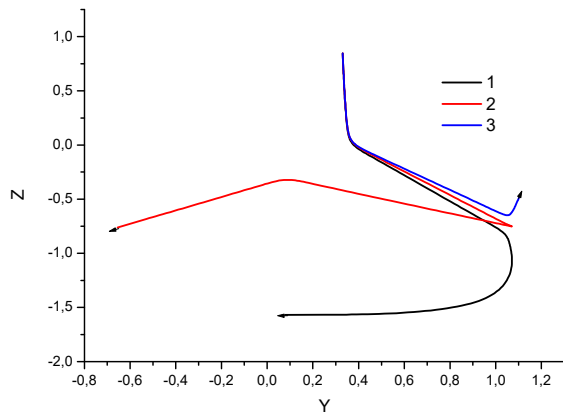


Figure 4. Characteristic trajectories of implanted O^+ ions in the $\text{SiO}_2(001)\langle 110 \rangle$ film at $E_0 = 3 \text{ keV}$ and $\psi = 10^\circ$

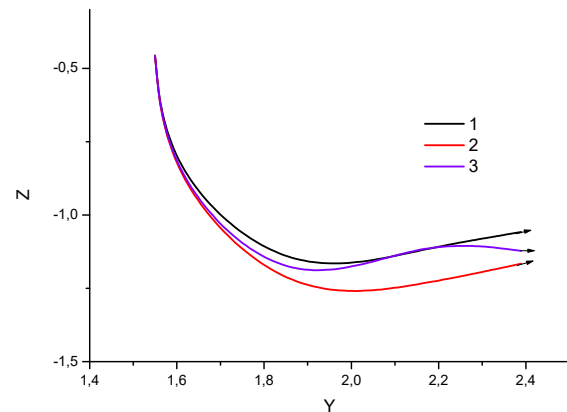


Figure 5. Characteristic trajectories of implanted O^+ ions in the $\text{SiO}_2(001)\langle \bar{1}10 \rangle$ film at $E_0 = 3 \text{ keV}$ and $\psi = 10^\circ$

Our calculations showed that the trajectories of the ions that remained (were implanted) in the films have different types. These trajectories were formed due to multiple scattering from the atomic chains under the surface layers, and they have a zigzag and linear shape in general.

CONCLUSION

We have studied the process of implantation of O^+ ions into $\text{SiO}_2(001)$ films using computer modeling. The dependence of the number of implanted O^+ ions into $\text{SiO}_2(001)$ films on the incidence angle has been obtained. It has been shown that the geometric parameters of the surface semichannels affect the process of ion implantation. The characteristic trajectories of the implanted ions on the films have been studied and the parameters of the implanted particles have been calculated. The obtained results make it possible to apply the ion implantation process to obtain materials with new parameters.

ORCID

● Uchkun O. Kutliev, <https://orcid.org/0000-0003-2241-2025>; ● Atabek S. Ashirov, <https://orcid.org/0000-0002-8731-7531>

REFERENCES

- [1] J.M. Haile, *Molecular Dynamics Simulation -Elementary Methods*, (Wiley-Interscience, New York, 1992).
- [2] D.P. Woodruff, D. Brown, P.D. Quinn, T.C.Q. Noakes, and P. Bailey, "Structure determination of surface adsorption and surface alloy phases using medium energy ion scattering," *Nuclear Instruments and Methods in Physics Research Section B: Beam Interactions with Materials and Atoms*, **183**(1-2), 128-139 (2001). [https://doi.org/10.1016/S0168-583X\(01\)00472-4](https://doi.org/10.1016/S0168-583X(01)00472-4)
- [3] D.M. Muradkabilov, D.A. Tashmukhamedova, and B.E. Umirzakov, "Applying low-energy ion implantation in the creation of nanocontacts on the surface of ultrathin semiconductor films," *Journal of Surface Investigation. X-ray, Synchrotron and Neutron Techniques*, **7**(5), 967–971 (2013). <https://doi.org/10.1134/S1027451013050376>
- [4] Y.S. Ergashov, and B.E. Umirzakov, "Structure and Properties of a Bilayer Nanodimensional $\text{CoSi}_2/\text{Si}/\text{CoSi}_2/\text{Si}$ System Obtained by Ion Implantation," *Technical Physics*, **63**(12), 1820–1823 (2018). <https://doi.org/10.1134/S1063784218120058>
- [5] Z. Xie, and X. Luo, "Energy losses of highly charged Ar^{q+} ions during grazing incidence on tungsten surfaces," *Frontiers in Physics*, **12**, 2024. <https://doi.org/10.3389/fphy.2024.1362594>
- [6] S.B. Utamuradova, S.K. Daliev, A.K. Khaitbaev, J.J. Khamdamov, K.J. Matchonov, and X.Y. Utemuratova, "Research of the Impact of Silicon Doping with Holmium on its Structure and Properties Using Raman Scattering Spectroscopy Methods," *East Eur. J. Phys. (2)*, 274-278 (2024). <https://doi.org/10.26565/2312-4334-2024-2-28>
- [7] S. Zainabidinov, S.I. Rembeza, E.S. Rembeza, et al., "Prospects for the use of metal-oxide semiconductors in energy converters," *Appl. Sol. Energy*, **55**, 5–7 (2019). <https://doi.org/10.3103/S0003701X19010146>
- [8] N.Y. Yunusaliyev, "The Gas-Sensitive Properties of Tin Dioxide Films," *East Eur. J. Phys. (4)*, 439-442 (2024). <https://doi.org/10.26565/2312-4334-2024-4-52>
- [9] U.O. Kutliev, M.U. Otabaev, M.K. Karimov, F.K. Masharipov, and I. Woiciechowski, "Scattering of low-energy Ne^+ ions from the stepped surface of $\text{InGaP}(001)\langle 110 \rangle$ at the small angles of incidence," *Physics and Chemistry of Solid State*, **24**(3), 542-548 (2023). <https://doi.org/10.15330/pcss.24.3.542-548>
- [10] U.O. Kutliev, M.U. Otabaev, and M.K. Karimov, "Investigation Ne ions scattering from the stepped $\text{InP}(001)\langle \bar{1}10 \rangle$ surface," *Journal of Physics: Conference Series*, **2388**(1), 012092 (2022). <https://doi.org/10.1088/1742-6596/2388/1/012092>
- [11] M.K. Karimov, F.O. Kuryozov, S.R. Sadullaev, M.U. Otabaev, and S.B. Bobojonova, "Investigation of Defect $\text{InP}(001)$ Surface by Low Energy Ion Scattering Spectroscopy," *Materials Science Forum*, **1049**, 192–197 (2022). <https://doi.org/10.4028/www.scientific.net/MSF.1049.192>

- [12] H.H. Brongersma, T. Grehl, E.R. Schofield, R.A. Smith, and H.R. ter Veen, "Analysis of the outer surface of platinum-gold catalysts by low-energy ion scattering," *Platinum Metals Review*, **54**(2), 81-85 (2010). <https://doi.org/10.1595/147106710X494358>
- [13] A. Rafati, Rik ter Veen, and D.G. Castner, "Low energy ion scattering: determining overlayer thickness for functionalized gold nanoparticles," *Surf. Interface Anal.* **45**(11-12), 2013-2016 (2013). <https://doi.org/10.1002/sia.5315>
- [14] A.S. Ashirov, U.O. Kutliev, S. Hakimov, and S.K. Ismailov, "Low Energy Ar⁺ Ions Scattering from SiO₂(001)-<110> Surface under Grazing Incidence," *Materials Science Forum*, **1049**, 152-157 (2022). <https://doi.org/10.4028/www.scientific.net/MSF.1049.152>
- [15] U. Kutliev, M. Karimov, B. Sadullaeva, and M. Otaboev, "Investigation of the ion scattering process from the A3B5 semiconductors by the computer simulation method," *COMPUSOFT: An International Journal of Advanced Computer Technology*, **7**(4), 2749-2751 (2018). <https://ijact.in/index.php/j/article/view/431/412>
- [16] M.T. Robinson, *MARLOWE Binary Collision Cascade Simulation Program, Version 15b, A Guide for Users*, (London, 2002).
- [17] M.T. Robinson, "Computer Simulation Studies of High-Energy Collision Cascades," *Nuclear Instruments and Methods in Physics Research Section B: Beam Interactions with Materials and Atoms*, **67**(1-4), 396-400 (1992). [https://doi.org/10.1016/0168-583X\(92\)95839-J](https://doi.org/10.1016/0168-583X(92)95839-J)
- [18] L.M. Kishinevsky, "Cross- sections of inelastic atomic collisions," *Izvestiya Phys. Ser.* **26**, 1410-1414 (1962). (in Russian)

ДОСЛІДЖЕННЯ ІМПЛАНТАЦІЇ ІОНІВ O⁺ У ПЛІВКИ SiO₂(001) ПРИ МАЛОКУТОВОМУ ІОННОМУ БОМБАРДУВАННІ

У.О. Кутлієв^а, А.С. Аширов^а, Г.Х. Аллаярова^б, А. Саїдова^а

^аУргенський державний університет, Ургенч, Узбекистан

^бКаришський державний університет, м. Кариші, вул. Узбекистан

Досліджено процес іонної імплантації при малокутовому іонному бомбардуванні плівки SiO₂ (001) при малих значеннях початкової енергії (до 5 кеВ). Поряд з розсіяними іонами O⁺ спостерігається імплантація іонів. Показано, що геометричні параметри поверхневого півканалу впливають на кут бомбардування, який ініціює процес імплантації. Встановлено, що у випадку неглибокого напівканалу процес імплантації спостерігається більше, ніж глибокого напівканалу при одному значенні кута падіння іонів. Отримано залежність імпантованих іонів від кута їх бомбардування. Виявлено, що кілька бомбардуючих іонів були імпантовані в глибокий поверхневий півканал. Це пояснюється впливом другого атомного ряду півканалу. Отримані результати представляють великий інтерес для вивчення процесу іонної імплантації.

Ключові слова: імплантація; іонне бомбардування; комп'ютерне моделювання; розсіювання іонів; фокусування

TIME-CONTROLLED SYNTHESIS OF CdTe QUANTUM DOTS FOR TUNABLE PHOTOLUMINESCENCE

 Adkhamjon I. Zokirov,  Bakhodir B. Akhmedov*

Fergana State University, Fergana, Uzbekistan

**Corresponding Author e-mail: vrrasulov83@gmail.com*

Received March 3, 2025; revised May 11, 2025; accepted May 19, 2025

We report the synthesis and time-dependent photoluminescence evolution of colloidal CdTe quantum dots (QDs), demonstrating that reaction duration can be used as an effective lever to tune their emission characteristics. By varying the synthesis time from 3 to 16 minutes, we observed a pronounced red-shift in the fluorescence maxima—spanning from near-UV (~348 nm) to visible-red (~646 nm) when excited at ~200 nm—and a corresponding increase in emission intensity. These trends, consistent with classical quantum confinement theory, suggest larger nanocrystal diameters and improved surface passivation emerge over the course of the reaction. Such behavior is crucial for optoelectronic and bioimaging applications, which often rely on precise emission wavelength control and high photoluminescence quantum yields. While the substantial rise in fluorescence intensity points to enhanced quantum yields, definitive quantification would require comparisons against well-characterized standards. Nonetheless, these findings highlight the relative ease with which CdTe QD emission properties can be modulated by adjusting key synthesis parameters. Future work targeting extended reaction protocols and advanced capping strategies may further refine emission profiles and long-term stability for applications in nano-optoelectronics, sensing, and biomedical imaging.

Keywords: *CdTe quantum dots; Fluorescence; Quantum confinement; Reaction time; Surface passivation; Photoluminescence*

PACS: 78.67.Hc, 78.55.-m, 81.07.Ta

INTRODUCTION

The study of CdTe quantum dots (QDs) has evolved considerably as researchers strive to understand and harness their unique size-dependent optical properties for diverse applications in bioimaging, optoelectronics, and solar energy conversion. Central to these properties is the quantum confinement effect, which arises when the QD radius approaches or falls below the exciton Bohr radius. Under these conditions, the electronic states become quantized, causing the band gap to widen as QD size decreases, and leading to corresponding shifts in absorption and photoluminescence (PL) spectra. Investigations have consistently shown that smaller QDs exhibit larger band gaps and therefore display blue-shifted emission, whereas larger QDs feature smaller band gaps and red-shifted photoluminescence [1,2,3]. Experimental work has linked these color variations directly to synthesis parameters, particularly reaction time and temperature. For instance, preparing CdTe QDs over extended periods or at higher temperatures results in larger crystallite sizes and a red-shift in both absorption and emission spectra [3,4,5,6]. These findings collectively illustrate how even minor adjustments to the synthesis process can dramatically alter the optical profile of CdTe QDs.

Complementing these experimental efforts, theoretical models like the Brus equation and the effective mass approximation (EMA) have guided interpretations of how QD size correlates with optical band gaps. The Brus equation modifies the standard Schrödinger equation to reflect quantum confinement in semiconductor nanocrystals, successfully reproducing the size-dependent band gap shifts observed in CdTe, CdS, ZnS, and similar materials [7,8]. However, its assumption of an idealized parabolic band structure sometimes conflicts with real systems that display nonparabolicity or multiple crystal phases [9,10]. The EMA provides an alternative perspective, simplifying complex electron-hole interactions by using effective carrier masses; although it is often accurate for relatively large QDs, the approximation may break down when quantum dots are too small, or when detailed surface states and local strain effects come into play [11,12]. These theoretical frameworks remain critical tools for designing experiments that target a specific spectral range—spanning from ultraviolet (~200 nm) to near-infrared (~800 nm)—and for identifying trends in absorption cross-sections and band-edge shifts [8,13].

A key factor in achieving high PL QYs and stable emission under various operating conditions is the deliberate passivation of surface traps, since unpassivated or defect-rich surfaces facilitate non-radiative recombination. Strategies involve either depositing inorganic salts or using chelating agents to seal undercoordinated sites and thereby suppress non-radiative decay [14,15]. In some cases, hybrid approaches incorporate multiple passivating species, which reduces hydroxyl traps, improves QD coupling in device films, and can even enhance solar cell efficiencies by a significant margin [16]. Solvent environments further influence QD stability; binary or ternary solvent systems can offer better dispersibility or more controlled QD growth compared to single-solvent protocols [17,18]. Nonetheless, even the best passivation strategies must account for photochemical degradation, a notable challenge in CdTe QDs. Under prolonged irradiation or certain buffer conditions, thiol ligands can detach, exposing fresh defect sites that precipitate QD aggregation and diminish PL [19,20]. Elevated synthesis temperatures, around 180°C in some protocols, can alleviate some of these

concerns by promoting better crystallinity and stoichiometry [21], yet controlling long-term photo-stability remains a fundamental obstacle. Parallel efforts thus explore cadmium-free alternatives (for example, AgInZnS QDs) to reduce toxicity and circumvent instability issues, though these materials often require distinct capping and passivation chemistries to match CdTe's optical performance [22].

In parallel, understanding the balance between radiative and non-radiative recombination pathways is crucial to optimizing QD devices in areas like optoelectronics. Radiative processes yield photon emission that underpins QD fluorescence, whereas non-radiative processes dissipate energy via phonons or defect-assisted transitions, thereby lowering PL QY [23,24]. Intrinsic defects such as cadmium vacancies represent efficient non-radiative centers, and their presence can degrade device performance by several percentage points [25]. In addition, more subtle processes like two-level recombination, where carriers first occupy a metastable intermediate before rapidly transitioning to a stable state, can raise the recombination rate significantly [26]. The external environment, including the dielectric medium and capping ligand coverage, can alter these dynamics by influencing exciton-phonon coupling and trap state energies [27,28].

Because of the inherent complexity of QD materials, researchers often employ a suite of complementary characterization methods. UV-Vis absorption and PL spectroscopy, which reveal excitonic features and relative band-gap changes, are the cornerstone tools [29]. Further methods like Fourier transform infrared (FTIR) spectroscopy or Raman spectroscopy capture vibrational information about ligands, as well as doping-induced changes in the lattice. Likewise, scanning electron microscopy (SEM) combined with energy dispersive X-ray spectroscopy (EDX) or inductively coupled plasma atomic emission spectrometry (ICP-OES) can confirm elemental composition and the ratio of precursors in final QD samples. Using multiple characterization techniques in tandem not only validates size and shape measurements but also helps disentangle the influences of surface functionalization and doping, ensuring that improvements in QD optical output can be reliably traced back to specific synthesis protocols or passivation steps.

Collectively, these studies suggest that continued advances in synthesis, passivation, and theoretical modeling will further expand the practical potential of CdTe QDs. Despite substantial headway in producing highly luminescent and stable QDs, persistent challenges include maintaining uniform quality across large-scale production, preventing photochemical degradation in demanding environments, and reducing the ecological risks posed by cadmium. Future research directions will likely incorporate additional *in situ* techniques for monitoring QD growth, develop refined theoretical tools that incorporate strain and surface complexities, and leverage machine learning algorithms to optimize synthesis in real-time. Such multidisciplinary efforts can substantially raise the performance benchmarks for CdTe QDs in next-generation devices, all while encouraging safer, more cost-effective, and environmentally responsible protocols that secure QDs' position as critical building blocks in modern nanotechnology.

METHODS

All experiments were performed under laboratory conditions that ensured cleanliness, safety, and reproducibility. Prior to any manipulations, all work surfaces and equipment were cleaned with ethanol, and personnel wore laboratory coats and protective gloves throughout. Inert conditions were maintained by purging glassware and reaction vessels with argon gas to remove atmospheric oxygen and moisture. Cadmium acetate dihydrate ($\text{C}_4\text{H}_6\text{CdO}_4 \cdot 2\text{H}_2\text{O}$) and tellurium (99% purity) were gently ground in separate mortar-and-pestle sets to obtain fine powders. Masses of these reagents were measured on an analytical balance, using small squares of aluminum foil to minimize loss of material and ensure accurate weighing. For the tellurium precursor, 24 mg of finely ground tellurium powder was transferred into a sealable glass vial, followed by the addition of 1.5 ml of tri-*n*-octylphosphine (TOP) via syringe. A small magnetic stir bar was placed inside the vial, which was then tightly sealed, purged with argon, and stirred under an inert atmosphere.

In a separate setup, 108 mg of cadmium acetate dihydrate was placed into a three-necked flask. Oleic acid (0.5 ml) and 20 ml of octadecene were then added to the same flask, along with a magnetic stir bar. One neck of the flask was equipped with an argon inlet, another contained the temperature probe that interfaced with the magnetic stirring hotplate, and the third was fitted with a sealed syringe port to allow reagent additions. The mixture was heated at 120°C for 1 hour under continuous argon flow, after which both this flask and the vial containing the tellurium–TOP solution were kept stirring on separate magnetic stirrers. After 2 hours, the tellurium–TOP mixture was taken off the stirrer; the three-necked flask containing cadmium acetate dihydrate, oleic acid, and octadecene was then heated under argon until the internal temperature reached 180°C. A 1.5 ml aliquot of the tellurium–TOP solution was withdrawn by syringe and quickly injected into the hot cadmium mixture. After 1 minute, an additional 0.5 ml portion of a cadmium acetate dihydrate/oleic acid/octadecene pre-mix (similarly prepared) was introduced, and its reaction time was carefully recorded. Further additions of 0.5 ml portions were made at 20-minute intervals, with a total of four injections. Once the desired reaction times had elapsed and the targeted synthesis stages were completed, the mixture was allowed to cool to room temperature under an argon blanket.

RESULTS

The fluorescence measurements obtained from the SHIMADZU RF-6000 spectrofluorophotometer for quantum dots synthesized at 3, 7, 9, and 16 minutes reveal clear time-dependent shifts in emission maxima and intensities under different excitation wavelengths, consistent with established quantum confinement phenomena in colloidal semiconductor nanocrystals. Examination of the emission profiles excited at approximately 200 nm indicates that the sample harvested

at 3 minutes exhibits its dominant emission feature near 348 nm with a peak intensity of about 5.88×10^5 arbitrary units, whereas the 7-minute sample shows an emission maximum at around 528 nm, displaying an intensity of roughly 5.08×10^5 . Notably, the 9-minute sample under the same excitation conditions red-shifts further to around 614 nm with an increased maximum intensity of approximately 9.87×10^5 , and by 16 minutes, the emission maximum extends to about 646 nm with a substantially higher peak intensity of around 3.06×10^6 . In parallel, measurements collected with an excitation near 400 nm unveil a similar pattern of progressive red-shifting: from ~410 nm (peak intensity $\sim 1.35 \times 10^6$) at 3 minutes, to ~546 nm ($\sim 3.41 \times 10^6$) at 7 minutes, ~628 nm ($\sim 9.84 \times 10^6$) at 9 minutes, and ~668 nm ($\sim 1.33 \times 10^7$) at 16 minutes (fig.1-fig.4). The consistent displacement of the emission maximum to longer wavelengths (higher nanometer values) over prolonged reaction times confirms that these cadmium tellurides (CdTe) quantum dots undergo size growth or increased crystallinity, aligning with the well-documented notion that larger quantum dots emit at lower energies (longer wavelengths) due to a reduction in the quantum confinement effect.

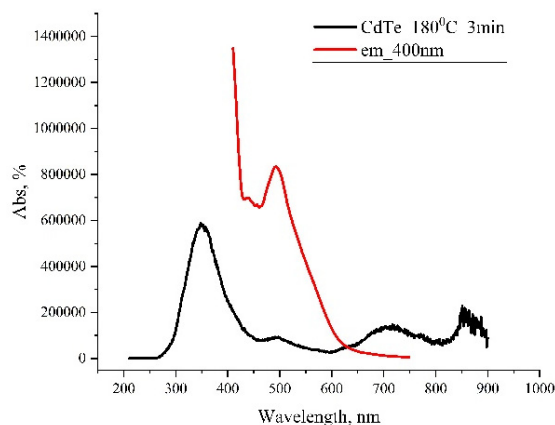


Figure 1. Emission spectra of CdTe QDs (3-minute synthesis) measured at two excitation wavelengths: 200 nm (black) and 400 nm (red). The shorter reaction time yields relatively higher-energy (blue-shifted) emission peaks, indicating smaller nanocrystal diameters

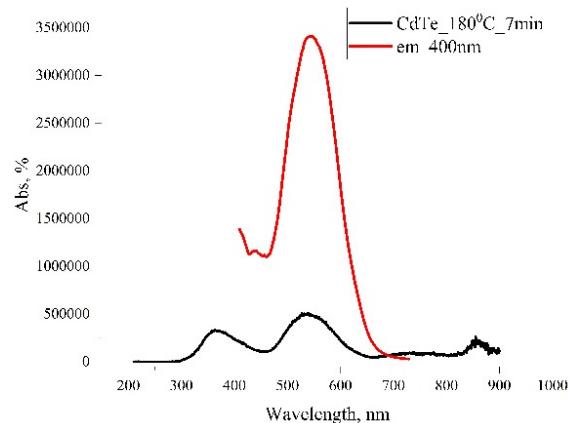


Figure 2. Emission spectra of CdTe QDs (7-minute synthesis) recorded at 200 nm excitation (black) and 400 nm excitation (red). Compared with the 3-minute sample, the emission peaks have shifted to longer wavelengths, reflecting increased particle size.

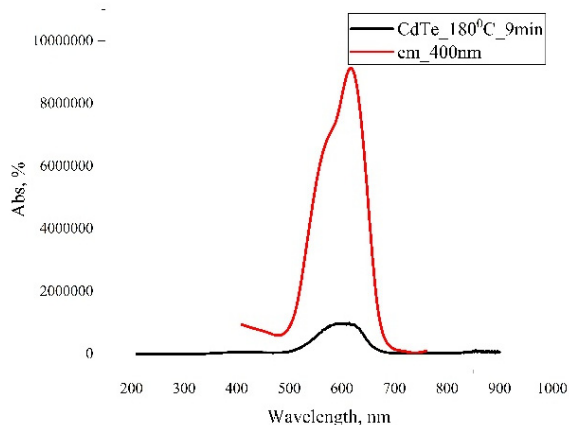


Figure 3. Emission spectra of CdTe QDs (9-minute synthesis), with excitation at 200 nm (black) and 400 nm (red). The pronounced red-shift and higher intensity suggest further growth of the nanocrystals and improved surface passivation.

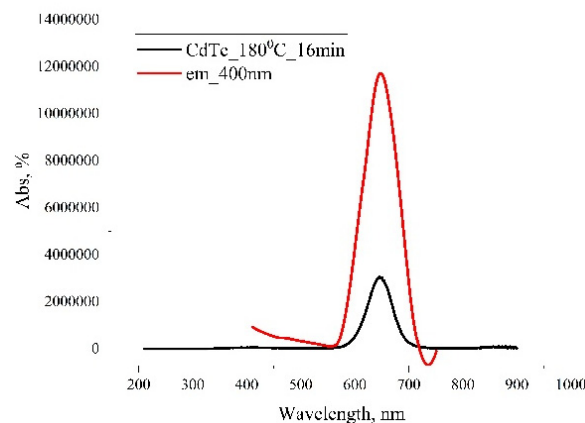


Figure 4. Emission spectra of CdTe QDs (16-minute synthesis) at 200 nm (black) and 400 nm (red) excitations. The most prominent red-shift and highest emission intensity of all samples underscore the largest average nanocrystal size reached within the studied reaction times.

Such marked red-shifts in fluorescence, coupled with the intensification of emission over time, are characteristic of colloidal quantum dot systems and can be understood in the context of exciton confinement: early in synthesis, smaller nanocrystals possess wider band gaps and thus fluoresce at higher energies. As reaction duration increases, dots grow and coalesce into larger crystalline domains, narrowing their band gap and shifting their emission toward the red region. This process is widely described in prior studies of CdTe and related systems, where an evolution from blue-green to orange-red emission is commonly reported and is frequently harnessed to tune optical properties for various applications. The progressive increase in emission intensity is similarly indicative of improved crystallinity or more efficient passivation of surface trap states, both of which can elevate the probability of radiative recombination. Although distinguishing between improvements in surface chemistry and pure particle growth requires complementary analytical methods (such

as transmission electron microscopy or X-ray diffraction), the growing intensities here are strongly suggestive of quantum dot surfaces becoming better stabilized or less defect-prone over time.

In some quantum dot experiments, fluorescence quantum yields can be approximated from relative integrated emission areas when measured against a reference fluorophore or when an absolute photoluminescence quantum yield setup is available. Given the data presented here, which comprise only emission intensities as a function of wavelength for the as-prepared quantum dots, it is not feasible to derive absolute quantum yields without additional information on the instrument's geometry, the incident photon flux, and either a well-characterized standard sample or integrating sphere measurements. The substantial increases in fluorescence intensity do suggest that quantum yields might be improving with longer synthesis times, but any numerical yield determination requires calibration against known standards under matched conditions. Literature on CdTe quantum dots generally indicates that proper surface passivation through thiol ligands and prolonged reflux can heighten quantum yields significantly, often from less than 10% to well over 50%, depending on the reaction environment, capping agents, and post-synthetic treatments. In the current context, the dramatic rise in raw fluorescence signal from 3 to 16 minutes is qualitatively aligned with such improvements, though exact quantification would demand additional experimental calibrations.

From a mechanistic standpoint, the correlation between reaction duration and progressive red-shifting is consistent with a diffusional growth model, wherein initial nuclei form during the early stages of reaction and subsequently ripen into larger nanocrystals. This ripening often follows an Ostwald-type process, with smaller, less stable crystallites dissolving and redepositing onto larger, more energetically favored particles. The net effect is a broadening of size distribution and an overall shift of the average crystal size toward larger diameters, translating to the observed movement of emission to the red. Parallel improvements in the structural order or surface coverage by capping ligands can ameliorate nonradiative decay pathways. Numerous studies of CdTe quantum dots synthesized in aqueous media under thiol stabilization attest to this dynamic, reinforcing that reaction control—whether by time, temperature, or reagent concentrations—offers a direct handle over emitted color and quantum yield.

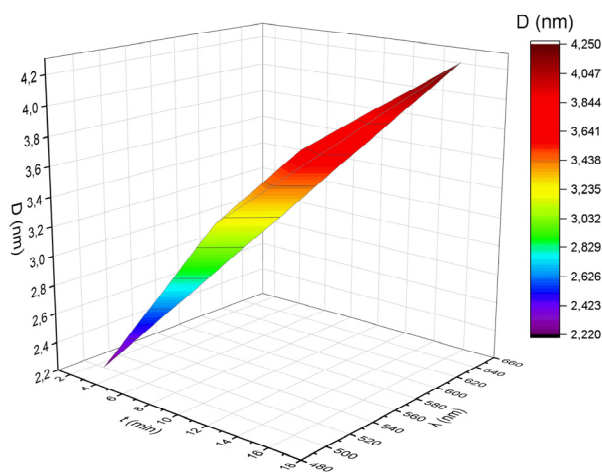


Figure 5. Three-dimensional plot illustrating how the estimated CdTe quantum dot diameter ($\langle D \rangle$, in nm) depends on synthesis time (t , in minutes) and emission wavelength (λ , in nm). Warmer (red) regions correspond to larger particle sizes, corroborating the progressive red-shift observed in Figures 1–4.

In light of these findings, the results strongly encourage further optimization of reaction duration as a straightforward lever to tailor the optical properties of CdTe quantum dots. Specifically, a 16-minute synthesis delivers the highest emission intensity and the greatest red-shift among the tested conditions, which could be especially advantageous for applications requiring long-wavelength emission with robust brightness, such as near-infrared bioimaging. The novelty and relevance of these observations reside in verifying that within a relatively short interval, one can systematically modulate fluorescence behavior to align with various technological demands—be it sensing, labeling, or incorporation into light-emitting diodes. Such tunability underscores the broader utility of quantum dots across nanoelectronics, photonics, and biomedical imaging. As future work, quantitative comparisons of quantum yield could be introduced by employing established reference fluorophores or absolute yield measurement protocols, thereby enabling a more precise link between particle size, crystallinity, and photoluminescence efficiency. The demonstrated capacity to alter emission maxima by nearly 300 nm over a quarter-hour reaction window highlights the potent versatility of solution-processed CdTe nanocrystals, substantiating their place at the forefront of ongoing research in functional nanomaterials.

CONCLUSIONS

This study confirms the strong influence of synthesis time on the optical characteristics of colloidal CdTe quantum dots, showing a systematic red-shift and enhanced fluorescence intensity as reaction duration increases. By comparing emission spectra at different time points (3, 7, 9, and 16 minutes) and excitation wavelengths (~ 200 nm and ~ 400 nm), we demonstrate that prolonged reaction times yield larger nanocrystals with narrower band gaps, as expected from

established quantum confinement principles. Concurrently, the increasing emission intensities across samples point to improved crystallinity or more efficient passivation of surface trap states over time. These observations emphasize the utility of relatively simple synthesis modifications—such as adjusting reaction duration—to finely tune the photoluminescence of CdTe QDs for diverse technological applications, from bioimaging to optoelectronics.

Nonetheless, while the significant rise in fluorescence suggests improved quantum yields, accurately determining absolute values would require further experiments with standard references or integrating-sphere measurements. Characterization methods such as transmission electron microscopy or X-ray diffraction could also provide direct confirmation of size evolution and crystallinity. Future work might investigate additional passivation agents and explore more precise temperature controls to further stabilize the QDs and minimize non-radiative losses. Broader adoption of these refined protocols could ultimately expand the range of wavelengths accessible to CdTe QDs and enhance their operational stability, fueling continued research and development in next-generation nano-optoelectronic and biophotonic devices.

ORCID

Adkhamjon I. Zokirov, <https://orcid.org/0000-0003-1651-1115>; Bakhodir B. Akhmedov, <https://orcid.org/0000-0003-4894-3588>

REFERENCES

- [1] P. Pooja, M. Rana, and P. Chowdhury, "Influence of size and shape on optical and electronic properties of CdTe quantum dots in aqueous environment," In IEEE International Conference on Photonics, **2136**, 040006 (2019). <https://doi.org/10.1063/1.5120920>
- [2] S. Sadjadi, F. Asgari, N. Farhadyar, and N. Molahasani, "Study of quantum size effects and optical characteristics in colloidal cd1-xsnxte quantum dots," Int. J. Nano Dimens. **5**(1), 57-61 (2014). https://www.sid.ir/EN/VEWSSID/J_pdf/1010420140108.pdf
- [3] E. Groeneveld, C. Delerue, G. Allan, Y.-M. Niquet, and C. de M. Donegá, "Size dependence of the exciton transitions in colloidal CdTe quantum dots," Journal of Physical Chemistry C, **116**(43), 23160–23167 (2012). <https://doi.org/10.1021/JP3080942>
- [4] S. Kiprotich, M.O. Onani, and F.B. Dejene, "High luminescent L-cysteine capped CdTe quantum dots prepared at different reaction times," Physica B: Condensed Matter, **535**, 202-210 (2018). <https://doi.org/10.1016/J.PHYSB.2017.07.037>
- [5] S. Kiprotich, F.B. Dejene, J. Ungula, and M.O. Onani, "The influence of reaction times on structural, optical and luminescence properties of cadmium telluride nanoparticles prepared by wet-chemical process," Physica B: Condensed Matter, **480**, 125-130 (2016). <https://doi.org/10.1016/J.PHYSB.2015.08.062>
- [6] J.S. Kamal, A. Omari, K.V. Hoecke, Q. Zhao, A. Vantomme, F. Vanhaecke, R. Capek, and Z. Hens, "Size-dependent optical properties of zinc blende cadmium telluride quantum dots," J. Phys. Chem. C, **116**(8), 5049–5054 (2012). <https://doi.org/10.1021/JP212281M>
- [7] A.A. Issa, and T.A. Hamoudi, "Theoretical studies of the optical properties of ZnS, ZnO and CdS nanopartical using the Brus equation," Tikrit Journal of Pure Science, **27**(3), 15–18 (2022). <https://doi.org/10.25130/tjps.v27i3.55>
- [8] A. Kafel, and S.N.T. Al-Rashid, "Study using the Brus equation to examine how quantum confinement energy affects the optical characteristics of cadmium sulfide and zinc selenide," International Journal of Nanoscience, **22**(04), 2350034 (2023). <https://doi.org/10.1142/S0219581X23500345>
- [9] S.T. Harry, and M.A. Adekanmbi, "Ground state confinement energy of quantum dots and the Brus equation: A mathematical approach," Current Perspective to Physical Science Research, **8**, 146-155 (2024). <https://doi.org/10.9734/bpi/cppsr/v8/7943e>
- [10] J.-L. Liu, "Mathematical modeling of semiconductor quantum dots based on the nonparabolic effective-mass approximation," Nanoscale Systems: Mathematical Modeling, Theory and Applications, **1**, 58-79 (2012).
- [11] H. Yeo, J. Lee, M.E. Khan, H. Kim, D.Y. Jeon, and Y.-H. Kim, "First-principles-derived effective mass approximation for the improved description of quantum nanostructures," J. Phys. Mater. **3**, 034012 (2020). <https://doi.org/10.1088/2515-7639/AB9B61>
- [12] N.B. Abdallah, C. Jourdana, and P. Pietra, "An effective mass model for the simulation of ultra-scaled confined devices," Mathematical Models and Methods in Applied Sciences, **22**(12), 1250039 (2012). <https://doi.org/10.1142/S021820251250039X>
- [13] A. Gusev, O. Chuluunbaatar, S.I. Vinitsky, K.G. Dvoyan, E.M. Kazaryan, H.A. Sarkisyan, V.L. Derbov, et al., "Adiabatic description of nonspherical quantum dot models," Physics of Atomic Nuclei, **75**, 1210–1226 (2012). <https://doi.org/10.1134/S1063778812100079>
- [14] D. Qin, X. Guo, B. Chen, and Z. Rong, "Surface passivated CdTe nanocrystalline film and surface passivation treatment method and application thereof," (2019). U.S. Pat. No. 6,906,339.
- [15] D. Mandal, D. Mandal, N.V. Dambhare, N.V. Dambhare, A.K. Rath, and A.K. Rath, "Reduction of hydroxyl traps and improved coupling for efficient and stable quantum dot solar cells," ACS Applied Materials & Interfaces, **13**(39), 46549–46557 (2021). <https://doi.org/10.1021/ACSAMI.1C11214>
- [16] Q. Zhang, H. Huang, J. Wang, M. Wang, S. Qu, Z. Lan, T. Jiang, et al., "A universal ternary solvent system of surface passivator enables perovskite solar cells with efficiency exceeding 26%," Advanced Materials, **36**(50), 2410390 (2024). <https://doi.org/10.1002/adma.202410390>
- [17] L.T.A. da Rosa, I.F.S. Aversa, E. Raphael, A.S. Polo, A. Duarte, M.A. Schiavon, and L.S. Virtuoso, "Improving photoluminescence quantum yield of CdTe quantum dots using a binary solvent (water + glycerin) in the one-pot approach synthesis," Journal of the Brazilian Chemical Society, **32**(4), 860-868 (2021). <https://doi.org/10.21577/0103-5053.20200237>
- [18] T. Dudka, S.V. Kershaw, S. Lin, J. Schneider, and A.L. Rogach, "Enhancement of the fluorescence quantum yield of thiol-stabilized CdTe quantum dots through surface passivation with sodium chloride and bicarbonate," Zeitschrift für Physikalische Chemie, **232**(9-11), 1399-1412 (2018). <https://doi.org/10.1515/ZPCH-2018-1130>
- [19] J. Ma, J.-Y. Chen, Y. Zhang, P.-N. Wang, J. Guo, W. Yang, and C. Wang, "Photochemical instability of thiol-capped CdTe quantum dots in aqueous solution and living cells: Process and mechanism," Journal of Physical Chemistry B, **111**(41), 12012-12016 (2007). <https://doi.org/10.1021/JP073351+>
- [20] A.S. Tsipotan, M.A. Gerasimova, A.S. Aleksandrovsky, S.M. Zharkov, S.M. Zharkov, and V.V. Slabko, "Effect of visible and UV irradiation on the aggregation stability of CdTe quantum dots," Journal of Nanoparticle Research, **18**, 324 (2016). <https://doi.org/10.1007/S11051-016-3638-0>

- [21] A. Ospanova, Y. Koshkinbayev, A. Kainarbay, T. Alibay, R.K. Daurenbekova, A. Akhmetova, A. Vinokurov, *et al.*, “Investigation of the influence of structure, stoichiometry, and synthesis temperature on the optical properties of CdTe nanoplatelets,” *Nanomaterials*, **14**(22), 1814 (2024). <https://doi.org/10.3390/nano14221814>
- [22] L. Wang, H. Zhang, C. Lu, and L. Zhao, “Ligand exchange on the surface of cadmium telluride quantum dots with fluorosurfactant-capped gold nanoparticles: Synthesis, characterization and toxicity evaluation,” *Journal of Colloid and Interface Science*, **413**, 140–146 (2014). <https://doi.org/10.1016/J.JCIS.2013.09.034>
- [23] T. Kümmell, S.V. Zaitsev, A. Gust, C. Kruse, D. Hommel, and G. Bacher, “Radiative recombination in photoexcited quantum dots up to room temperature: The role of fine-structure effects,” *Physical Review B*, **81**, 241306(R) (2010). <https://doi.org/10.1103/PHYSREVB.81.241306>
- [24] C.H. Wang, T.T. Chen, Y.-F. Chen, M.-L. Ho, C.-W. Lai, and P.-T. Chou, “Recombination dynamics in CdTe/CdSe type-II quantum dots,” *Nanotechnology*, **19**, 115702 (2008). <https://doi.org/10.1088/0957-4484/19/11/115702>
- [25] S.R. Kavanagh, A. Walsh, and D.O. Scanlon, *Rapid recombination by cadmium vacancies in CdTe*, (Zenodo, 2021). <https://doi.org/10.5281/zenodo.4541602>
- [26] J. Yang, L. Shi, L.-W. Wang, and S.-H. Wei, “Non-radiative carrier recombination enhanced by two-level process: A first-principles study,” *Scientific Reports*, **6**, 21712 (2016). <https://doi.org/10.1038/SREP21712>
- [27] M. Califano, “Origins of photoluminescence decay kinetics in CdTe colloidal quantum dots,” *ACS Nano*, **9**(3), 2960–2967 (2015). <https://doi.org/10.1021/NN5070327>
- [28] B. Omogo, J. Aldana, and C.D. Heyes, “Radiative and non-radiative lifetime engineering of quantum dots in multiple solvents by surface atom stoichiometry and ligands,” *Journal of Physical Chemistry C*, **117**(5), 2317–2327 (2013). <https://doi.org/10.1021/JP309368Q>
- [29] M.A. Ruiz-Robles, F. Solis-Pomar, G.T. Aguilar, M.M. Mijares, R.G. Arteaga, O.M. Armenteros, C.D. Gutiérrez-Lazos, *et al.*, “Physico-chemical properties of CdTe/Glutathione quantum dots obtained by microwave irradiation for use in monoclonal antibody and biomarker testing,” *Nanomaterials*, **14**(8), 684 (2024). <https://doi.org/10.3390/nano14080684>

КЕРОВАНІЙ У ЧАСІ СИНТЕЗ КВАНТОВИХ ТОЧОК CdTe ДЛЯ РЕГУЛЬОВАНОЇ ФОТОЛЮМІНЕСЦЕНЦІЇ

Адхамжон І. Зокіров, Баходір Б. Ахмедов

Ферганський державний університет, Фергана, Узбекистан

Ми повідомляємо про синтез і залежну від часу еволюцію фотолюмінесценції колоїдних квантових точок (КТ) CdTe, демонструючи, що тривалість реакції можна використовувати як ефективний важіль для налаштування їхніх характеристик випромінювання. Змінюючи час синтезу від 3 до 16 хвилин, ми спостерігали виражене червоне зміщення максимумів флуоресценції – від ближнього УФ (~348 нм) до видимого червоного (~646 нм) при збудженні при ~200 нм – і відповідне збільшення інтенсивності випромінювання. Ці тенденції, що відповідають класичній теорії квантового обмеження, припускають, що в ході реакції з’являються більші діаметри нанокристалів і покращена пасивація поверхні. Така поведінка має вирішальне значення для оптоелектронних і біовізуалізаційних програм, які часто покладаються на точний контроль довжини хвилі випромінювання та високі квантові виходи фотолюмінесценції. Хоча значне підвищення інтенсивності флуоресценції вказує на підвищені квантові виходи, остаточне кількісне визначення вимагатиме порівняння з добре охарактеризованими стандартами. Тим не менш, ці висновки підкреслюють відносну легкість, з якою властивості випромінювання КТ CdTe можна модулювати шляхом регулювання ключових параметрів синтезу. Майбутня робота, спрямована на розширені протоколи реакції та передові стратегії обмеження, може ще більше вдосконалити профілі викидів і довгострокову стабільність для застосувань у нанооптоелектроніці, зондуванні та біомедичних зображеннях.

Ключові слова: квантові точки CdTe; флуоресценція; квантове обмеження; час реакції; пасивація поверхні; фотолюмінесценція

STRUCTURAL CHARACTERISTICS AND OPTICAL PROPERTIES OF SiC THIN FILMS PRODUCED BY THE RF-PVD METHOD

✉ M.A. Davlatov^{a,b}, ✉ K.T. Davranov^a, ✉ X.T. Dovranov^{a*}, ✉ S.N. Xusanov^b,

✉ A.R. Kodirov^a, S. Xolikulova^a

^aKarshi State University, Karshi, 180100, Uzbekistan

^bKarshi Engineering and Economic Institute. Karshi, 180100, Uzbekistan

*Corresponding Author e-mail: quvondiqdavronm@gmail.com

Received November 14, 2024; revised December 19, 2024; revised April 4, 2025; accepted April 12, 2025

We studied the silicon carbide semiconductor compound, which is widely used as the most characteristic material in the preparation of semiconductors. In the radio frequency (RF) mode of the magnetron sputtering device, 300-400 nm thick SiC thin films were formed in an Ar environment as a reactive gas in a vacuum of 10^{-4} Torr. In the radio frequency mode, a power of 240 W with a frequency of 100 kHz and D=70% were used. The maximum sputtering speed of the magnetron was 50 Å/s. A circular silicon carbide (SiC) target with a diameter of 76.2 mm and a compound content of (99.9%) was used. X-ray analysis of the obtained films was performed on an XRD-6100 device and the Miller indices were determined. In addition, the optical parameters of the thin films were determined. FTIR spectroscopic analysis showed a relative decrease in the transmission spectrum in the far-IR region from 13.1% to 8.9% with increasing SiC film thickness in the range of 480-400 cm^{-1} . Characteristic peaks associated with Si-C and C \equiv C vibrations were also detected. A characteristic Si-C stretching absorption was observed at a wave number of 780 cm^{-1} , where the IR absorption was 88.7%. At a wave number of 2180 cm^{-1} , it corresponds to a triple covalent bond of C \equiv C. The results showed that the optical and electrical properties of SiC films can be easily tuned by changing the Si and C concentrations in the coating for the same film thickness.

Keywords: Magnetron sputtering; Silicon carbide; X-ray phase analysis; Transmission spectrum; Refractive index; FTIR

PACS: 81.15.Jj, 78.66.Sq, 78.20.Bh

INTRODUCTION

Silicon carbide is the most effective material for the production of semiconductors. Silicon carbide powder is also used as a nuclear fuel for fusion reactors [1-2]. SiC mainly exhibits strong chemical bonding, strength, and at the same time, better electrical, optical, and thermal properties than other materials, which is the basis for its effective use in many electronic devices [3-5]. Since silicon carbide thin films have a wide optical energy gap, it can be used in the production of UV detectors. The study of the properties of nanoscale materials is one of the important problems facing modern solid-state physics. The properties of such materials can differ significantly from the properties of both bulk materials and individual nanoparticles that make up the composition [16]. Thus, nanocomposite materials are the basis for the creation of new materials with specific structural, electronic, and optical properties, which are determined by the size, shape, and arrangement of the nanoparticles in their composition.

Recent research results show that silicon carbide is one of the materials that can replace traditional materials in the preparation of semiconductor materials. Due to the electronic properties of silicon carbide thin films, it is one of the main materials in the preparation of new-age optoelectronic and photoelectronic devices. Silicon carbide thin films are used for energy storage in LEDs, nanoelectronics, optoelectronics and photoelectronics, and various other sensors.

Silicon carbide thin films can be deposited by various methods, such as plasma-enhanced chemical vapor deposition (PE-CVD), molecular beam epitaxy (MBE), laser-assisted deposition (PLD), and radio-frequency magnetron sputtering (RF-PVD). Of the various options, reactive magnetron sputtering is the most widely used due to its relative simplicity, high deposition rate, good adhesion, and low production cost [6]. In this work, the optical and X-ray structural properties of SiC films grown by radio frequency RF magnetron sputtering were studied.

EXPERIMENTAL TECHNIQUE

In this study, SiC thin films were deposited on the surface of a silicon monocrystalline substrate using a radio frequency magnetron sputtering device. The deposition process was performed at a temperature of 400 °C using an automatically controlled vacuum furnace. The sputtering rate during the deposition of silicon carbide thin films in an argon atmosphere at a vacuum of 10^{-4} Torr was 50 Å/s, and a power of 240 W at a frequency of 100 kHz and D=70% were used for 6-8 minutes in the reactive radio frequency mode. The maximum sputtering rate of the magnetron was 50 Å/s. A circular silicon carbide (SiC) target with a diameter of 76.2 mm and a compound composition of (99.9%) was used [7,8].

Powder X-ray diffraction is a method for studying the structural properties of a material using X-ray diffraction (X-ray diffraction) from a powder or polycrystalline sample of the material under study [9,10]. The results of the study

are manifested in the dependence of the radiation intensity on the angle of incidence. The advantage of this method is that it is very convenient for determining the structural composition of each substance, even if its structure is unknown. A thin film of silicon carbide was studied by X-ray diffraction and elemental analysis. The identification of the samples was carried out based on the diffraction patterns recorded on a computer-controlled XRD-6100 (Shimadzu, Japan) apparatus.

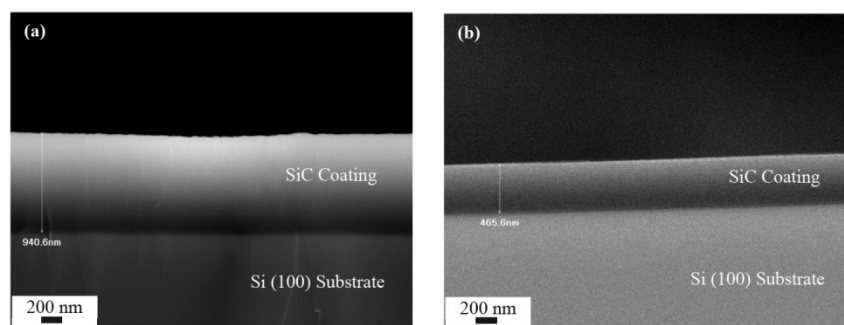


Figure 1. Cross-sectional SEM micrographs of SiC films deposited at a methane flow rate of 35% (a) without external heating at -50°C (b) with external heating at -250°C [13]

The deposition parameters of thin silicon carbide films deposited by reactive DC magnetron sputtering were studied. According to SEM results, the coating thickness decreased significantly with increasing gas (methane) flow rate and temperature. It is also clear from microstructural examinations that denser coatings were formed with increasing deposition temperature. Figure 1 shows the observed changes in coating thickness and morphology [13].

RESULTS AND THEIR DISCUSSION

X-ray diffraction analysis

Figure 2 shows the X-ray diffraction (XRD) patterns for a silicon carbide thin film grown by radio frequency (RF) magnetron sputtering. The X-ray diffraction patterns of a silicon carbide thin film with a thickness of 300 nm show five peaks at diffraction angles. These peaks correspond to angles of 35, 41, 59, 71, and 75. The Miller indices correspond to the (111), (020), (202), (311), and (222) planes, respectively [14].

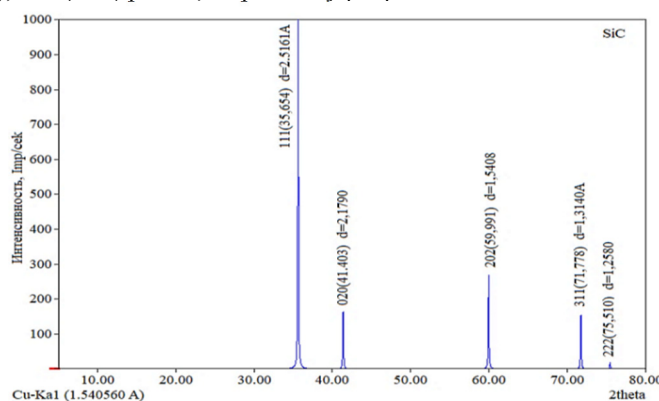


Figure 2. XRD analysis and Miller indices of a silicon carbide thin film grown on a silicon monocrystalline substrate are presented.

Figure 3 shows the crystal structure of SiC. It was found that the silicon carbide crystal lattice is cubic (pr. gr. Pbnm) and consists of two chemical elements: Si, C. This result was obtained by using the Profix software to obtain the “cif” results of the X-ray spectrum data obtained using the XRD-6100 measuring device, and our results were compared with the results of SiC films grown by other methods [15].

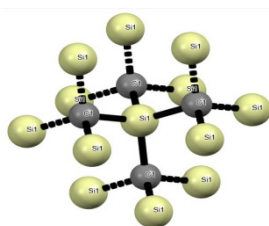


Figure 3. Crystal structure (cubic structure pr. gr. Pbnm)

Figure 4 shows the transmission spectra of SiC thin films of different thicknesses measured using the Qatr-10 (diamond crystal) attachment of the FTIR device. Magnetron sputtering has a strong and direct effect on the optical

properties of the films obtained in different modes. In general, according to the results obtained in the infrared transmission spectrum in the range of 400–3000 cm^{-1} , a significant transmission spectrum was obtained for films with a thickness of 300 nm and 400 nm. With increasing thickness, the transmission spectrum in the range of 400–480 cm^{-1} in the far-IR region showed a relative decrease from 13.1% to 8.9%. The low value of the transmission in the IR region is part of the optical properties of SiC, where its values are associated with the value of the optical band gap in the UV region.

Infrared spectroscopy analysis

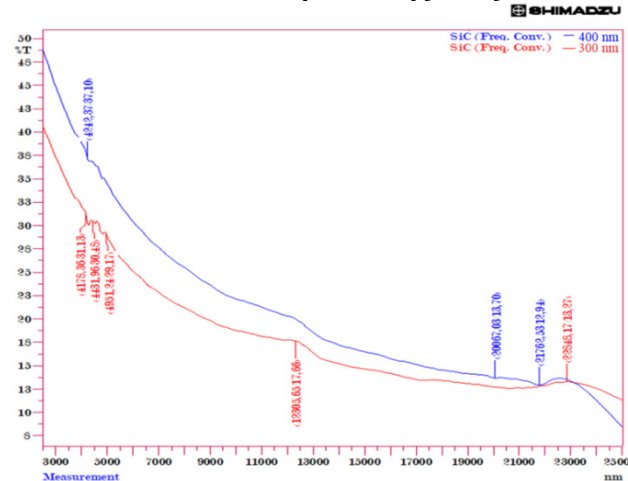


Figure 4. Transmission spectrum of 300–400 nm thick SiC thin films

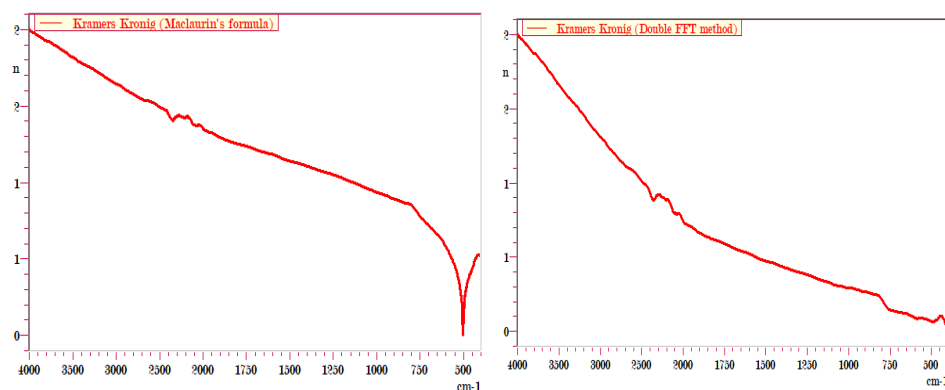


Figure 5. Double FFT method and Maclaurin's spectra based on the processing of the FTIR spectrum of SiC thin films.

The refractive index of the film was calculated based on the processing of the infrared transmission spectrum of SiC thin films, and the refractive index was found to be 2.62 by the Double FFT method according to the Kramers-Kronig function [17]. Based on the Maclaurin formula [18], the infrared absorption corresponding to the wave number of 490 cm^{-1} is confirmed to be $n=2.6$. The absorption spectra of SiC films with a thickness of 300 nm and 400 nm at infrared wavelengths are presented in Figure 6. The absorption (A) values were estimated based on the transmission values. It was observed that the optical absorption values decreased. This makes such a film suitable for use in the production of optoelectronic devices. According to the results of the ultraviolet absorption spectrum of silicon carbide, the refractive index at 632.8 nm is 2.63.

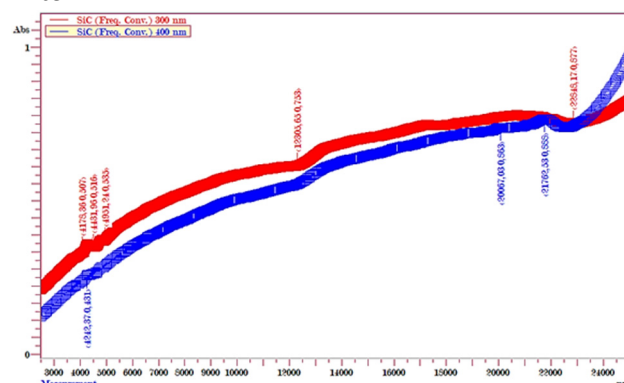


Figure 6. Infrared absorption spectra of SiC thin films with a thickness of 300 nm and 400 nm.

The results of the analysis of SiC thin films were carried out using a Fourier transform infrared spectrophotometer to determine the molecular vibrations. This analysis allows us to assess the quality of the material. As can be seen from the FTIR spectrum, since there are no excessive vibrations, we conclude that there are no impurities or defects in the film. Also, characteristic peaks associated with Si-C and C≡C vibrations were detected. At a wave number of 780 cm^{-1} , where the IR absorption was 88.7%, a characteristic Si-C stretching absorption was observed. At a wave number of 2180 cm^{-1} , it corresponds to a triple covalent bond of C≡C. The covalent characters of Si-C-Si and C-Si-C bonds are characterized by three base potentials [11]. By analyzing the FTIR spectra, the dependence of the photon energy on the Kubelka-Munk [7] function $(ah\nu)^2$ for SiC was obtained. Based on the obtained results, the band gap for the SiC film was calculated. According to the calculation results, the band gap for SiC is 3.2 eV, which is an extrapolated straight line of the curve between $(h\nu)$ and $(ah\nu)^2$. SiC thin films can be widely used in electronic and optical engineering, optoelectronics, solar selective coatings, blue light-emitting diodes, and phototransistors due to their unique properties as a result of the formation of a radio frequency magnetron sputtering device.

CONCLUSIONS

In a radio frequency (100 kHz, D=70%) magnetron sputtering device, 320 nm thick and well-adhered SiC thin films were successfully grown on Si (111) and glass substrates. According to the results of XRD analysis, it was found that the silicon carbide crystal lattice is cubic (pr. gr. Pbnm) and is a compound of two chemical elements: Si, C. FTIR spectroscopic analysis showed a relative decrease in the transmission spectrum in the far-IR region from 13.1% to 8.9% with an increase in the thickness of the SiC film. Also, characteristic peaks associated with Si-C and C≡C vibrations were detected. A characteristic Si-C stretching absorption was observed at a wave number of 780 cm^{-1} , where the IR absorption was 88.7%. At a wavenumber of 2180 cm^{-1} , it corresponds to a triple covalent bond of C≡C. The study is promising for the future study of the formation mechanism of SiC films and the improvement of their optical properties.

ORCID

●M.A. Davlatov, <https://orcid.org/0000-0002-1160-7831>; ●K.T. Davranov, <https://orcid.org/0000-0002-2373-3026>
 ●X.T. Dovranov, <https://orcid.org/0000-0003-1476-6552>; ●S.N. Xusanov, <https://orcid.org/0000-0002-1700-5997>
 ●A.R. Kodirov, <https://orcid.org/0000-0002-0721-6109>

REFERENCES

- [1] D. Shan, D. Sun, M. Wang, and Y. Cao, "Investigation of the Electronic Properties of Silicon Carbide Films with Varied Si/C Ratios Annealed at Different Temperatures," *Crystals*, **14**(1), 45 (2024). <https://doi.org/10.3390/cryst14010045>
- [2] Z.D. Sha, X.M. Wu, and L.J. Zhuge, "Structure and photoluminescence properties of SiC films synthesized by the RF-magnetron sputtering technique," *Vacuum*, **79**(3-4), 250-254 (2005). <https://doi.org/10.1016/j.vacuum.2005.04.003>
- [3] A. Valovič, J. Huran, M. Kučera, A.P. Kobzev, and Š. Gaži, "Properties study of silicon carbide thin films prepared by electron cyclotron resonance plasma technology," *European Physical Journal: Applied Physics, EDP Sciences*, **56**(2), 24013 (2011). <https://doi.org/10.1051/epjap/2011110153>
- [4] T. Tavsanoğlu, E.O. Zayim, O. Agirseven, and S. Yildirim, "Optical, electrical and microstructural properties of SiC thin films deposited by reactive DC magnetron sputtering," *Thin Solid Films*, **674**, 1-6 (2019). <https://doi.org/10.1016/j.tsf.2019.01.047>
- [5] M.Sh. Sardar, M.N. Husin, G. Mohyuddin, F. Ashraf, M. Cancan, M. Alaeiyan, and M.R. Farahan, "Computation of Sombor Indices for Some Classes of Silicon Carbides," *Mathematical Statistician and Engineering Applications*, **71**(3s3), 81-97 (2022). <https://doi.org/10.17762/msea.v71i3s3.350>
- [6] A. Qamar, A. Mahmood, T. Sarwar, and N. Ahmed, "Synthesis and characterization of porous crystalline SiC thin films prepared by radio frequency reactive magnetron sputtering technique," *Applied Surface Science*, **257**(15), 6923-6927 (2011). <https://doi.org/10.1016/j.apsusc.2011.03.033>
- [7] R. Gerhardt, *Properties and Applications of Silicon Carbide*, (InTech, 2011).
- [8] V. Sulyaeva, A. Kolodin, M. Khomyakov, A. Kozhevnikov, and M. Kosinova, "Enhanced Wettability, Hardness, and Tunable Optical Properties of SiC_xN_y Coatings Formed by Reactive Magnetron Sputtering," *Materials*, **16**(4), 1467 (2023). <https://doi.org/10.3390/ma16041467>
- [9] K.T. Dovranov, M.T. Normuradov, K.T. Davranov, and I.R. Bekpulatov, "Formation of Mn₄Si₇/Si(111), CrSi₂/Si(111), and CoSi₂/Si(111) thin films and evaluation of their optically direct and indirect band gaps," *Ukrainian Journal of Physics*, **69**(1), 20-25 (2024). <https://doi.org/10.15407/ujpe69.1.20>
- [10] I.R. Bekpulatov, G.T. Imanova, S.H. Jabarov, B.E. Umirzakov, K.T. Dovranov, V.V. Loboda, I.X. Turapov, *et al.*, "The solid-phase ion-plasma method and thermoelectric properties of thin CrSi₂ films," *J. Mater. Sci: Mater. Electron.* **35**, 1426 (2024). <https://doi.org/10.1007/s10854-024-13163-6>
- [11] M.T. Normuradov, Sh.T. Khozhiev, K.T. Dovranov, Kh.T. Davranov, M.A. Davlatov, and F.K. Khollokov, "Development of a technology for the production of nano-sized heterostructured films by ion-plasma deposition," *Structure of materials, Ukr. J. Phys.* **68**(3), 210-215 (2023). <https://doi.org/10.15407/ujpe68.3.210>
- [12] Kh.T. Davranov, M.T. Normuradov, M.A. Davlatov, K.T. Dovranov, T.U. Toshev, and N.A. Kurbonov, "Preparation of calcium titanate perovskite compound, optical and structural properties," *East Eur. J. Phys.* (3), 350-354 (2024). <https://doi.org/10.26565/2312-4334-2024-3-40>
- [13] T. Tavsanoğlu, E. Baskurt, and O. Yucel, "Optical and Tribological Properties of Silicon Carbide Thin Films Grown by Reactive DC Magnetron Sputtering," *Key Engineering Materials*, **484**, 145-151 (2011). <https://doi.org/10.4028/www.scientific.net/KEM.484.145>

- [14] M. Fraga, M. Massi, and H. Masiel, "Nitrogen doping of SiC thin films deposited by RF magnetron sputtering," *Journal of Materials Science: Materials in Electronics*, **19**(8-9), 835-840 (2008). <https://doi.org/10.1007/s10854-007-9487-y>
- [15] A. Taylor, and D.S. Laidler, "The Formation and Crystal Structure of Silicon Carbide," *British Journal of Applied Physics*, **1**(7), 174 (2002). <https://doi.org/10.1088/0508-3443/1/7/303>
- [16] K.M. Pitman, A.M. Hofmeister, A.B. Corman, and A.K. Speck, "Optical properties of silicon carbide for astrophysical applications," *Astronomy & Astrophysics*, **483**, 661-672 (2008). <https://doi.org/10.1051/0004-6361/20078468>
- [17] P. Bruzzone, R.M. Carranza, J.R. Collet Lacoste, and E.A. Crespo, "Kramers Kronig transforms calculation with a fast convolution algorithm," *Electrochimica Acta*, **48**, 341-347 (2002). [https://doi.org/10.1016/S0013-4686\(02\)00677-1](https://doi.org/10.1016/S0013-4686(02)00677-1)
- [18] N.G. Marley, J.S. Gaffney, J.C. Baird, C.A. Blazer, P.J. Drayton, and J.E. Frederick, "An Empirical Method for the Determination of the Complex Refractive Index of Size-Fractionated Atmospheric Aerosols for Radiative Transfer Calculations," *Aerosol Science and Technology*, **34**, 535-549 (2001). <https://doi.org/10.1080/027868201750296322>

СТРУКТУРНІ ХАРАКТЕРИСТИКИ ТА ОПТИЧНІ ВЛАСТИВОСТІ ТОНКИХ ПЛІВОК SiC, ОТРИМАНИХ МЕТОДОМ RF-PVD

М.А. Давлатов^{a,b}, К.Т. Давранов^a, Х.Т. Довранов^a, С.Н. Хузанов^b, А.Р. Кодіров^b, С. Холікулова^a

^aКаршинський державний університет, Карші, 180100, Узбекистан

^bКаршинський інженерно-економічний інститут, Карші, 180100, Узбекистан

Проведено дослідження напівпровідникової сполуки карбиду кремнію, яка широко використовується як найбільш характерний матеріал для виготовлення напівпровідників. У радіочастотному (RF) режимі пристрою магнетронного розпилення тонкі плівки SiC товщиною 300-400 нм були сформовані в середовищі Ar у вигляді реакційноздатного газу у вакуумі 10^{-4} Торр. У радіочастотному режимі використовувалася потужність 240 Вт з частотою 100 кГц і D=70%. Максимальна швидкість розпилення магнетрона становила 50 Å/с. Використовували круглу мішень з карбиду кремнію (SiC) діаметром 76,2 мм і вмістом сполуки (99,9%). Рентгенографічний аналіз отриманих плівок проводили на приладі XRD-6100 і визначали індекси Міллера. Крім того, були визначені оптичні параметри тонких плівок. Спектроскопічний аналіз FTIR показав відносне зниження спектра пропускання в дальній ІЧ-області з 13,1% до 8,9% зі збільшенням товщини плівки SiC в діапазоні 480-400 cm^{-1} . Також були виявлені характерні піки, пов'язані з коливаннями Si-C і C≡C. Характерне поглинання при розтягуванні Si-C спостерігалось при хвильовому числі 780 cm^{-1} , де ІЧ-поглинання становило 88,7%. При хвильовому числі 2180 cm^{-1} це відповідає потрібному ковалентному зв'язку C≡C. Результати показали, що оптичні та електричні властивості плівок SiC можна легко налаштувати, змінюючи концентрації Si та C у покритті для однакової товщини плівки.

Ключові слова: магнетронне розпилення; карбід кремнію; рентгенофазовий аналіз; спектр пропускання; показник заломлення; FTIR

Zn₂SnO₄ THIN FILMS FOR PHOTOVOLTAICS: STRUCTURAL OPTIMIZATION AND CHARGE TRANSPORT ANALYSIS

 **Fakhriddin T. Yusupov***,  **Tokhirbek I. Rakhmonov**,  **Dadakhon Sh. Khidirov**,
 **Shakhnoza Sh. Akhmadjanova**,  **Javokhirbek A. Akhmadaliyev**

Fergana State Technical University, Fergana, Uzbekistan

**Corresponding Author e-mail: yusupov.fizika@gmail.com*

Received February 5, 2025; revised April 2, 2025; accepted April 12, 2025

In this study, (Zn,Sn)O thin films were synthesized and characterized for potential application as buffer layers in photovoltaic devices. The films were deposited using thermal evaporation in a high-vacuum chamber, followed by a controlled oxidation process in a pure oxygen atmosphere to achieve a ZnO-based oxide layer. Post-deposition annealing was conducted at various temperatures (400°C–550°C) to enhance crystallinity and phase composition. X-ray diffraction (XRD) analysis confirmed the formation of a highly crystalline Zn₂SnO₄ phase, with the optimal structure obtained at 550°C. Optical characterization revealed a temperature-dependent bandgap narrowing effect, significantly influencing transmittance and reflectance spectra. Electrical properties were assessed via Hall effect and current-voltage (I-V) measurements, indicating an increase in carrier mobility and conductivity at higher annealing temperatures. The charge transport mechanism in Ni-(Zn,Sn)O-pSi-Ni heterostructures was analyzed using the space-charge-limited current (SCLC) model, revealing that carrier injection is the dominant transport process. The results demonstrate that (Zn,Sn)O thin films exhibit superior optoelectronic properties, making them promising candidates for photovoltaic and optoelectronic applications.

Keywords: (Zn,Sn)O thin films; Photovoltaic applications; Thermal evaporation; X-ray diffraction; Optical properties; Electrical transport; Hall effect; Charge carrier mobility; Heterostructures

PACS: 78.20.-e, 73.61.Ga, 85.60.-q, 68.55.-a

INTRODUCTION

The continuous advancement in photovoltaic (PV) technology demands the development of highly efficient and stable materials for next-generation solar cells. Among various oxide semiconductors, Zn₂SnO₄ (zinc stannate) thin films have emerged as promising candidates due to their wide bandgap, excellent optical transmittance, and superior charge transport properties [1]. These characteristics make Zn₂SnO₄ an attractive alternative to conventional buffer layers in PV devices, potentially improving light absorption and charge carrier dynamics at the heterojunction interface. The performance of Zn₂SnO₄ thin films is heavily influenced by deposition techniques, annealing processes, and compositional tuning [2]. Thermal evaporation followed by controlled oxidation in an oxygen-rich environment enables precise structural and electronic tailoring, enhancing their suitability for optoelectronic applications. Notably, post-deposition annealing plays a crucial role in modifying crystallinity, phase composition, and defect states - factors that significantly impact electrical conductivity and band alignment. Despite its potential, optimizing the electronic and optical behavior of Zn₂SnO₄ remains a challenge, primarily due to the complex interplay between defect formation, charge carrier mobility, and bandgap engineering [3]. This study systematically investigates the structural, optical, and electrical properties of (Zn,Sn)O thin films, deposited via high-vacuum thermal evaporation and subjected to post-deposition annealing at various temperatures (400°C–550°C). By employing X-ray diffraction (XRD), UV-Vis spectrophotometry, Hall effect measurements, and current-voltage (I-V) analysis, we explore the impact of annealing on phase purity, carrier transport, and optoelectronic performance. Additionally, the charge transport mechanisms in Ni-(Zn,Sn)O-pSi-Ni heterostructures are analyzed using the space-charge-limited current (SCLC) model, providing deeper insights into carrier injection and conduction behavior.

The findings presented in this work contribute to the ongoing efforts in semiconductor material optimization for photovoltaic applications. By understanding the role of annealing and charge transport dynamics, we aim to establish Zn₂SnO₄ as a viable buffer layer material, paving the way for enhanced light conversion efficiency and long-term stability in solar cell architectures [2].

EXPERIMENTAL METHODOLOGY

The deposition of (Zn, Sn)O thin films was carried out in a high-vacuum chamber, where a controlled atmosphere was maintained by evacuating air and subsequently introducing a precise mixture of argon and oxygen gases. In our previous studies [4-6], we have employed this method to investigate the electro-physical and optical properties of both pure zinc oxide and doped zinc oxide thin films. In this regard, various techniques, including physical methods such as RF sputtering [7,8] and chemical approaches like spray pyrolysis [9,10], have been reported for the fabrication of ZTO thin films. This study focuses on the thermal oxidation process, in which Zn-Sn thin films, deposited via thermal

evaporation, undergo oxidation in a pure oxygen atmosphere, forming a ZnO-based oxide layer. The method was applied to different substrates, including silicon, sapphire, and glass to evaluate the feasibility of fabricating heterostructures for optoelectronic and photovoltaic applications.

The deposition parameters were optimized to ensure the formation of nanocrystalline ZnO thin films with a preferential c-axis orientation, an essential factor in enhancing their optoelectronic and electrical properties. The substrate temperature was maintained at 200°C and the working pressure of the Ar+O₂ gas mixture was regulated at 2.3×10^{-2} Pa. The thickness of the ZnO films, ranging from 1.5–2 µm, was precisely controlled using a quartz crystal thickness monitor (IC5) [5].

Following deposition, the films underwent post-deposition thermal annealing in air at different temperatures (400°C, 450°C, 500°C, and 550°C) for 2 hours to promote oxidation and improve crystallinity. The annealing process facilitated the transformation of the Sn/Zn bilayer into a well-defined Zn₂SnO₄ phase while optimizing its structural, electrical, and optical properties. The structural characterization of the annealed films was conducted using X-ray diffraction (XRD) with Cu K α radiation ($\lambda = 1.5406$ Å) to analyze the phase composition, crystallinity, and preferential orientation. The average crystallite size was determined using the Debye-Scherrer equation. The optical properties were investigated through UV-Vis spectrophotometry over a wavelength range of 200–1500 nm, measuring optical transmittance and reflectance to determine the bandgap energy [11].

Electrical properties were characterized using Hall effect measurements and current-voltage (I-V) characterization. The carrier concentration, resistivity, and Hall mobility were determined using a four-probe setup. The I-V characteristics of Ni-(Zn, Sn)O-pSi-Ni heterostructures were recorded at temperatures ranging from 350°C to 550°C to evaluate the diode behavior and charge transport mechanism [12]. The space-charge-limited current (SCLC) model was applied to analyze carrier transport under high-field conditions.

These optimized fabrication and characterization methods ensure a comprehensive evaluation of (Zn, Sn)O thin films for their potential use as buffer layers in photovoltaic and optoelectronic applications.

RESULTS AND DISCUSSION

X-ray Diffraction (XRD) Analysis of Sn/Zn Annealed at Different Temperatures

Figure 1 shows the X-ray diffraction (XRD) patterns of Sn/Zn bilayers annealed at 400°C, 450°C, 500°C, and 550°C reveal significant changes in crystallinity, phase composition, and oxidation state as a function of annealing temperature.

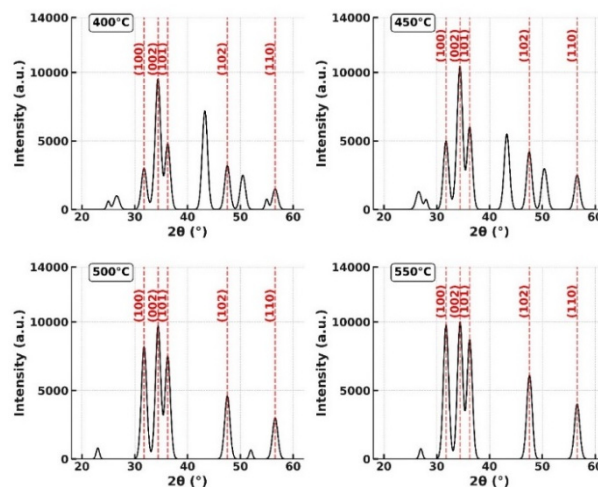


Figure 1. X-ray diffraction (XRD) patterns of (Zn,Sn)O thin films annealed at different temperatures (400°C–550°C)

The diffraction peaks correspond to key crystallographic planes of the hexagonal wurtzite ZnO phase, indexed as (100), (002), (101), (102), and (110). At lower annealing temperatures (400°C and 450°C), the XRD spectra exhibit broad diffraction peaks with lower intensity, indicating a lower degree of crystallinity and incomplete oxidation of the Sn/Zn bilayer. The presence of metallic Zn and Sn peaks suggests that the oxidation process is still in progress. Similar results were reported by R. Ramarajan et al. [13], where Zn, Sn, ZnO, and SnO phases were identified in as-deposited ZTO thin films prepared using a comparable approach. However, the findings of our study demonstrate a distinct advantage due to the simplicity and efficiency of the selected deposition methods, offering a more practical and scalable route for thin-film fabrication. As the annealing temperature increases, the peaks become sharper and more intense, confirming an improvement in crystallinity. At 500°C, most of the metallic Zn and Sn phases disappear, and at 550°C, a well-defined ZnO phase is obtained with strong preferential orientation along the (101) plane.

This trend indicates that increasing the annealing temperature enhances the oxidation process and promotes the formation of a stable ZnO phase. Using the Debye-Scherrer equation:

$$D = \frac{0.9\lambda}{\beta \cos \theta}, \quad (1)$$

where D is the crystallite size, λ is the X-ray wavelength (~ 1.5406 Å for Cu K α radiation), β is the full width at half maximum (FWHM), and θ is the Bragg angle, an increase in crystallite size with higher annealing temperatures can be inferred [14,15]. This suggests that thermal activation enhances grain growth, reducing microstrain and defect density within the crystal lattice.

The transition from a mixed Sn/Zn phase to a highly crystalline ZnO phase at 500°C and 550°C has direct implications for electrical and optical properties. At lower annealing temperatures, the residual metallic Zn and Sn phases contribute to electrical conductivity, potentially leading to a mixed metallic-semiconducting behavior [16]. However, at 500°C and 550°C, the formation of a well-ordered ZnO phase with improved crystallinity enhances its semiconductor properties, including a widening of the optical band gap (~ 3.2 eV) and reduced charge carrier scattering.

In summary, the XRD analysis confirms that annealing plays a crucial role in determining the structural and phase composition of ZnO-based thin films. The optimal annealing temperature for obtaining a pure, highly crystalline ZnO phase is 550°C, where a well-ordered wurtzite structure is achieved. This finding is essential for applications in optoelectronics and photovoltaics, where high structural purity and crystallinity are required for efficient charge transport and light absorption.

Figures 2 and 3 illustrate the transmittance and reflectance spectra of Sn/Zn thin films annealed at 400°C, 450°C, 500°C, and 550°C in air for 2 hours. Optical measurements were conducted in the 200–1500 nm wavelength range to analyze how annealing influences the films light absorption, transmission, and reflection characteristics. Similar results were obtained by Acharya et al. [17] for ZTO thin films fabricated using the co-evaporation technique. However, our study highlights the effectiveness of vacuum thermal evaporation followed by annealing, providing a simpler and more controlled approach for achieving high-quality (Zn,Sn)O thin films.

The transmittance spectra (Figure 2) demonstrate a systematic decrease in optical transmission with increasing annealing temperature. At 400°C, the transmittance reaches a peak of $\sim 85\%$ in the near-infrared region (900–1500 nm), but as the annealing temperature rises to 550°C, transmittance declines to $\sim 65\%$ in the same spectral range. This reduction can be attributed to multiple factors: (i) a redshift in the absorption edge from ~ 370 nm at 400°C to ~ 410 nm at 550°C, indicative of bandgap narrowing caused by increased carrier concentration and defect incorporation; (ii) enhanced optical absorption due to improved crystallinity and the formation of Sn-rich secondary phases, which introduce localized electronic states acting as additional absorption centers; and (iii) interference fringes in the spectra, suggesting variations in film thickness and refractive index modifications as a function of annealing temperature. At shorter wavelengths (200–500 nm), transmittance is significantly reduced, particularly for films annealed at 550°C, where it falls below 10% at 250 nm, due to strong interband transitions.

The reflectance spectra (Figure 3) indicate a progressive increase in reflectance as the annealing temperature rises, especially in the visible and near-infrared regions (500–1500 nm).

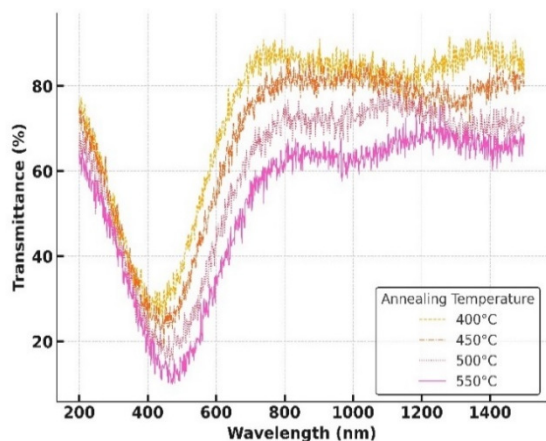


Figure 2. Effect of annealing temperature on the optical transmittance of Zn₂SnO₄ thin films

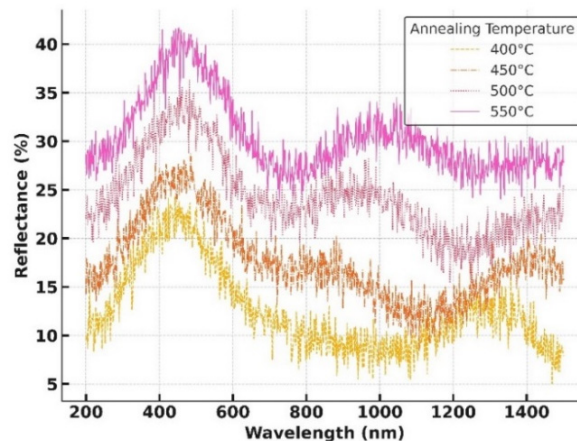


Figure 3. Effect of annealing temperature on the optical reflectance of Zn₂SnO₄ thin films

Reflectance values increase from $\sim 10\%$ at 400°C to $\sim 25\%$ at 550°C, with a more pronounced difference beyond 1000 nm. The observed reflectance enhancement is primarily driven by (i) increased surface roughness, which promotes more diffuse scattering and reflection; (ii) higher free carrier concentration, leading to modifications in the dielectric function and an increase in infrared reflectance due to free carrier absorption; and (iii) structural phase evolution, where a transition from ZnO-dominated films to SnO₂-rich compositions influences the refractive index and light interaction properties. Notably, the reflectance spectra exhibit intersections at ~ 700 nm and ~ 1200 nm, indicative of transitions in optical behavior correlated with phase evolution and carrier dynamics.

These findings confirm that annealing temperature plays a crucial role in tailoring the optical properties of Sn/Zn thin films. Increasing the annealing temperature results in decreased transmittance and increased reflectance, primarily due to bandgap narrowing, defect-induced absorption, and carrier concentration variations.

Figure 4 illustrates the dependence of resistivity, carrier concentration, and Hall mobility on doping concentration in (Zn,Sn)O thin films.

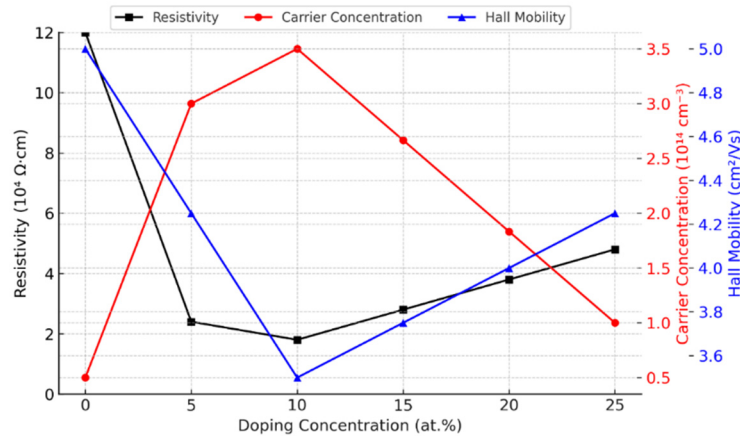


Figure 4. Effect of Sn doping on electrical transport properties of Zn_2SnO_4 thin films

The electrical transport properties of Zn_2SnO_4 thin films, synthesized via vacuum thermal evaporation followed by controlled annealing, were analyzed to understand the dependence of resistivity ($\Omega \cdot \text{cm}$), carrier concentration (cm^{-3}), and Hall mobility (cm^2/Vs) on Sn doping concentration (0–25 at.%).

The resistivity (ρ) variation follows the classical conductivity relation in semiconductors:

$$\sigma = qn\mu, \quad (2)$$

where $\sigma = 1/\rho$ is the electrical conductivity, q is the elementary charge, n is the carrier concentration, and μ is the Hall mobility [18]. The experimental data show a strong inverse correlation between resistivity and doping concentration up to 10 at.%, indicating an increase in free carrier density. Beyond this, resistivity stabilizes, which suggests the onset of ionized impurity scattering and compensation effects, as described by the Matthiessen's rule, where multiple scattering mechanisms contribute additively to the total resistivity.

The carrier concentration (n) increases with Sn doping up to 20 at.%, consistent with the Shockley-Read-Hall (SRH) recombination model, where additional doping introduces donor levels that contribute free electrons to the conduction band. However, at higher doping concentrations, a slight decline in carrier density suggests the formation of compensating defects, such as Sn interstitials (Sn_i^{2+}) or oxygen vacancies (V_O), which act as deep-level traps, reducing the effective carrier density. This behavior is characteristic of heavily doped semiconductors, where self-compensation limits the maximum achievable carrier concentration [19].

The Hall mobility (μ) initially decreases with increasing doping concentration due to ionized impurity scattering, following the Brooks-Herring and Conwell-Weisskopf models [20], where mobility is given by:

$$\mu \propto \frac{T^{3/2}}{N_d \ln(1+C/N_d)}, \quad (3)$$

where N_d is the ionized donor concentration, T is the absolute temperature, and C is a constant related to screening effects.

The decrease in mobility up to 15 at.% suggests that increased doping introduces Coulombic scattering centers, degrading transport properties. However, at higher Sn concentrations (≥ 15 at.%), mobility increases, which indicates a transition to grain boundary-limited conduction, where improved crystallinity reduces carrier scattering at interfaces, enhancing transport pathways. This phenomenon aligns with the Seto model, where grain boundary potential barriers are mitigated at higher doping levels.

Impedance spectroscopy and hot probe measurements confirm that Zn_2SnO_4 remains an **n**-type semiconductor across all doping levels, with a conduction mechanism primarily governed by ionized impurity and grain boundary scattering. The observed trends highlight the role of doping-induced defect states, band edge modifications, and charge compensation effects in determining the electrical transport properties of Zn_2SnO_4 thin films.

Electrical Behavior and Transport Mechanisms in Ni- Zn_2SnO_4 -pSi-Ni Heterostructures

Figure 5 presents the temperature-dependent I-V characteristics of Ni- Zn_2SnO_4 -Si-Ni heterostructures measured at different annealing temperatures (350°C, 400°C, 450°C, 500°C, and 550°C). The logarithmic scale indicates variations in current conduction behavior as a function of applied voltage, highlighting the influence of annealing temperature on electrical properties. In heterostructures, a direct current (DC) flow occurs when the nickel electrode is connected to the positive terminal, with the current being influenced by monopolar injection of charge carriers. This behavior is observed in the logarithmic coordinate system of the volt-ampere characteristics (VAC), where the current-voltage curve displays distinct linear, quadratic, and sharp increases in current, suggesting different conduction regimes. The presence of monopolar injection indicates that charge transport is facilitated by electrons injected from the silicon side, with the flow

being restricted by spatial charge traps within the dielectric material and at the dielectric-semiconductor interface. This implies that in the Ni-Zn₂SnO₄-pSi-Ni heterostructures, the current is likely carried by electrons injected from silicon.

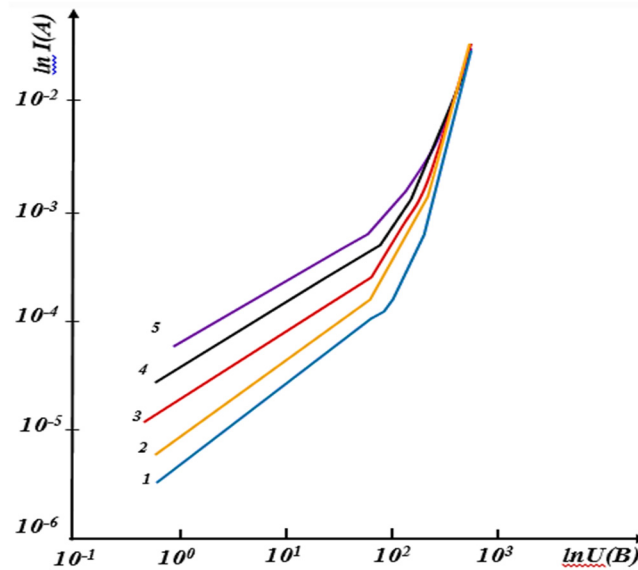


Figure 5. Temperature-dependent I-V characteristics of Ni-Zn₂SnO₄-Si-Ni heterostructures at the following temperatures: 1- 350 °C; 2- 400 °C; 3- 450 °C; 4- 500 °C; 5- 550 °C

The VAC of these structures reveals a three-part behavior: ohmic ($I(U)$), quadratic ($I(U^2)$), and exponential increase in current ($I(U^{m+1})$), where $m > 2$. The current flow from silicon is mainly attributed to the injection of electrons from the silicon side into the Ni-Zn₂SnO₄ layer. The quadratic region in the VAC is expressed by the following relation for monopolar injection [21]:

$$J = \frac{9\epsilon\mu\theta U^2}{8d^3} \quad , \quad (4)$$

where ϵ is the dielectric constant, μ is the drift mobility, U is the applied voltage, d is the thickness of the layer, and θ is the injection factor.

With values of $\epsilon = 8.3$, $\mu \approx 12.0 \text{ cm}^2/\text{V}\cdot\text{s}$, $d = 1 \times 10^{-4} \text{ cm}$, $J = 1.9 \times 10^{-2} \text{ A/cm}^2$, and $U = 30 \text{ V}$, the injection factor θ can be estimated as:

$$\theta = \frac{8Jd^3}{9\epsilon\mu U^2} = 3.3 \times 10^{-5} \quad . \quad (5)$$

This low injection factor suggests the presence of high trap concentrations within the Zn₂SnO₄ layer and at the Zn₂SnO₄-pSi interface. The trap concentration is calculated using the formula:

$$N_t = \frac{2\epsilon U}{ed^2} \quad , \quad (6)$$

which results in a value of $N_t = 3.82 \times 10^{16} \text{ cm}^{-3}$. Additionally, the trap depth can be estimated as:

$$E_r = \frac{kT \ln N_0}{g\theta N_r} \quad , \quad (7)$$

where N_r is the trap concentration. Based on this calculation, the trap depth is found to be $E_r = 0.45 \text{ eV}$.

When the nickel electrode is connected to the negative terminal, electrons are injected into the Zn₂SnO₄ layer, which exhibits a high resistance. The VAC in this case shows linear characteristics on a $\ln I$ and \sqrt{U} coordinate system, which strengthens with increased temperature. This behavior can be explained by the Schottky barrier mechanism. To determine the potential barrier height between Zn₂SnO₄ and Ni, the temperature dependence of VAC was studied. The potential barrier height is calculated using the formula:

$$\phi_B = -kT \ln \frac{I_0}{I_{\text{SAT}}^2} \quad . \quad (8)$$

The value of ϕ_B is found to be $0.75 \pm 0.085 \text{ eV}$. Notably, the VAC shows Schottky characteristics up to 10 V, but the current growth slows with increasing voltage, which might be related to tunneling effects or mixed conduction.

In the Ni-Zn₂SnO₄-Si-Ni heterostructures, when the aluminum electrode is connected to the positive terminal, the current is determined by monoenergetic traps (with $E_a = 0.45 \text{ eV}$, $N_t = 3.82 \times 10^{16} \text{ cm}^{-3}$). When the aluminum electrode

is connected to the negative terminal, the main role is played by the Ni-Zn₂SnO₄ interface, with the VAC explained by the Schottky mechanism. This behavior is linked to the p-n junction formed between the Zn₂SnO₄ and p-Si layers, where charge carrier motion is enhanced in the forward direction and significantly limited in the reverse direction. These characteristics ensure the effective use of the heterostructure as a rectifier in electronic circuits, optoelectronic devices, and photovoltaic systems [22].

CONCLUSIONS

In this study, the structural, optical, and electrical properties of (Zn,Sn)O thin films were systematically investigated for their potential application as buffer layers in photovoltaic devices. The films were synthesized via thermal evaporation followed by a controlled oxidation process in an oxygen-rich environment. Post-deposition annealing at varying temperatures (400°C–550°C) played a crucial role in enhancing crystallinity and phase stability. X-ray diffraction (XRD) analysis confirmed the successful formation of a Zn₂SnO₄ phase, with the optimal crystalline quality observed at 550°C.

Optical characterization revealed a bandgap narrowing effect with increasing annealing temperature, attributed to enhanced carrier concentration and defect states. The transmittance spectra indicated a systematic decrease in transparency, while reflectance measurements demonstrated an increase in optical scattering at higher annealing temperatures, affecting the film's light absorption properties – an essential factor in photovoltaic applications.

Electrical measurements, including Hall effect and I-V characterization, highlighted the impact of annealing on charge transport properties. The carrier mobility and conductivity exhibited significant improvements at optimized annealing conditions, with the space-charge-limited current (SCLC) model supports the conclusion that carrier injection is the dominant conduction mechanism in Ni-(Zn,Sn)O-pSi-Ni heterostructures. Additionally, impedance spectroscopy and hot probe measurements established the n-type conductivity of the Zn₂SnO₄ films across all doping levels, with transport mechanisms primarily governed by ionized impurity and grain boundary scattering.

The findings demonstrate that (Zn,Sn)O thin films exhibit excellent optoelectronic properties, making them viable candidates for integration as buffer layers in photovoltaic devices. The ability to tailor crystallinity, bandgap energy, and charge transport characteristics through annealing and doping provides an avenue for optimizing their performance in next-generation solar cells and optoelectronic applications. Further research should focus on doping-induced modifications to refine defect engineering strategies and enhance charge carrier mobility for improved device efficiency.

ORCID

- Fakhridin T. Yusupov, <https://orcid.org/0000-0001-8937-7944>
- Tokhirbek I. Rakhmonov, <https://orcid.org/0000-0002-6080-6159>
- Dadakhon Sh. Khidirov, <https://orcid.org/0000-0003-1391-4250>
- Shakhnoza Sh. Akhmadjanova, <https://orcid.org/0009-0002-1568-3281>
- Javoxirbek A. Axmadaliyev, <https://orcid.org/0009-0001-7753-1462>

REFERENCES

- [1] M.K. Pham, P.H. Dang, and T.V. Huynh, “Studying the structural, optical, and electrical characteristics of Zn₂SnO₄ films using a direct current magnetron sputtering method,” *Ceramics International*, **50**(4), 6824–6835 (2023). <https://doi.org/10.1016/j.ceramint.2023.12.026>
- [2] N.M. Martin, T. Törndahl, M. Babucci, F. Larsson, K.A. Simonov, D. Gajdek, L.R. Merte, *et al.*, “Atomic Layer Grown Zinc-Tin Oxide as an Alternative Buffer Layer for Cu₂ZnSnS₄-Based Thin Film Solar Cells: Influence of Absorber Surface Treatment on Buffer Layer Growth,” *ACS Applied Energy Materials*, **5**(11), 13971–13980 (2022). <https://doi.org/10.1021/acsaelm.2c02579>
- [3] E. Gnenna, N. Khemiri, and M. Kanzari, “Development and characterization of (Zn,Sn)O thin films for photovoltaic application as buffer layers,” *SN Appl. Sci.* **2**(2), 1–9 (2020). <https://doi.org/10.1007/S42452-020-1971-5>
- [4] Z.X. Mirzajonov, K.A. Sulaymonov, T.I. Rakhmonov, F.T. Yusupov, D.Sh. Khidirov, and J.S. Rakhimjonov, “Advancements in Zinc Oxide (ZnO) thin films for photonic and optoelectronic applications: a focus on doping and annealing processes,” *E3S Web of Conferences*, **549**, 03013 (2024). <https://doi.org/10.1051/e3sconf/202454903013>
- [5] N.A. Sultanov, Z.X. Mirzajonov, F.T. Yusupov, and T.I. Rakhmonov, “Nanocrystalline ZnO Films on Various Substrates: A Study on Their Structural, Optical, and Electrical Characteristics,” *East European Journal of Physics*, (2), 309–314 (2024). <https://doi.org/10.26565/2312-4334-2024-2-35>
- [6] F.T. Yusupov, T.I. Rakhmonov, M.F. Akhmadjonov, M.M. Madrahimov, and S.S. Abdullayev, “Enhancing ZnO/Si Heterojunction Solar Cells: A Combined Experimental and Simulation Approach,” *East European Journal of Physics*, (3), 425–434 (2024). <https://doi.org/10.26565/2312-4334-2024-3-51>
- [7] N.E. Sung, H.K. Lee, K.H. Chae, J.P. Singh, and I.J. Lee, “Correlation of oxygen vacancies to various properties of amorphous zinc tin oxide films,” *J. Appl. Phys.* **122**, 085304 (2017). <https://doi.org/10.1063/1.5000138>
- [8] Shajan, Nirmal and Dhanasingh, Bharathi Mohan, “RF magnetron sputtering of Zn₂SnO₄ thin films: optimising microstructure, optical and electrical properties for photovoltaics,” *Journal of Materials Science: Materials in Electronics*, **35**, 882 (2024). <https://doi.org/10.1007/s10854-024-12648-8>
- [9] V.V. Ganbavle, M.A. Patil, H.P. Deshmukh, and K.Y. Rajpure, “Development of Zn₂SnO₄ thin films deposited by spray pyrolysis method and their utility for NO₂ gas sensors at moderate operating temperature,” *J. Anal. Appl. Pyrolysis*, **107**, 233–241 (2014). <https://doi.org/10.1016/j.jaap.2014.03.006>
- [10] B. Zaidi, N. Houaidji, A. Khadraoui, S. Gagui, C. Shekhar, Y. Özen, K. Kamli, *et al.*, “Structural, Optical and Electrical Properties of Zn_xSn_{1-x}S Thin Films Deposited by Chemical Spray Pyrolysis,” *Journal of Nano Research*, **61**, 72–77 (2020). <https://doi.org/10.4028/WWW.SCIENTIFIC.NET/JNANOR.61.72>

- [11] X. Li, Z. Su, S. Venkataraj, S.K. Batabyal, and L.H. Wong, "8.6% Efficiency CZTSSe solar cell with atomic layer deposited Zn–Sn–O buffer layer," *Sol. Energy Mater. Sol. Cells*, **157**, 101–107 (2016). <https://doi.org/10.1016/j.solmat.2016.05.032>
- [12] M.K. Jayaraj, K.J. Saji, K. Nomura, T. Kamiya, and H. Hosono, "Optical and electrical properties of amorphous zinc tin oxide thin films examined for thin film transistor application," *J. Vac. Sci. Technol. B*, **26**, 495 (2008). <https://doi.org/10.1116/1.2839860>
- [13] R. Ramarajan, M. Kovendhan, D.T. Phan, K. Thangaraju, R.R. Babu, K.J. Jeon, and D.P. Joseph, "Optimization of Zn₂SnO₄ thin film by post oxidation of thermally evaporated alternate Sn and Zn metallic multi-layers," *Appl. Surf. Sci.* **449**, 68–76 (2018). <https://doi.org/10.1016/j.apsusc.2018.01.029>
- [14] M.S. Abd Aziz, M.S. Salleh, G. Krishnan, N. Mufti, M.F. Bin Omar, and S.W. Harun, "Structural, Morphological and Optical Properties of Zinc Oxide Nanorods prepared by ZnO seed layer Annealed at Different Oxidation Temperature," *Malaysian Journal of Fundamental and Applied Sciences*, **18**(3), 383–392 (2022). <https://doi.org/10.11113/mjfas.v18n3.2538>
- [15] S.W. Chang, K. Ishikawa, and M. Sugiyama, "RF magnetron sputtering deposition of amorphous Zn–Sn–O thin films as a buffer layer for CIS solar cells," *Phys Status Solidi C*, **12**, 688–691 (2015). <https://doi.org/10.1002/pssc.201400255>
- [16] J.Y. Hwang, and S.Y. Lee, "Effect of Annealing Temperature on Electrical Properties and Stability of Si–Zn–Sn–O Thin Film Transistors Under Temperature Stress," *Transactions on Electrical and Electronic Materials*, **19**(1), 15–19 (2018). <https://doi.org/10.1007/S42341-018-0011-2>
- [17] R. Acharya, Y.Q. Zhang, and X.A. Cao, "Characterization of zinc–tin–oxide films deposited by thermal co-evaporation," *Thin Solid Films*, **520**, 6130–6133 (2012). <https://doi.org/10.1016/j.tsf.2012.05.087>
- [18] K. Ellmer, "Hall Effect and Conductivity Measurements in Semiconductor Crystals and Thin Films," in: *Characterization of Materials*, (2012), pp. 1–16. <https://doi.org/10.1002/0471266965.COM035.PUB2>
- [19] A. Treglia, F. Ambrosio, S. Martani, G. Folpini, A.J. Barker, M.D. Albaqami, F. De Angelis, *et al.*, "Effect of electronic doping and traps on carrier dynamics in tin halide perovskites," *Materials Horizons*, **9**(6), 1763–1773 (2022). <https://doi.org/10.1039/d2mh00008c>
- [20] D. Rode, and J. Cetnar, "Electron mobility of heavily doped semiconductors including multiple scattering by ionized impurities," *Journal of Applied Physics*, **134**, 075701 (2023). <https://doi.org/10.1063/5.0165201>
- [21] N. Sultanov, Z. Mirzajonov, and F. Yusupov, "Technology of production and photoelectric characteristics of AlB 10 heterojunctions based on silicon," *E3S Web of Conferences*, **458**, 01013 (2023). <https://doi.org/10.1051/e3sconf/202345801013>
- [22] J.H. Lee, B.H. Lee, J. Kang, M.S. Diware, K. Jeon, C. Jeong, S.Y. Lee, and K.H. Kim, "Characteristics and Electronic Band Alignment of a Transparent p-CuI/n-SiZnSnO Heterojunction Diode with a High Rectification Ratio," *Nanomaterials*, **11**(5), 1237 (2021). <https://doi.org/10.3390/NANO11051237>

ТОНКІ ПЛІВКИ Zn₂SnO₄ ДЛЯ ФОТОВОЛЬТАЇКИ: СТРУКТУРНА ОПТИМІЗАЦІЯ ТА АНАЛІЗ ПЕРЕНЕСЕННЯ ЗАРЯДУ







Фахріддін Т. Юсупов, Тохірбек І. Рахмонов, Дадахон Ш. Хідіров, Шахноза Ш. Ахмаджонова,
Жавохірбек А. Ахмадалиєв

Ферганський політехнічний інститут, Фергана, Узбекистан

У цьому дослідженні синтезовано та охарактеризовано тонкі плівки (Zn,Sn)O для потенційного використання як буферних шарів у фотовольтаїчних пристроях. Плівки були осаджені методом термічного випаровування у високовакуумній камері, а потім піддані контрольованому процесу окислення в атмосфері чистого кисню для утворення ZnO-оксидного шару. Післяосадочний відпал проводився при різних температурах (400°C–550°C) для покращення кристалічності та фазового складу. Аналіз рентгенівської дифракції (XRD) підтвердив формування високо-кристалічної фази Zn₂SnO₄, при цьому оптимальна структура була досягнута при 550°C. Оптична характеристика виявила температурно-залежне звуження забороненої зони, що суттєво вплинуло на спектри пропускання та відбивання. Електричні властивості оцінювали за допомогою вимірювань ефекту Холла та струм-напругових (I-V) характеристик, які показали збільшення рухливості носіїв заряду та електропровідності при підвищених температурах відпалу. Механізм перенесення заряду в гетероструктурах Ni-(Zn,Sn)O-pSi-Ni був проаналізований за допомогою моделі струму, обмеженого просторовим зарядом (SCLC), що виявило домінуючі процеси інжекції носіїв заряду. Отримані результати демонструють, що тонкі плівки (Zn,Sn)O мають відмінні оптоелектронні властивості, що робить їх перспективними кандидатами для фотовольтаїчних та оптоелектронних застосувань.

Ключові слова: (Zn,Sn)O тонкі плівки; фотоелектричні застосування; термічне випаровування; рентгенівська дифракція; оптичні властивості; електротранспорт; ефект Холла; рухливість носіїв заряду; гетероструктури

EFFECT OF GAMMA IRRADIATION ON THE DIELECTRIC PROPERTIES AND X-RAY PHASE ANALYSIS OF THE POLYPROPYLENE Na⁺MONTMORILLONITE COMPOSITE

 **Rasmiyya L. Mammadova**^a,  **Kamala M. Guseinova**^{b,c,*},  **Kifayat A. Guliyeva**^b,
 **Khayal Sh. Valibayov**^d,  **Vafa E. Atayeva**^d,  **Dilara M. Qafarova**^e

^aKarabakh University, Khankendi, Azerbaijan

^bSumgait State University, Sumgait, Azerbaijan

^cKhazar University, Baku, Azerbaijan

^dSheki Regional Scientific Centre, Sheki, Azerbaijan

^eAzerbaijan University of Architecture and Civil Engineering, Baku, Azerbaijan

*Corresponding Author e-mail: kemale.huseynova@sdu.edu.az

Received January 10, 2025; revised April 29, 2025; in final form May 6, 2025; accepted May 12, 2025

Effect of γ -irradiation on the dielectric properties of polymer composites based on polypropylene (PP) with Na⁺-montmorillonite (MMT) nanoparticles has been investigated. It has been found that γ -irradiation in the dose range of 100-200 kGy leads to slight deterioration in the dependences of $\epsilon = f(T)$ (a) and $\text{tg}\delta = f(T)$ of the polypropylene-based composite with Na⁺MMT filler. Further increasing the radiation dose, a sharp increase in ϵ and $\text{tg}\delta$ above the temperature ~ 440 K has been observed. The obtained results show that after irradiation, the active centers, radicals, and defects formed in the polymer structure interact with filler nanoparticles, reducing the mobility of the polymer chain and consequently decreasing the values of ϵ and $\text{tg}\delta$ of the composite. But at an irradiation dose of 300 kGy, the properties of the interphase layer deteriorate as a result of incipient destruction, which leads to an insignificant increase in the values of ϵ and $\text{tg}\delta$. The results of the analyses showed that the introduction of Na nanoclays (MMT) into polypropylene in an amount of 0.5% by volume leads to some improvement in the dielectric properties before and after irradiation. It is assumed that the deterioration of the dielectric properties during irradiation in composites occurs due to changes in the crosslinking and destruction processes in the polymer matrix and at the polymer-filler interphase boundary. It is shown that due to γ -irradiation of polymer composites, it is possible to expediently control its dielectric and electrophysical properties.

Keywords: Polypropylene; Na⁺-montmorillonite; Gamma irradiation; Dielectric constant; Dielectric energy loss

PACS: 71.20 Nr; 72.20 Fr

INTRODUCTION

One of the promising fields of materials science is the creation of new composite polymer materials with unique properties. Introduction of a filler into a polypropylene (PP) matrix considerably modifies the structure and properties of composite materials due to interfacial interactions and the formation of a boundary nanolayer near the filler particles. This identifies the peculiarities of the temporary distribution of the local field in certain regions of the polymer system and the frequency dispersion of the effective complex dielectric permittivity of composite materials. The use of polymer materials enables the development fundamentally new designs of various types of products, helps to reduce their weight, operating and transportation costs, improves their quality and appearance [1-4].

Polymer composites have been known to be very sensitive to the effects of various ionizing radiation. The literature research in this direction reveals that low doses of radiation exposure led to a relative improvement in physical properties, whereas high doses lead to the destruction of materials, worsening their physical properties. In this perspective, the study of electrophysical properties of polymer composites before and after exposure to γ -irradiation is significant. Exposure to ionizing radiation leads to changes in the properties of the supramolecular structure (SMS) of the matrix and the boundary layer as a result of the processes of crosslinking, destruction and oxidation and, therefore, to a change in the electroactive properties of the composites, which consists of studying their electrophysical properties, i.e. temperature and frequency dependences of electrical conductivity (σ) and dielectric characteristics (ϵ and $\text{tg}\delta$) [5-8].

Literature data analysis showed that introduction of Dk₁ and Dk₂ types of nanoclays into polypropylene in the amount of 2% by volume content leads to some improvement in physical and mechanical properties. In these works, however, there is no information about the structure of these fillers and the degree of their compatibility with the matrix. But it should be noted that depending on the deposit, montmorillonite (MMT) has different modifications and differ in particle size. The use of Na⁺MMT as modifiers is related, firstly, to the amount of quaternary ammonium guanine cations in them and, secondly, to the good adhesion of clay with polar polyolefin molecules [9].

In this context, the presented work is aimed at studying electrophysical properties and relaxation processes in initial and irradiated polymer composites (PP/Na⁺MMT). Despite the large-scale study of Na⁺MMT characteristics the dielectric, electrophysical properties and peculiarities of interfacial phenomena in its composites with polymers remain understudied. In our opinion, research in this direction will end in the future with the creation of electroactive composite materials with new characteristics and converters based on them.

EXPERIMENTAL PART

Composites were prepared using polypropylene (PP) as the polymer matrix and nanoscale sodium montmorillonite (Na^+MMT) particles as the reinforcing filler. Sodium montmorillonite is a type of smectite clay mineral, which typically forms through the long-term weathering of volcanic ash and rocks, often aided by biological activity, such as the actions of lichens and fungi. The structure of Na^+MMT consists of layered silicate sheets with a very fine crystal grain size, typically less than 100nm. These layers carry a net negative charge, which is balanced by exchangeable cations such as Na^+ located in the interlayer spaces. This charge asymmetry enables montmorillonite to interact with a wide range of chemical species. Due to its layered structure and high specific surface area, Na^+MMT can adsorb both cationic and anionic substances, making it highly versatile in composite and environmental applications. Even nonionic substances can be retained through secondary valence forces, such as van der Waals interactions or hydrogen bonding. Furthermore, the interlayer space within montmorillonite crystals can accommodate various molecules, allowing for intercalation and improving dispersion in polymer matrices.

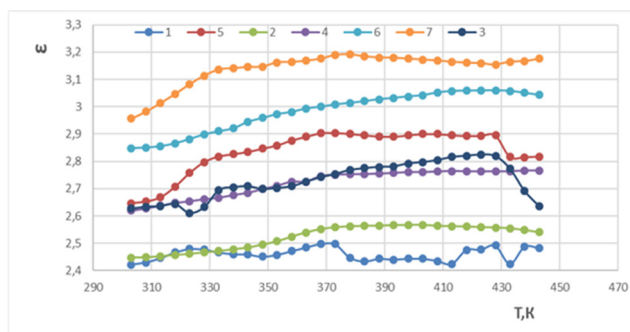
The samples were prepared from mixtures of PP and Na^+MMT powders in different component ratios, and then from these mixtures, by hot pressing at the melting point of the polymer matrix under a pressure of 15 MPa for 10 minutes, PP/ Na^+MMT nanocomposites were prepared in the form of a film, with subsequent cooling. The samples were obtained in different temperature-time crystallization modes, namely, slow cooling (SC), when the samples are cooled to room temperature at a rate of 2 deg/min, and rapid cooling (RC) in an ice-water mixture at a rate of 30 deg/min [9].

For the preparation of the composites, disc-shaped samples were fabricated by homogeneously mixing polypropylene with varying volume fractions (x vol.%) of Na^+MMT particles. The MMT filler particles had sizes up to 100 nm. The mixture was processed to ensure uniform distribution of the clay particles within the polymer matrix, which is critical for achieving reliable and reproducible dielectric properties. To characterize the electrical performance of the resulting composites, dielectric measurements were conducted using an E7-20 immittance meter. The frequency range for these measurements spanned approximately from 25 Hz to 10^6 Hz. This wide frequency range allowed for the analysis of different polarization mechanisms and charge transport phenomena within the composite material. The results help to evaluate how the inclusion of Na^+MMT affects the dielectric behavior of the polypropylene matrix and can provide insight into the composite's potential applications in electronics, insulation, or barrier materials. X-ray phase analysis was carried out on a Bruker D2 diffractometer. Cu Ka ($\lambda=1.541780$ Å) was used as the light source passing through a nickel filter in the same mode. The reflection measurement error did not exceed $\theta=\pm 0,020$ [10].

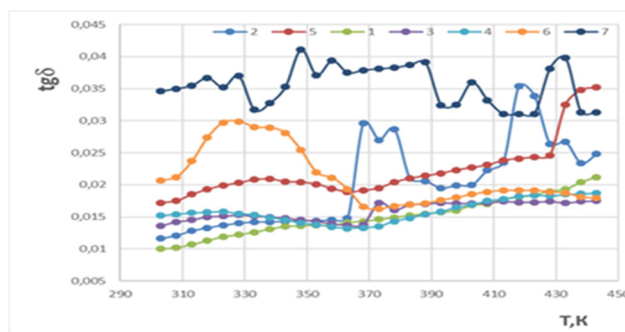
RESULTS AND DISCUSSION

For comparison with irradiated samples, the given dependences reflect the results of the initial polymer and composite based on it. It is known that polypropylene is a polar, polycrystalline polymer and has a certain dipole moment, which is reflected in the temperature dependences of ϵ and $\text{tg}\delta$.

Fig.1 depicts the temperature dependences of $\epsilon = f(T)$ (a) and $\text{tg}\delta = f(T)$ (b) of the initial polypropylene composite with 0, 0.5, 2, 3, 5, 6, 7 vol.% Na^+MMT fillers measured at a frequency of $\nu = 1$ kHz. It is clear from Fig.1(a) that the dielectric constant (ϵ) of the initial PP varies slightly in the temperature range of 320–450 K. Furthermore, in the dependence of $\epsilon = f(T)$, small maxima were observed in the temperature range of 330–333 K, 370–380 K, and 430–433 K, due to the sample inhomogeneity. According to Fig.1a, curve 2, when Na^+ (0.5 vol.%) is added to the polymer, the values of ϵ do not change in the temperature range of 300–350 K, and it increases slightly with a further increase in temperature. Meanwhile, the previously observed maxima in the range of 370–380 K and 430–433 K are not observed, which may be associated with an increase in the mobility of the polymer chain. The result obtained is confirmed by our previous results. Fig.1 (a) illustrates that with further increase in Na content (2; 3 and 5 vol.%) in the polymer, ϵ increases exponentially in the range of 320–450 K. It is also evident from Fig. 1(a) that the samples containing 2 and 3 vol.% Na^+MMT show a decline in dielectric constant in curves 4 and 5 over the temperature of 440 K.



a



b

Figure 1a. Temperature dependence of $\epsilon = f(T)$ before irradiation of the PP+vol.% Na^+MMT composite at a frequency of $\nu = 1$ kHz. 1-0%; 2-0.5%; 3-7%; 4-6%; 5-5%; 6-3%; 7-2%

Figure 1b. Temperature dependence of $\text{tg}\delta = f(T)$ before irradiation of the PP+vol.% Na^+MMT composite at a frequency of $\nu = 1$ kHz. 1-2%; 2-3%; 3-5%; 4-6%; 5-7%; 6-0.5%; 7-0%

Figure 1b. demonstrates the temperature dependence of $\text{tg}\delta = f(T)$ before irradiation of the PP/(0, 0.5, 2, 3, 5, 6, 7 vol.%) Na^+MMT composite at a frequency of $\nu = 1$ kHz. The dependences demonstrate that the introduction of Na^+MMT into the polymer leads to a rather pronounced maximum of $\text{tg}\delta$ in the initial composite, which is due to dielectric losses during dipole relaxation and relaxation of the accumulated charge at the interphase boundary of the amorphous and crystalline phases in the polymer matrix and matrix with Na^+MMT . Comparison of the curves points out that the observed maximum in $\varepsilon = f(T)$ and the corresponding shoulder in the dependence of $\text{tg}\delta = f(T)$ of the composite is considered to be the result of the relaxation of the charge accumulated at the polymer-filler interface, which is released upon crosslinking of the polymer matrix.

To study the effect of γ -irradiation on the dielectric properties in PP/ Na^+MMT composites, the dependences of $\varepsilon = f(T)$ and $\text{tg}\delta = f(T)$ were investigated at $T=300$ K at various radiation doses. Figure 2 represents the temperature dependence of $\varepsilon = f(T)$ after irradiation of the PP/(0, 0.5, 2, 3, 5 vol.%) Na^+MMT composite with 200 kGy at a frequency of $\nu = 1$ kHz. Fig. 2(a) demonstrates that upon irradiation with a dose of 200 kGy in the dependence of $\varepsilon = f(T)$, a sharp increase in the curves is observed at 440 K only for samples 1 and 5.

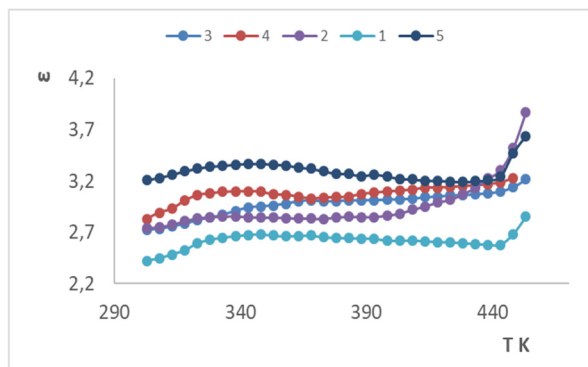


Figure 2a. Temperature dependence of $\varepsilon = f(T)$ after irradiation of the PP/ Na^+ MMT composite with 200 kGy at a frequency of $\nu = 1$ kHz. 1-0%; 2-2%; 3-3%; 4-5%; 5-0.5%

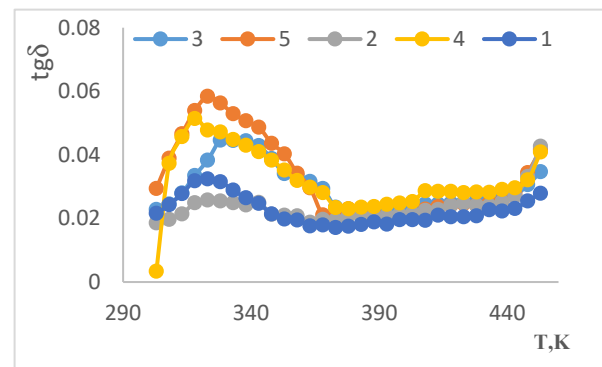


Figure 2b. Temperature dependence of $\varepsilon = f(T)$ and $\text{tg}\delta = f(T)$ after irradiation of the PP/ Na^+ MMT composite with 200 kGy at a frequency of $\nu = 1$ kHz. 1- 0.5%; 2-5%; 3-3%; 4-2%; 5-0%

With a further increase in the radiation dose (300 kGy, Fig. 3(a)), the dielectric constant values change slightly in the temperature range of 320-440 K, and a sharp increase is observed at $T>440$ K. This means that at $T>440$ K, polymer degradation begins due to the interaction of the polymer matrix with radiation defects and filler nanoparticles.

Fig. 3 (b) demonstrates the temperature dependence of $\text{tg}\delta = f(T)$ after irradiation of the PP/(0, 0.5, 2, 3, 5 vol.%) Na^+MMT composite with 300 kGy at a frequency of $\nu = 1$ kHz. Figure 3(b) reveals that in the polymer irradiated at the dose of 300 kGy, $\text{tg}\delta$ does not change in the range of 350-420K, and a sharp increase begins at the subsequent temperature rise (curve 1). In samples with introduced nanoclay (curves 2-5) in the range of 310-350 K, $\text{tg}\delta$ increases slightly after irradiation and then remains constant. At temperatures $T>440$ K a significant increase in $\text{tg}\delta$ occurs, indicating a decrease in the properties of the composite material and the onset of degradation.

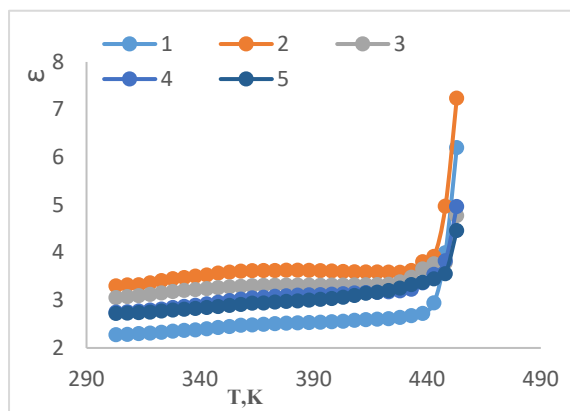


Figure 3a. Temperature dependence of $\varepsilon = f(T)$ after irradiation of the PP/ Na^+ MMT composite with 300 kGy at a frequency of $\nu = 1$ kHz. 1-0%; 2-7%; 3-6%; 4-5%; 5-2%

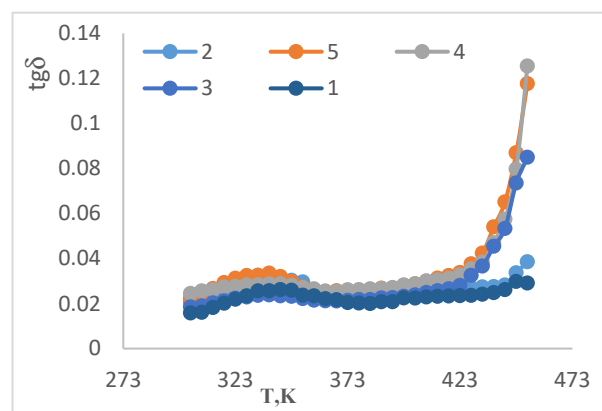


Figure 3b. Temperature dependence of $\text{tg}\delta = f(T)$ after irradiation of the PP/ Na^+ MMT composite with 300 kGy at a frequency of $\nu = 1$ kHz. 1-2%; 2-3%; 3-5%; 4-6%; 5-7%; 6-0%

To study the impact of irradiation on relaxation processes in PP/ Na^+MMT composite, their frequency dependences of $\varepsilon = f(\nu)$ and $\text{tg}\delta = f(\nu)$ at $T = 298$ K were comparatively analyzed. These dependencies allow estimating the intensity of molecular mobility of different relaxing processes. Fig. 4 (a) and (b) represent the dependences of $\varepsilon = f(\nu)$ and $\text{tg}\delta = f(\nu)$ before irradiation measured at a temperature of $T = 298$ K (b). Figure 5 (a) and (b) show the dependences of $\varepsilon = f(\nu)$ (a) and $\text{tg}\delta = f(\nu)$ after irradiation, measured at a temperature of $T = 298$ K.

As is known [11], the transition of the polymer matrix from glassy to highly elastic state in the polymer-filler system leads to a decrease in the orientation stability of dipoles and an increase in the mobility of the polymer chain. And the relaxation properties of the composite depend very strongly on these processes and the measurement temperature. At low temperatures $T \sim 298$ K, Figs. 4(a), 4(b), 5(a), 5(b), relaxation maxima in the dependence of $\text{tg}\delta = f(\nu)$ of the initial and irradiated samples of PP/Na⁺MMT composites are not revealed and only an increase at high frequencies is observed in the measured frequency range.

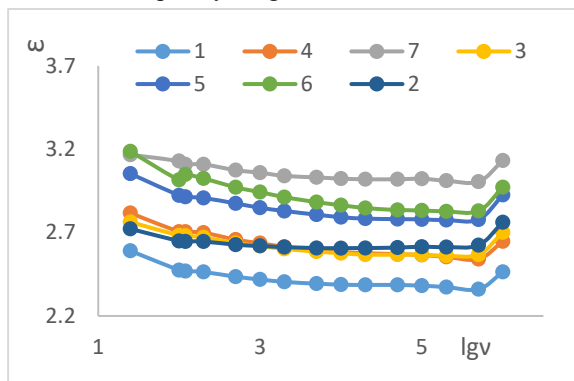


Figure 4a. Frequency dependence of $\varepsilon = f(\nu)$ before irradiation of the PP/Na⁺ MMT composite at a temperature of $T=298$ K. 1-0%; 2-2%; 3-3%; 4-5%; 5-6%; 6-7%

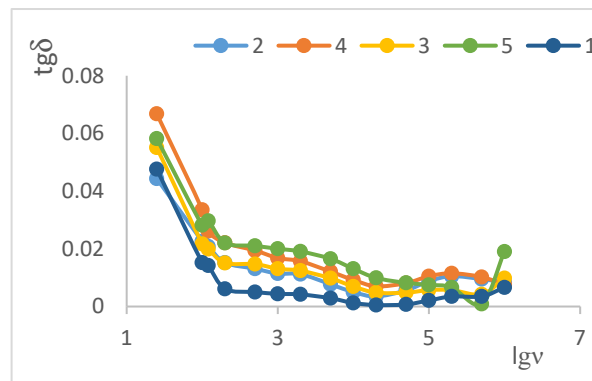


Figure 4b. Frequency dependence of $\text{tg}\delta = f(\nu)$ before irradiation of the PP/Na⁺ MMT composite at a temperature of $T=298$ K. 1-3%; 2-5%; 3-7%; 4-2%; 1-0%

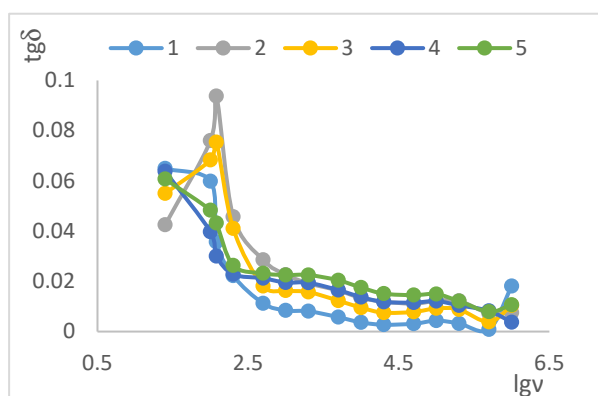


Figure 5 a. Frequency dependence of $\text{tg}\delta = f(\nu)$ after irradiation of the PP/Na⁺ MMT composite with 100 kGy at a temperature of $T=298$ K. 1-0%; 2-0.5%; 3-7%; 4-6%; 5-5%; 6-2%

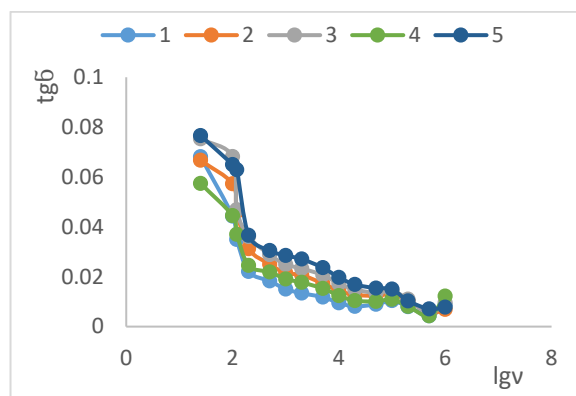


Figure 5 b. Frequency dependence of $\text{tg}\delta = f(\nu)$ after irradiation of the PP/Na⁺ MMT composite with 300 kGy at a temperature of $T=298$ K. 1-0%; 2-0.5%; 3-7%; 4-6%; 5-5%; 6-2%

The findings indicate that after irradiation the formed active centers, radicals and defects in the polymer structure interacting with filler nanoparticles lead to a decrease in the mobility of the polymer chain and, therefore, to a decrease in the values of ε and $\text{tg}\delta$ of the composite. However, at a radiation dose value of 300 kGy, the properties of the interphase layer deteriorate as a result of the onset of degradation, which leads to a minor increase in the values of ε and $\text{tg}\delta$. γ -irradiation is commonly known to ionize the polymer chain, resulting in crosslinking and chain rupture by free-radical mechanism. The forming ions then cause chemical interactions between molecules at different concentrations in the second phase. The degree of crosslinking depends on the polymer structure, phase morphology, gamma irradiation with controlled dose and duration, and the nature of the gamma radiation source.

Based on the literature [12], it is also known that the introduction of fillers into the polymer matrix in composites leads mainly to a decrease in the mobility of the macromolecules of the polymer chain. During gamma radiation exposure, the polymer chains interaction with the filler surface increases during crosslinking and decreases with degradation. The dependence of $\text{tg}\delta = f(\nu)$ makes it clear that the maxima of the samples at radiation doses of 100 and 300 kGy are shifted towards low frequencies relative to the initial one, which is associated with crosslinking and a decrease in the mobility of polymer chains.

The Figure 6 represents the X-ray diffraction patterns of different samples of the composite. As can be seen, with increasing the amount of MMT in the composite, the intensity of the reflexes decreases in the range of values $2\theta=13-25^\circ$. This happens by decreasing the size of PP crystallites, i.e. due to the formation of new supramolecular structures.[13]

According to the results presented, the effect of radiation on the relaxation of volume charges accumulated in the polymer-filler interphase boundary can be observed. In the dependence of $\text{tg}\delta = f(\nu)$ for the initial PP/Na⁺MMT composite, the observed flat maximum measured at a temperature of $T \sim 298$ K consists of two components: the relatively low-frequency one corresponds to the relaxation of the volume charge in the interfacial boundary, and the high-frequency one corresponds to the relaxation dipoles in the matrix.

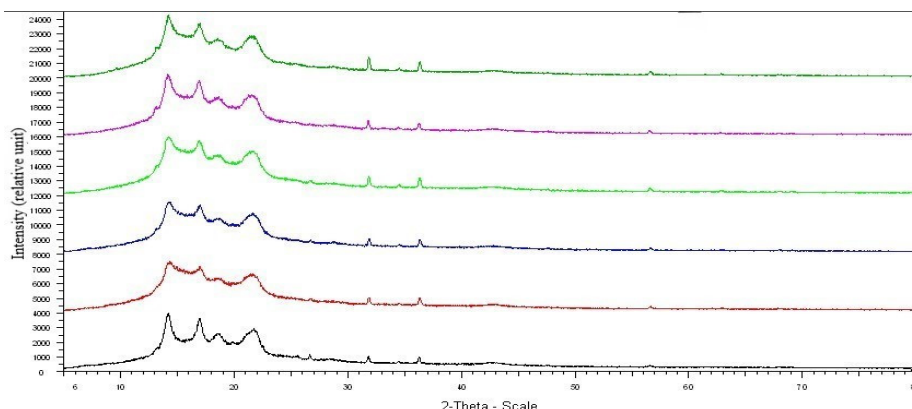


Figure 6. The figure represents the X-ray diffraction patterns of different samples of the composite PP+vol.% Na⁺MMT composite (—) – 0 %; (—)– 2%; (—) - 0,5%; (—) - 3%; (—) - 4%; (—) - 5%.

CONCLUSIONS

Hence, on the basis of investigation of frequency and temperature dependences of dielectric coefficients (ϵ , $\tan\delta$) in γ -irradiated polymer composites with Na⁺ montmorillonite (MMT) nanoparticles, the nature of dielectric losses, crosslinking and degradation mechanism have been revealed.

Having compared the obtaining results of temperature and frequency dependences of electrophysical properties of the initial and γ -irradiated PP/Na⁺MMT composite, it is possible to state that observed changes in these properties are determined by the ratio of crosslinking and degradation processes occurring in the polymer matrix and in the interphase boundary of the polymer with filler. It has been demonstrated that due to γ -irradiation of polymer composites its dielectric and electrophysical properties can be reasonably controlled. This offers opportunities for creating fundamentally new types of products.

ORCID

✉ Rasmiyya L. Mammadova, <https://orcid.org/0000-0003-1179-9252>; ✉ Kamala M. Guseinova, <https://orcid.org/0009-0004-8950-2900>
✉ Kifayat A. Guliyeva, <https://orcid.org/0009-0003-5430-056X>; ✉ Khayal Sh. Valibayov, <https://orcid.org/0009-0005-2353-5950>
✉ Vafa E. Atayeva, <https://orcid.org/0000-0002-9886-2500>; ✉ Dilara M. Qafarova, <https://orcid.org/0000-0002-8927-2592>

REFERENCES

- [1] C.S. Ha, and A.S. Mathews. "Polyimides and High-Performance Organic Polymers," in: *Advanced Functional Materials*, (Springer, Germany, 2011). https://doi.org/10.1007/978-3-642-19077-3_1
- [2] W.K. Busfield, and J.H. O'Donnell. "Effects of gamma radiation on the mechanical properties and crystallinity of polypropylene film," *European Polymer Journal*, **15**(4), 379-387 (1979). [https://doi.org/10.1016/0014-3057\(79\)90157-5](https://doi.org/10.1016/0014-3057(79)90157-5)
- [3] M.Z. Rong, M.Q. Zhang, and W.H. Ruan, "Surface modification of nanoscale fillers for improving properties of polymer nanocomposites: a review," *Mater. Sci. Technol.* **22**, 787-796 (2006). <https://doi.org/10.1179/174328406X101247>
- [4] A. Dutta, and A.K. Ghosh, "Investigation on γ -irradiated PP/ethylene acrylic elastomer TPVs by rheological and thermal approaches," *Radiation Physics and Chemistry*, **144**, 149-158 (2018). <https://doi.org/10.1016/j.radphyschem.2017.11.007>
- [5] A.A. Moez, S.S. Aly, and Y.H. Elshaer, "Effect of gamma radiation on low- density polyethylene (LDPE) films: optical, dielectric and FTIR studies," *Spectrochimica Acta Part A: Molecular and Biomolecular Spectroscopy*, **93**, 203-207 (2012). <https://doi.org/10.1016/j.saa.2012.02.031>
- [6] S. Sinha Ray, and M. Okamoto, "Polymer/layered silicate nanocomposites: a review from preparation to processing," *Progress in Polymer Science*, **28**(11), 1539-1641 (2003). <https://doi.org/10.1016/j.progpolymsci.2003.08.002>
- [7] N. Gasanov, F. Khallokov, et al. "Optical Absorption Edge of $\text{TiIn}_{1-x}\text{Yb}_x\text{S}_2$ Single Crystals and the Effect of Electron Irradiation on their Bandgap," *Norwegian Journal of development of the International*, (124), 86-90 (2024). <https://zenodo.org/records/10515000>
- [8] R.S. Madatov, R.M. Mamishova, A. Abasova, and Sh. Alahverdiyev, "Differential-thermal analysis and a microscopic study of the effect of γ -radiation on CuTiSe_2 single crystal," *International Journal of Modern Physics B*, **37**(30), 2350265 (2023). <https://doi.org/10.1142/S021797922350265X>
- [9] M.A. Ramazanov, S.A. Abasov, R.L. Mamedova, and A.A. Rasulova. "Effect of the Structure and Charge State on the Strength Properties of Nanocomposites Based on PP + Dk_2 Films," *Surface Engineering and Applied Electrochemistry*, **47**(6), 481-483 (2011). <https://doi.org/10.3103/S1068375511060160>
- [10] A. Sukhanova, A. Boyandin, N. Eriletskaya, T. Shalygina, A. Shabanov, A. Vasiliev, I. Obvertkin, et al. "Composite Polymer Granules Based on Poly- ϵ -Caprolactone and Montmorillonite Prepared by Solution-Casting and Melt Extrusion," *Polymers (Basel)*, **15**(20), 4099 (2023). <https://doi.org/10.3390/polym15204099>
- [11] A.A. Bakhsh, "Gamma-Ray Modified Polymer/Clay Composites: Synthesis, Characterization, and Formulation Optimization Using Multivariate Calculus and Graph Theory," *Energies*, **14**(9), 2724 (2021). <https://doi.org/10.3390/en14092724>
- [12] R.S. Madatov, and R.M. Mamishova, "A study of the effect of γ -radiation on the current-carrying mechanism in the P- CuTiS_2 single crystal," *J. Modern Physics Letters B*, **38**(30), 2450295 (2024). <https://doi.org/10.1142/S0217984924502956>
- [13] M.E. Gouda, and T.Y. Elrasasi, "Impact of gamma irradiation on structural and dielectric properties of CuI-PVA/PEDOT : PSS polymer nanocomposite," *IOSR J. Appl. Phys.* **7**, 22-30 (2015). <https://www.iosrjournals.org/iosr-jap/papers/Vol7-issue6/Version-2/D07622230.pdf>

**ВПЛИВ ГАММА-ОПРОМІНЕННЯ НА ДІЕЛЕКТРИЧНІ ВЛАСТИВОСТІ ТА РЕНТГЕНОФАЗОВИЙ АНАЛІЗ
КОМПОЗИТУ ПОЛІПРОПІЛЕН Na+МОНТМОРИЛОНІТ****Расмія Л. Маммадова^a, Камала М. Гусейнова^{b,c}, Кіфаят А. Гулієва^b, Хаял Ш. Валібайов^d,****Вафа Е. Атаєва^d, Ділара М. Кафарова^e**^a*Карабахський університет, Ханкенді, Азербайджан*^b*Сумгайтський державний університет, Сумгайт, Азербайджан*^c*Хазарський університет, Баку, Азербайджан*^d*Шекінський регіональний науковий центр, Шекі, Азербайджан*^e*Азербайджанський університет архітектури та цивільного будівництва, Баку, Азербайджан*

Досліджено вплив γ -опромінення на діелектричні властивості полімерних композитів на основі поліпропілену (ПП) з наночастинками Na⁺-монтморилоніту (ММТ). Було виявлено, що γ -опромінення в діапазоні доз 100-200 кГр призводить до незначного погіршення залежностей $\epsilon = f(T)$ (а) та $\text{tg}\delta = f(T)$ композиту на основі поліпропілену з наповнювачем Na+ММТ. При подальшому збільшенні дози опромінення спостерігається різке збільшення ϵ та $\text{tg}\delta$ вище температури ~ 440 К. Отримані результати показують, що після опромінення активні центри, радикали та дефекти, що утворюються в структурі полімеру, взаємодіють з наночастинками наповнювача, зменшуючи рухливість полімерного ланцюга та, як наслідок, зменшуючи значення ϵ та $\text{tg}\delta$ композиту. Але при дозі опромінення 300 кГр властивості міжфазного шару погіршуються внаслідок початкового руйнування, що призводить до незначного збільшення значень ϵ та $\text{tg}\delta$. Результати аналізів показали, що введення наноглин Na (ММТ) у поліпропілен у кількості 0,5% за об'ємом призводить до деякого покращення діелектричних властивостей до та після опромінення. Вважається, що погіршення діелектричних властивостей під час опромінення в композитах відбувається через зміни процесів зшивання та руйнування в полімерній матриці та на міжфазній межі полімер-наповнювач. Показано, що завдяки γ -опроміненню полімерних композитів можна доцільно контролювати їх діелектричні та електрофізичні властивості.

Ключові слова: поліпропілен; Na⁺-монтморилоніт; гамма-опромінення; діелектрична проникність; втрати діелектричної енергії